University of Nottingham
UK | CHINA | MALAYSIA

Ensuring the quality of components produced by metal additive manufacturing using laser generated ultrasound

Sarah Everton MEng (Hons)

Thesis submitted to University of Nottingham
for the degree of Doctor of Engineering

October 2017

Abstract

Laser powder bed fusion offers many advantages over conventional manufacturing methods, such as the integration of multiple parts which can result in significant weight-savings. The increased design freedom that layer-wise manufacture allows has also been seen to enhance component performance at little or no added cost. However, for such benefits to be realised, the material quality must first be assured.

Laser ultrasonic testing is a non-contact inspection technique which has been proposed as suitable for in-situ monitoring of metal additive manufacturing processes. The thesis presented here explores the current capability of this technique to detect manufactured, seeded and process generated sub-surface “defects” in Ti6Al4V samples, ex-situ. The results are compared with X-ray computed tomography reconstructions, focus variation microscopy and destructive testing.

Whilst laser ultrasound has been used to successfully identify a range of material discontinuities, further work is required before this technique could be implemented in-situ.

Acknowledgments

I would like to thank my supervisors Phill Dickens, Chris Tuck and Ben Dutton for their guidance and encouragement proffered throughout the duration of my EngD.

I am thankful for the assistance offered by many of the staff and technicians at the University of Nottingham within the Centre for Additive Manufacturing and Manufacturing Metrology teams. At Manufacturing Technology Centre, I am grateful for the help offered by both the Additive Manufacturing and Non Destructive Testing and Metrology groups.

The funding provided by University of Nottingham, Manufacturing Technology Centre and Engineering and Physical Sciences Research Council under Award No. 1361477 is kindly acknowledged.

Lastly, I would like to give my heartfelt thanks to my Family and Friends for their unwavering love and support.

Contents

List of figures and tables

Figures

Tables

Acronyms and nomenclature

List of acronyms

2D	Two dimensional
3D	Three dimensional
AC	Alternating current
AM	Additive manufacturing
ASTM	American society for testing and materials
CAD	Computer aided design
COM	Communication port
DC	Direct current
DDC	Ductility dip cracking
DED	Directed energy deposition
DMLS	Direct metal laser sintering
EDM	Electrical discharge machining
FEA	Finite element analysis
FEM	Finite element modelling
FFT	Fast Fourier transform
FVM	Focus variation microscopy
GA	Gas atomised
HAZ	Heat affected zone
HIP	Hot isostatic pressing
ISO	International Organisation for Standardisation
L	Longitudinal
LU	Laser ultrasound
MD	Manufactured defect
MTC	Manufacturing Technology Centre
Nd:YAG	Neodymium-doped yttrium aluminium garnet
NDT	Non-destructive testing
OH	Over heating
PBF	Powder bed fusion

PC	Personal computer
PD	Process defect
PREP	Plasma rotated electrode powder
R	Rayleigh
S	Shear
SAC	Strain age cracking
SD	Seeded defect
SEM	Scanning electron microscope
SIG	Special interest group
SLM	Selective laser melting
TGM	Temperature gradient mechanism
UK	United Kingdom
UoN	University of Nottingham
XCT	X-ray computed tomography

Nomenclature

Hz	Hertz
Sq	Area roughness parameter
W	Watts

Chapter 1 - Introduction

Additive manufacturing (AM) has matured rapidly in recent years due to a developed understanding of AM processes and materials and the ever-increasing understanding and sharing of the underlying design principles. As a result, technology growth has been reported annually in the Wohler's report, across many manufacturing sectors [1]. For aerospace in particular, the potential to reduce leadtimes, weight and cost appeals, as does the increased design freedom [2]. However, further exploitation is currently hindered by a lack of material quality and quality assurance. In-situ monitoring and closed-loop control of AM processes have been identified as a priority areas for research and development in the AM field [3, 4].

The laser powder bed fusion (PBF) process has a large number of input parameters, some of which are interdependent [5]. In order to produce components with sufficient material integrity for the aerospace sector, an understanding of the effect of changing these parameters is required and consequently, many studies have been undertaken [6, 7]. A wide range of "defects" are known to occur during AM processing, the most common of which are material discontinuities such as pores, inclusions and cracks [8].

Porosity is considered most significant as pores reduce the effective load carrying capacity of a material and also act as stress concentrators, providing effective crack initiation sites [9]. Pores can be further categorised by size, shape and content such as "spherical, gas filled" [10], "elongated, powder filled" [11, 12] or "keyhole" pores [13].

For every alloy, a processing window can be determined which indicates the AM processing conditions necessary to manufacture "fully dense"

parts [14]. Outside of this window, the different types of pores can result from a variety of processing conditions. When excess energy is applied to the powder bed, the over-melting regime is entered, also known as "conduction mode" and with sufficient energy, the transition to "keyhole mode" is made [13]. Conversely, if insufficient energy is applied to the powder bed, irregular, elongated pores can result. Selection of parameters which allow an insufficient overlap of adjacent meltpools in a single layer can also yield irregular, elongated pores [15].

Ideally, these "defects" would be eradicated as process understanding matures and a tighter control of input parameters is achieved. However, for applications where material integrity must be ensured, in-situ monitoring will allow for identification of any "defects" during manufacture.

Many non-destructive, monitoring methods for laser-PBF and electron beam-PBF have been explored to date to aid process understanding [16], but could also be implemented for in-situ inspection. Thermographic [17-20] and visual monitoring methods [21-26] are common, but are limited to observing only the surface of the AM build. Ultrasonic devices would enable sub-surface inspection, but are limited by their inability to operate on rough, AM surfaces, irregularly shaped objects and at high temperatures.

Laser generated ultrasound (LU) is well suited to in-situ inspection of AM processes. Laser techniques are non-contacting, thus do not exhibit any coupling problems; they can be used for rapid scanning and are amenable to use in hostile environments. Although LU has been shown to be capable of detecting the types of "defects" generated during additive manufacture [27, 28], there have been a limited number of experiments

applying laser ultrasonic inspection directly to additively manufactured materials [29-31].

In this study, LU was successfully investigated on Ti6Al4V test pieces built by laser powder bed fusion, both on as-built and post processed surfaces and with artificial “defects”, manufactured by wire electrical discharge machining (EDM), as well as on samples with seeded, powder filled voids. The LU system has been investigated on samples designed to include a “defect zone” embedded close to the surface, within a fully dense block. X-ray computed tomography (XCT) has been used for validation and focus variation microscopy (FVM) used to analyse the sample top surface.

For the first time, a comprehensive overview of laser PBF “defect” types and generation mechanisms has been collated and this understanding has been utilised to manufacture samples with both isolated material discontinuities and zones of material discontinuities, intentionally. LU has been carried out on as-built laser PBF surfaces to detect post-build, manufactured “defects” and “defects” generated through manipulation of the AM build file and build parameters.

This thesis is comprised of six main chapters. In the first chapter, a comprehensive review of literature pertaining to the above topics is given, including an overview of additive manufacturing, material discontinuities and non-destructive testing techniques previously investigated. In the second chapter, the theory of ultrasound is explained, in particular the generation and detection of ultrasound, using lasers. The AM and LU equipment used is also detailed and the procedures for experimental work and post-processing of the resulting data are discussed.

In Chapter 4, results from LU scanning on test pieces with different surface roughness conditions and with manufactured through holes are presented. In Chapter 5, a method for artificially creating voids at a known location within a test piece manufactured by laser powder bed fusion is investigated. In Chapter 6, AM build parameters are manipulated to try and replicate the conditions which promote the formation of naturally occurring porosity.

Chapter 7 explores an alternative method for establishing the window of detection for the LU system using finite element analysis (FEA). The methodology presented, using sequential transient FEA analysis to create B-scans for LU is novel.

Conclusions are collated in Chapter 8 and opportunities for future work in this field are outlined. A full list of all references used throughout the preceding chapters is presented in Chapter 9 and supporting documentation made available as appendices in Chapter 10.

Chapter 2 - Literature review

2.1 Introduction

In this chapter, an overview of each powder bed fusion (PBF) process is given and the advantages and disadvantages of production by additive manufacturing (AM) outlined. Ensuring the quality of components produced by AM methods has been identified as a key barrier for uptake of these technologies. A comprehensive review of the types of material discontinuities which can form during laser-PBF processing is followed by a review of non-destructive testing (NDT) methods investigated to date. Laser ultrasonic testing is identified as a potential method for in-situ monitoring of laser-PBF. A review of current and past projects carried out is presented, for both experimental and simulated/modelled work. Areas for development of work and new research opportunities have been identified.

2.2 Additive manufacturing

Additive manufacturing is defined as "the process of joining materials to make parts from 3-D model data, usually layer upon layer, as opposed to subtractive manufacturing and formative manufacturing methodologies" [32]. There are seven classifications which are used to group similar AM technologies together: binder jetting, directed energy deposition (DED), material extrusion, material jetting, PBF, sheet lamination and vat photopolymerisation. The focus of this work is on the metal PBF process which has the potential for use in the aerospace sector for the manufacture of production parts.

Historically, a number of terms have been used to refer to the various AM processes, with a manufacturer often adopting its own term, in some

cases a registered trademark. Common terms are outlined in Table 1 which has been adapted from the ASTM classifications [33].

Table 2-1 - AM terminology

ASTM classification	AM process	Machine manufacturer	Commercial name
Powder bed fusion (PBF)	Laser -PBF	EOS	Direct metal laser sintering (DMLS)
		Concept Laser	LaserCUSING
		Renishaw	Selective laser melting (SLM)
		Realizer	Selective laser melting (SLM)
		Phenix	Selective laser melting (SLM)
		Matsuura	Selective laser melting (SLM)
	Electron beam-PBF	ARCAM	Electron beam melting (EBM)

2.2.1 Powder bed fusion

Information relating to the PBF processes, including operation and feedstock used is presented here. Although grouped in a single category within the AM hierarchy, there are a number of differences between the laser and electron beam PBF processes. Each process is introduced in more detail and the key differences highlighted below:

2.2.1.1 *Processing*

The powder bed fusion processes are layer-wise technologies which directly melt metal, using a high-power source such as a laser or electron beam. The process steps for both laser-PBF and electron beam-PBF are broadly the same and are shown in Figure 2-1.

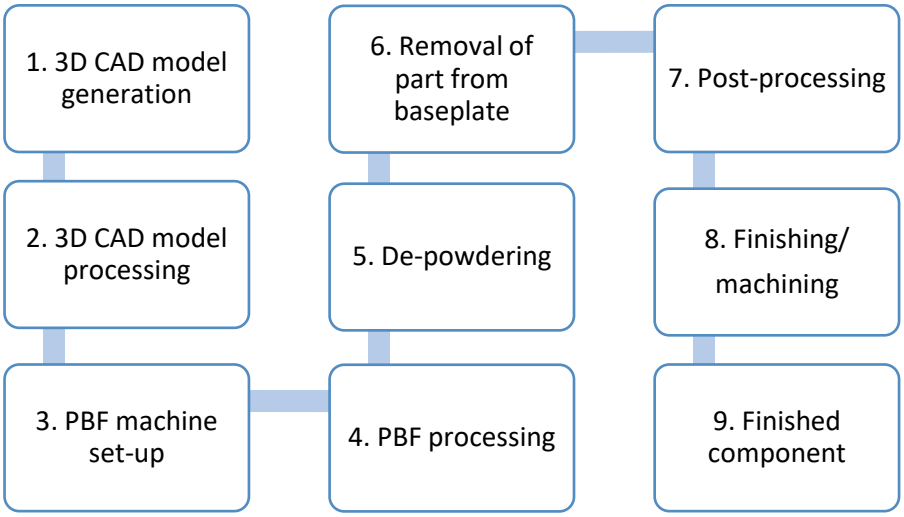

Figure 2-1 - Flow diagram of typical PBF manufacturing process.

1. A 3-D geometry of the desired component is first created using a computer aided design (CAD) software package.
2. The geometry is then loaded into an AM file editor such as OpenSTL™ or Materialise Magics™. Historically, a '.STL' file has been used, but industry is moving towards using an 'Additive Manufacturing File' ('.AMF') as outlined in the ASTM International standard F2915-12 [34]. In the editor, the file is "fixed", prepared and enhanced before being oriented on the virtual build platform. Any required supports are added before the file is sliced and outputted to the PBF machine [35].
3. The build platform is prepared and inserted into the machine. The input parameters are selected and powder added to the feed system.
4. During PBF processing, the energy source is directed in a pre-defined pattern, fully melting the desired area of powder. The build platform is then lowered and a fresh layer of powder is delivered. The bed is adjusted by a pre-defined increment normal to the build plane and the build process is repeated until all of the layers have been melted; the repeated stage of the PBF process is shown in Figure 2-2.

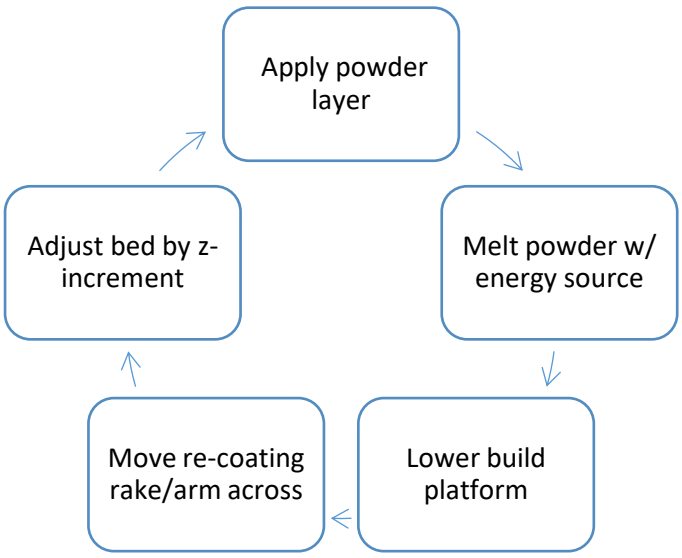

Figure 2-2 - Repeated steps of EBM process.

5. Once the build has been completed, the component is then extracted from the resulting volume of powder and the unprocessed powder subjected to recycling, where possible.
6. The component can now be removed from the baseplate. Alternatively, stress-relieving heat treatments can be applied at this stage, prior to removal of the component from the build plate.
7. Removal of any build supports takes place next.
8. Due to the "rough" nature of the PBF surfaces, surface finishing and conventional machining of any interfaces is sometimes necessary.
9. The finished component is subject to a final inspection before being packed for delivery or sent for assembly.

2.2.1.2 *Feedstock*

A powder feedstock used for PBF processes, stored in a hopper until needed, is then spread thinly over the processing surface by a recoating arm or rake. In the case of metallic processing, it is known that the homogeneity of the powder layer relates directly to the final quality of the material (see section 2.4 Material discontinuities).

The pre-alloyed powders used are typically specified to have particle size distributions in the range 45 - 100 μm for electron beam [36] and <70 μm for laser PBF [37].

There are a number of ways in which the powder can be manufactured, the most common being by 'gas atomisation' (GA) or the 'plasma rotating electrode process' (PREP). GA powder is produced by pouring molten metal through a tundish nozzle. As the molten metal falls under gravity, droplets form which are quenched by the atomisation ring of high pressure gas jets, forming powder particles [38]. PREP is a centrifugal atomisation process during which molten metal from a rotating consumable bar forms droplets which cool into spherical powder particles. The bars are typically 60 - 65 mm in diameter and rotate at up to 15,000 rpm [39]. The scanning electron microscope (SEM) images shown in Figure 2-3 allow a visual comparison of powders produced by each of the two methods.

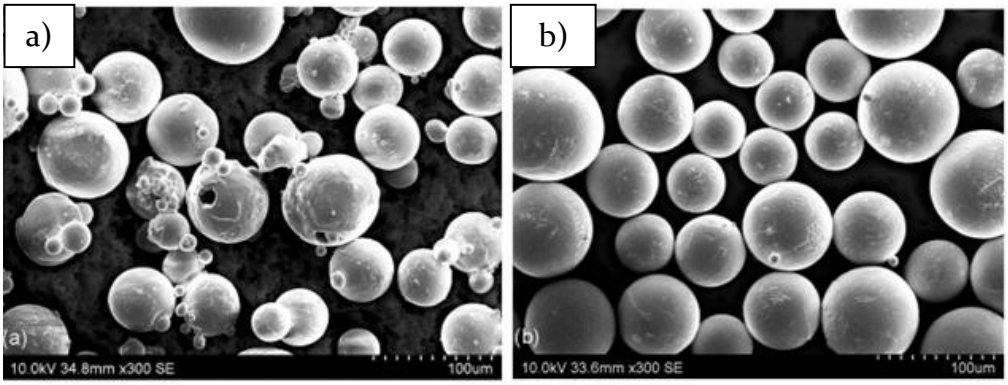

Figure 2-3 - SEM images of Ti6Al4V powder showing surface morphology: (a) GA; (b) PREP [40].

GA produces powder with a wider particle size distribution, with smaller particles present. The powder has an approximately spherical morphology with rough surfaces. There is a high affinity for particles to agglomerate, forming satellites. It should also be noted that the GA

powder shows some surface pores. In contrast, the PREP powder particles have a narrower size distribution and are generally larger. The surfaces are predominantly smooth and the particles are mostly singular in nature [40]. This is an advantage as powder flowability and packing density are greatly increased [41].

For further information about powder feedstock, the reader is directed to the comprehensive review authored by Dawes, Bowerman and Trepleton [42].

2.2.1.3 *Laser-PBF*

There are many manufacturers of laser-PBF machines such as Renishaw, EOS and Concept Laser. Each have their own features, but all operate on broadly the same principles. A schematic of a typical laser-PBF machine is shown in Figure 2-4.

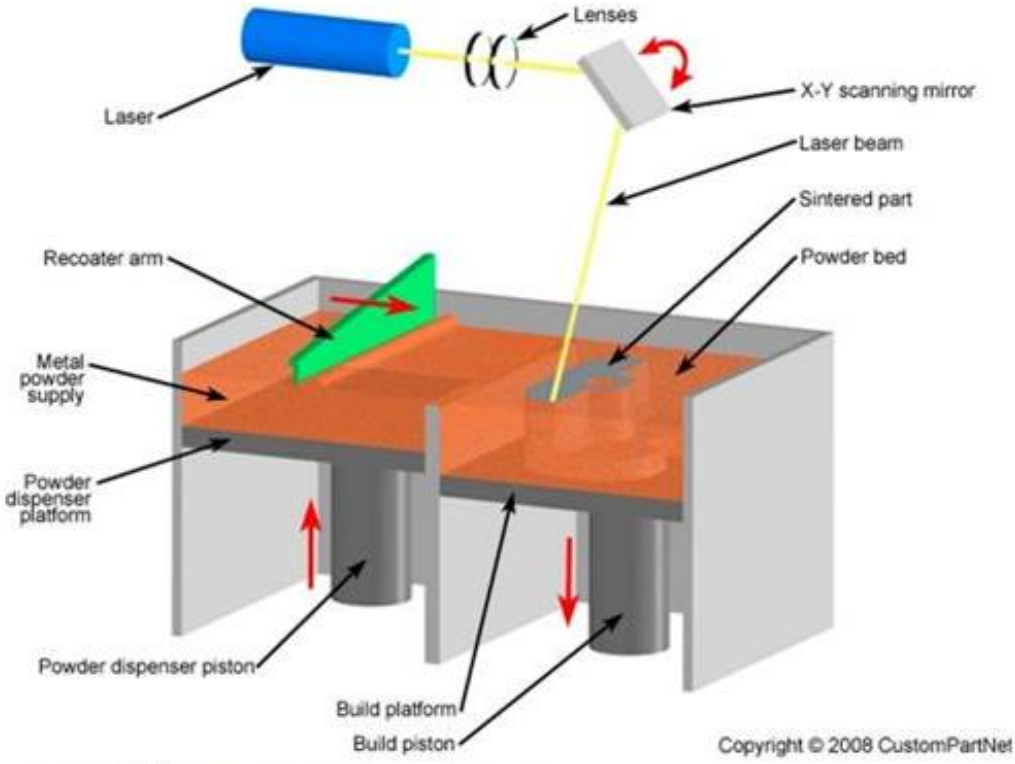

Figure 2-4 - Schematic showing laser-PBF hardware [43].

There are over fifty input factors to consider when setting up a laser PBF build, with processing taking place in a controlled atmosphere, usually Argon for reactive materials [44]. A laser beam (200 W – 1 kW) is focussed and directed using a series of lenses and a galvanometer to melt powder below in the pre-defined pattern. The build volume limits the size of components with most industrial systems using 250 mm *x* 250 mm or 400 mm *x* 400 mm build plates. Scanning speeds up to 2000 mm s^{-1} and a powder layer thickness of 20-100 microns [45] are typical. Scanning speeds are limited by the galvanometer inertia and consequently, laser-PBF is considered a "slow" process [46].

Processing is carried out at a relatively low temperature and no pre-sintering is needed, therefore removal of unmelted powder post-build is straightforward and powder recycling procedures are simplified. Cooling

from this comparatively low processing temperature takes a short amount of time, meaning that the time between subsequent builds is reduced.

In order to limit component distortion caused by the high levels of residual stress inherent in a build, strong supports are required to anchor the component to a build plate. Removal of the component from the build plate and support structures adds an extra process step.

2.2.1.4 *Electron beam-PBF*

The Swedish company Arcam AB are currently the sole manufacturer of patented electron beam PBF machines although a system by scanning electron microscope company, JEOL USA, is thought to be close to market. The Arcam AB system is shown in Figure 2-5 [47]. The machines use an electron optical system similar to those used for scanning electron microscopes (SEM) and electron beam welding units and their processing rates are much higher than for laser-PBF.

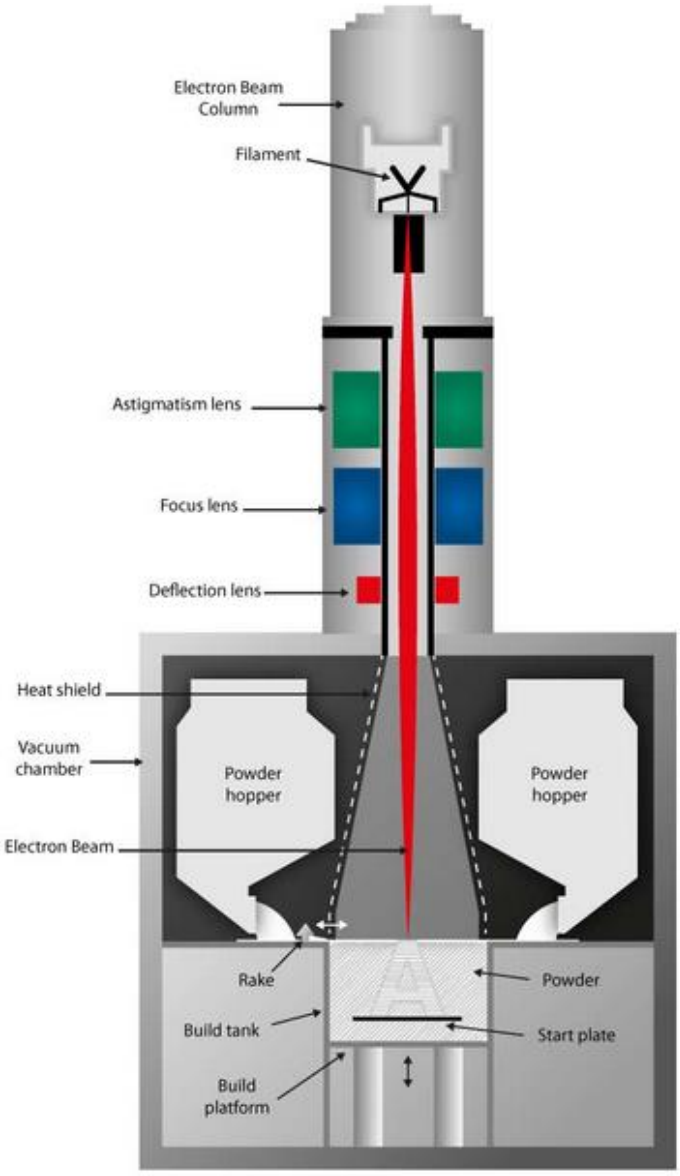

Figure 2-5 – Schematic showing electron beam-PBF hardware [48].

The electron gun, generates an electron beam which is focussed and then deflected by a series of lenses and electromagnetic coils, directing the beam across the build envelope. The process takes place at high temperature in a near vacuum, and claims to produce stress relieved components with material properties comparable to worked, wrought alloys [17].

For common Titanium alloy Ti6Al4V, the start plate is heated to approximately 750 °C [49] and the powder is preheated using a low beam current to above 600°C, causing the small powder particles present to partially or completely melt, bonding the larger particles together as a binder might do [50]. If the powder wasn't sintered, the impact of the electron beam could cause the powder particles to be pushed away, potentially forming material discontinuities. The preheat phase also reduces the thermal gradient between the melted layer and the rest of the powder, thereby reducing the residual stress within the part [51]. As a result of the preheating, a partially sintered block is produced, with the fully melted components inside; removal of powder from internal channels can be difficult.

Due to the high processing temperatures, long cooling cycles are required before builds can be removed and the machines re-set. It should also be noted that only electrically conductive alloys can be processed by electron beam-PBF. Although the processing rate for electron beam-PBF is in the region of four times faster that of laser-PBF, there is a trade off with reduced dimensional accuracy and increased surface roughness of the final component.

2.3 Aerospace drivers for additive manufacturing

AM has matured rapidly in recent years due to development of AM processes and materials and an ever-increasing understanding of the underlying design principles. As a result of these developments, commercial exploitation of AM has been seized by industrialists across many manufacturing sectors, particularly Aerospace [52]. The opportunities AM avails and the barriers to adoption of AM technology for the sector are discussed below.

2.3.1 Opportunities

With the introduction of layer-wise manufacturing techniques, some of the current limitation of design for manufacture by conventional means no longer exist. A designer no longer needs to consider access paths for conventional tooling, or be constrained to specifying constant cross-section channels in subtractively manufactured components. For applications such as aero-engine design where the movement of air and oil for optimised cooling can produce enormous performance benefits, manufacture by AM is particularly attractive. Cooling channels can be directed to avoid overheating at known hotspots and channel shapes and areas can be modified to control flow further.

Additionally, engine performance could be improved further by utilising lattice structures to save weight (Figure 2-6). Softwares are being developed to biomimetically optimise components based on their strength requirements during operation. An added benefit of designing lattice structures is the cost savings made by reducing material waste.

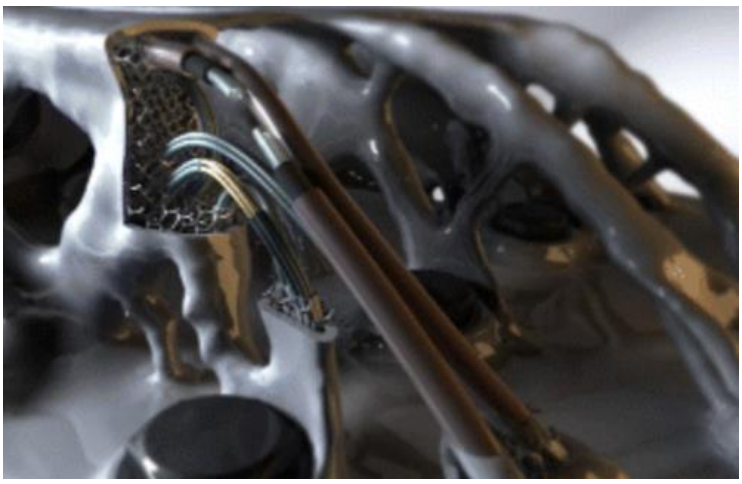

Figure 2-6 - Example of lattice structures utilised for lightweight component design [53].

Even without implementing a design for AM approach, using AM for manufacture of development components can significantly shorten the manufacturing leadtimes for designs. The lack of tooling required means that a greater number of design iterations can be trialled in a fixed time, meaning a more mature product reaching the market, or instead the development programmes can be shortened.

2.3.2 Barriers

Whilst the benefits of AM are abundant, the rapid development of the technology gives rise to a number of challenges which need to be overcome before widespread uptake. In particular, the supply chain for raw materials, AM processing and post processing are not mature enough to handle full scale production rates. Many of the aerospace manufacturers are looking to in-house solutions, in collaboration with machine manufacturers, however, the initial capital outlay required is significant. The limited processing rates of current PBF machines is a major contributor to the high cost of manufacture of AM components. Selection of components is also restricted by the limited build volumes available. In order to fully realise the benefits of AM, components must

be designed specifically with AM in mind and as yet, a set of proven design rules has not been published and endorsed by any of the global standards committees or AM organisations.

The greatest single barrier is that of materials. The choice of materials for AM is growing at a rapid rate, but the characterisation of materials created by AM is very expensive and extremely time consuming. Ensuring the quality of components is essential.

The 2012 report issued by the UK AM special interest group (SIG) titled "Shaping our national competency in additive manufacturing" highlights a lack of robust AM processes as a key barrier to the adoption of AM in the UK. A critical factor to this deficiency is the limited control and monitoring of processes, in-situ [33]. In-situ data acquisition, in order to enable closed-loop control and detection of material discontinuities, was similarly highlighted as a key barrier to implementation and as a priority area for research and development in the US National Institute of Standards and Technology 2013 "Measurement science roadmap for metal-based additive manufacturing"[3]. The layer-wise nature of AM allows an opportunity to identify these discontinuities and re-process an area to "heal" it, using closed-loop control.

2.4 Material discontinuities

There are a number of different types of material discontinuities which can be generated during laser-PBF processing which could detrimentally affect the final performance of a component. It is useful to categorise the different material discontinuities produced, based on their appearance. Explanations of the mechanisms by which these "defects" are generated are given and these are linked to the process inputs selected and the resulting processing conditions. Understanding the conditions under which "defects" are generated and simplifying the terminology used to describe these "defects" will aid the drive for quality improvement required for widespread implementation of the technology.

The flowchart displayed in Figure 2-7 summarises the links found in literature between inputs that have been selected incorrectly or errors made when setting up a build (green), the ensuing processing condition (red) and the material discontinuity which results (blue). The orange arrows are used where a link has been found. Importantly, the generation of one "defect" type can result in a processing condition which generates a second and so on.

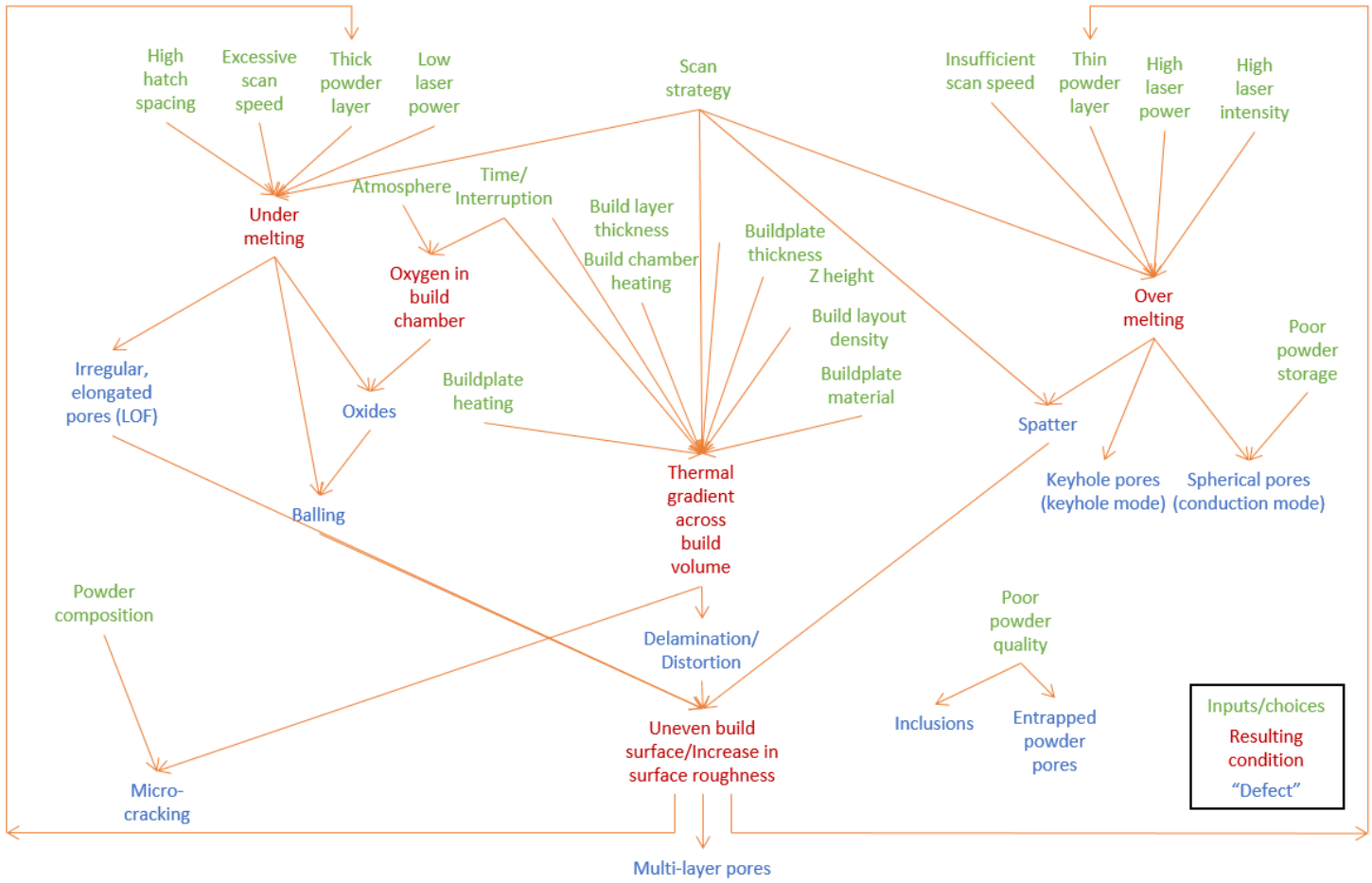

Figure 2-7- Flowchart showing laser PBF inputs (green), processing conditions (red) and resulting "defects" (blue).

2.4.1 Pores

Porosity is a term used to express the volume of voids (empty spaces) within a material and is usually conveyed as a percentage density. Pores or voids act as stress concentrators, which can promote early onset plasticity and localisation of strains, adversely affecting the material performance [10]. As such, understanding the different mechanisms that are responsible for the generation of different types of pores within AM materials is key.

Pores can result under a variety of different processing conditions. Figure 2-8 shows the relative density of different parts produced with varying scan speeds and laser powers in aluminium alloy $AlSi_{10}Mg$ [11]. The identified trends for each set power indicate a transition from porosity caused by over-melting to porosity caused by under-melting, each of which yield different pore types.

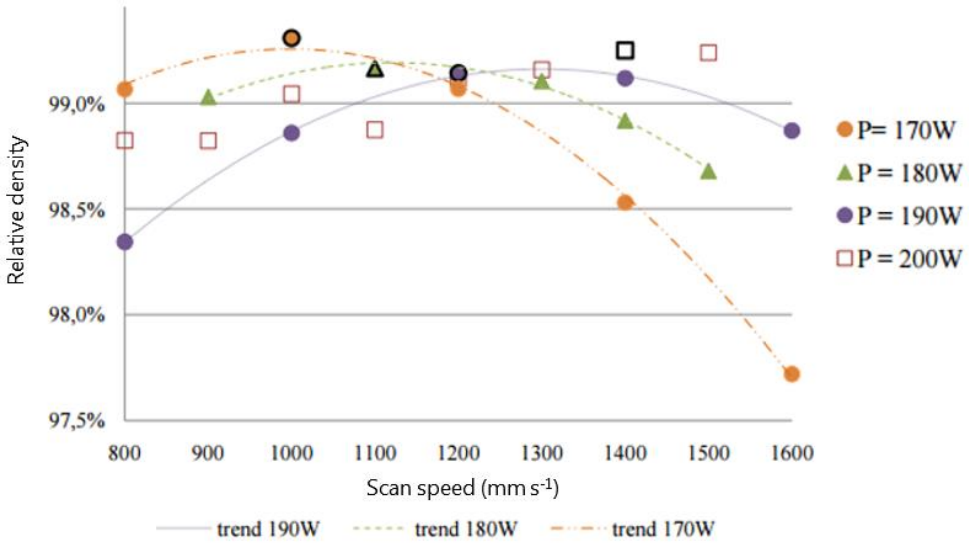

Figure 2-8- Relative density of AlSi10Mg parts produced at different scan speeds and laser powers produced by laser-PBF [11].

For each alloy, a processing window can be determined such as the one shown in Figure 2-9. In this case, components produced in Zone I are classed as "fully dense", Zone II indicates conditions for over-melting and Zone III for under-melting. In the "OH" zone, extreme over-melting results in an incomplete build.

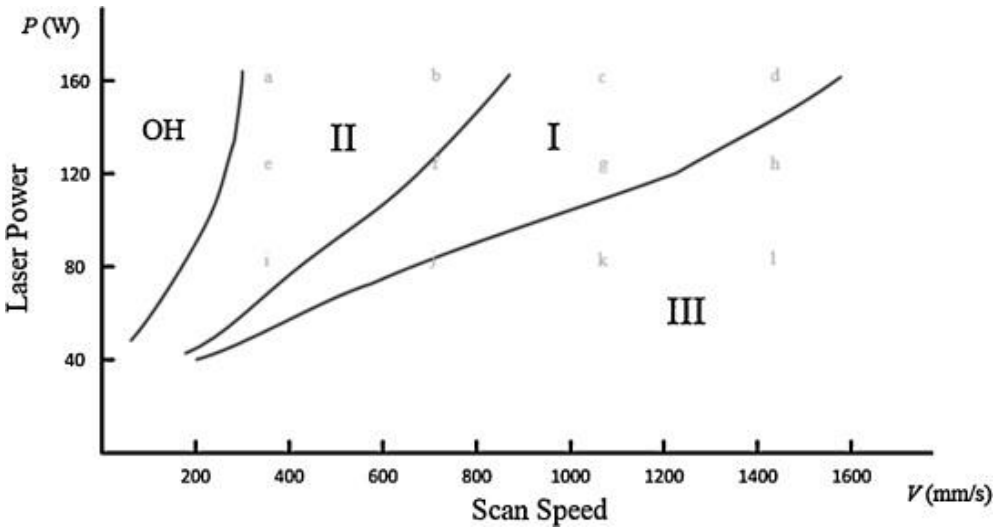

Figure 2-9 - Process window for laser-PBF of Ti6Al4V with 30 µm layers and fixed hatch spacing [14].

2.4.1.1 *Over-melting*

Over-melting conditions result when excess energy is applied to the powder bed. As with laser welding, the selection of laser power, scan speed and beam size affects whether conditions for "conduction mode" or "keyhole mode" are met; each mode yields pores with different characteristics. In "conduction mode", the depth of the meltpool is controlled by thermal conductivity of the surrounding material [13] and the meltpool depth is typically equal to half the meltpool width [54]. In "keyhole mode", the power density of the laser beam is sufficient to cause evaporation of the metal and the formation of a plasma above the meltpool. The presence of the vapour cavity enables deeper penetration of the laser and meltpool depths of up to six times the meltpool width result [13]. The images in Figure 2-10 show

meltpool cross sections for the transition from over-melting conditions (bottom left) to under-melting (top right) [12]. The transition from "conduction" to "keyhole" mode melting for an alloy can be expressed in terms of a normalised enthalpy, but is dependent on the powder thickness and powder size distribution [13].

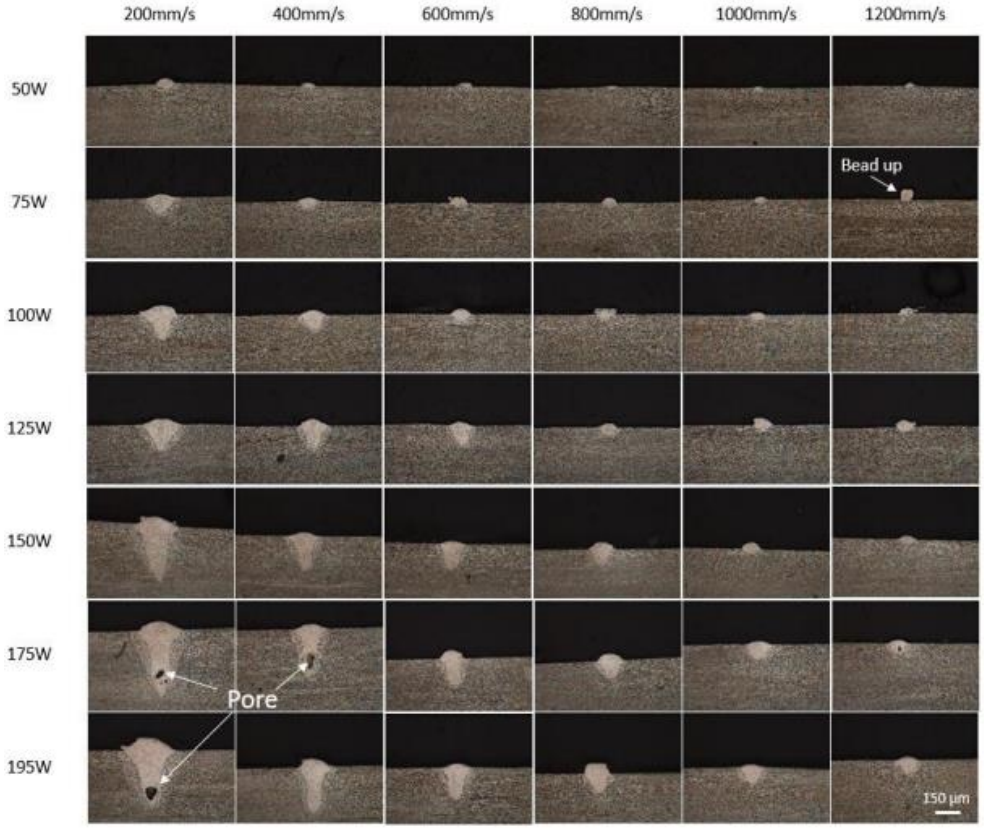

Figure 2-10 - Cross-sections showing series of meltpool depths with transition from conduction to keyhole mode melting [12].

2.4.1.1.1 Conduction mode - Spherical pores (gas porosity)

Spherical, gas filled pores result when gas bubbles form due to vaporisation of low melting point alloy constituents, as a consequence of over-melting. Gas pores are distinguished by their spherical shape and are thought to form before and/or during solidification (as a bubble must be supported by the surrounding liquid as is cools to keep its shape) [55]. Spherical pores are typically smaller than 100 µm in diameter and show high levels of circularity [56], as seen in Figure

2-11a. As the trapped bubbles form within previously processed layers of the material, they are not always evident on the processing surface [57], but can be seen when sectioning through a sample.

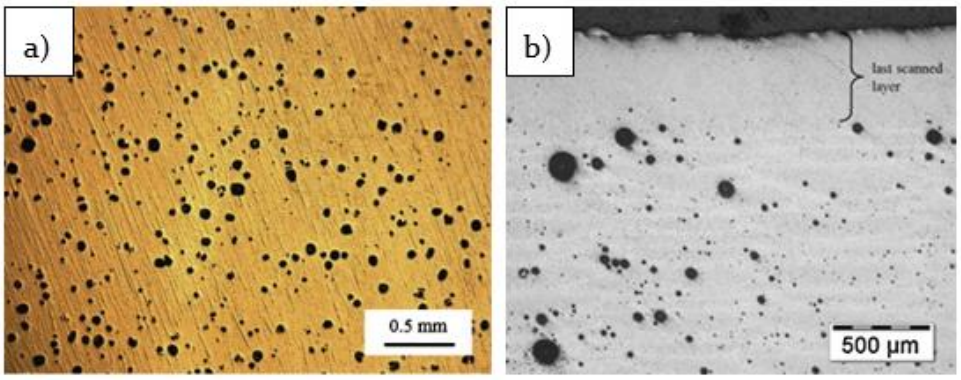

Figure 2-11 – a) Cross section of Ti6Al4V sample (parallel to top surface) [57] and b) cross section of AlSi10Mg sample (side section) [55].

In aluminium alloys, spherical pores are attributed to hydrogen porosity. Hydrogen pores result when the local hydrogen content in the meltpool exceeds the maximum solubility in liquid aluminium. The use of a high laser power and reduced scan speed increases the size of the heat affected zone (HAZ) created around the meltpool. In the HAZ, under these conditions, trapped hydrogen can diffuse in the already existing pore nuclei, increasing the density of pores (Figure 2-11b). A powder drying strategy can be used on Aluminium alloys to eliminate moisture as a hydrogen source [55].

In general, decreasing the melt pool solidification rate allows time for gas bubbles to escape and reduces the overall porosity level. In samples with high levels of porosity, larger spherical pores are found. It is believed that when high temperatures are sustained, pore growth is promoted [10]. Utilising an AM scan strategy which decreases the melt pool solidification rate thereby promoting a slower cooling rate such as a double scan with a rotation of 90 degrees between layers can reduce porosity [55]. Powder characteristics, in particular flowability,

have been found to influence porosity by limiting the powder packing density after recoating [58]. A lower packing density can lead to an unstable meltpool and give rise to conditions for over-melting and if an uneven build surface results, subsequent under-melting can occur.

2.4.1.1.2 Keyhole pores – keyhole mode

Keyhole pores are anisotropic in shape [15] (as seen in Figure 2-12) and are so-called because they are also commonly seen during keyhole-mode welding as a result of depression cavity collapse [13]; this process has been modelled as seen in Figure 2-13.

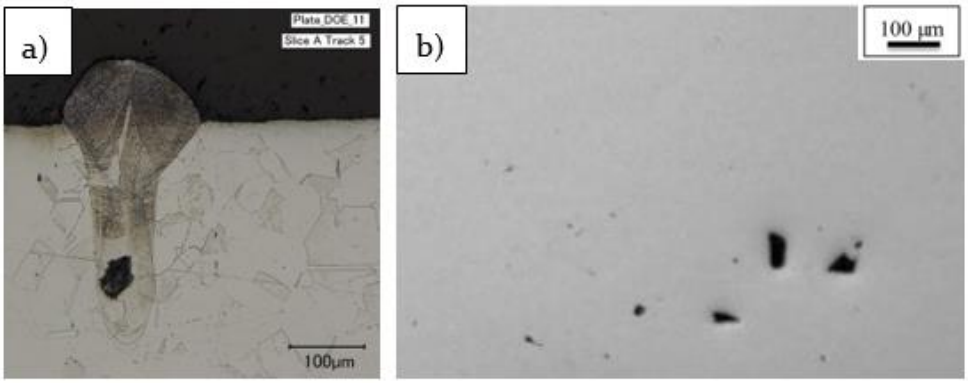

Figure 2-12 – a) Image showing characteristic keyhole melt pool shape and pore in 316L S [13] and b) cross section through AISI 420 SS sample [15].

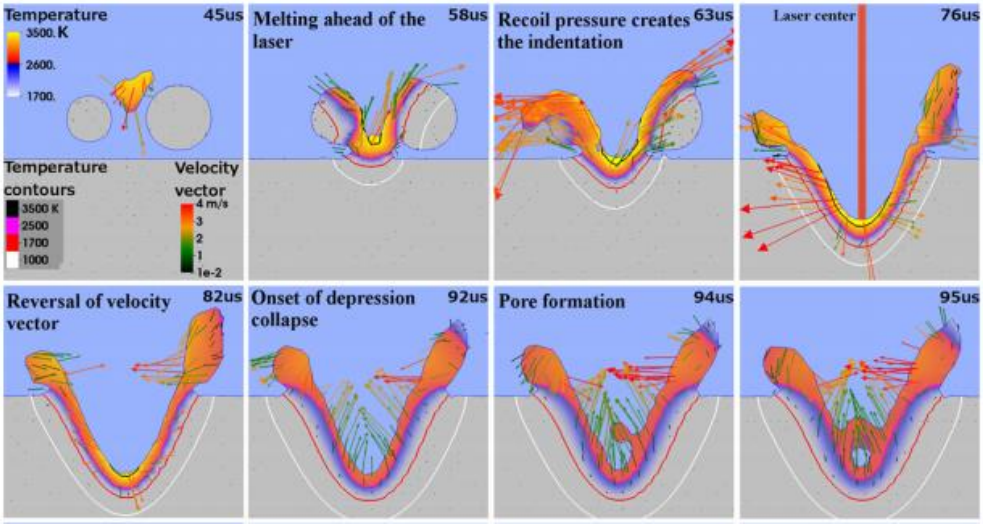

Figure 2-13 - Modelling of cavity formation, depression collapse and void entrapment based on high-speed camera studies of meltpools [59].

Processing in the keyhole regime should be avoided to decrease pore formation due to depression collapse and local powder denudation which can lead to formation of elongated pores [59]. Keyhole "defects" have been found close to the edges of a part. It is known that when using a back and forth scanning strategy, the laser has a dwell time when turning at the end of a track. At these points, a keyhole can form, when otherwise operating in conduction mode, or an existing keyhole can become unstable and collapse, creating a void [60].

2.4.1.2 *Under-melting*

2.4.1.2.1 Irregular, elongated pores

Elongated pores are commonly termed "lack of fusion defects" and result due to under-melting i.e. when there is insufficient penetration for full melting. This can occur due to low laser power or high scan speed where voids are created between layers, or where an excessive track spacing is selected and the voids appear between melt pools, at meltpool boundaries or between hatch lines [11, 61]. Elongated pores between layers often display a concave characteristic which is visible when a part is sectioned, as seen in Figure 2-14b [56].

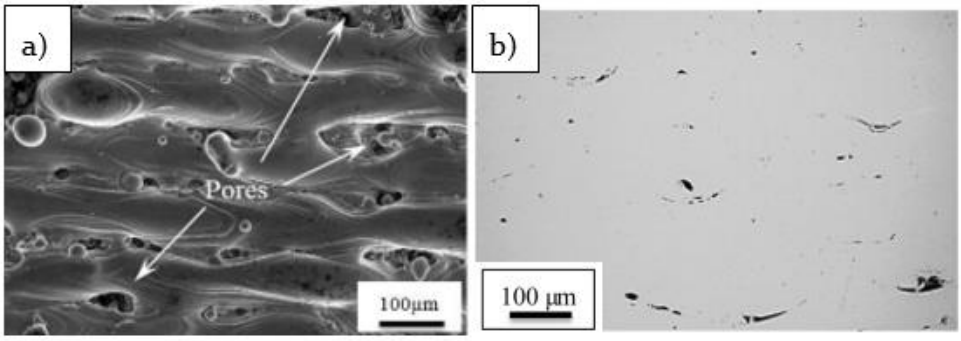

Figure 2-14 – (a) top surface of under-meltedTi6Al4V sample [56] and (b) microscopic cross-section (y-z) of elongated pores [15].

Elongated voids caused due to excessive track spacing appear with linear regularity as seen in Figure 2-15.

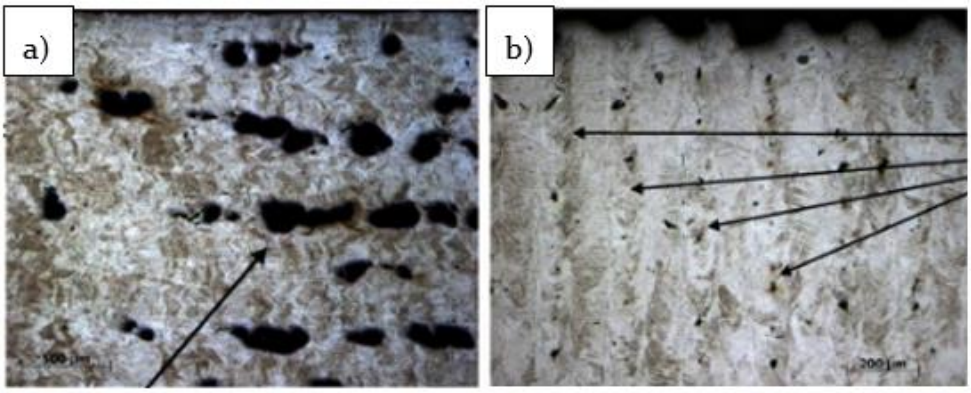

Figure 2-15 - Micrographs of elongated, aligned voids a) x-y plane and b) x-z plane[62].

When under-melting occurs during layer processing, the top surface can be left with multiple pores such as those visible in Figure 2-14b [15]. When the subsequent powder layer is drawn over, a thicker powder layer results in these areas, potentially promoting insufficient penetration of future layers, further compounding the problem and potentially leading to cross-layer porosity.

Another cause of linear pore generation (between adjacent melt tracks) is attributed to denudation of the powder adjacent to the melt pool, caused by the ambient gas flow and the induced powder motion [63]; this is only just beginning to be studied.

Work is being carried out on modelling melt pools to enable predictions of melt pool characteristics for new materials, saving costly and time consuming experimental activity when considering processing a new alloy [64, 65].

2.4.1.2.2 Multi-layer pores

Systematic, elongated pores can also be formed across the build layers and can be termed multi-layer porosity (Figure 2-16); this is thought to be caused by heat from the laser source conducting radially due to the powder region having a lower thermal conductivity than the solidified region [62]. Where the effect of reduced laser power on formation of pores has been studied, it was found that pores were generated at the same locations on each layer. As the layers were built up, the impact of an uneven build surface on each subsequent layer lead to further porosity in the same locations and pore chains were formed [66]. Multi-layer porosity can be reduced by adjusting processing parameters to improve the surface roughness of a processed layer [67].

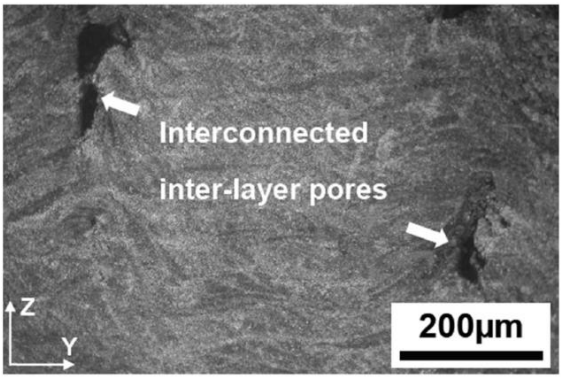

Figure 2-16 – Showing an SEM image of inter-layer pores (y-z) [66].

Alternatively, a scan strategy which rotates the build by a prime number of degrees can be selected on some processing machines [68]. Although this minimises the occurrence of chains, selection of parameters must ensure penetration of the resulting thicker powder zones for full consolidation, otherwise elongated, lack of fusion pores can result (Figure 2-17).

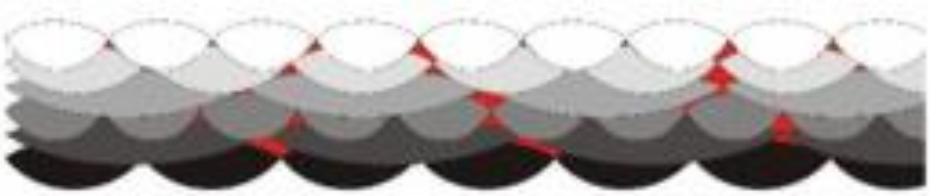

Figure 2-17 - Schematic of tracks with a rotation of 67 degrees after each layer highlighting areas (red) where full melting might not be achieved [68].

Post-processing can go some way to "healing" the porosity seen in AM components although for larger surface contacting or flat, disc like shaped voids, the efficiency of hot isostatic pressing (HIP) treatment is reduced [69].

2.4.2 Cracking

A crack is defined as "a fracture type discontinuity characterised by a sharp tip and high ratio of length and width to opening displacement" [70]. Cracking occurs when the stresses in the component exceed the local ultimate tensile strength of the material [43]. Depending on the scale of the resulting cracks, the terms macro-cracking (or delamination) and micro-cracking are commonly used.

In the case of laser PBF, stresses can be thermally induced during manufacture by differential heating or cooling of the component. Hence, the formation of thermally induced "cracks" can be minimised by controlling the temperature gradient across the build, during processing.

2.4.2.1 *Macro-cracking*

Residual stresses are those that remain within a component, after it has reached equilibrium, without any external loading. Macro-cracking results from type I residual stresses (or macro-stresses) which vary on a part-scale and are generated when thermal gradients and differential cooling rates are present [71]. There are thought to be two

mechanisms that cause high levels of residual stress during PBF processing. The first is termed the temperature gradient mechanism (TGM). As the processing laser inputs energy to the surface, a local thermal expansion of the top layer occurs, but the expansion is limited by the underlying layers. Under the second mechanism, thermal contraction of the molten top layers during cool down is inhibited by the solid layer underneath. Both scenarios result in the upper layer under tensile stress and the bulk material below under compressive stress [71]. When external loads are applied to the surface tensile pre-stresses, cracks can propagate readily. Examples of macro-cracking can be seen in Figure 2-18.

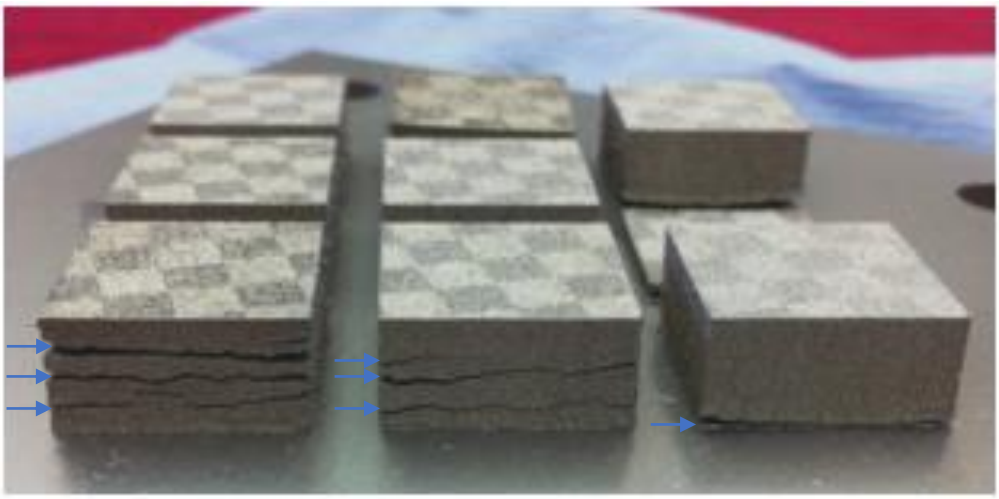

Figure 2-18 – Macro-cracking (or delamination) between layers within component and between component and build plate [72]. Cracking indicated with arrows.

There are a number of factors which affect the thermal profile across a build, such as the chosen build plate material, build plate thickness and pre-heating strategy [71]. Build plate heating has been found to be a most influential factor in reducing residual stress caused by TGM. The build set up including build layout/density of components and chosen scan strategy can result in localised heating, as cooling rates are altered. For example, selection of an island scanning strategy

utilises shorter scanning lines which yield higher temperature gradients but in a smaller area, therefore reducing the overall residual stress of the component [73]. Selecting a scan strategy which re-melts layers has been found to enhance the likelihood of cracking in materials with high hardness; as the cooling rate is increased due to the surrounding solid material having a higher thermal conductivity value than the powdered material. A higher fraction of brittle phases form and cracking is therefore enhanced [72]. Build chamber heating can also be utilised to reduce the temperature gradient across the bed. Additionally, post-processing heat treatments can be applied to reduce the residual stress, prior to removal of a component from the build plate.

2.4.2.2 *Micro-cracking*

Micro-cracks are not always detectable by conventional non-destructive testing methods, but can be detrimental to a components material properties, if present. As laser PBF processing and welding are inherently similar processes, common cracking mechanisms occurring in welding are also found in laser PBF samples. The term "weld cracking" is used to describe a number of mechanisms which occur during processing, such as solidification cracking, liquidation cracking, ductility-dip cracking (DDC) and also strain-age cracking (SAC), which can arise during post-process heat treatments [74]. At high laser powers, solidification cracking dominates and at low powers, liquidation or grain-boundary cracking dominates [74]. Alloys with a high gamma prime (γ') content are particularly susceptible to weld cracking and thus are also more difficult to process by laser PBF (Figure 2-19a) [75]. The material ductility reduces at intermediate temperatures and under residual stress, the ductility dip cracking mechanism forms grain boundary cracks [76].

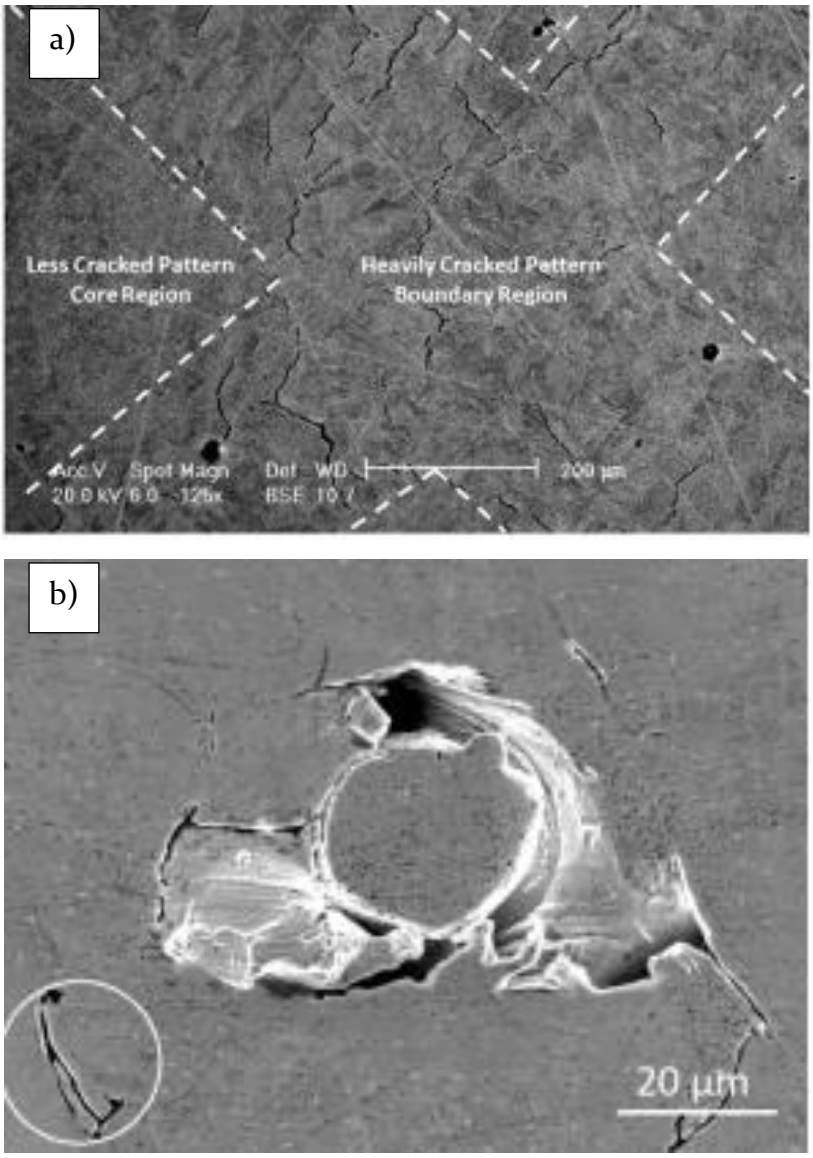

Figure 2-19 – a) SEM micrograph of x-y plane showing micro-cracking in a CM247LC sample at high-angle grain boundary [75] and b) thermally induced micro-cracking caused by processing under high thermal gradients with high laser power and scan speed [77].

Cracking is focussed on areas with high-angle grain boundaries (mis-orientation of neighbouring grains over 15 degrees). Cracking can be reduced by employing a back-and-forth scanning strategy, rather than an island strategy although this is known to increase residual stresses, leading to macro-cracking [73]; the effect of scan strategy on thermal gradients is being investigated experimentally and through modelling [78]. Alternatively, for alloys which form a solid solution, cracking

density can be reduced by modifying the alloy composition to increase solid solution strengthening elements and reduce undesired “tramp” elements [58, 79]. “Tramp” elements are those which are not always specified in the alloy grade, but trace amounts are considered acceptable for casting where no detrimental effect on material properties results. For example, Stainless Steel 304 alloy can have up to 0.3% “tramp” copper without adversely affecting the ductility behaviour. In some alloys, micro-cracks can be post-processed using HIP to close contained cracks to an acceptable level for use [75].

2.4.3 Other material discontinuities

Along with foreign body inclusions, which can be introduced to the laser PBF process through inadequate process control, other “defects” such as the formation of oxides can limit the mechanical properties of the processed material. The importance of selecting conditions which result in the recoating of an even powder layer for subsequent processing is also highlighted.

2.4.3.1 *Oxides*

Oxidation is of particular concern when processing aluminium alloys. Discolouration on the top surface of a finished component shows that a thin oxide film is formed on top of every layer during processing, as a result of oxygen present in the build chamber. With each subsequent layer, the oxide film on the top surface of the melt pool is vaporised and the lower surface film broken up and stirred into the melt pool via the Marangoni effect [80].

The power of the laser must be high enough to break through the oxide layer formed on the top surface of the solidified meltpool. The oxide layer at the "side" of each track remains undisturbed and is present within the final component, impacting component quality. It is also worth noting that this mechanism can trap unmelted powder particles between tracks (Figure 2-20).

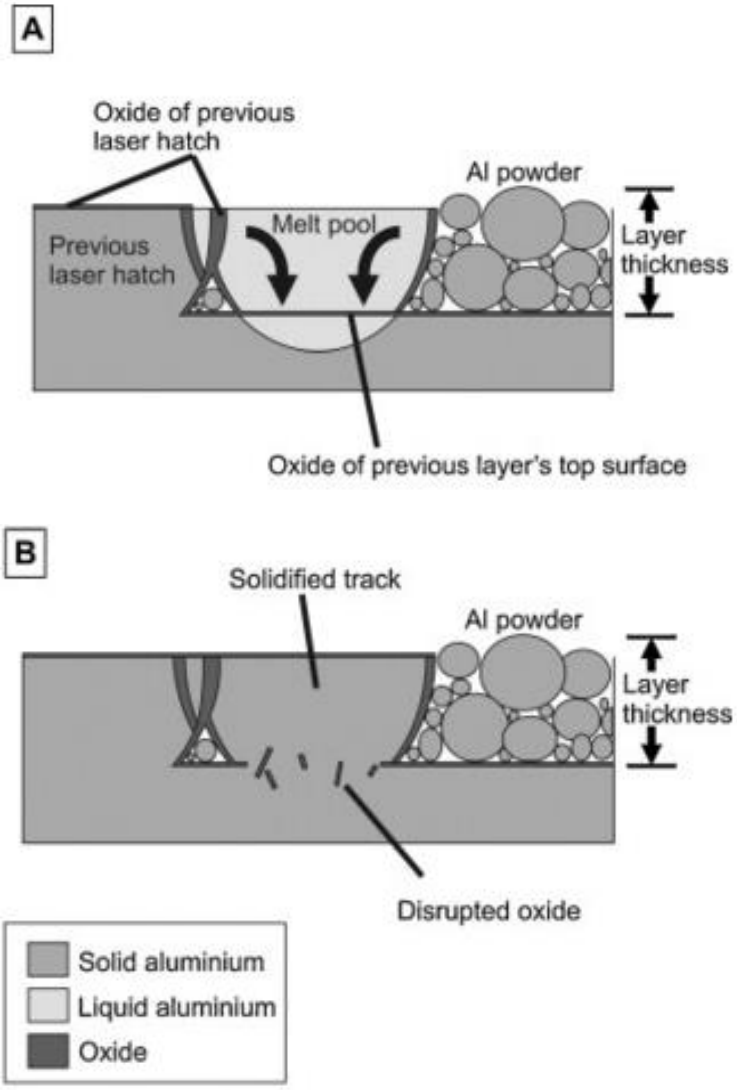

Figure 2-20 - Schematic showing oxide layer disruption at base and presence at side wall locations [80].

The thin oxide films and unmelted particles are seen when examining the fracture surface of a broken sample after mechanical testing (Figure 2-21a) and discolouration of the external surfaces can be an

indicator of internal oxidation (Figure 2-21b). Whilst it is infeasible to eliminate these oxides entirely, reducing the level of oxygen gas within the build chamber and considering the scan strategy can limit their significance. When thicker oxide layers are present, the stability of the melt pool can be affected and "balling" can occur [81].

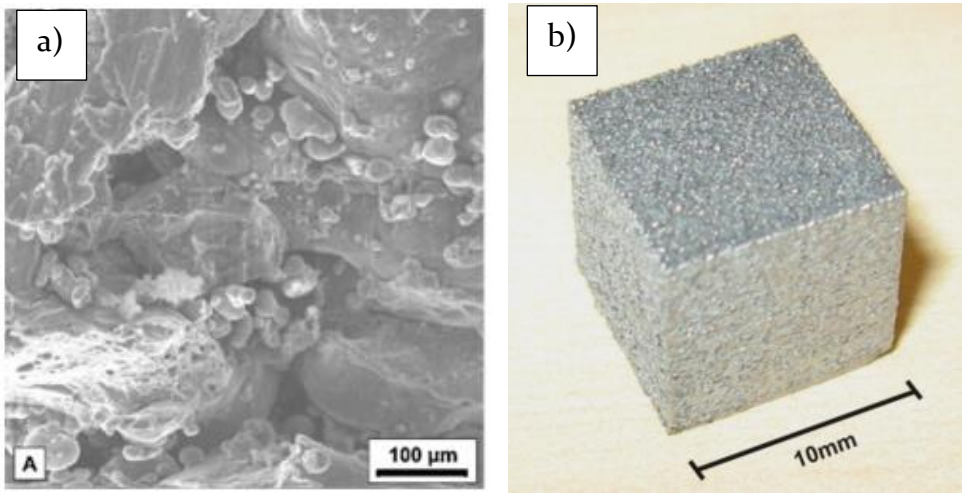

Figure 2-21 - a) SEM micrograph of fracture surface and b) discolouration on final surface on Aluminium alloy sample produced by laser-PBF [80].

2.4.3.2 *Balling and spatter*

Balling results when molten metal fails to wet with the substrate below; surface tension dominates and a rounded bead is formed as seen in Figure 2-22a [12]. This behaviour is known to occur with insufficient laser penetration, at lower laser powers when scanning at higher speeds [82]. The solidified bead hampers uniform melting of the subsequent layer when deposition of the powder layer is obstructed [83].

Conversely, when excessive energy is applied, vaporisation of the melt pool can occur. The recoil pressure which results can eject molten material, termed spatter (Figure 2-22b).

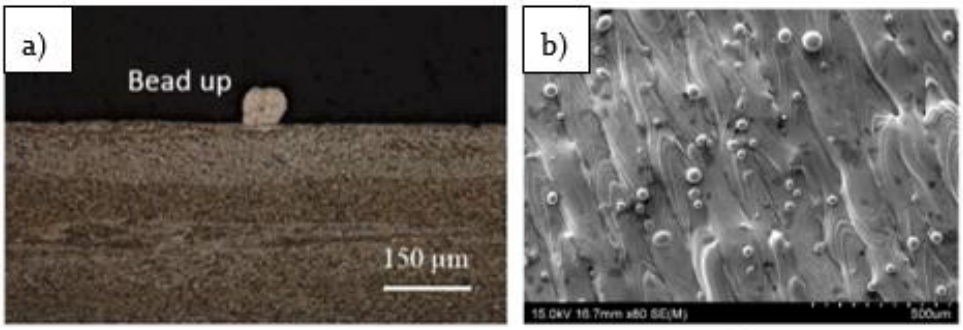

Figure 2-22 - Showing a) a cross section through a balled Ti-6Al-4V particle [12] and b) an SEM image of spatter particles on the top surface of a CoCrMo alloy [68], produced by laser-PBF.

When the molten material rapidly solidifies on the powder bed, particles larger than the build layer thickness can result. When the recoater arm next passes, these spatter particles can be scraped from the surface, leaving pits (Figure 2-23a) [57].

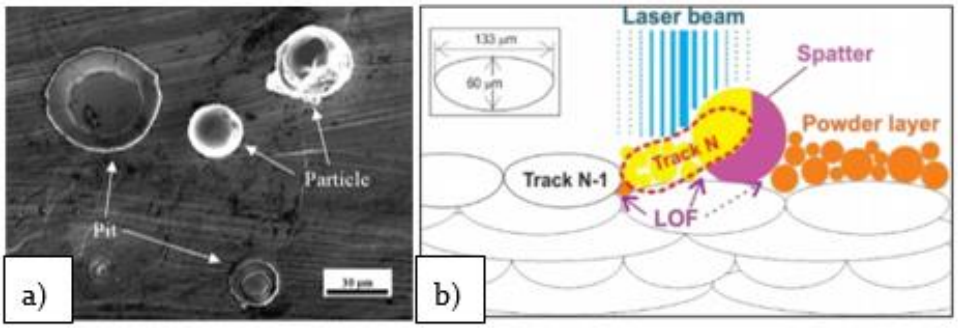

Figure 2-23 – Showing a) spatter particles on top surface and resulting pits from removal of these Ti-6Al-4V balls during recoating with a solid blade during laser-PBF [6] and b) schematic of interrupted powder layer caused by presence of a large spatter particle [68]

Droplets can be ejected from the meltpool speeds approaching 10 m/s. Most are ejected rearwards, but some larger liquid droplets have been observed being projected forwards. These droplets are in the region of 100 µm diameter [63]. If the solid spatter particles are not dislodged by the recoated blade causing pitting, they can inhibit the distribution of the powder layer [68]. Ahead of the spatter particle, a thicker than intended zone can be left which alters the layer thickness and result in

lack of fusion material discontinuities. Alternatively, the zone after the particle can be denuded as seen in Figure 2-23b.

In order to reduce the level of spatter during processing, less aggressive heating regimes are recommended [84]. Employing a re-melting strategy has been seen to improve the surface roughness of the top layer (Figure 2-24), although this is at the expense of processing time [15].

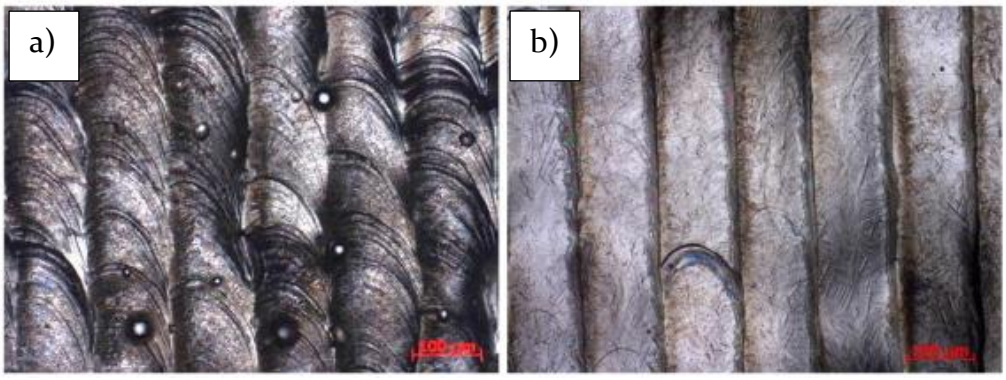

Figure 2-24- Images showing a) surface produced using a single laser-PBF melt strategy and b) the reduction in spatter achieved using a re-melting strategy for SS 316L alloy [15].

In summary, many types of material discontinuities can arise due to poor selection of laser PBF process parameters. In some cases, several different mechanisms can be responsible for the generation of the same "defect" type. In order to minimise component porosity or limit part cracking, understanding these generation mechanisms and their dependency is key.

When considering the processing of a new alloy, it is important to understand the combination of inputs which result in over or under-melting the material. Once this window has been established, avoiding extreme thermal gradients will reduce cracking on a micro- and macro- scale. Selection of a parameter set which avoids creation of an uneven build surface will prevent the cyclic generation of "defects".

The powder composition, manufacture method, storage and handling must be tightly controlled to avoid unwanted contamination and conditions which result in “defect” generation.

Additionally, it is important to note that the metal surfaces produced by AM methods vary quite significantly from those generated by conventional manufacturing processes and are generally very complex and irregular [85]. The top surface of a laser-PBF component is dominated by weld tracks formed by the solidified melt-pools which indicate the build strategy employed and result in a wave-like topology. Spherical protrusions caused by adhering unmelted or partially-melted powder and spatter particles are frequently present [84]; cavities caused by removal of these adhered and spattered particles or balling phenomena can also exist. These conditions can be challenging for optical inspection methods. A thorough characterisation of laser-PBF surfaces has been published by Senin et. Al. [85].

2.5 Non-destructive testing for additive manufacturing

A number of non-contact, non-destructive testing (NDT) methods have already been applied for in-situ inspection of the types of AM "defects" described. The benefits and challenges of implementing these methods are summarised in the following paragraphs and described in full detail in the Author's review paper [16]. An overview is given here:

2.5.1 Thermal

Infrared cameras and other thermographic techniques have been applied for in-situ measurement during AM in two main ways – to detect the formation of pores, or to capture a snapshot of the temperature gradient within each layer which can influence the mechanical properties of the material produced. Studies have been carried out on electron beam [17-19] and laser [20] PBF systems.

Although these methods have been shown to demonstrate potential, it has been found that only relative temperatures can be stated, without developing a further understanding of emissivity values when solid/powder materials are present simultaneously. When using temperature comparison methods to integrate control systems, accurate predictions are required from modelling packages which require further development. Any interface between externally mounted monitoring equipment and the build chamber must be cleaned and protected to allow reasonable imaging to be carried out. Equipment positioned inside the build chamber requires protection from metallisation etc. To date, real-time closed loop control has been limited by computer processing and capacity issues.

2.5.2 Visual

Vision systems such as high speed cameras and laser profile scanners also have potential to be integrated into additive manufacturing systems. High speed cameras record fast-moving images as photographs which can then be played back in slow-motion. High speed cameras have been applied for in-situ measurement of electron beam [21] and laser [22, 24-26, 86] PBF processes in order to observe a variety of process characteristics. Melt pool sizes and movements have been monitored, as have the machine build areas for evidence of part curling or recoater blade wear; image analysis remains a manual task which is a drawback.

2.5.3 Other

X-ray computed tomography (XCT) is increasingly being utilised to aid the understanding of pore size and distribution within AM samples [67, 87, 88]. A series of 2D images are taken and the slices stacked to reconstruct a 3D profile of a "defect" (Figure 2-25). XCT offers many benefits over destructive cross-sectioning which has conventionally been used for pore analysis, such as the ability to assess a whole 3D volume, rather than having to select a 2D slice. Additionally, pore sizes and shapes can be altered by metal smearing during destructive processing. The resolution that can be achieved is limited by the size of the component [87].

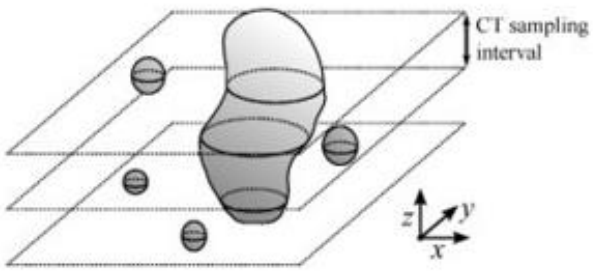

Figure 2-25 - Schematic of a multilayer pore showing as three individual pores under X-ray CT analysis [87] .

Conventional ultrasonic characterisation of flaws using piezoelectric devices for generating and detecting ultrasonic waves has widespread application. For example, ultrasonic testing has been found to be effective for detecting flaws, thickness, grain size, density/porosity and mechanical properties of materials produced by ultrasonic consolidation [89]. However, piezoelectric devices have several disadvantages, including bond variability, inability to operate on irregularly shaped objects and limitations for high temperature application. For in-situ inspection of additive manufactured components, surface topography prevents the use of conventional, transducer based methods [90].

Laser generated ultrasonic characterisation, however, is well suited for in-situ inspection of additive manufacturing. Laser techniques are non-contacting, thus don't exhibit any coupling problems; they can be used for rapid scanning, are amenable to use in hostile environments, particularly at high temperatures and can operate on irregularly shaped objects. Laser ultrasound (LU) is particularly appropriate for ceramic and composite materials [91] and has been identified as showing promise as a method for monitoring powder DED component integrity [92].

2.5.4 Applications of laser ultrasound

Techniques using ultrasonic waves generated by means of laser-based photo-acoustic principles are in common use and many applications can be found in both biomedical and dental diagnostics [93, 94], non-destructive testing of composites [95, 96] and materials characterisation of metals [97, 98]. LU has a wide range of application and has, for example, been used to successfully identify sub-surface material discontinuities in friction stir welded, aluminium alloy samples [99] and to measure wall thicknesses in thin sheets [100]. The

suitability of laser ultrasound for topography measurement has also been proven [101]. Ultrasonic attenuation measurements are also well suited for the microstructural characterisation of materials; the technique is capable of investigating materials with large or small grains [102, 103]. As ultrasonic wave velocities change with differing material grain orientation, anisotropy could be assessed [104]. Surface breaking "defects" are easily detected as they act like filters – a proportion of the wave is reflected and a portion transmitted. The amplitude is dependent on the crack depth and transmitted wave amplitude reduces exponentially with depth [105].

A number of journal and conference papers have been published utilising LU to find AM type "defects". Initially, only simple geometries were considered, such as notches or slots machined normal to a simple block sample surface with a fixed crack depth (1 – 4 mm) at a range of angles (30 – 150 °) [106]. Finite element modelling (FEM) was used to generate a model which was validated using the experimentally acquired data. This enabled an angled "defect" to be identified from the matching of experimentally observed wave arrival times to those predicted theoretically. "Defects" were also found through examination of the data in the frequency domain but could not be identified in the temporal domain alone [107]. Experiments were also carried out using electromagnetic acoustic transducers (EMATs), but the higher spatial resolution of the laser system allowed a larger range of angles and depths to be successfully characterised [105].

In the rail industry, rolling contact fatigue cracks and stress corrosion cracks often propagate in a complex manner, meaning that branched cracks which occur at an angle to a wedge surface are more representative than a simple notched sample. The effect of wedge angle on the behaviour of laser generated ultrasound waves have been

investigated [108]. It has been shown that the transmission of ultrasonic waves in the region of an angled surface-breaking crack has some dependence on the angle of the "defect". It is therefore necessary to have some knowledge of material discontinuities' internal geometry, before an accurate depth profile can be obtained [108].

2.5.5 Laser ultrasound of additively manufactured surfaces

Although LU has been shown to be capable of detecting the types of material discontinuities generated during additive manufacture, there have been a limited number of experiments applying laser ultrasonic inspection directly to additively manufactured materials. The prominent studies that have been carried out are summarised below:

In 2004, a study using laser generated surface waves to assess both 316L stainless steel and Ti6Al4V test pieces, manufactured by powder DED was undertaken [90]. Pores were simulated in the 316L stainless steel and Ti6Al4V test pieces using blind holes generated by electro-discharge machining (EDM) at 0.5 mm, 1.0 mm and 1.5 mm diameters within 0.4 mm or 0.8 mm of the surface. The difficulty of signal identification is highlighted, recognising that signals from material discontinuities can overlap with signals caused by other features such as surface roughness. If the signal of interest is weaker, it can be difficult to separate. Signal processing methods were investigated, particularly wavelet analysis. The paper demonstrates that this technique can be applied using a computationally efficient process, to effectively localise the "defects" present.

Following on from this work, United States patent (US 7,278,315 B1) was awarded, entitled *"Laser-Ultrasonic detection of sub-surface defects in processed metals"* [28]. Subsequently, United States patent (US 8,243,280 B2) entitled *"Laser ultrasonic measurement system with*

movable beam delivery" [109] was granted. The patent covers the use of a laser ultrasonic inspection system where the generation laser is transmitted via a moveable mechanical link, controlled by a robot. An optical scanner directs the generation and detection lasers onto the workpiece and an interferometer is optically coupled to the scanner.

In 2007, a European patent claiming a method of producing an object by deposition including the non-destructive analysis of the properties of each layer by inducing a laser-generated non-contact interference pattern and retrieving "defect" and material properties of the layer was filed. EU patent (EP 1 815 936 B1) entitled *"Methodof* [sic] *producing an object including testing and/or analysis of object"* was granted in 2009 [110]. Following on from this, a series of experiments were carried out on Waspaloy, MERL76 and IN718 samples sourced from powder and wire DED and PBF processes [111]. The polished specimens were tested at room temperature to assess how well high frequency surface acoustic waves could propagate on the surface.

The attenuation was found to vary greatly across the samples and this is thought to be due to material microstructure variations. Anisotropy and mean grain size affects the scattering and acoustic aberration. Additionally, manufacturing derived faults such as lack of consolidation and voids could be responsible. The additively manufactured steel and nickel based samples did not transmit sound at the frequency applied (82 MHz), although forged samples in the same materials did. The titanium samples responded well to the technique. The surface acoustic wave velocities were also measured using spatially resolved acoustic spectroscopy (SRAS) and encouragingly, the technique was found to show promise for identification of cracks.

LU has also been identified along with laser thermography and eddy current testing as potential NDT methods for powder DED components [30]. The study had success in quantifying “defects” in Inconel alloy 600 test pieces manufactured by powder DED [112]. Artificial discontinuities, 150 – 500 μm diameter at 13 – 700 μm depth were created using both laser drilling and micro-EDM; the size and position of the holes was measured using high resolution microscopy. A laser ultrasound system was used to take measurements at 0.1 mm intervals along the as--built deposition track. The depth and size of the “defects” were extrapolated from the data although this is, at present, a manual task and no indication is given as to how accurate this is, or to what resolution the “defects” can be sized. Finite element modelling (FEM) of the process has also been found to be an effective way of gaining a deeper understanding of the ultrasonic wave propagation allowing for further optimisation of the laser equipment set up [31].

2.6 Opportunities for development

The above studies have succeeded in using LU, ex-situ on materials manufactured by AM methods, although the PBF samples had to be polished to reduce the surface roughness. The other experiments were carried out on samples produced by powder DED which has a lower surface roughness. A system which is capable of assessing PBF as-built samples has not yet been investigated.

The “defects” studied were through-holes created artificially using EDM or voids created by diffusion bonding two samples together. No naturally occurring “defects” or “defects” produced intentionally during manufacture have yet been investigated.

There has been very little work carried out in terms of validation of the LU results seen. No evidence of comparison with X-ray computed tomography has been seen.

The limits of detection by LU for reference samples with a range of hole sizes at different depths for voids in an Inconel 718 sample, produced by powder DED have been established. The same model could be investigated for different materials and different manufacturing methods; this could be validated using FEA modelling.

Little consideration has yet been made as to the feasibility of incorporating a LU system in an AM processing environment or indeed to the business case considerations. An assessment of the current technologies will guide the future development of LU equipment to match the needs for in-situ inspection of AM surfaces.

2.7 Standards

Finally, it should be noted that the need for AM standards, in particular specification standards for NDT for AM, has been recognised and is being addressed through co-operation between the International Organization for Standardization (ISO) and ASTM, with the formation of joint groups between ISO TC261 and ASTM F42 [113]. These collaborations will enable the joint development of AM standards in the areas of:

- *'Terminology'*
- *'Standard test artefacts'*
- *'Requirements for purchased AM parts'*
- *'Design guidelines'*
- *'Standard Specification for Extrusion Based Additive Manufacturing of Plastic Materials*
- *'Standard practice for metal PBF to meet rigid quality requirements'*
- *'Specific design guidelines on PBF'*
- *'Qualification'*
- *'Quality assurance and post processing of PBF metallic parts'*
- *'Non-destructive testing for AM parts'*

The standardisation process is on-going although the following standards documents have been released in the UK by British Standards Institute (BSI), in close co-operation with ISO and ASTM:

- ISO/ASTM 52921:2013 - Standard terminology for additive manufacturing. Coordinate systems and test methodologies [114]
- ISO/ASTM 52915:2016 - Standard specification for additive manufacturing file format (AMF) Version 1.2 [115]

- ISO/ASTM 52900:2015 – Additive manufacturing. General principles. Terminology [32]
- BS ISO 17296-4:2014 - Additive manufacturing. General principles. Overview of data processing [116]
- BS ISO 17296-3:2014 - Additive manufacturing. General principles. Main characteristics and corresponding test methods [117]
- BS ISO 17296-2:2015 - Additive manufacturing. General principles. Overview of process categories and feedstock [118]

Chapter 3 – Theory of ultrasound and overview of experimental equipment

3.1 Introduction

In this chapter, further background is given relating to ultrasonic waves, their generation and the use of laser interferometry for their detection. The experimental approach taken to ascertain the capability of laser ultrasonic testing equipment for detecting sub-surface pore-like "defects" is then described. The processing methods and detail relating to the equipment used is also given.

3.2 Ultrasound

Ultrasonic testing or ultrasonics uses sound waves to analyse materials, above the range of human hearing which is 20 Hz to 20 kHz. Ultrasonic techniques can be used for dimensional measurement, material characterisation and, as in this case, for flaw detection. All of these methods are based on vibrations within the material. All materials are comprised of atoms which can be stimulated into vibration about their equilibrium positions. Ultrasonics utilises mechanical waves caused by particles which contain many atoms moving in harmony. When the particles are displaced by a force from their equilibrium position, elastic restoring forces in combination with the inertia of the particles result in oscillatory motion within the material.

3.2.1 Wave types

Waves can be categorised into four different types based on their mode of oscillation: longitudinal waves, shear waves, surface waves and plate waves. Plate waves are only generated in thin materials. When an ultrasonic wave reaches an interface or interacts with "defect" within a

material, mode conversion between wave types can occur. Further detail is given below:

3.2.1.1 *Longitudinal waves*

In longitudinal waves, the oscillations occur in the direction of wave propagation. Since compressional forces are active in these waves, they are also called pressure or compressional waves and given the symbols, 'P' or 'L'. A schematic is shown in Figure 3-1.

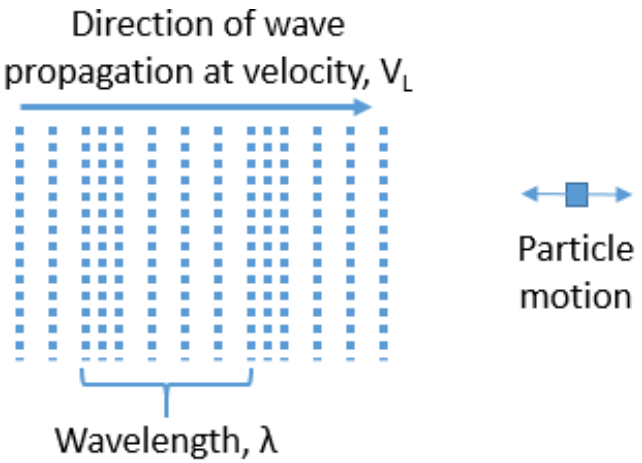

Figure 3-1 - Longitudinal wave propagation.

Longitudinal wave speed, V_L is given by Equation 1:

$$V_L = \sqrt{\frac{\lambda+2\mu}{\rho}} = \sqrt{\frac{E(1-\sigma)}{\rho(1+\sigma)(1-2\sigma)}} \qquad \text{Equation 1}$$

where ρ is the density, λ is Lame's first constant, μ is the shear modulus, E is the Young's modulus and σ is the Poisson's ratio [119].

3.2.1.2 *Shear waves*

Shear (S), or transverse waves oscillate normal to the direction of propagation. Shear waves are relatively weak compared to longitudinal waves. A schematic is shown in Figure 3-2.

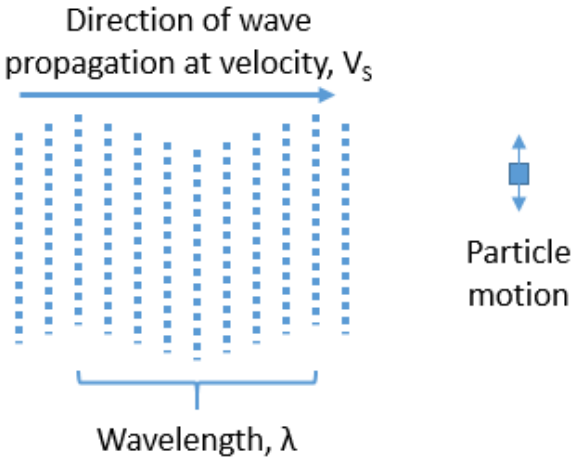

Figure 3-2 - Shear wave propagation.

Shear wave speed, V_s is given by Equation 2:

$$V_S = \sqrt{\frac{\mu}{\rho}} = \sqrt{\frac{E}{2\rho(1+\sigma)}} \qquad \text{Equation 2}$$

where ρ is the density, μ is the shear modulus, E is the Young's modulus and σ is the Poisson's ratio [119]. It should be noted that V_L is always greater than V_S, thus longitudinal waves will always propagate faster and arrive first to a detector at a fixed distance from the source. Consequently, longitudinal waves are often termed P-waves or primary waves, and shear waves are termed secondary or S-waves. Both longitudinal and shear waves can be termed 'bulk' waves as they can propagate through the body of a material.

3.2.1.3 *Surface waves*

Surface waves are often termed Rayleigh waves, named after their discoverer. They travel along the surface of elastic materials and penetrate a distance roughly equal to their wavelength, λ which is defined in Equation 3:

$$\lambda = \frac{\nu}{f} \qquad \text{Equation 3}$$

where ν is the wave velocity and f is the frequency.

Particle displacement follows an elliptical orbit (Figure 3-3), so the waves are especially good at following the surface around a curve [120].

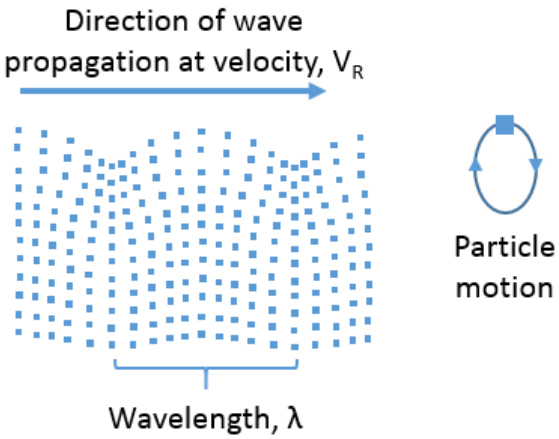

Figure 3-3 - Schematic showing elliptical orbit of Rayleigh wave particles.

Surface waves travel at a velocity (V_R) between 0.87 and 0.95 the speed of a shear wave and are particularly useful for characterising surface or near-surface material discontinuities as the intensity (amplitude) decays with distance, $r^{-1/2}$, rather than r^{-1} for bulk waves [121]. V_R is given by Equation 4:

$$V_R = V_S \cdot \frac{0.862+1.14\sigma}{1+\sigma} \qquad \text{Equation 4}$$

where V_s is the shear wave velocity and σ is the Poisson's ratio

3.2.1.4 *Plate waves*

Plate waves can only be generated in materials with thickness equal to a few wavelengths. The most common are Lamb waves, named after their discoverer. These guided waves propagate through plate-like structures with two parallel, stress-free boundaries. A number of modes of particle vibration are possible with the two most common being symmetrical and asymmetrical. It is not anticipated that plate-like artefacts will be encountered in the following study.

3.2.1.5 *Mode conversion*

When sound waves encounter an interface at an angle, one form of wave energy can be transformed into another and conversion between wave types can occur, termed mode conversion. This can complicate interpretation of the ultrasonic signal returned to a detector. If the detector is moving relative to the artefact being interrogated, but at a fixed distance from a generation source, reflected or refracted waves from side walls will take differing amount of time to be returned. This is also the case for artefacts with a non-uniform cross-section.

The diagram in Figure 3-4 shows some of the wave paths including those that travel directly from generation to detection points (direct paths) and also some reflected and mode converted paths.

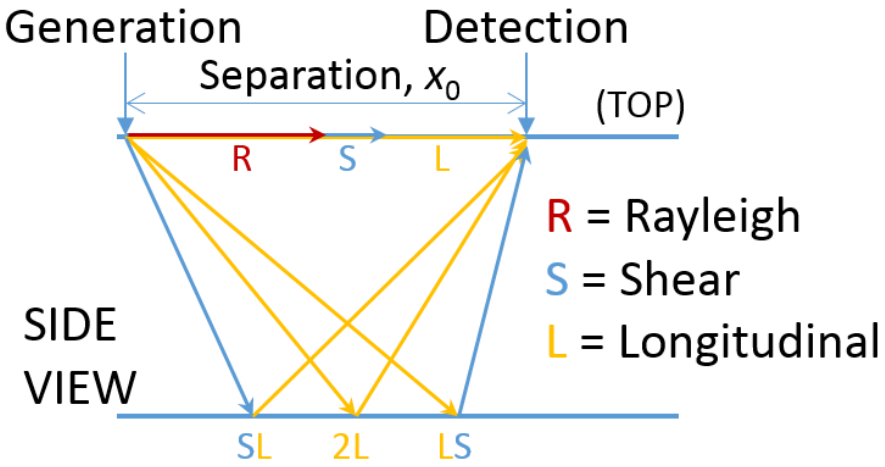

Figure 3-4 – Schematic showing direct wave paths (L, S and R) and reflected wave paths (SL, 2L and LS) in a sample with parallel edges.

The presence of a sub-surface "defect" causes the incident waves to be diffracted and returned along a shorter path, potentially in a shorter time than for a wave reflected or mode converted at the sample edge (Figure 3-5).

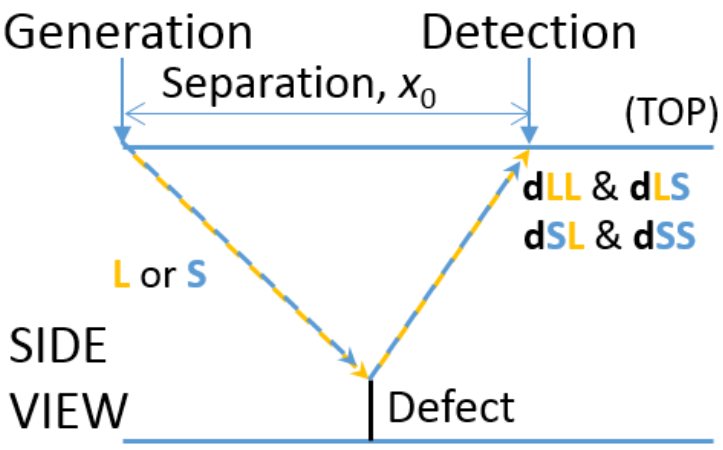

Figure 3-5 - Schematic showing shorter wave paths for waves diffracted by a sub-surface "defect" - dLL is an incident L wave diffracted as an L wave, dLS is an incident L wave diffracted and returning as an S wave (i.e. mode converted).

When a material discontinuity is present close to the sample surface, at a depth within the attenuation zone of a Rayleigh wave, the Rayleigh wave travelling along the sample surface can be scattered, resulting in a waveform with a broadened peak. Surface waves are also reflected from any material discontinuity.

3.2.2 Visualisation methods

For ultrasonic inspection using the time-of-flight technique, the signal received at a detector which is a fixed distance (x_0) from the generation source is predominantly displayed as an A-scan or B-scan.

3.2.2.1 *A-scans*

If the amplitude response (y-axis) at the detector is recorded as a function of time (x-axis), then an A-scan is generated for that location. An example is shown in Figure 3-6; labelling indicates the different wave type arrivals. Any material discontinuities can be identified by comparing the signal amplitude with a scan from an area with no known "defects". The position of a material discontinuity can be estimated using the diffracted and reflected signals from the initial pulse and the reflections.

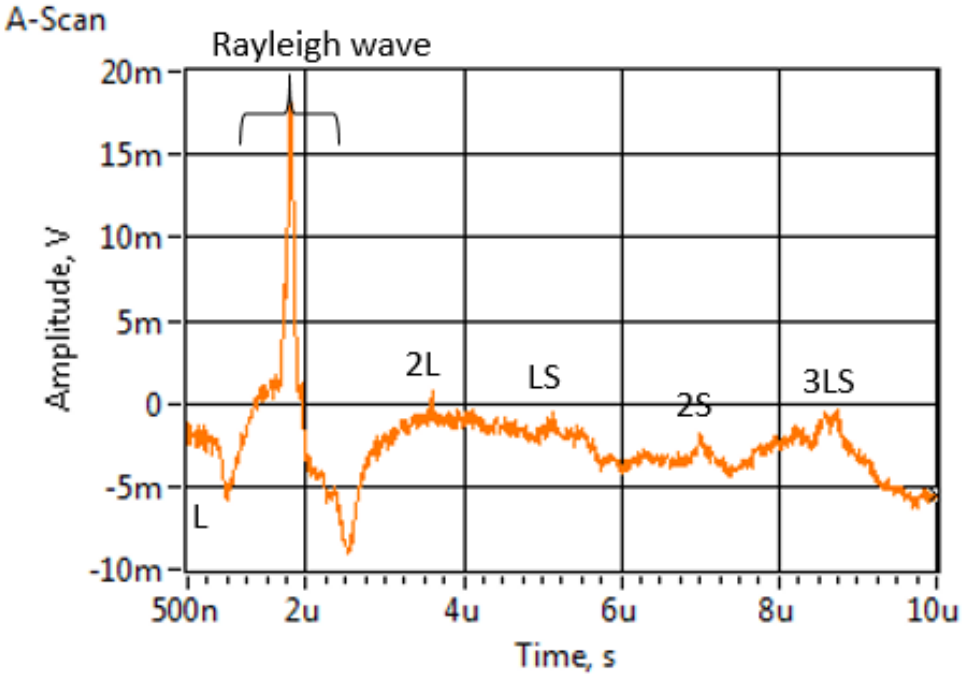

Figure 3-6 - Example A-scan indicating arrival of direct, reflected and mode-converted waves.

3.2.2.2 *B-scans*

A B-scan is a collection of A-scans which have been effectively stacked up; the x-axis of the A-scan becomes the y-axis on the B-scan and the y-axis of the A-scan then becomes the z-axis on the B-scan. It displays a profile view of the test specimen typically utilising travel time (x- axis) vs. linear position of the receiver (y- axis) [120]. A colour represents the amplitude of the returned signal, equivalent to the y-axis on an A-scan. An example B-scan is shown in Figure 3-7. The diagonal lines that can be seen are reflections from the end walls of the sample, as the laser unit moves farther from one end, the time for the wave to travel to the detection point increases. Similarly, the laser unit moves towards the other end of the sample and the wave travel time decreases.

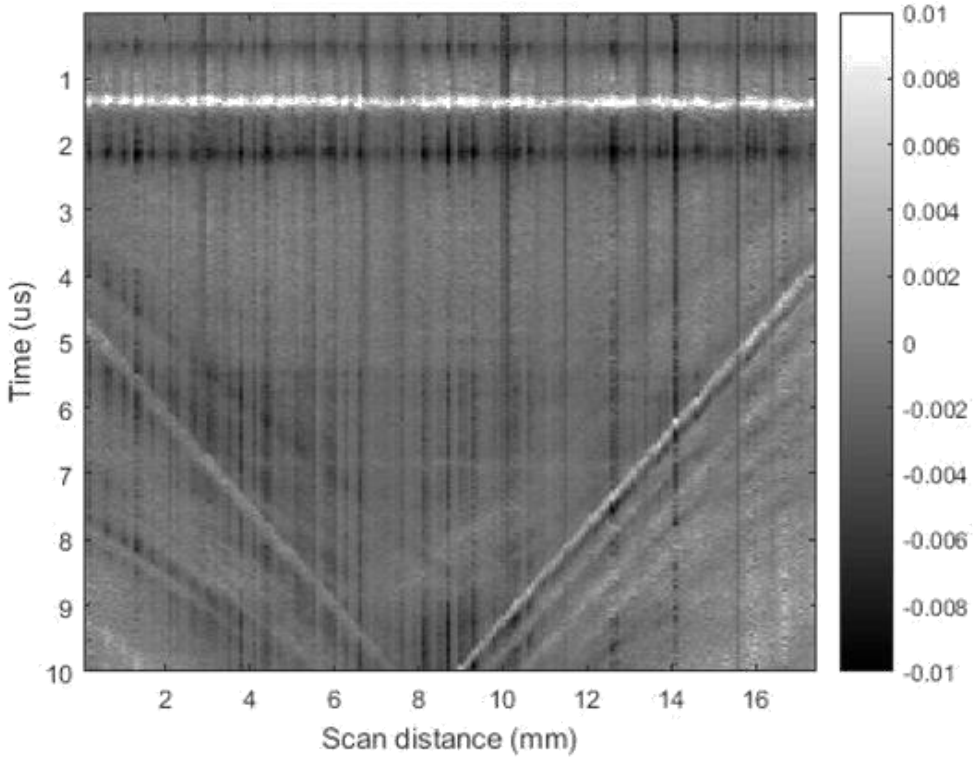

Figure 3-7 - Example B-scan.

More detail regarding the expected arrival times and influence of the presence of a "defect" on the signal is given in Chapters 4-6.

3.1.1.1 Post-processing signal data

In addition to generating A-scans and B-scans from the signal data, mathematical transformations can be applied to obtain further information from that signal that is not readily available in the raw signal. Fast Fourier Transforms (FFTs) which convert received power as a function of frequency are common. Wavelet transforms have also be used for improved signal detection [122]. Wavelet transforms are a mathematical way of analysing a signal when the signal frequency varies over time.

3.3 Laser ultrasound

All information in this chapter so far has been regarding ultrasound in general. In this section, details of laser-generated ultrasound and laser-based detection methods are given.

A typical laser ultrasound testing system comprises a pulsed laser to generate ultrasonic waves, a continuous-wave detection laser, an interferometer, an oscilloscope and a PC, as shown in Figure 3-8.

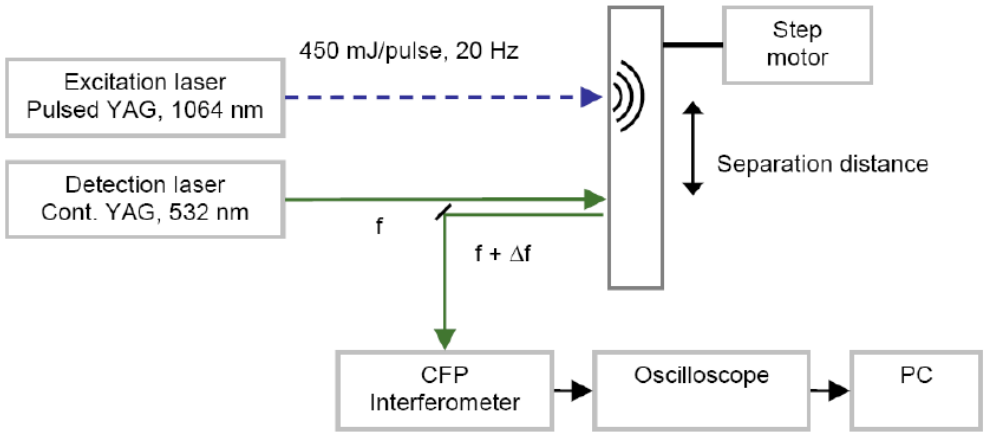

Figure 3-8 – Example laser ultrasound set up [123].

3.3.1 Generating ultrasonic waves using a laser

The technique rests on absorption of an incident laser light pulse and energy conversion through a thermoelastic process resulting in the generation of ultrasonic waves [124]. The waves are generated by three mechanisms, depending on the power density of the incident laser light pulse. The changing stress and strain fields produced just beneath the surface of the material act as sources of elastic waves.

At low power densities, ultrasonic waves are caused by the rapid thermal expansion of the material being irradiated and the frequency of the resulting waves is dependent on the spatial distribution (laser spot size)

and temporal frequency (pulse repetition rate) content of the incident beam [111]. This is termed the thermoelastic regime (Figure 3-9 left). At intermediate power densities, radiation pressure contributes to wave generation and a second mechanism, the transfer of momentum, also contributes to the generation of ultrasound waves. At high energy densities, the surface of the material is ablated and ultrasonic waves are produced by the momentum transfer of the ejected material. A plasma forms at the surface of the material which produces an impulsive recoil force after the plasma expands; this is termed the ablation regime (Figure 3-9 right) [91]. The dominant ultrasonic wave mode generated by a laser source is a Raleigh wave [125].

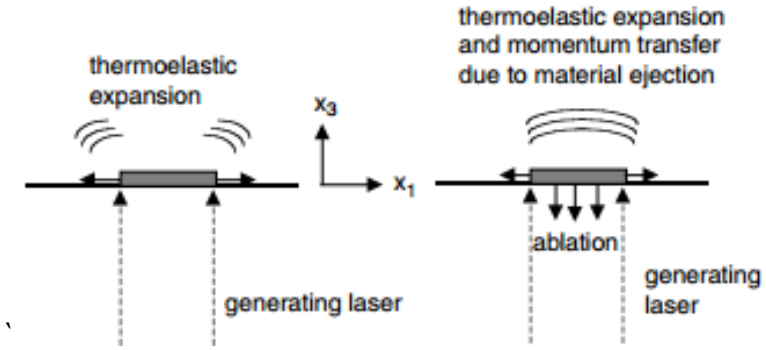

Figure 3-9 – Ultrasonic wave generation schematics showing the thermoelastic and ablation regimes [119].

3.3.2 Detection laser and interferometry

Optical interferometers use light which has been reflected from a surface, to measure the displacement of the surface. The returned light interferes with a reference beam, often a continuous wave laser, and a difference in phase or frequency is used to measure the surface displacement. Systems which use phase difference between the returned and reference signals are termed 'homodyne' and systems which use frequency are termed 'heterodyne' [126].

Laser-PBF surfaces can present a challenge for optical inspection because unlike from an optically polished surface, the reflected light is scattered [127]. Scattered light is not phase related, due to multiple optical scattering at the surface, and is diffused over a wide angle. This irregular angular distribution of the intensity of scattered light is termed a 'speckle pattern' characteristic. In their simple forms, neither interferometry system has been found to function accurately with the speckled beams returned from rough, AM-style surfaces stimulated by an ultrasonic source. Consequently, both system variants have been modified to try and adapt them for use with non-polished surfaces [128]. Using a photorefractive material such as photo-electromotive force (photo-EMF) crystals in adaptive homodyne interferometer allows for processing of a speckled signal [129], using the arrangement shown in Figure 3-10.

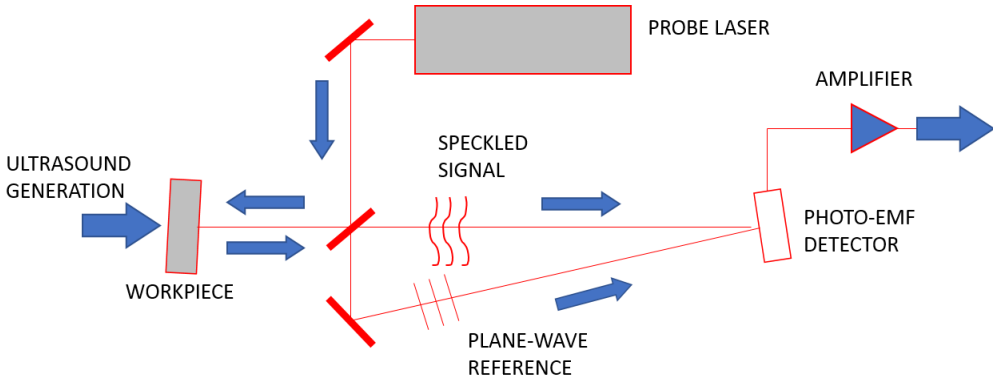

Figure 3-10 - Schematic of photo-EMF interferometer [129].

Modern adaptive receivers are insensitive to noise at lower frequencies and can therefore be used dynamically, translating along the sample surface to take subsequent measurements at a given interval [90].

3.4 Equipment

The following section details the equipment used for LU testing and the AM systems used to build test pieces for interrogation. Unless otherwise stated, the equipment is located at University of Nottingham, UK. The LU system resides at sponsor company Manufacturing Technology Centre, in Ansty, UK.

3.4.1 LU system

The laser pumping and cooling units are positioned outside the enclosure and the laser unit is mounted in the measurement head as shown in Figure 3-11. The generation laser is a class IV, Q-switched neodymium-doped yttrium aluminium garnet (Nd:YAG) laser with a wavelength of 1064 nm, capable of delivering 200 mJ energy with each 20 ns pulse, at 20 Hz frequency. A remote wand is used to select the flashlamp and q-switch settings and operate the laser. Optics are employed to focus the laser into a line, yielding a Rayleigh wave with shorter duration and higher bandwidth [92], enhancing the directionality of the Rayleigh wave, normal to the line.

The detection laser is a 1550 nm ± 10 nm wavelength fibre laser which operates in continuous wave mode with an output power of 10 W. The Optech APM-1 analogue processing module contains a temporal differentiator for high-pass filtering and a linear, low-noise amplifier.

The interferometer is an Optech AIR-1550-TWM adaptive interferometric receiver which includes a demodulator, FHY optical head, and linking fibres. The detector bandwidth is 125 MHz and displacement sensitivity is better than 2×10^{-7} nm RMS $(W/Hz)^{1/2}$. The FHY fiber head is supplied with 25 mm diameter collection optics with

three objectives – 50, 100 and 200 mm. The FHY spot size is 200 μm with the 50 mm objective.

Alignment signals are provided by an internal piezo mirror. Blocking is employed at 1064 nm wavelength to eliminate the generation laser. An adaptive interferometer was selected in order to be able to process the speckled wavefront expected to be returned from a rough surface, such as an as-built AM surface. The returned speckled signal is combined with the reference beam inside a photorefractive crystal which enables coherent detection and also adapts to any changes in wavefronts caused by mechanical disturbances.

The Optech SP-1 continuously variable fiber power splitter and guide beam module allows for a 0 – 100 % division of power into the probe beam (mounted in the measurement head) and the reference beam which is outputted to the interferometer.

The guide beam injects a class I red laser beam into the probe fiber so that the probe beam can be visualised safely for alignment purposes.

The generation laser and detection optics are mounted within the measurement head as shown in Figure 3-12 and the beam separation can be adjusted remotely from 0 to 50 mm.

The measurement head can be operated at a stand-off of 80 - 230 mm from the workpiece and the spot sizes can be adjusted using interchangeable lenses with varying focal lengths. The generation beam spot diameter can be further reduced by up to 3 times, using the optional beam expanding telescope.

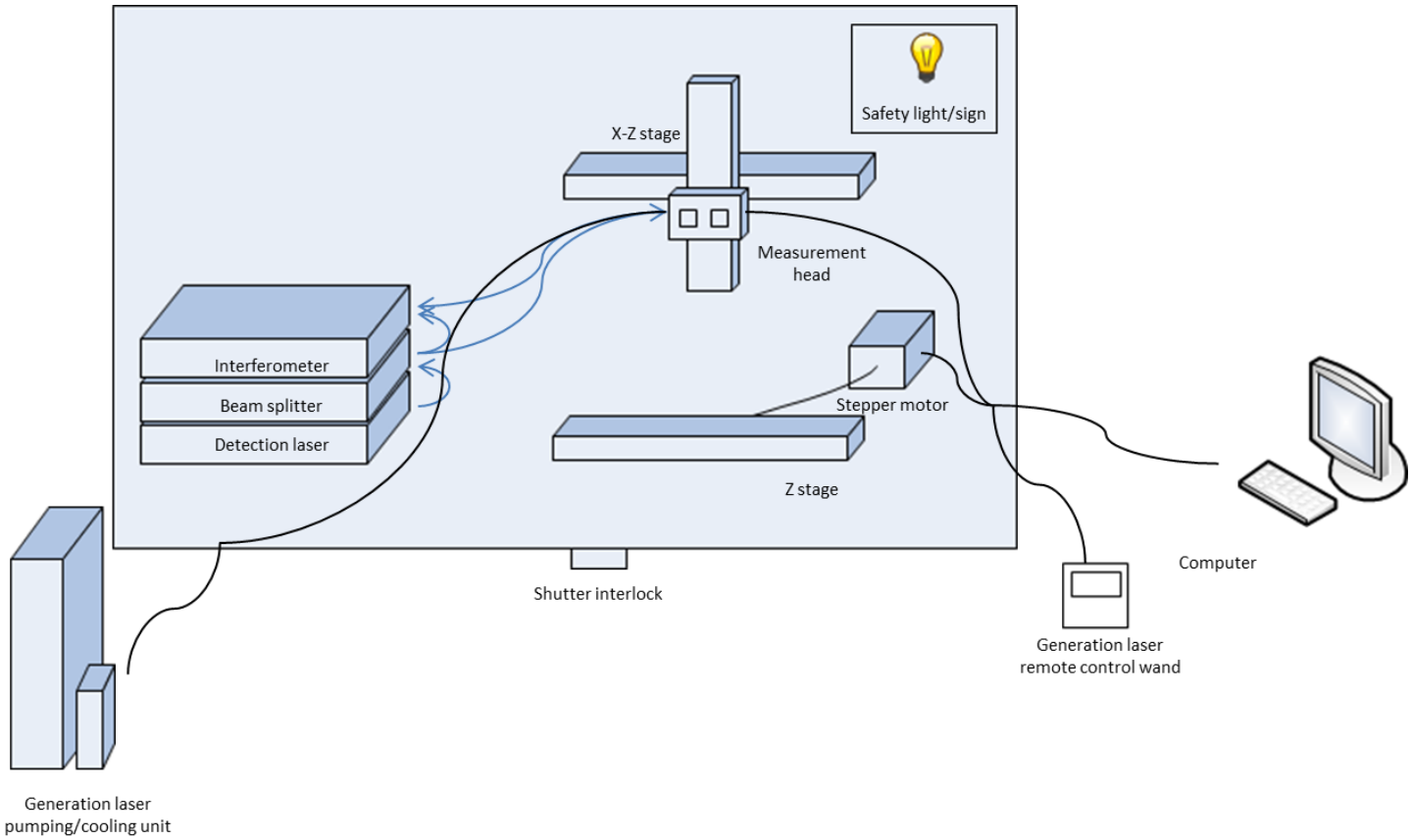

Figure 3-11 - Schematic of LU system.

Various optical lenses are available for the system which when swapped enable the beam diameter on the target to be adjusted. Example beam diameters are shown for each given focal length in Table 3-1. Spherical and cylindrical lenses can be used to generate a line or a spot respectively.

Table 3-1 - Showing beam diameter (mm) which can be achieved using lenses with various focal lengths (mm).

Beam	Focal length, f (mm)	Beam diameter on target (um)
Detection (50 mm aperture, 100 mm collimator)	100	≈ 200
	250	≈ 500
Generation (assuming single focusing lens)	150	≈ 600
	200	≈ 800
	300	≈ 1200
	350	≈ 1400

The measurement head is mounted onto a two-stage linear translation platform using an adapter bracket. The bracket is designed so that the measurement head can be mounted in two different orientations, allowing for side-by-side and in-line measurement.

The stages are remotely controlled via serial cable and can travel up to 250 mm at 5 μm resolution. Unless otherwise stated, the measurement head was orientated for in-line measurements so that the generation laser line follows the detection laser spot. A trigger timing module is implemented to provide external triggering of the generation and detection lasers.

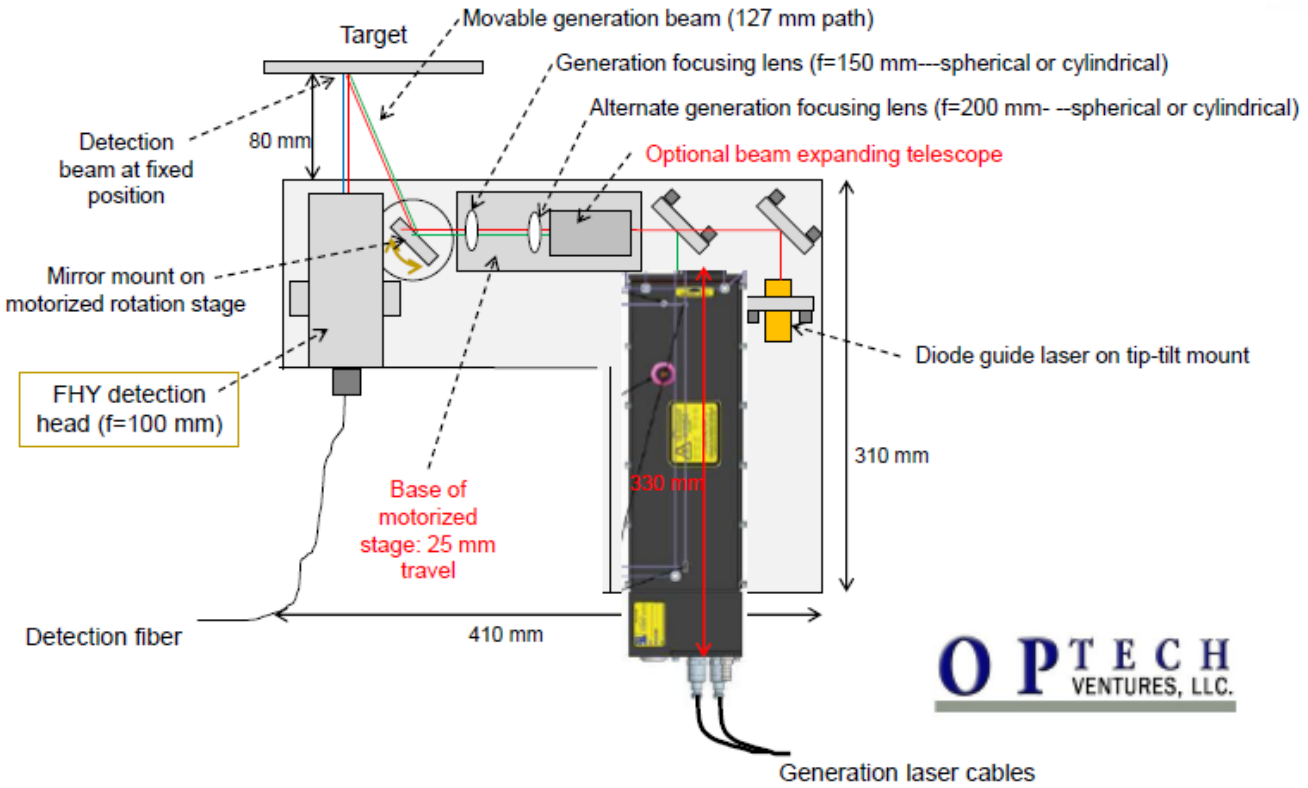

Figure 3-12 - Measurement head - Optech Ventures LLC.

The high-class laser ratings require the laser systems to be contained within an interlocked enclosure, in order to comply with MTC site health and safety policies. All systems can be controlled remotely for safe operation. Two webcams are employed to view the inside of the enclosure, when sealed.

3.4.2 AM systems

3.4.2.1 *ReaLizer SLM 50*

The ReaLizer GmbH SLM 50 is a desktop device with a build volume of 70 mm diameter and 40 mm z-height. The machine utilises a fibre laser which can deliver between 20 and 120 W in an Argon atmosphere. A layer thickness between 20 and 50 µm can be selected. ReaLizer control software is used to prepare and input the build files.

3.4.2.2 *Renishaw AM250*

A Renishaw AM250 was also available with a build volume of 250 *x* 250 *x* 300 mm. The machine has a 200 W laser and a minimum layer thickness of 20 µm. 'Marcam Autofab' or 'Materialise Magics' softwares are used to prepare and input the build files.

3.5 Experimental procedure

In order to assess the capability of laser ultrasonic testing equipment for detecting sub-surface pore-like “defects”, a series of test pieces were manufactured by laser powder bed fusion. Following completion of the AM build, the test pieces were removed from the baseplates by wire-electrical discharge machining (EDM) and discontinuities added by post-processing, where required.

The test pieces were scanned by LU, translating the measurement head across the top of the test piece, over areas where materials discontinuities were known to be. In some cases, the side walls and bulk material (areas with no intended material discontinuities) were also scanned. Data was then extracted for subsequent post-processing.

Additionally, focus variation microscopy (FVM), X-ray computed tomography (XCT) and destructive analysis were carried out where appropriate. These techniques were employed to measure the size and position of material discontinuities, to compare the surface roughness before and after processing and to assess the porosity of the bulk material.

More detail regarding the LU testing procedure and post-processing techniques used is given in the following sections.

3.5.1 Laser ultrasonic testing procedure

A full set of work instructions for operation of the laser ultrasound equipment were written and are now routinely used by all operators. In summary, once switched on a period of time (roughly a minute) is allowed for the generation laser cooling unit pump to stabilise, before all required softwares are loaded and the necessary communication (COM) ports selected.

LU scans are controlled from a PC using bespoke software, LaserScan created by Optech Ventures using LabView. Acquisition parameters such as number of points (1000 - 1250), total scanning time (5 – 10 μs) and number of averages (2 - 64) are set using the "NI-Scope Setup" tab shown in Figure 3-13. The number of scanning points, step sizes and the stage velocities (5 – 30 mm s^{-1}) are set using the "Scan Setup" tab shown in Figure 3-14.

Once the test pieces are placed under the LU system measurement head, the guide beams are used to select the start and end positions for the lasers (Figure 3-15). This allows the number of scanning points to be calculated using the desired step size (typically 0.1 – 0.25 mm) and the 'HOME' position to be set. The guide lasers are also used to visually focus the detection laser, altering the position of the measurement head in the Z-direction as necessary.

After completing these steps, the enclosure is secured and the lasers activated. The oscilloscope is used to ensure the maximum direct current (DC) signal voltage is returned (a measure of the laser light reflected from the sample surface). Typically, this is achieved by defocusing the detection laser slightly and iterating back towards the focussed position. Incidentally, defocussing the generation laser increases the spot size on the sample; this has the effect of increasing the wavelength and therefore the penetration into the test piece. When the acquired DC trace has been optimised as far as possible, the scan can be started. To maximise the DC current returned, the laser was operated in the ablative regime.

The alternating current (AC) signal returns a voltage reading corresponding to the out-of-plane surface displacement at the detection point. Once the scan has concluded, the data can be viewed in 'LaserScan' and extracted as text files for post-processing in Matlab.

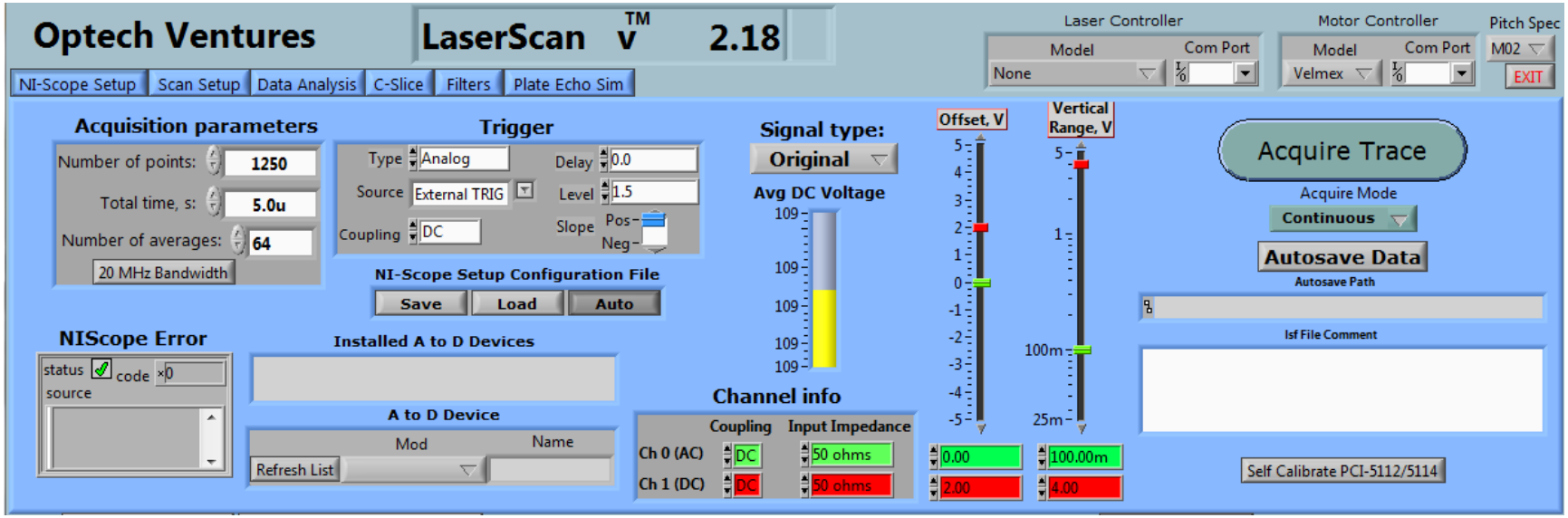

Figure 3-13 - LaserScan software – screenshot of 'NI-Scope setup' tab.

Figure 3-14 - LaserScan software - screenshot of 'Scan setup' tab.

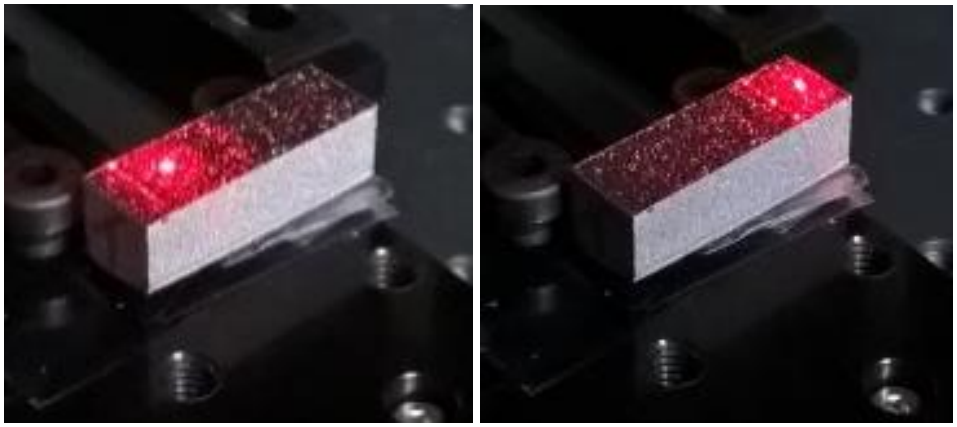

Figure 3-15 - Photographs showing start and end positions of the generation laser line and detection laser spot, indicated by guide beams.

3.5.2 Processing in Matlab

Once the AC and DC data is imported into Matlab, the AC signal values are first divided through by the average DC voltage measured at that translation point. As the received AC signal from the detector is dependent on light being reflected from the sample surface, at positions of low light, the AC value will be low; dividing by the average DC value at each point normalises this effect as far as possible.

Filtering is then employed to increase the signal-to-noise ratio by eliminating the high-frequency noise. A-scans and B-scans can then be plotted as necessary. In this instance, a low-pass filter is used to attenuate the content of a signal above a cut-off frequency, whilst allowing lower frequencies to pass; a cut-off limit of 10 MHz was found to be optimum with a sample rate of 60 MHz. A schematic of the filter is shown in Figure 3-16.

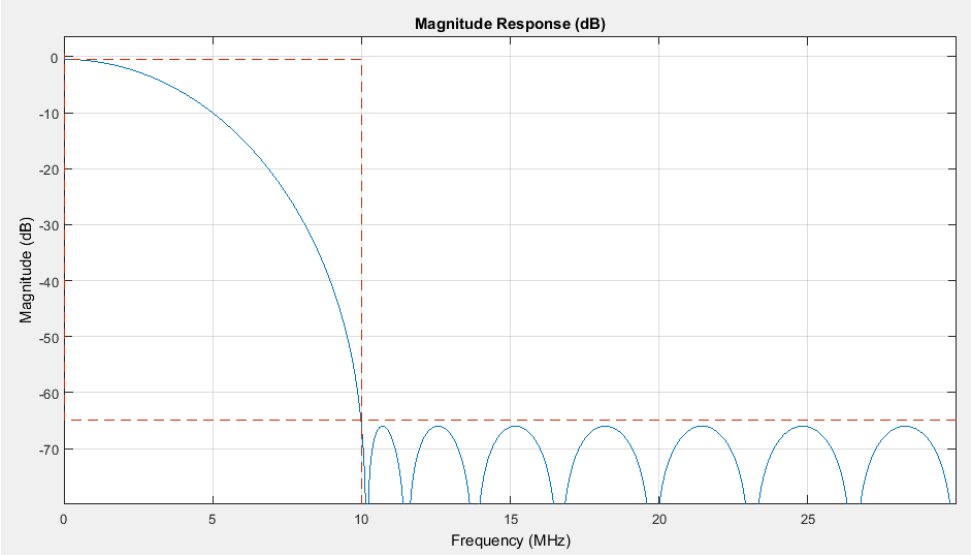

Figure 3-16 – Bode plot for low-pass filter emloyed.

Additionally, analysis of the frequency component of the fast Fourier transforms (FFTs) of the Rayleigh waves is undertaken to garner further information. To do this, the signal is windowed to 1 μs around the Rayleigh wave and zero-padding employed to extend the signal up to a bin length of 2^n (2048) .

Chapter 4 - Post-build “defects” study

4.1 Introduction

This chapter details a study carried out to investigate the LU system on test pieces manufactured by laser-PBF, considering the effects of surface roughness. Through-holes were manufactured in the AM samples to mimic porosity and allow a window of detection to be established; this is compared to anticipated resolution and attenuation values for the system.

Additional experiments include assessing the similarity of repeat LU scans and looking at ways to optimise the LU process, including minimising the time taken for each scan. The effect of LU proximity to test piece edges is also considered. X-ray computed tomography and destructive analyses are used to support these activities.

4.2 Methodology

For this study, test pieces were designed with through-holes at various diameters and depths, parallel to the top surface. Three blocks of Ti6Al4V (shown in Figure 4-1) which had been built by laser-PBF, using a Renishaw AM250 machine were used.

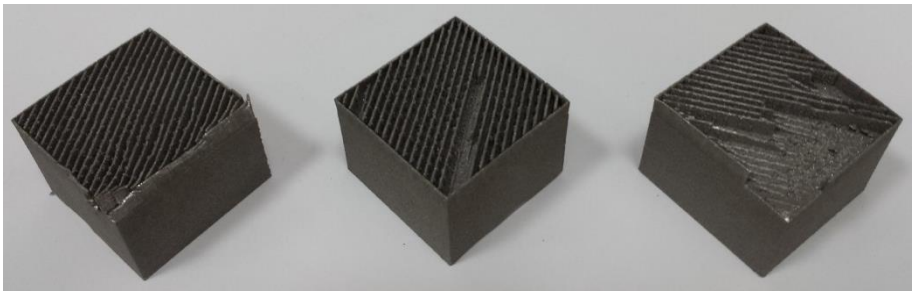

Figure 4-1 - Ti6Al4V samples produced by laser-PBF – upturned showing support structures partially removed, by hand.

The 30 *x* 30 *x* 23 mm samples were produced at a power of 200 W at point distance 75 µm, 125 µs exposure time at 150 µm hatch spacing and a scan angle increment of 67 °. Support structures were used to anchor the sample to the build plate which were subsequently removed (Figure 4-2a) to yield 3-off 30 *x* 30 *x* 20 mm test pieces (Figure 4-2b).

The 'time-of-flight' method was used to estimate the sequence of ultrasonic waves arriving at the detector, for different test piece geometries and a test piece width of 10 mm was selected to avoid wave interference. In particular, it is important to avoid the ultrasonic signals from waves reflected from the side walls arriving at the same time as the direct Rayleigh wave. Subsequently, wire-EDM was used to cut each sample as shown in Figure 4-2c into 6-off 10 *x* 30 *x* 10 mm test pieces (Figure 4-2d). To provide a reference, test pieces were also manufactured from Ti6Al4V wrought stock material.

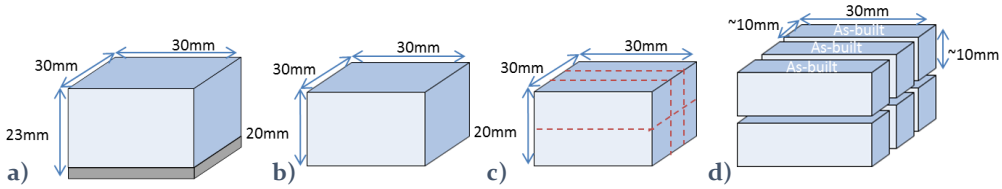

Figure 4-2 - a) starting sample dimensions, b) without support structures, c) cutting lines, d) final sample sizes.

The resulting 18 test pieces are shown in (Figure 4-3). A total of 9-off test pieces with an 'as-built' laser-PBF top surface (position references, 1.1, 1.2, 1.3, 2.1, 2.2, 2.3, 3.1, 3.2 and 3.3) and 9-off test pieces with an EDM top surface resulted (position references, 1.4, 1.5, 1.6, 2.4, 2.5, 2.6, 3.4, 3.5 and 3.6). A further set of 10 x 30 x 10mm test pieces were cut with wire EDM from the wrought billet stock.

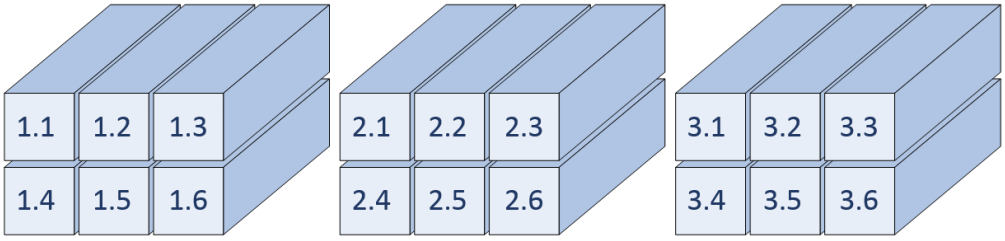

Figure 4-3 - Schematic giving position references from larger samples, for wire-EDM test pieces.

To mimic the effect of a void when LU scanning along the top surface of the sample, through-holes were manufactured in the test pieces by EDM parallel to the top surface, at various distances from the top surface. Utilising the previously carried out time-of-flight calculations used to size the test pieces, a design with a 10 mm "defect-free" zone and four through holes (a-d), machined at 5 mm intervals in the x-direction, was created (shown schematically in Figure 4-4).

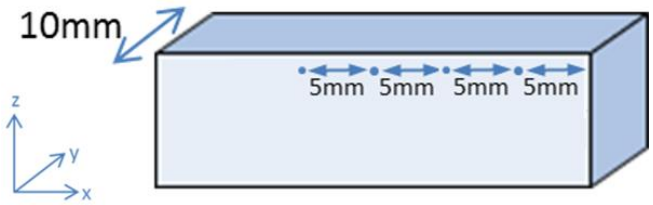

Figure 4-4 - Schematic showing minimum recommended hole spacing in x-direction.

A range of holes with different diameters at different z-distances were desired, to establish a window of detection for the LU system. The term z-distance here refers to the minimum distance in the z-direction between the sample edge (top surface) and the hole edge (Z), rather than the z-distance from the top edge to the hole centre (Z_C) – shown in Figure 4-5.

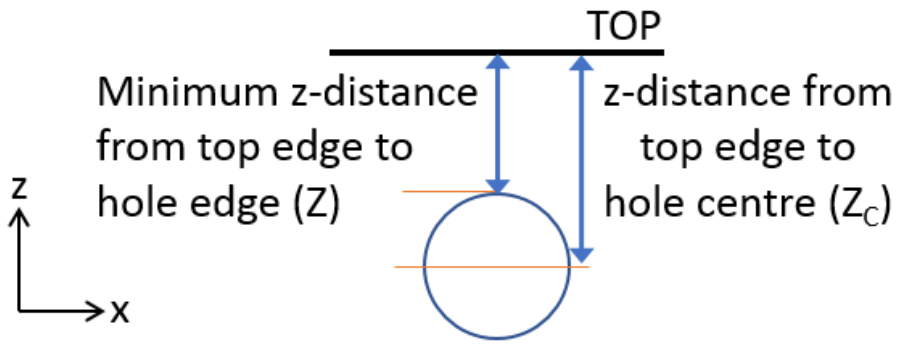

Figure 4-5 - Schematic showing z-distances from top edge to hole edge (Z) and top edge to hole centre (Z_C).

The minimum hole diameter achievable was limited by availability of guides required for the EDM process. Consequently, holes with 0.3 mm, 0.5 mm and 1 mm diameters were specified at a range of z-distances: 0.125 mm, 0.25 mm, 0.5 mm, 0.75 mm and 1 mm.

The z-distances and hole diameters were randomised to give 4 test piece designs (A-D) with a combination of 4 different holes (a-d), at different depths (Table 4-1).

Table 4-1 - Showing randomised hole diameters (Ø) at corresponding z-distances (Z).

Des.	A		B		C		D	
Hole	Z (mm)	Ø (mm)	Z (mm)	Ø (mm)	Z (mm)	Ø (mm)	Z (mm)	Ø (mm)
a	0.75	1	1	0.3	0.125	0.3	0.25	0.3
b	0.5	1	0.25	1	1	1	0.5	0.6
c	0.125	1	0.125	0.6	1	0.6	0.75	0.6
d	0.25	0.6	0.75	0.3	0.5	0.3	0.125	0.3

Twelve test pieces were created from the four sample designs, in the three different top surface material conditions - laser-PBF 'as built', laser-PBF EDM and billet EDM. Each test piece was allocated a reference code - details are summarised in Table 4-2; for the billet EDM test pieces, no position reference applies.

Table 4-2 – Summary of post-build, manufactured defects test pieces with test piece design, reference to original location in provided sample and top surface condition.

Test piece reference code	Design	Position ref.	Surface condition
M1	A	3.3	AM as-built
M2	B	2.1	AM as-built
M3	C	3.1	AM as-built
M4	D	1.2	AM as-built
M5	A	3.4	AM EDM
M6	B	2.5	AM EDM
M7	C	1.4	AM EDM
M8	D	1.6	AM EDM
M9	A	n/a	Billet EDM
M10	B	n/a	Billet EDM
M11	C	n/a	Billet EDM
M12	D	n/a	Billet EDM

The EDM hole diameters and z-distances have been validated using an Alicona InfiniteFocus, optical 3D micro coordinate system shown in Figure 4-6. A 10x magnified scan was taken over the area of each hole and test piece edge.

Figure 4-6 – a) Alicona InfiniteFocus and b) sample mounted under turret.

The in-built Alicona software suite was used to remove any form present due to the inspection surface not being parallel to the x-y plane. The 2D measurement tool within the software was then used to automatically fit a circle to the hole. The "N-point" option was selected meaning greater than three points around the circle circumference were selected before the circle was automatically placed. A number of lines were then drawn between the circle and sample edges. The minimum line length was used as the z-distance. Values were given in microns to four decimal places. An example image is shown in Figure 4-7.

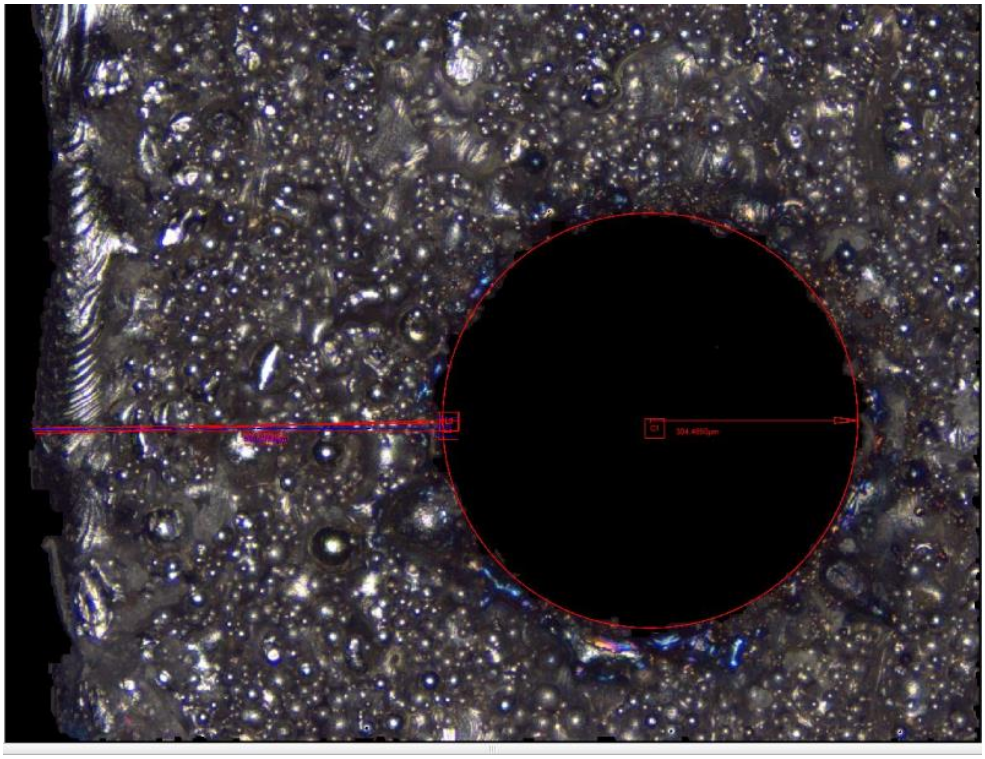

Figure 4-7 - Example image of hole with best-fit circle and z-distance measurement lines shown in red.

All z-distances and hole diameters were measured at entry and exit points. However, as the test pieces were LU scanned down the centre, an average of these values has been used for all further analyses. The values are shown in Table 4-3.

Significant variation was found between the desired dimensions and those actually achieved by EDM. Holes with 0.3 mm, 0.5 mm and 1 mm diameters were specified as these were the guides available for the electrode, however 0.3 mm guides were unavailable at the time the job was completed; instead, 0.5 mm guides were used. Using the 0.5 mm guides, hole diameters between 0.592 mm and 0.963 mm were generated. Using the 1.0 mm guides, hole diameters between 1.073 mm and 1.265 mm were manufactured. Z-distances between 0.261 mm and 1.226 mm were achieved.

Table 4-3 - Showing measured z-distances, Z (mm) and corresponding hole diameters, Ø (mm) for all test pieces.

	Ref.	M1		M2		M3		M4	
AM – As built	Hole	Z (mm)	Ø (mm)	Z (mm)	Ø (mm)	Z (mm)	Ø (mm)	Z (mm)	Ø (mm)
	A	0.774	1.095	0.726	0.701	0.456	0.625	0.417	0.581
	B	0.514	1.091	0.261	1.145	0.801	1.176	0.398	0.669
	C	0.471	0.963	0.437	0.614	0.92	0.661	0.593	0.662
	D	0.299	1.103	0.472	0.650	0.360	0.708	0.807	0.638
	Ref.	M5		M6		M7		M8	
AM – EDM'd	Hole	Z (mm)	Ø (mm)	Z (mm)	Ø (mm)	Z (mm)	Ø (mm)	Z (mm)	Ø (mm)
	a	0.678	1.161	0.874	0.643	0.518	0.651	0.563	0.615
	b	0.462	1.123	0.394	1.241	0.945	1.148	0.619	0.563
	c	0.406	1.108	0.570	0.592	0.931	0.621	0.790	0.615
	d	0.445	0.669	0.683	0.598	0.725	0.603	0.926	0.648
	Ref.	M9		M10		M11		M12	
Billet - EDM'd	Hole	Z (mm)	Ø (mm)	Z (mm)	Ø (mm)	Z (mm)	Ø (mm)	Z (mm)	Ø (mm)
	a	0.690	1.101	0.990	0.690	0.494	0.638	0.485	0.682
	b	0.461	1.091	0.444	1.094	1.226	1.265	0.516	0.604
	c	0.409	1.073	0.823	0.617	0.651	0.666	0.487	0.623
	d	0.472	0.697	0.725	0.633	0.529	0.626	0.836	0.638

4.3 Laser ultrasound results

In this section, LU results are presented and discussed for each experiment within this study. First though, examples of each image type are shown in the following section to demonstrate the application of the theory used for LU analysis, which was introduced in Chapter 3.

Unless otherwise stated, all samples were scanned from the "defect free" zone to the far end, translating in 0.25 mm steps over 108 steps.

4.3.1 Examples of schematics and images produced for each test piece

A schematic of each test piece in the x-z plane has been generated to show the intended and/or the achieved hole diameters and corresponding z-distances; an example is shown in Figure 4-8, for test piece M1. Where comparisons between samples are made, the schematics are sometimes shown to aid interpretation of the B-scans.

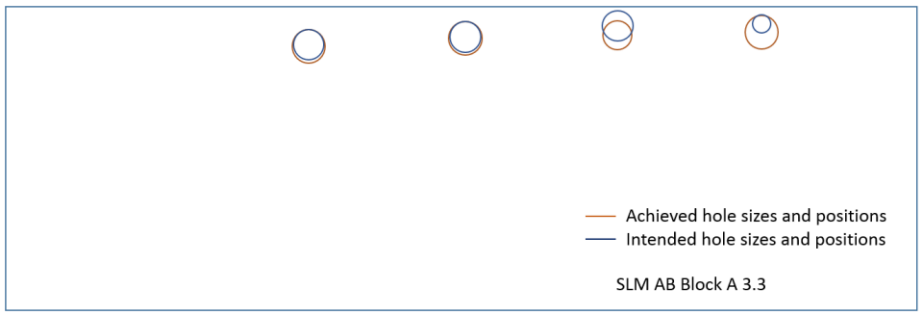

Figure 4-8 - Schematic showing intended and achieved hole sizes and positions for M1.

A-scans have been plotted to give comparisons between the received signals at different locations on a single test piece (Figure 4-9) or to compare signals across test pieces in terms of magnitude, for example.

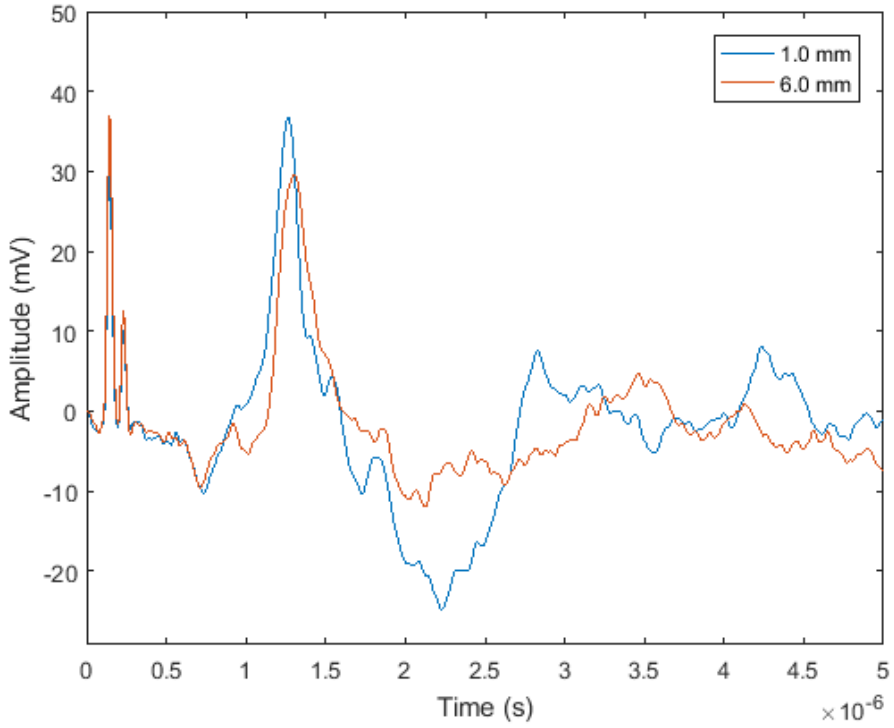

Figure 4-9 - A-scan of M1 at 1.0 mm (away from hole) and 6.0 mm (over hole) translation.

B-scans have been plotted using processed, rather than raw data. Images with greater clarity have been achieved by taking the raw data and removing the DC offset, applying a low pass filter and removing the high amplitude portion of the signal associated with the triggering of the laser; greyscale values were adjusted accordingly. For reference, a B-scan generated from the raw data is shown here in Figure 4-10 and the enhanced B-scan shown in Figure 4-11.

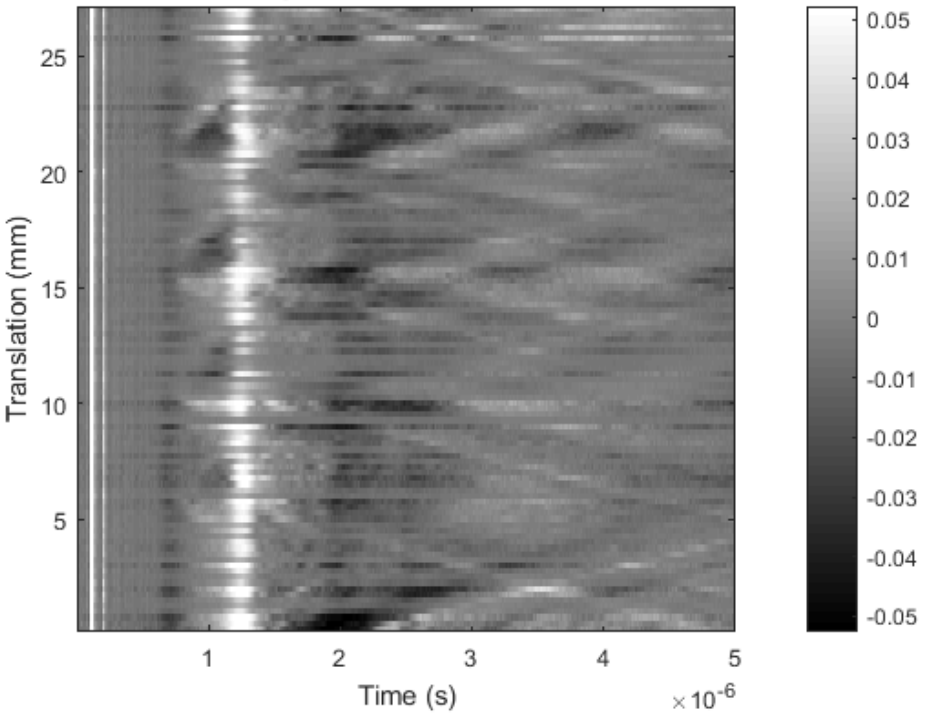

Figure 4-10 – B-scan of M1 from Raw data.

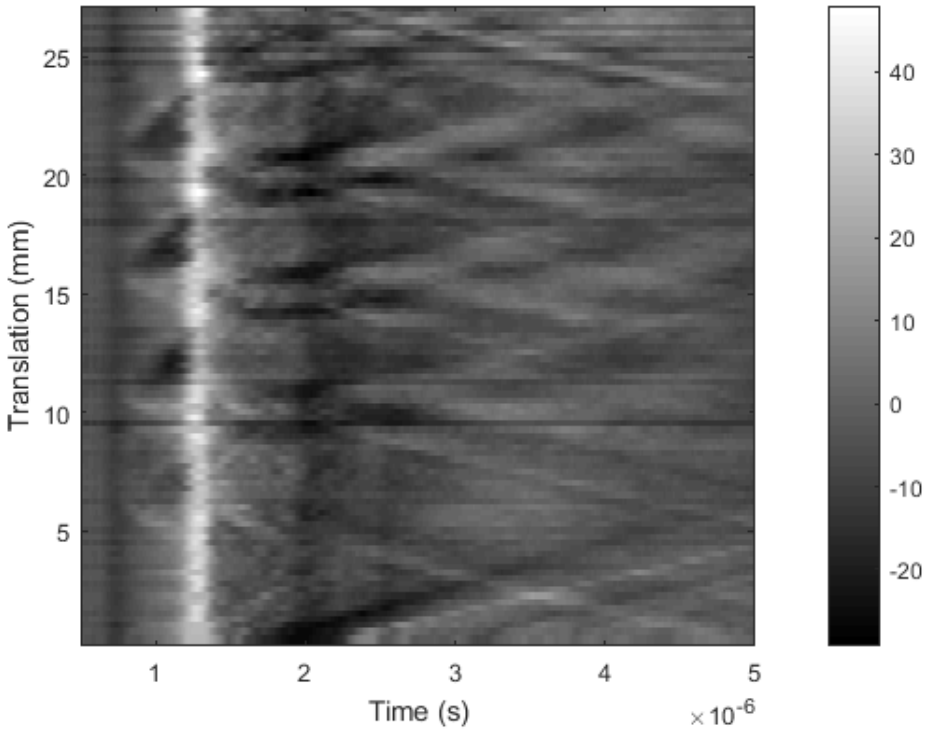

Figure 4-11 - B-scan of M1 with DC offset removed, low-pass filter applied at 10 MHz and shot noise removed.

In order to ensure the B-scan images were analysed in a systematic manner, the same interrogation process was followed for each analysis. Firstly, all images were viewed at a minimum size of 160 *x* 200 mm on a monitor with a minimum resolution of 1024 x 768 pixels. Secondly, features of interest described below and marked on Figure 4-12 were identified and overlaid. Finally, the series of standard wave arrivals indicated on Figure 4-13 were identified and overlaid. The key features are described in more detail below:

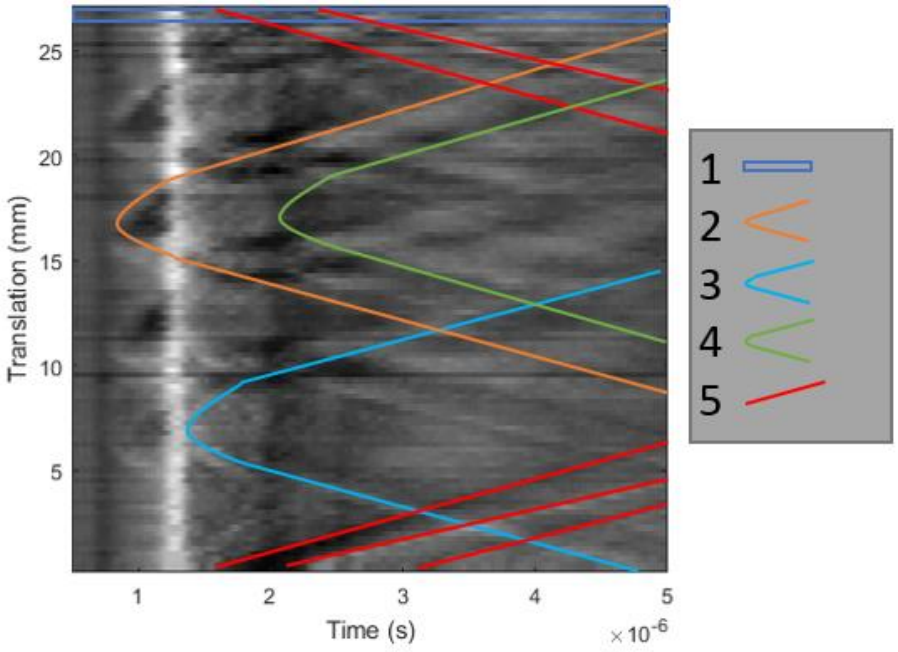

Figure 4-12 - B-scan of M1 with DC offset removed, low-pass filter applied at 10 MHz and shot noise removed – features of interest marked.

The enhanced B-scans shown above have several key features, described previously in Chapter 3:

1. Areas of signal drop-out, likely caused by changes in working distance between measurement head and sample, defocussing the laser. Alternatively caused by local surface features which increase light scattering.

2. Characteristic parabolic indication of a “defect” caused by diffracted longitudinal wave which has been reflected of the bottom of the test piece.
3. Characteristic parabolic indication of a “defect” caused by diffracted Rayleigh wave.
4. Characteristic parabolic indication of a “defect” caused by diffracted longitudinal wave which has been reflected of the sidewall of the test piece.
5. Reflected waves from sample end walls. As the measurement head translates over the sample, the arrival times of the reflected waves from the starting end wall increase. Similarly, the time of flight to the other end wall decreases so a trail with an inverted gradient is also present.

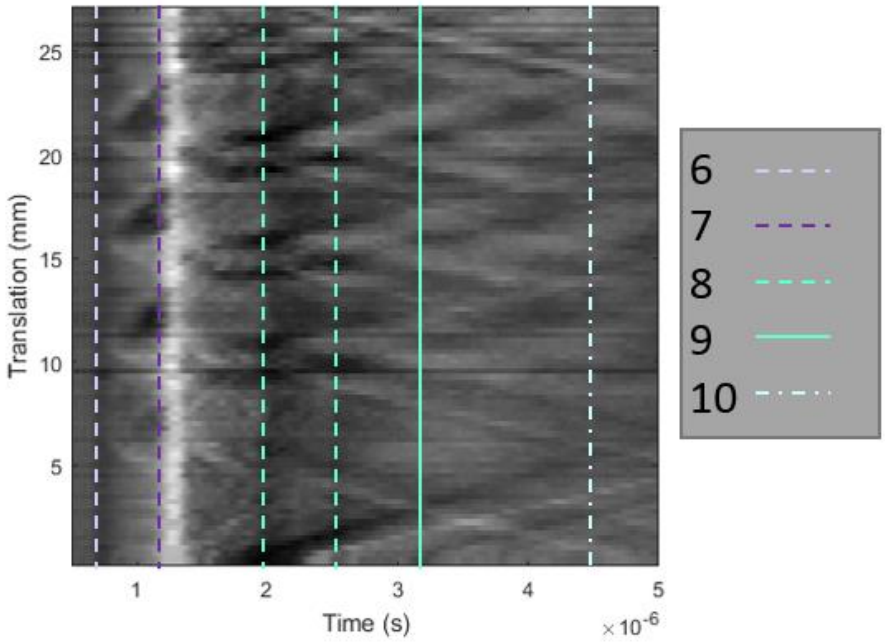

Figure 4-13 - B-scan of M1 with DC offset removed, low-pass filter applied at 10MHz and shot noise removed - wave arrivals indicated.

6. Direct (skimming) longitudinal wave arrival.
7. Direct Rayleigh wave arrival.

8. Longitudinal waves arriving having been reflected off the side walls of the sample. The presence of two distinct wave arrivals indicates the test piece was not scanned centrally. If the test piece was scanned exactly down the centre of the top surface, the waves would arrive at the same time and only a single indication would result.
9. Longitudinal wave arriving having been reflected off the bottom of the sample – also given the nomenclature 2L.
10. SL and LS waves arriving having reflected off the bottom of the sample and been mode converted.

To interrogate the diffracted (reflected) longitudinal wave and the diffracted direct Rayleigh waves (2 and 3), the signals have been limited to the 0.4 – 1.4 μs section and all remaining data points zero padded (i.e. changed to 0's). The signal length has been limited to 1064 points and a FFT performed. A FFT plot such as the one shown in Figure 4-14 results – only one half of the symmetrical plot is shown.

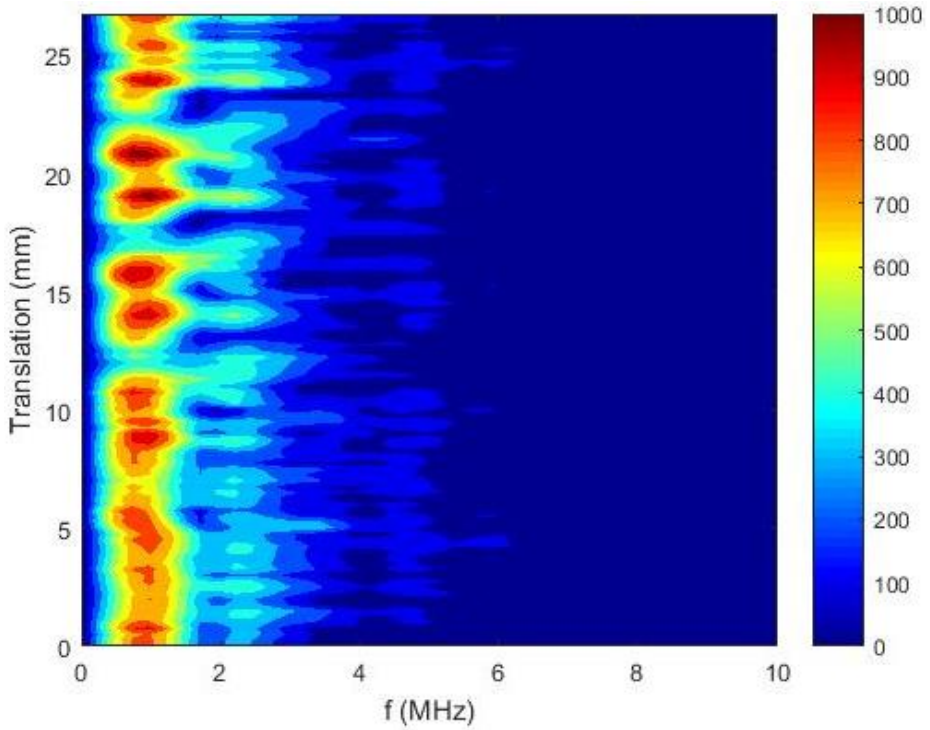

Figure 4-14 - FFT plot of M1 in Rayleigh wave window (0.4 – 1.4 μs).

A schematic of the test piece and a cropped FFT plot are shown in Figure 4-15 and aligned, matching the y-axis with the 26 mm path translated along the test piece. The Rayleigh wave frequency in the region of 1MHz – areas of signal enhancement are seen at translations, corresponding to the detector being positioned at the hole edges.

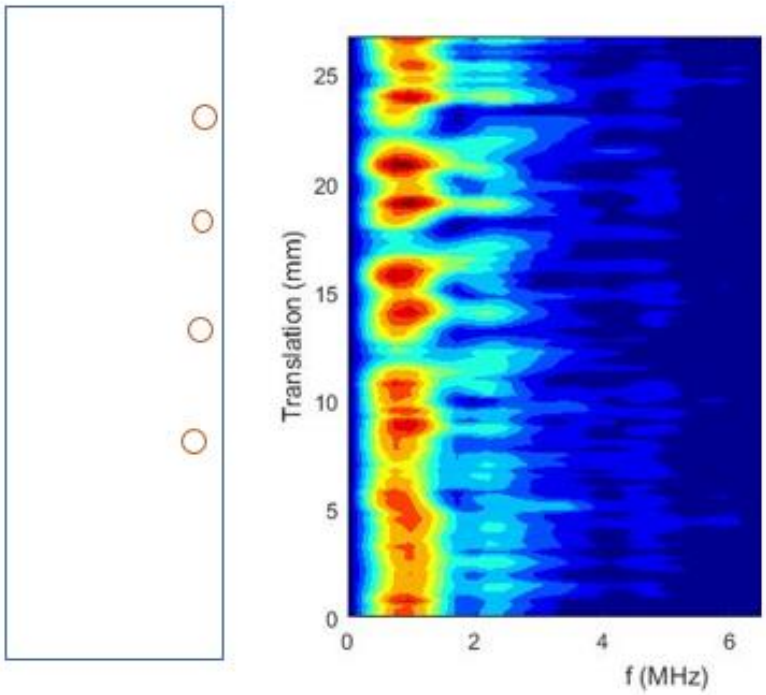

Figure 4-15 – Cropped FFT plot of M1 in Rayleigh wave window (0.4 – 1.4 μs) with schematic of test piece for comparison.

4.3.2 Experiment 1 - Effect of surface condition

Images were taken of the three test piece surfaces using FVM over a 750 *x* 500 μm area, at 20X magnification after LU processing (Figure 4-16). The area roughness parameter S_q, calculated as the root mean square height over an area, was measured for each sample. S_q is equivalent to the standard deviation of the heights measured and is an areal extension of R_q [130].

The image in Figure 4-16a shows the laser-PBF surface for M4 which returned a surface roughness, S_q of 13.2 μm. The AM scan tracks can be seen running diagonally with the characteristic chevron pattern evident. Some spatter particles and cavities are evident on the surface. By contrast, Figure 4-16b shows the laser-PBF sample M7 with an EDM top surface which has a surface roughness value, S_q of 4.6 μm. The billet EDM sample M9, shown in Figure 4-16c, has a surface roughness value S_q of 4.7 μm.

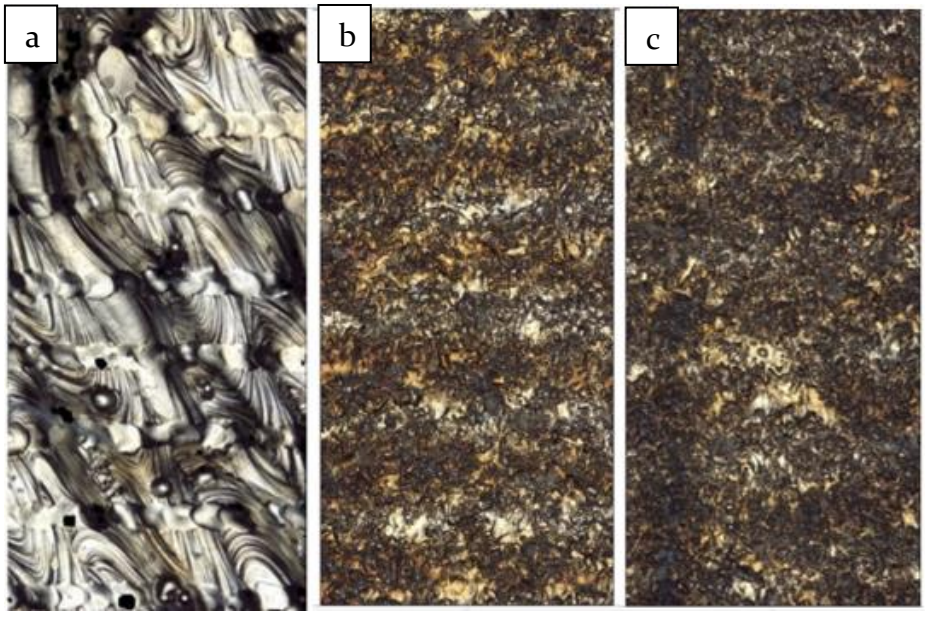

Figure 4-16 - FVM images of sample surface roughness (covering an area of 700 *x* 1500 μm) for a) M4, – laser-PBF as-built, b) M7 – laser-PBF EDM and c) M9 – Billet EDM.

As expected when using a photo-EMF detector, a higher magnitude response was detected when scanning the rougher surface (M4 – blue), shown in Figure 4-17.

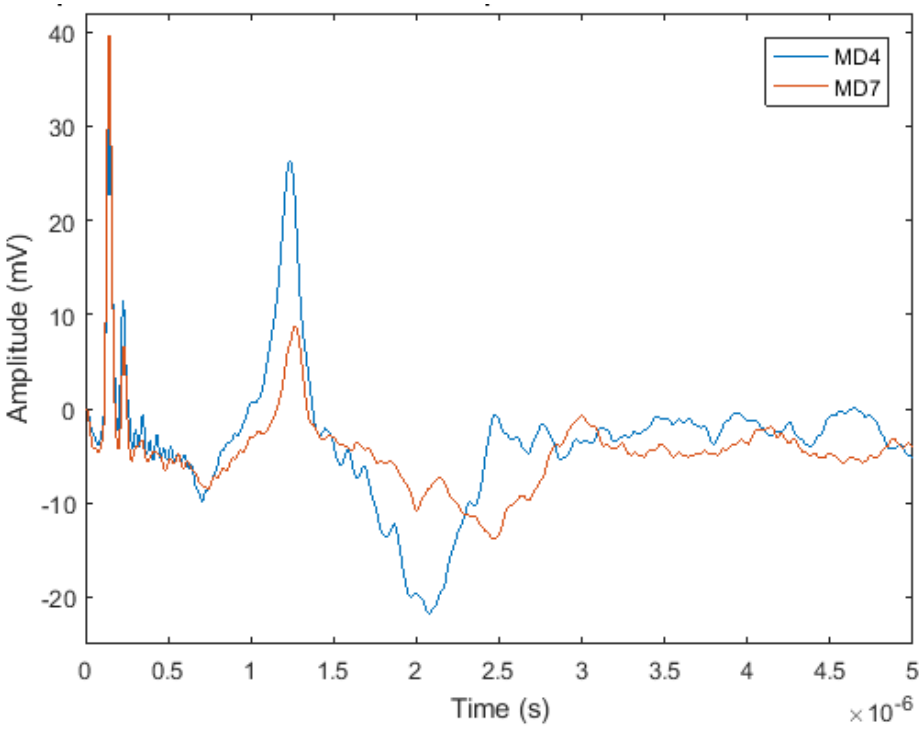

Figure 4-17 - Comparison of laser-PBF (M4) and EDM (M7) top surface A-scans at 1.0 mm translation, away from known "defect" locations.

The increased signal magnitude displayed in the A-scan for the laser-PBF surface of test piece M4 yields a B-scan with greater resolution. This can be seen in Figure 4-18a where many more full and partial parabolic indications of "defects" are visible. The B-scan for M7 shown in Figure 4-18b shows fewer indications and has a series of horizontal striations resulting from the fluctuations in DC signal received.

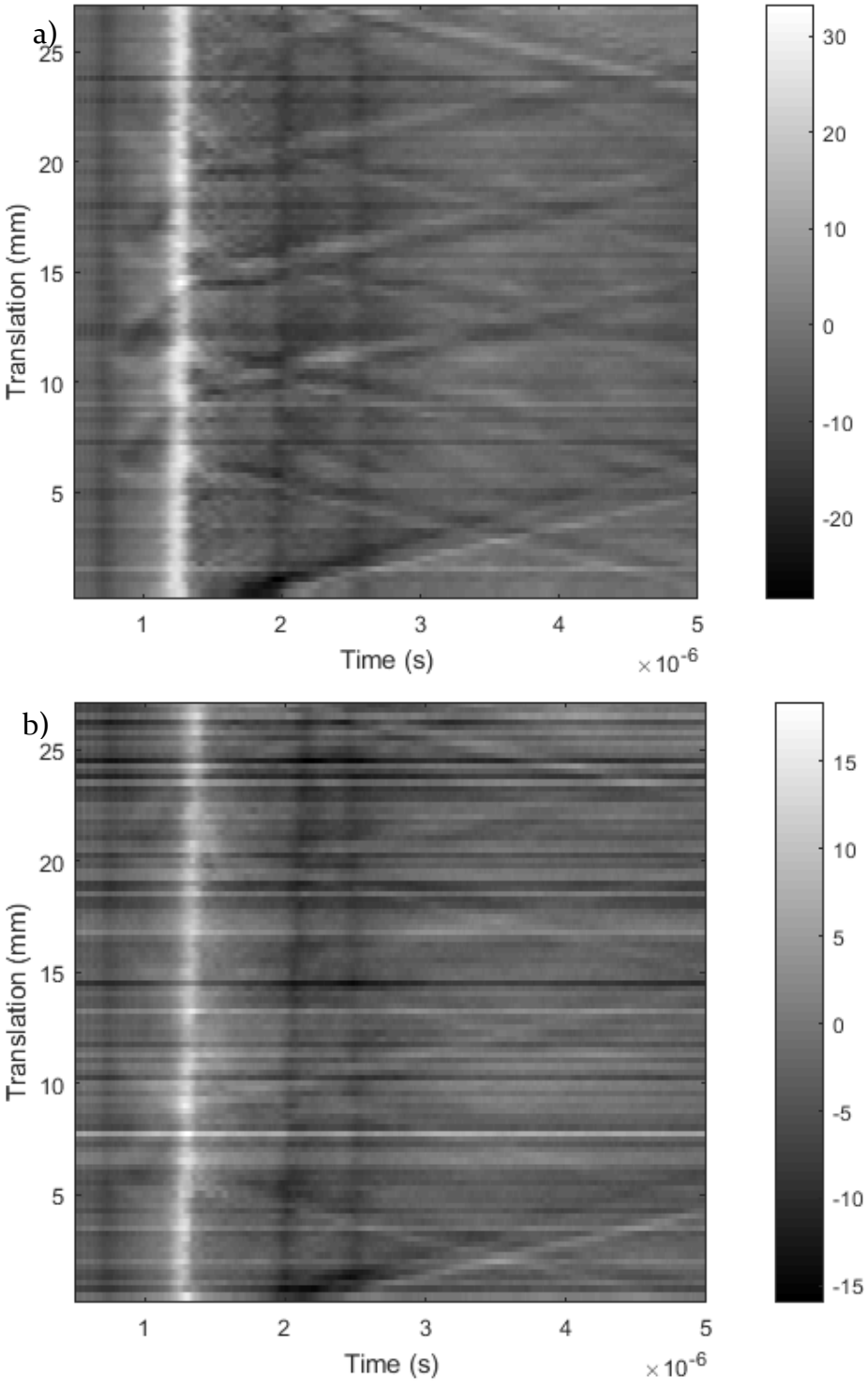

Figure 4-18 – a) M4 B-scan (13.2 μm Sq) and b) M7 B-scan (4.6 μm Sq) showing improved resolution, resulting from increased magnitude signal returned from laser-PBF surface.

4.3.3 Experiment 2 - Window of detection

Ultrasound can propagate large distances in solids. Attenuation is caused by spreading (inverse square law in three dimensions), absorption in material and scattering from interaction with a discontinuity or grain boundary. Surface waves only act in 2 dimensions so are detected with large amplitude and do not attenuate due to spreading. A Rayleigh wave is expected to be detected at depths up to half of its wavelength [92]; for Rayleigh waves in Ti6Al4V, this is equivalent to a depth of approximately 1.5 mm.

B-scans of each test piece (M1-12) have been assessed for indications of features such as those detailed in Figure 4-12. An overview of the B-scans with identified indications is shown in Figure 4-19, with the individual B-scans available in Appendix 10.1 . A graph plotting the EDM hole diameter against z-distance is shown in Figure 4-20. Markers are used to distinguish between test piece surface finish; M1-4 have square markers, M5-8 have triangles and M9-12 have circles. Colours are used to designate whether a full or partial longitudinal and/or Rayleigh parabola is indicated.

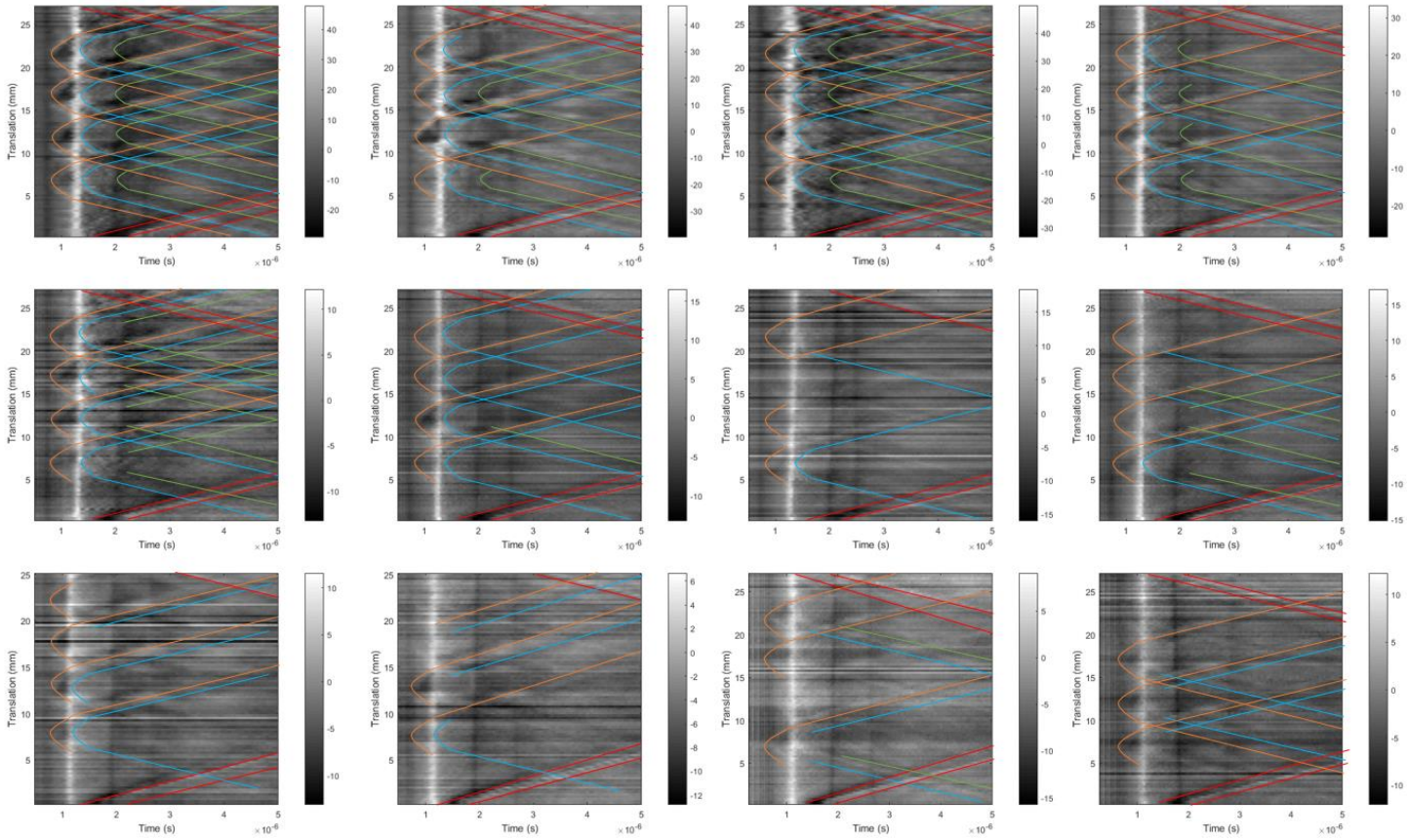

Figure 4-19 - Summary of B-scans for M1-12 with identified indications.

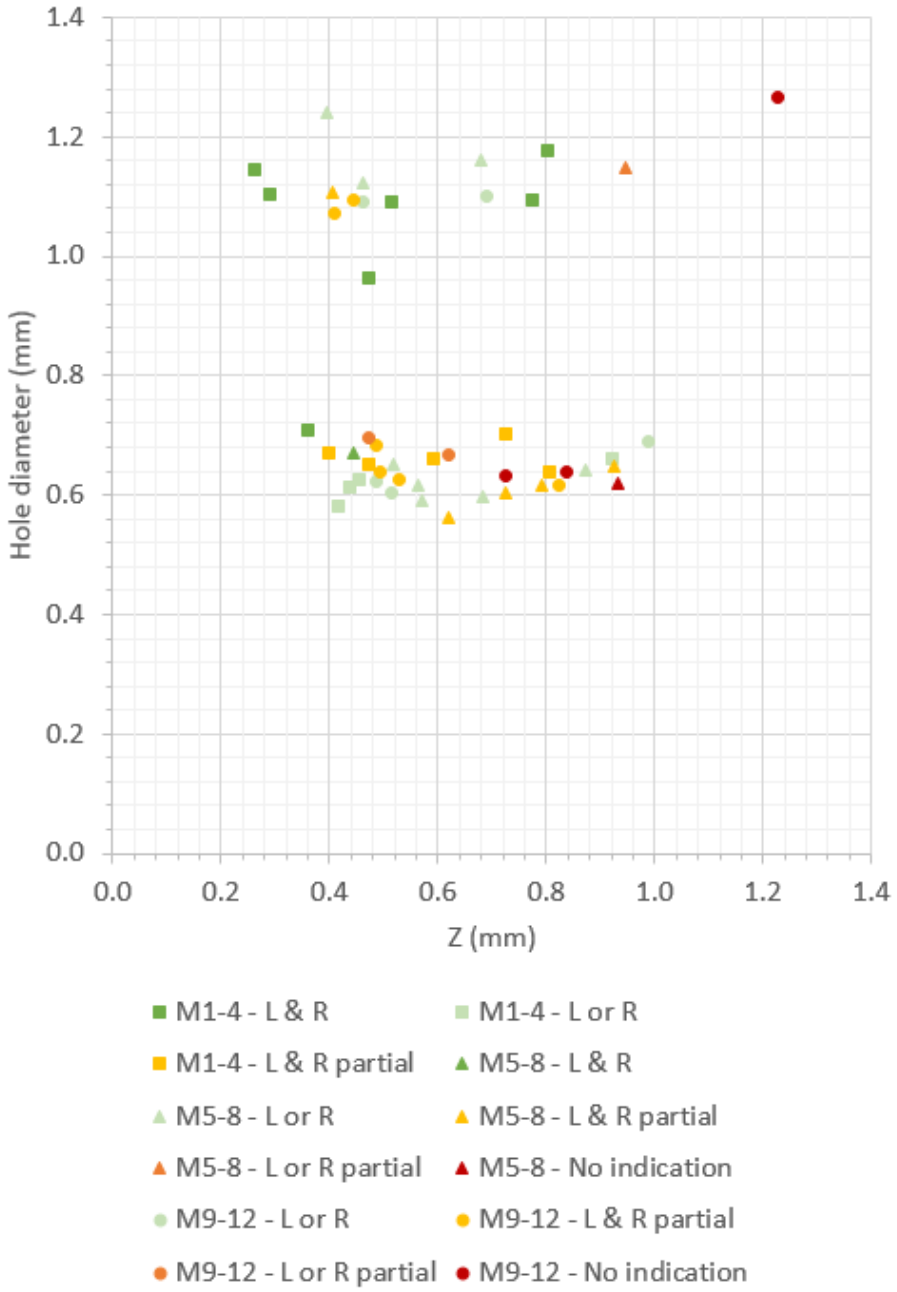

Figure 4-20 - Graph of z-distance (mm) vs. hole diameter (mm), using shapes to indicate top surface finish and colour to give a level of indications.

From interrogating the B-scans using the method described in Section 4.3.1 , all laser-PBF top surface test pieces (square markers) yielded at least partial longitudinal and Rayleigh wave parabolas meaning all 16 holes were indicated, to some degree, on the B-scan. The B-scans for the group of larger diameter holes, created with the 1 mm EDM guides, had full longitudinal and Rayleigh wave parabolas evident. The B-scans from the EDM top surface, AM test pieces (triangular markers) showed full longitudinal and Rayleigh parabolas for only one hole (M5-d) although partial indications were visible for all but hole M7-c. Although there is a general trend that more indications were shown for the larger holes and for those nearest the surface, there are some anomalies.

Comparatively fewer "good" indications could be identified from the B-scans for the EDM surface blocks cut from the billet material (circular markers). None of the holes were indicated by full longitudinal and Rayleigh parabolas and three of the holes gave no indications whatsoever (M10-d, M11-b and M12-d).

To summarise, all but four of the 48 through-holes were indicated on the B-scans in some way; the four unidentified holes were all in test pieces with an EDM surface finish. It is probable that the reduced resolution of the B-scans generated from the EDM surfaces has hindered identification of the indications.

29 out of 32 holes in the smaller hole diameter grouping could be identified to some degree, including all 20 with a 0.563 – 0.708 mm diameter, up to a z-distance of 0.622 mm. Similarly, for the larger hole diameter grouping 15/16 holes could be identified, with those

with diameters in the range 0.963 – 1.241 mm, up to a z-distance of 1.148 mm giving a full or partial indication.

All the void diameters replicated here were well in excess of the smallest (100 μm) diameter limit anticipated for the system. Similarly, all holes created were at depths below the 1.5 mm limit calculated based on attenuation of the Rayleigh wave. However, not all of the holes were indicated on the LU B-scans. Further work is required to revise these theoretical limits, based on detection of AM representative "defects". This was investigated in Chapter 5 and Chapter 6 .

4.3.4 Experiment 3 – Comparisons of repeated scans

Each test piece was scanned three times, utilising the motorised stage to return the measurement head to the starting position after each LU scan. The enclosure was not entered and the test piece therefore not touched between scans so this is not a true (industrially recognised) repeatability test. The resulting B-scans are shown in Figure 4-21, Figure 4-22 and Figure 4-23.

No differences are distinguishable visually between the three B-scans. Each shows a data drop out at 9.5 mm translation and the same pattern of indicated holes after the longitudinal and Rayleigh wave arrivals.

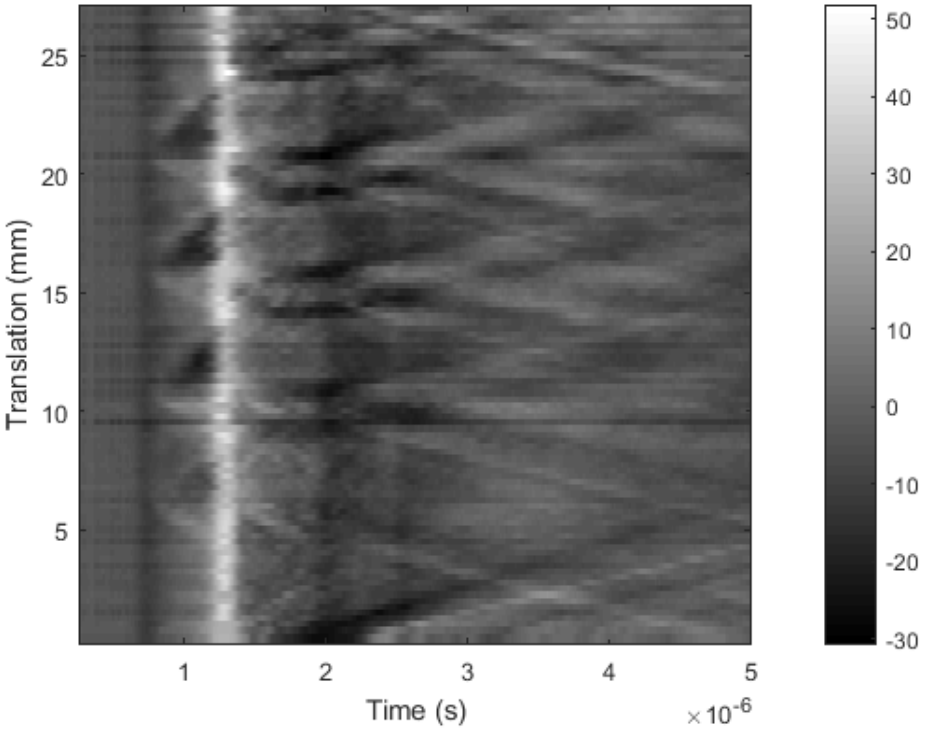

Figure 4-21 - B-scan of M1 - scan 1.

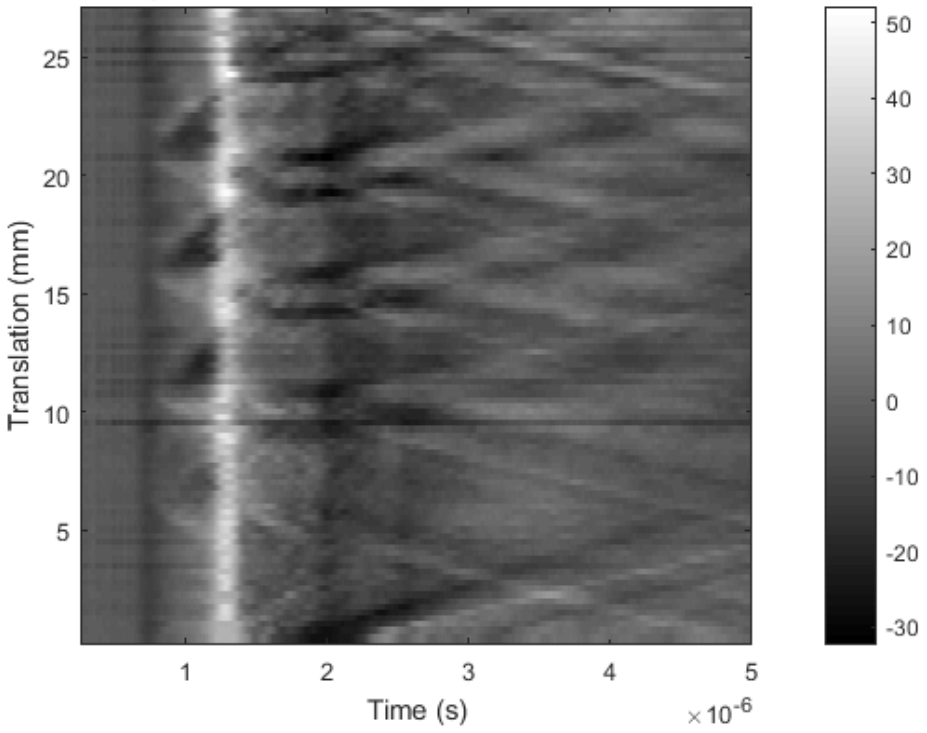

Figure 4-22 - B-scan of M1 - scan 2.

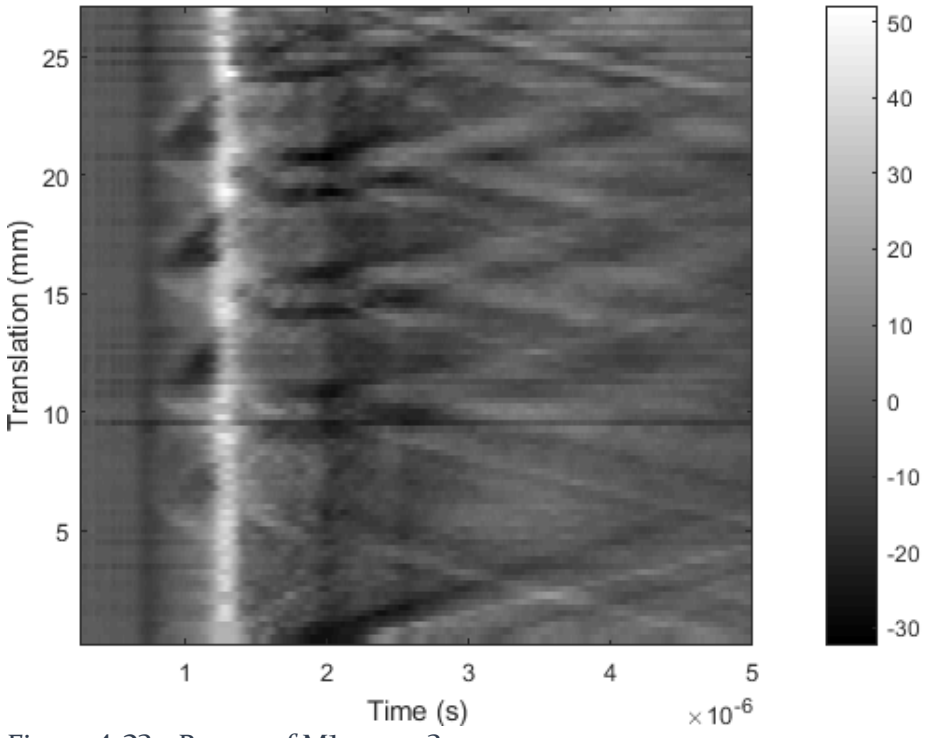

Figure 4-23 - B-scan of M1 - scan 3.

Plotting A-scans for the three repeat scans of M1 at 1.0 mm translation (Figure 4-24), it can be seen that there is generally good agreement between the signals; the second and third scans in particular rarely deviate. The first scan is generally at a lower magnitude than the second and third signals, suggesting that the initial scan in the ablative regime does perhaps alter the surface condition slightly, this was investigated further in section 6.3.8 .

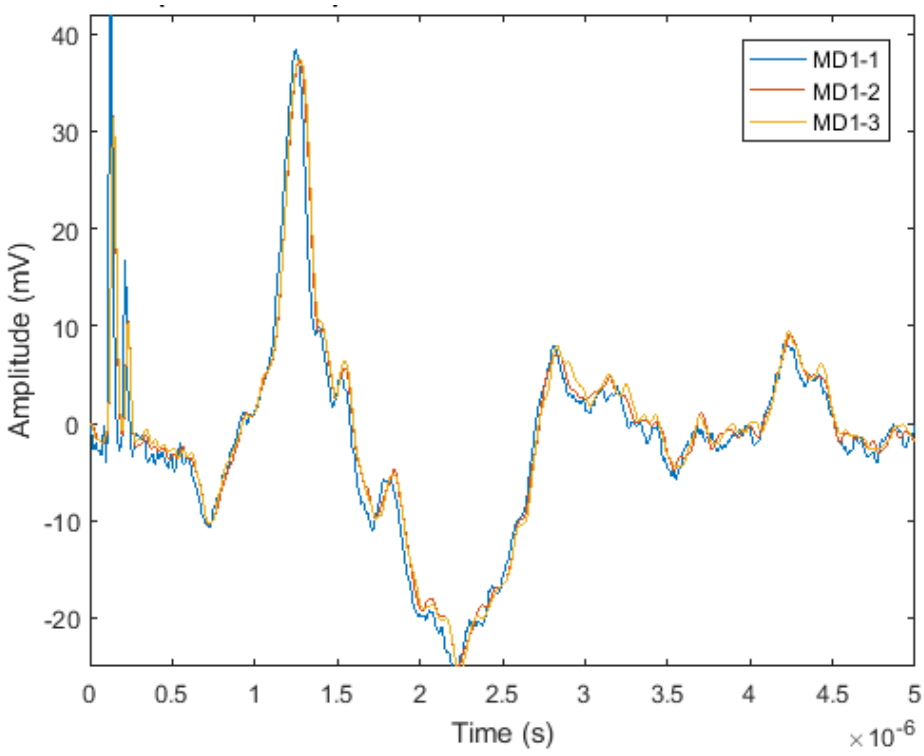

Figure 4-24 - A-scans at 1.0 mm translation for M1 repeat scans 1-3.

4.3.5 Experiment 4 – LU scanning times

Based on recommendations from the LU equipment manufacturer, the LU scans were set up with a temporal averages setting of 64 and a 0.25 mm step size. This means that 64 repeat signals were taken, to improve the signal-to-noise ratio, at each 0.25 mm translation increment and the averaged signal displayed. Although this approach yields good quality data, the average scan time for a translation of 27 mm was approaching 7 minutes.

With a view to using LU in the future as an in-situ monitoring technique, this time would need to be significantly reduced for the process to be viable. There are several approaches which could be taken to reduce this to a more acceptable time, such as reducing the number of averages selected or increasing the translation step size; these options have been investigated in this experiment.

4.3.5.1 *No of averages*

B-scans were taken of M4 (AM, as-built top surface), reducing the number of temporal averages from the recommended setting, by a factor of 2 each time from 64 to 32 and so on. The total scanning time elapsed was recorded in each case.

The B-scans were assessed visually for the indications identified in the highest quality scan shown in Figure 4-25.

Reducing the temporal average down to 4 reduced the total time taken to scan a 27 mm line by 80%, from 6 minutes and 49 seconds to 1 minute and 23 seconds. The B-scan, shown in Figure 4-26 has decreased in resolution, but the same visual indications can be picked out.

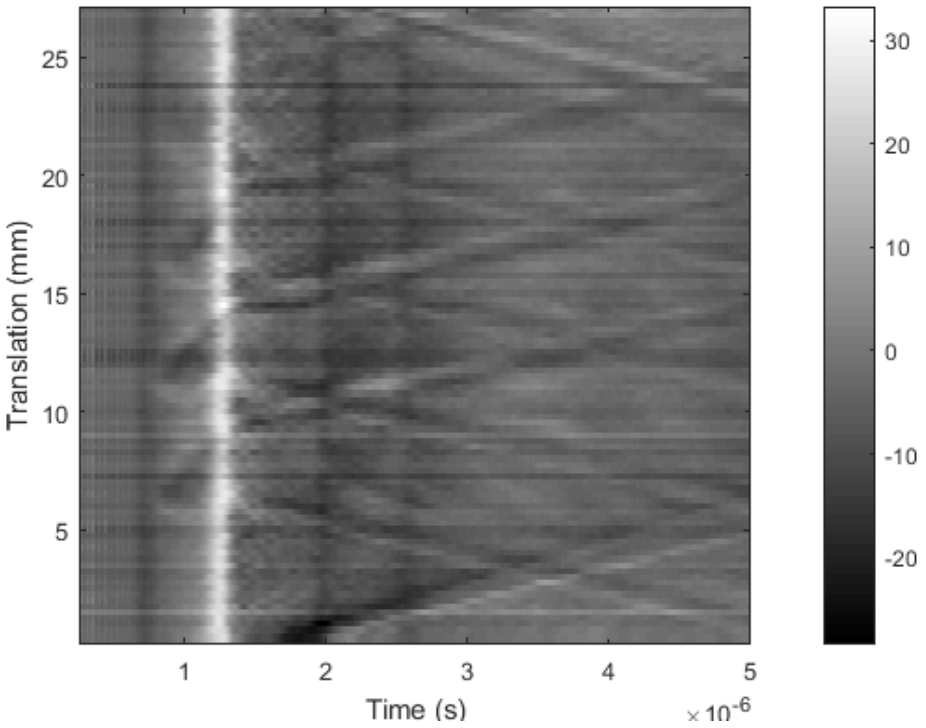

Figure 4-25 - B-scan of M4 with 64 averages.

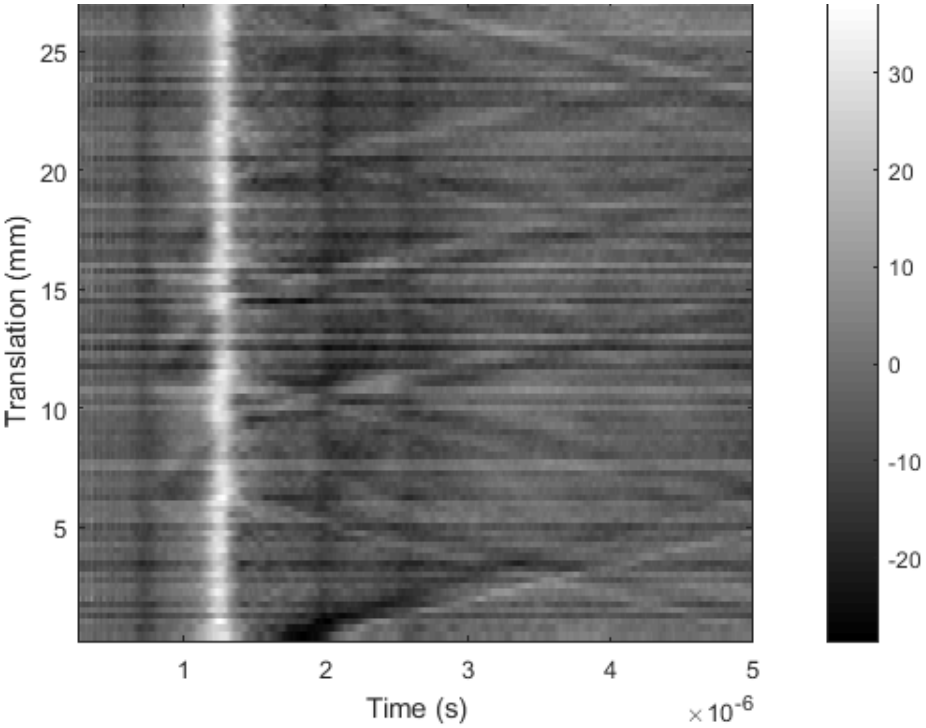

Figure 4-26 - B-scan of M4 with 4 averages.

A further reduction to 2 averages only reduced the scan time by a further 11 seconds and yielded a poor quality B-scan (Figure 4-27). The horizontal striations caused by the increased noise make it difficult to distinguish the previously identifiable features caused by the large material discontinuities.

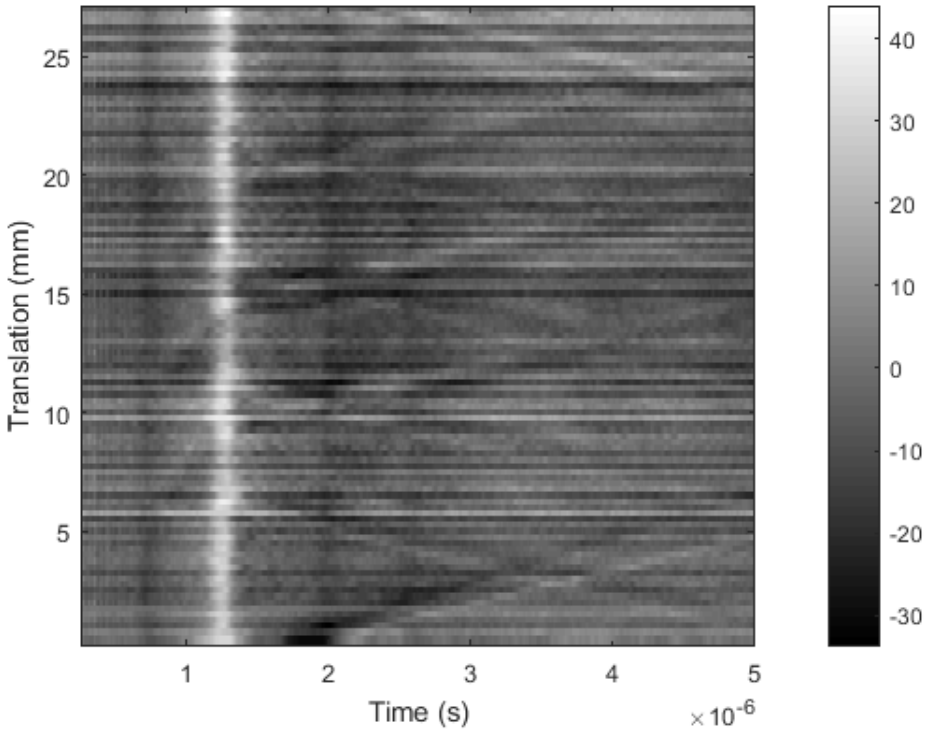

Figure 4-27 - B-scan of M4 with 2 averages.

4.3.5.2 *Step size*

An alternative approach investigated the reduction of the overall LU scan time by increasing the step size from the recommended 0.25 mm to 0.5 mm and to 1.0 mm, thus reducing the total number of signals acquired. In each case the total scanning time was reduced by 50% to 3 minutes and 24 seconds and 1 minute and 42 seconds respectively. Although this approach yielded a good time reduction, the B-scans for M1 (AM, as-built top surface) yielded were of poor quality.

The B-scan resulting from the recommended settings is shown in Figure 4-28 and the four through-holes can be identified from the parabolic indications in the diffracted longitudinal wave returned from the bottom of the test piece, the diffracted Rayleigh wave and the diffracted longitudinal wave reflected off the sidewall.

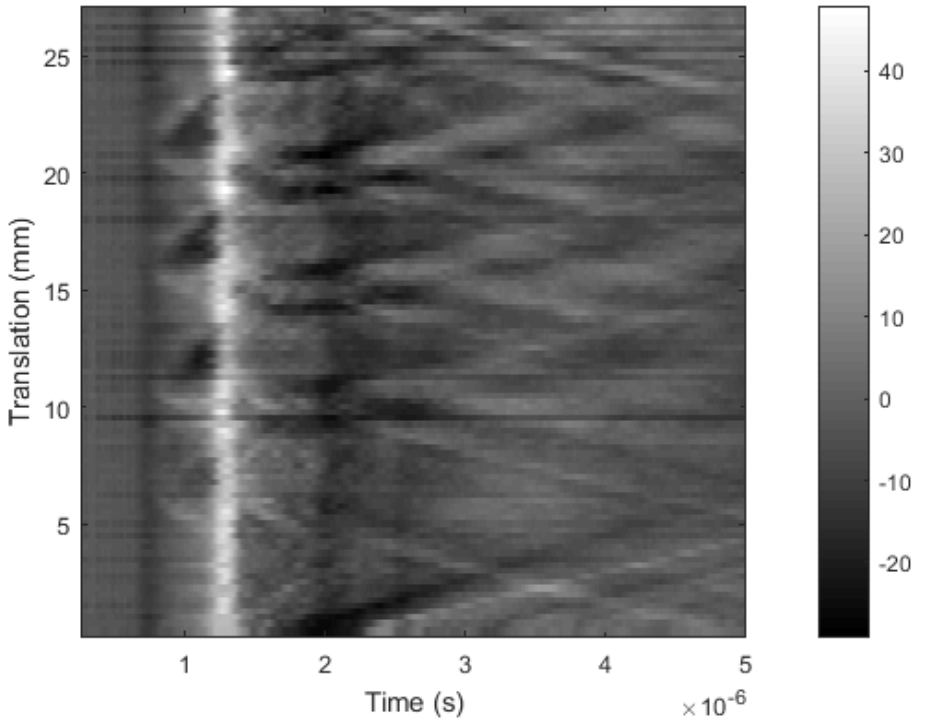

Figure 4-28 - B-scan of M1 scanned at 0.25 mm intervals.

Figure 4-29 and Figure 4-30 show B-scans for the 0.5 mm and 1.0 mm step sizes. In both cases, the resolution has degraded to the point that the only identifiable indications are the top of the diffracted longitudinal wave returned from the bottom of the test piece. In the 1.0 mm case, even this is hard to distinguish from the noise.

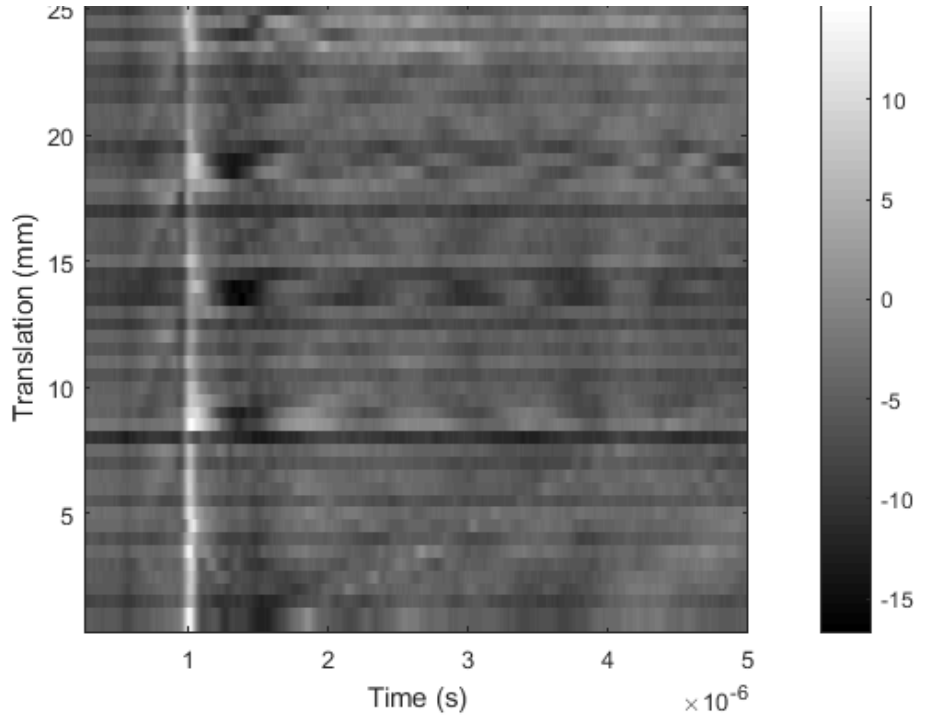

Figure 4-29 - B-scan of M1 scanned at 0.5 mm intervals.

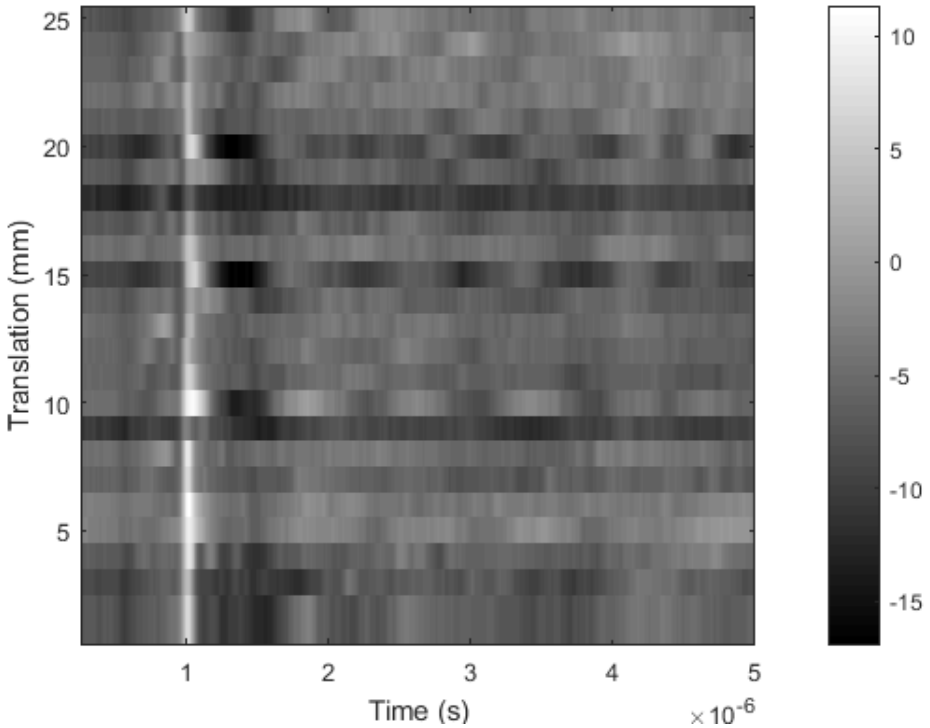

Figure 4-30 - B-scan of M1 scanned at 1.0 mm intervals.

From these experiments, it can be concluded that it is possible to reduce the time taken for a LU translation of 27 mm to 1 minute and 23 seconds by reducing the number of averages taken at each translation point from the recommended 24, to 4. This reduction can be achieved with an acceptable loss of resolution in the B-scan, however the maximum recommended step size of 0.25 mm should be adhered to.

Another factor influencing the total scanning time is the time taken translating the measurement head between scans. Using a translation stage with an increased stage velocity could further reduce the scan time. Increasing the generation laser power is an alternative approach that could be investigated in future work.

4.3.6 Experiment 5 - Proximity to edges

In all cases, the LU scan has been performed roughly down the centreline of a sample, in order to avoid arrival of waves reflected from the side-walls at the same time zone as the direct Rayleigh wave. However, should LU be implemented as an in-situ monitoring method, it is likely that scans would need to be carried out on thin walled features. As such, a scan was carried out with the lasers translating close to the sample side-wall, a B-scan is shown in Figure 4-31 with the corresponding B-scan roughly along the centreline in Figure 4-32.

The longitudinal wave arriving from the wall adjacent to the scan arrives very soon after the Rayleigh wave and only one reflection is visible, rather than the two seen when scanning centrally. The second longitudinal wave, reflected off the far side wall must either arrive outside the 5 μs window or attenuate before it reaches the detector. Although this reduced arrival time does mean that the parabolas from the diffracted Rayleigh wave and diffracted, longitudinal wave from the nearest side wall overlap, it is still possible to identify indications of a material discontinuity. In addition, extra indications are highlighted in Figure 4-31 which are not visible in Figure 4-32.

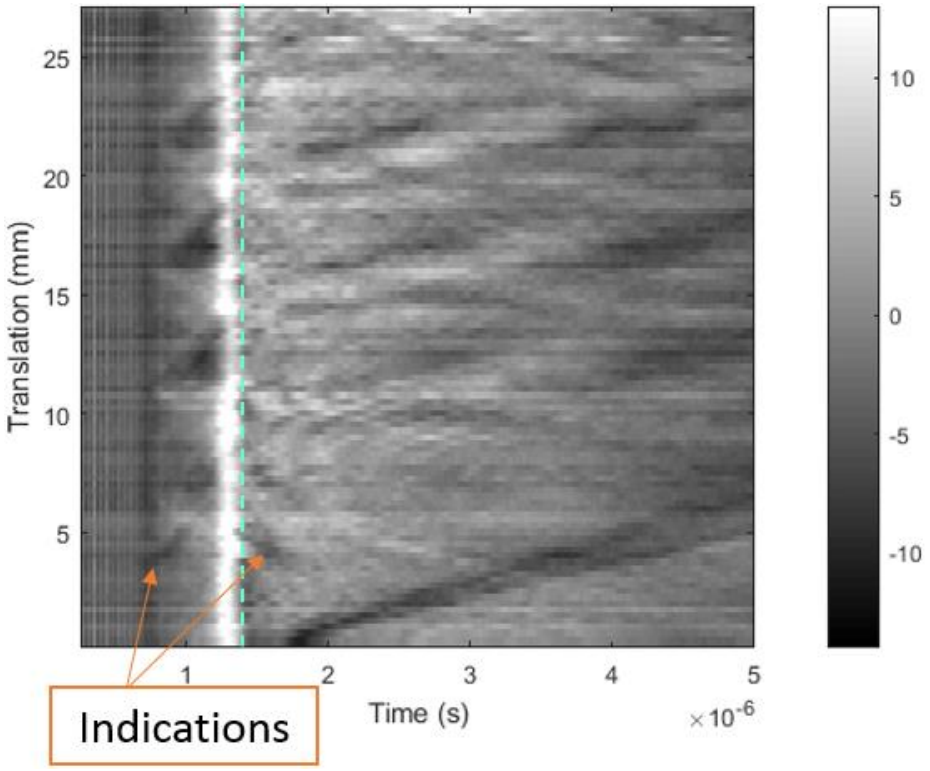

Figure 4-31 - B-scan of M5 translating very close to side-wall.

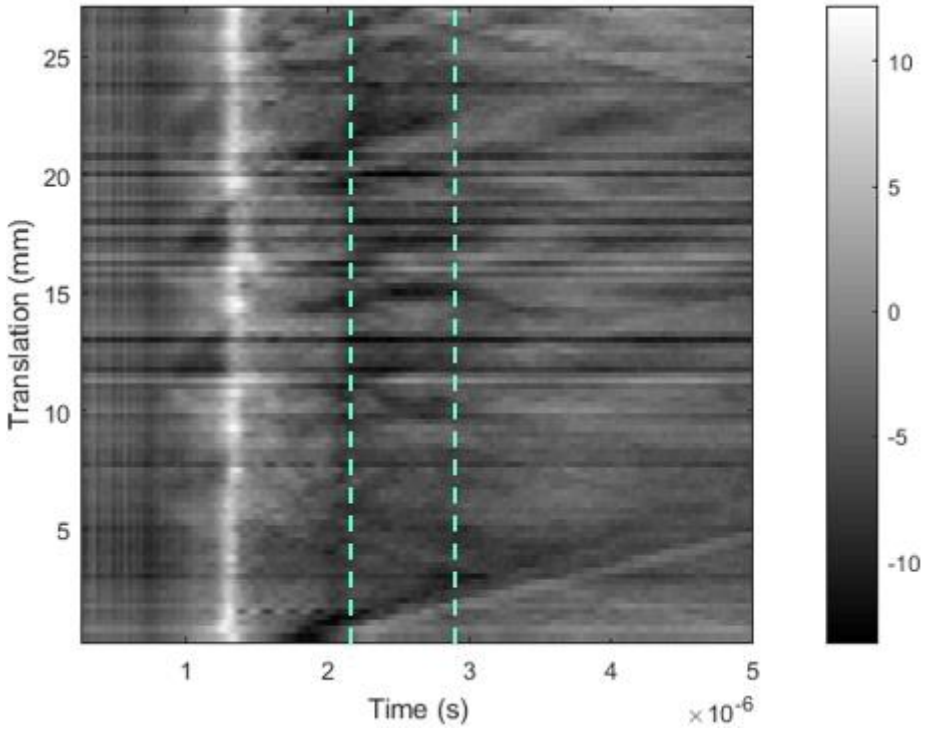

Figure 4-32 - B-scan of M5 along centreline.

4.4 Further analysis

In order to further understand the results gathered from the LU scanning, X-ray computed tomography (XCT) and destructive analysis have been employed.

4.4.1 X-ray computed tomography

Six of the twelve test pieces (M3-6, M9 and M12) have been scanned using XCT to determine whether any additional material discontinuities are present, in addition to those manufactured by wire-EDM.

A Nikon XT H 225 ST @ 225 kV was used to take the XCT scans at MTC. For each test piece, 1600 images were taken at approximately 10.6X magnification. Settings of 186 kV, 220 μA, copper 1 mm filter and .08 exposure were selected, resulting in a scan time for each test piece of 30 minutes. The scans were reconstructed using Volume Graphics' "VGSTUDIO MAX 3.0" software for interrogation. The software displays views in three planes (x-y, y-z and x-z) along with a 3D reconstruction of the test piece. The grayscale values can be adjusted using the histogram in the "opacity manipulation area".

Following manual alignment in the software, a region of interest was created for the top 3 mm of the test piece (in z-direction) and the automated defect recognition (ADR) algorithm run to identify any voids present. Thresholds were applied for void detection at a probability threshold of 0.5 and minimum size of 0.15 mm diameter. An example of the visual result returned is shown in Figure 4-33 for M3 (AM, as-built top surface).

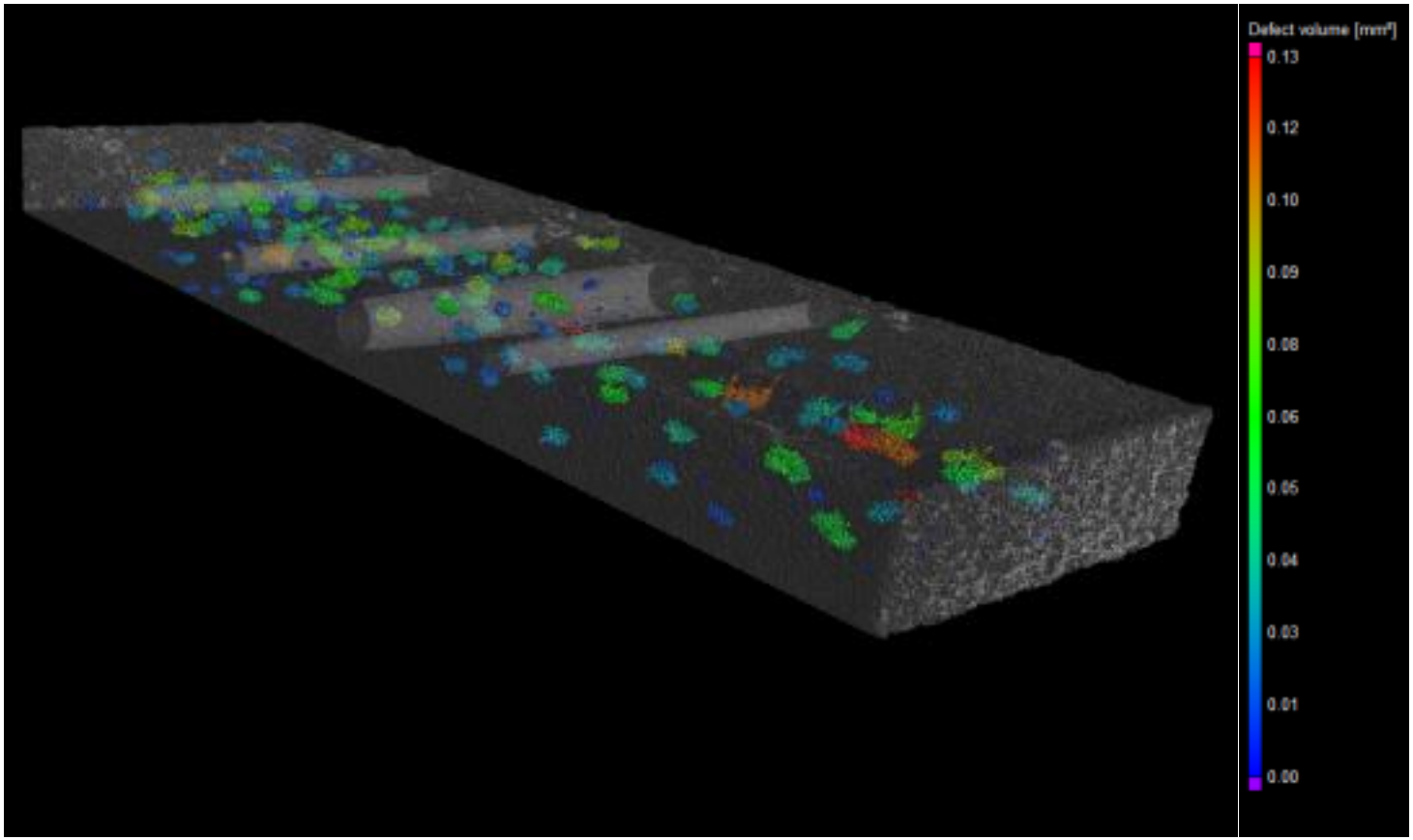

Figure 4-33 - Screenshot from Volume Graphics showing result of automatic defect recognition for M3.

The void data was also extracted numerically for further analysis in 'MS Excel'. The colour scale on the image relates to the identified "defect" volume – blue is close to 0.00 mm^3 and red up to 0.13 mm^3.

The ADR algorithm for M3 returned 171 possible voids in the top 3 mm of the test piece, of these 117 are within 1.5 mm of the test piece surface and 37 are located along the path scanned by the laser, if a 3 mm wide path is assumed. A similar analysis was carried out for each test piece – the results shown in Table 4-4.

It was found that M3 and M5 have a significantly greater number of voids identified. Both test pieces were cut from the same AM sample block 3, suggesting that different build parameters were used for this build although this could not be validated as the original build files were not available.

B-scans taken of M3 and M4 which was cut from sample block 1 are shown in Figure 4-34 and Figure 4-35; both have AM as-built surfaces. On comparing the two B-scans it is evident that in Figure 4-34, there is a significantly greater amount of noise than in Figure 4-35 and there are more instances of signal drop out, although the B-scan is visually suggestive of the presence of unintended material discontinuities in M3, as indicated by the XCT scan.

Table 4-4 - Showing number of voids identified by ADR in different regions of test pieces.

Test piece reference code	Position ref.	Total voids identified by ADR	Voids within 1.5 mm of top surface (z-direction)	Voids within 1.5 mm of top surface and within 3 mm central channel (y-direction)	Voids within 1.5 mm (x), 3 mm centrally (y) and along scanning path
M3	3.1	171	117	45	37
M4	1.2	11	2	0	0
M5	3.4	160	66	17	13
M6	2.5	12	7	0	0
M9	n/a	0	0	0	0
M12	n/a	0	0	0	0

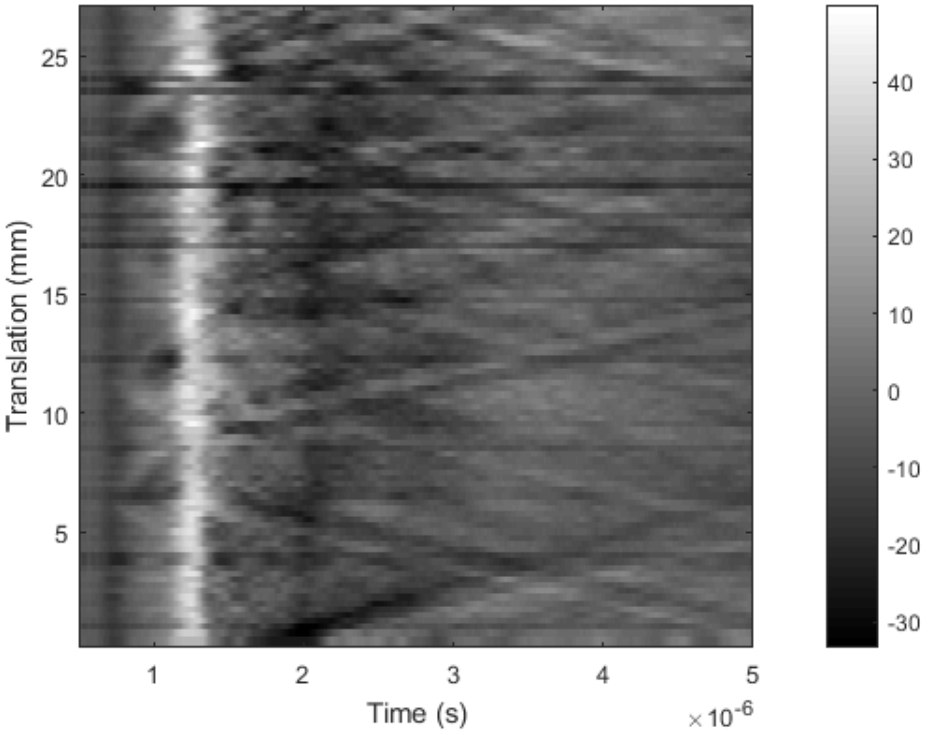

Figure 4-34 - B-scan of M3 – cut from sample block 3.

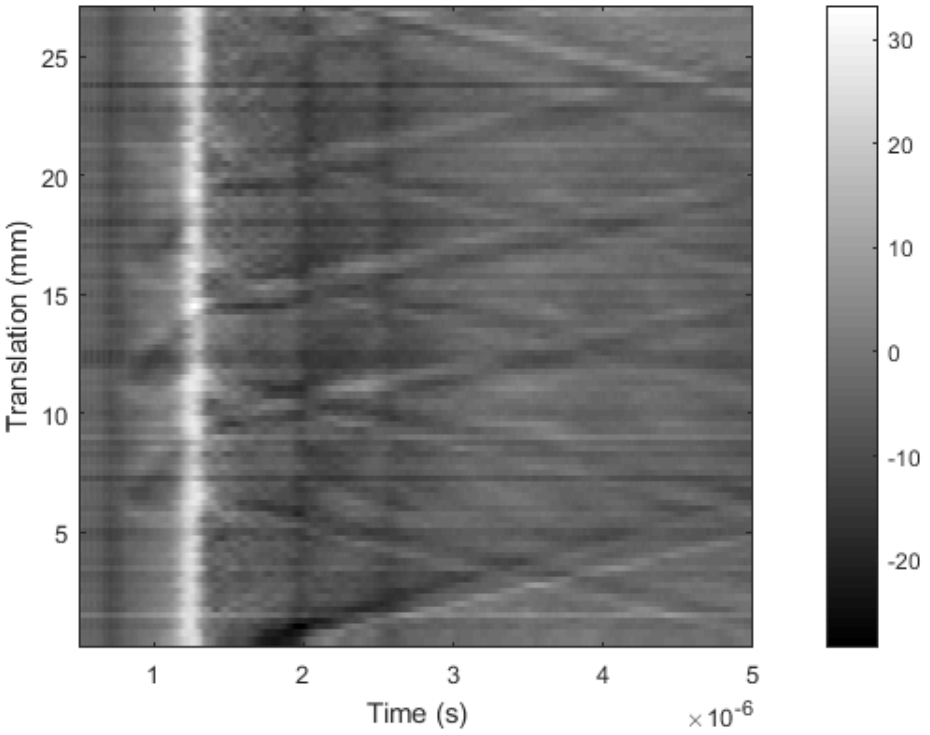

Figure 4-35 – B-scan of M4 – cut from sample block 1.

4.4.2 Destructive

For M4 (AM, as-built top surface), 11 voids were identified by ADR on the XCT reconstructions, within the top 3 mm of the test piece (Table 4-4). Only two voids were identified in the additional LU scanning line regions; one in scanning line 2, and one in scanning line 3. Both indications were of large voids, greater than 700 µm diameter, but they were at 2.0 mm and 2.8 mm below the surface, respectively; beyond the anticipated limit of detection for the LU system.

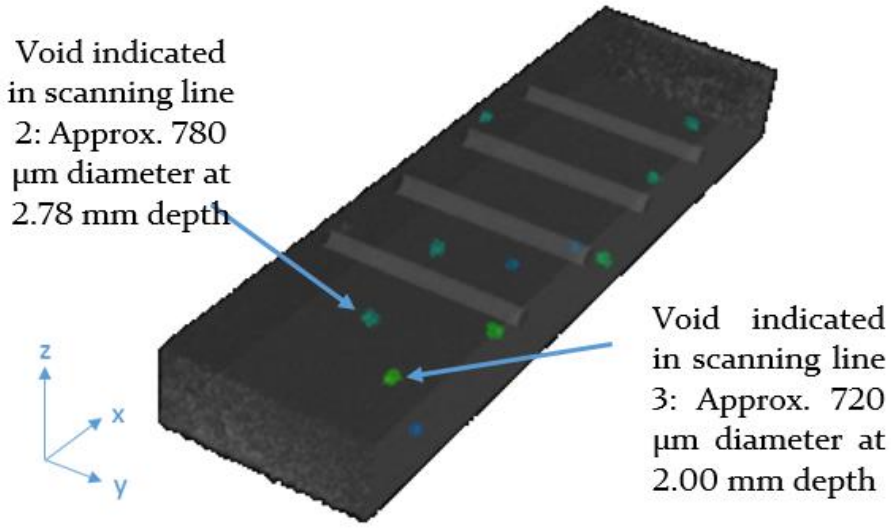

Figure 4-36 - Extract from 'Volume Graphics' showing voids in M4 region of interest identified by automated defect recognition software.

To interrogate this test piece further, additional LU scans were taken along the scanning lines shown in Figure 4-37.

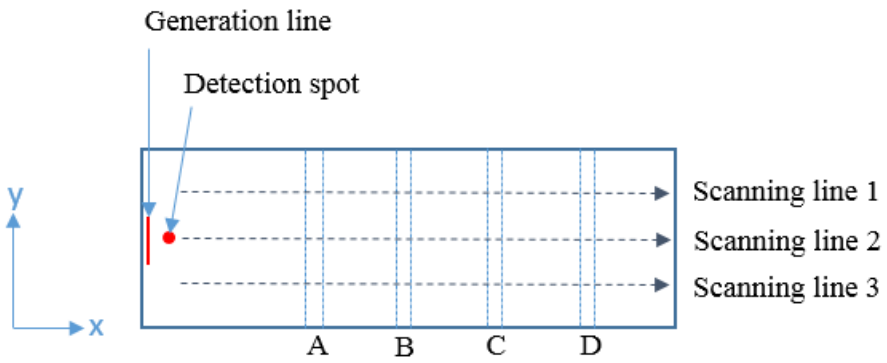

Figure 4-37 - Schematic showing laser starting positions, the four hole positions and the three laser scanning lines.

No additional indications of naturally occurring porosity were identified from the B-scans.

A Robo-Met.3D automated serial sectioning machine was then used to generate reconstructed microscope images of an area between holes A and B, indicated in Figure 4-38.

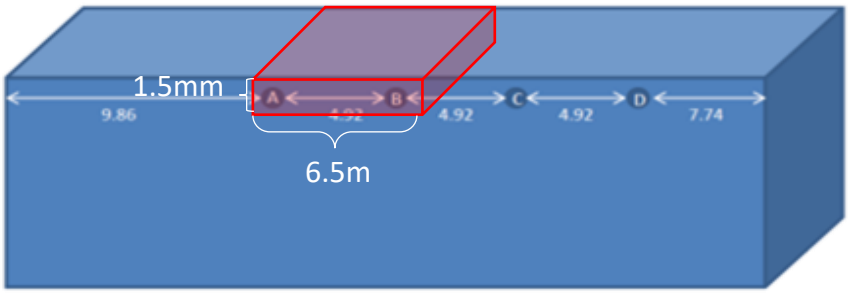

Figure 4-38 – Schematic (left) showing area of interest (red) for destructive evaluation of M4.

The micrograph images obtained were compared directly with the XCT reconstructions to identify any naturally occurring "defects" in this area and a reasonable correlation found, albeit with poor contrast. Obvious material discontinuities identified on the micrographs were linked to deviations in the greyscale in the XCT reconstructions, taken as indications of "defects" (Figure 4-39).

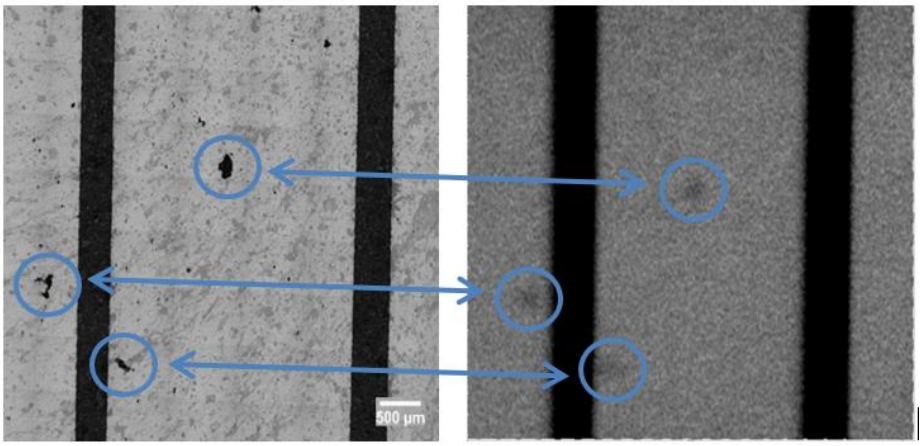

Figure 4-39 – Images showing good correlation between micrograph (left) and XCT image (right) of M4, at 643 µm depth.

It was concluded that the XCT gives a good representation of the sample integrity. However, not all of the naturally occurring "defects" found by destructive analysis were identified by the ADR algorithm; this was probably due to the very small changes in greyscaled value.

After overlaying the LU scanning lines on the micrographs, it was found that there was one void present in the region destructively analysed, which had not been indicated from the repeated B-scans (Figure 4-40).

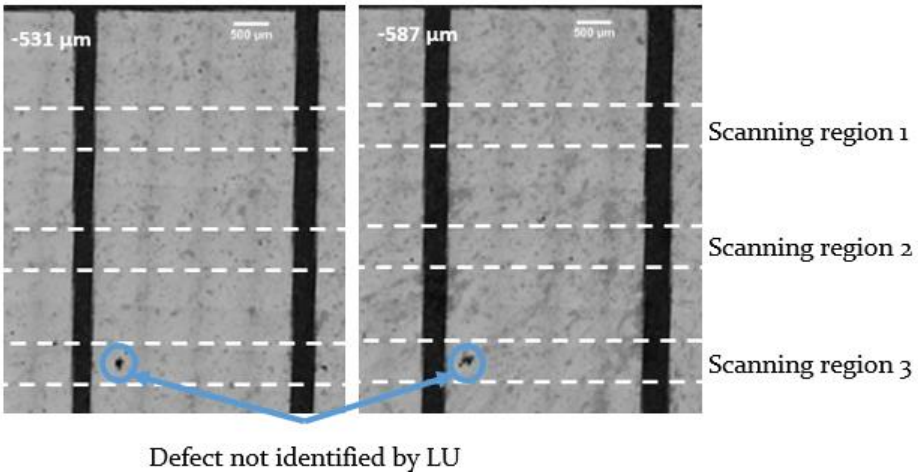

Figure 4-40 - Micrograph images at depths of 531 µm and 587 µm, overlaid with the scanning line regions for LU. "A defect", previously unidentified by laser ultrasound, is highlighted.

The unidentified "defect" has dimensions of approximately 200 *x* 150 *x* 100 µm and is located 250 µm from the EDM'd "hole A" at a depth of roughly 530 µm from the top surface. For reference, "hole A" has a diameter of 580 µm and is 417 µm below the test piece surface. It is thought that the presence of such a large, manufactured "defect" in the vicinity of the naturally occurring "defect" is having a masking effect.

4.5 Summary

When using a photo-EMF detector, a higher magnitude response is detected when LU scanning the rougher AM surfaces. The increased signal magnitude displayed in the A-scan for the laser-PBF surface of test piece M4 yields a B-scan with greater resolution; Many more full and partial parabolic indications of "defects" are visible. The B-scan for the test pieces with EDM surface roughness conditions show fewer indications and have a series of horizontal striations, corresponding to the fluctuations in DC signal received.

All but four of the 48 through-holes manufactured were indicated on the B-scans in some way; the four unidentified holes were all in test pieces with an EDM surface finish. It is probable that the reduced resolution of the B-scans generated from the EDM surfaces has hindered identification of the indications. 29 out of 32 holes in the smaller hole diameter grouping could be identified to some degree, including all 20 with a 0.563 – 0.708 mm diameter, up to a z-distance of 0.622 mm. Similarly, for the larger hole diameter grouping 15 out of 16 holes could be identified, with those with diameters in the range 0.963 – 1.241 mm, up to a z-distance of 1.148 mm giving a full or partial indication. These voids were fully not representative of AM voids but were within the anticipated limit of detection of the system, calculated from literature. However, not all of the manufactured defects were detected. Further work carried out to establish the actual limit of detection for this LU system is detailed in Chapters 5 and 6, supported by modelling work in Chapter 7.

Plotting A-scans for the three repeat scans of a single test piece, it can be seen that there is generally good agreement between the signals; the second and third scans in particular rarely deviate. The first scan is generally at a lower magnitude than the second and third signals, suggesting that the initial scan in the ablative regime does perhaps alter the surface condition slightly, this will be investigated in the process defects study, detailed in Chapter 6.

It is possible to reduce the time taken for a LU translation of 27 mm to 1 minute and 23 seconds by reducing the number of averages taken at each translation point from the recommended 24, to 4. This reduction can be achieved without an unacceptable loss of resolution in the B-scan, however the maximum recommended step size of 0.25 mm should be adhered to. Another factor influencing the total scanning time is the time taken translating the measurement head between scans. Using a translation stage with an increased stage velocity could further reduce the scan time. Increasing the generation laser power is an alternative approach that could be investigated in future work.

When scanning in close proximity to a test piece edge, the longitudinal wave arriving from the wall adjacent to the scan arrives very soon after the Rayleigh wave and only one reflection is visible, rather than the two seen when scanning centrally. The second longitudinal wave, reflected off the far side wall was not detected. Although this reduced arrival time does mean that the parabolas from the diffracted Rayleigh wave and diffracted, reflected longitudinal wave from the nearest side wall overlap, it is still possible to identify the same indications of the four large

through-holes. In addition, extra indications were visible on the revised scanning path.

In order to further understand the results gathered from the LU scanning, X-ray computed tomography (XCT) and destructive analysis have been employed. Six of the twelve test pieces (M3-6, M9 and M12) have been scanned using XCT to determine whether any additional material discontinuities were present, in addition to those manufactured by wire-EDM. The ADR analysis found that M3 and M5 had a significantly greater number of voids identified. Both test pieces were cut from the same sample block 3, suggesting that poor build parameters were used for this build. On comparing B-scans for test pieces cut from sample block 1 and 3, there is a significantly greater amount of noise and more instances of signal drop out in the block 3 case, although nothing is visually suggestive of the presence of unintended material discontinuities. The increased noise level could be indicative of the elevated porosity.

A single test piece with laser-PBF top surface (M4) was selected for further LU processing and destructive analysis. 11 voids were identified by ADR on the XCT reconstructions, within the top 3 mm of the test piece. Only two voids were identified in the additional LU scanning regions; one in scanning region 2, and one in scanning region 3. Both indications were of large voids, greater than 700 μm diameter, but they were at 2.0 mm and 2.8 mm below the surface, respectively; beyond the anticipated limit of detection for the LU system. Destructive analysis of the area between holes a and b was carried out using an automated, serial sectioning machine. The micrograph images obtained were compared directly with the XCT

reconstructions to identify any naturally occurring “defects” in this area and a reasonable correlation found, albeit with poor contrast. It was concluded that the XCT gives a good representation of the sample integrity. However, not all of the naturally occurring “defects” found by destructive analysis were identified by the ADR algorithm; this was probably due to the very small changes in greyscaled value.

After overlaying the LU scanning lines on the micrographs, it was found that there was one void present in the region destructively analysed, which had not been indicated from the repeated B-scans. It is thought that the presence of such a large, manufactured “defect” in the vicinity of the naturally occurring “defect” is having a masking effect.

In this chapter, the LU system has been shown to be capable of scanning a laser PBF as-built surface, meaning that LU could be considered for in-situ inspection in the future. Test pieces were generated using laser PBF and through-holes drilled using EDM, to simulate the presence of voids. Analysis of the B-scans generated using LU only indicated the presence of 44 out of the 48 machined holes, where all were expected to have been within the calculated sensitivity of the system. Further work to establish the actual sensitivity of the system for detection of more representative AM “defects” is be carried out in chapters 5 and 6.

Chapter 5 - Seeded “defects” study

5.1 Introduction

In this chapter, a method for artificially creating voids at a known location within an AM test piece is reported. XCT is used to assess the test pieces for any resulting material discontinuities and for any naturally occurring, unintended porosity. Voids with increasing diameter and voids at increasing z-distances are seeded, to continue the work previously carried out to establish the window of detection of the LU system.

5.2 Methodology

Test pieces were designed with different sized spherical voids below the surface, at various z-distances. Titanium alloy, Ti6Al4V, test pieces were produced by laser PBF on a Realizer SLM50 AM machine, using 40 µm layers, 100 W power, 20 µm point distance, 40 µs exposure and 90 µm hatch spacing; a double scan strategy was employed. The build was set up using ‘Materialise Magics’ software and a standard set of 3 mm support structures added to anchor the test pieces to the build plate. These would later be removed manually, using a light hammer and chisel.

Twenty 10 x 10 x 10 mm cubes with spherical voids (50 to 500 µm diameter) below the top surface at various z-distances (40 µm to 3 mm) were manufactured in two batches of ten in the arrangement shown in Figure 5-1. Additionally, a 30 *x* 10 *x* 10 mm oblong test piece with multiple voids was manufactured with a “defect free” zone ahead of four evenly spaced 200 µm voids, at 250 or 500 µm

below the top surface; a solid AM block was also made for reference (Figure 5-2).

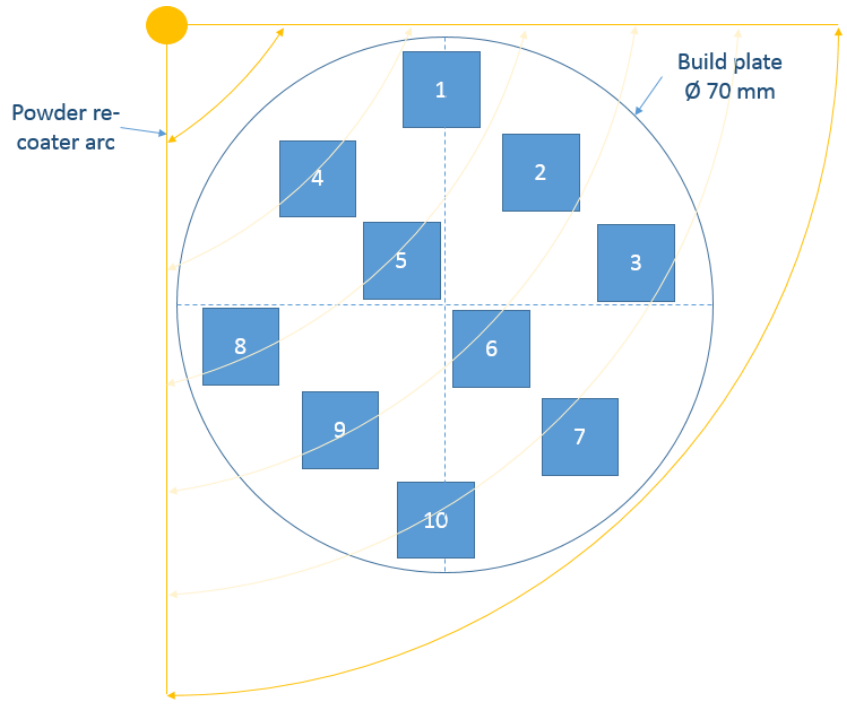

Figure 5-1 - Schematic showing batch build positions for cube test pieces.

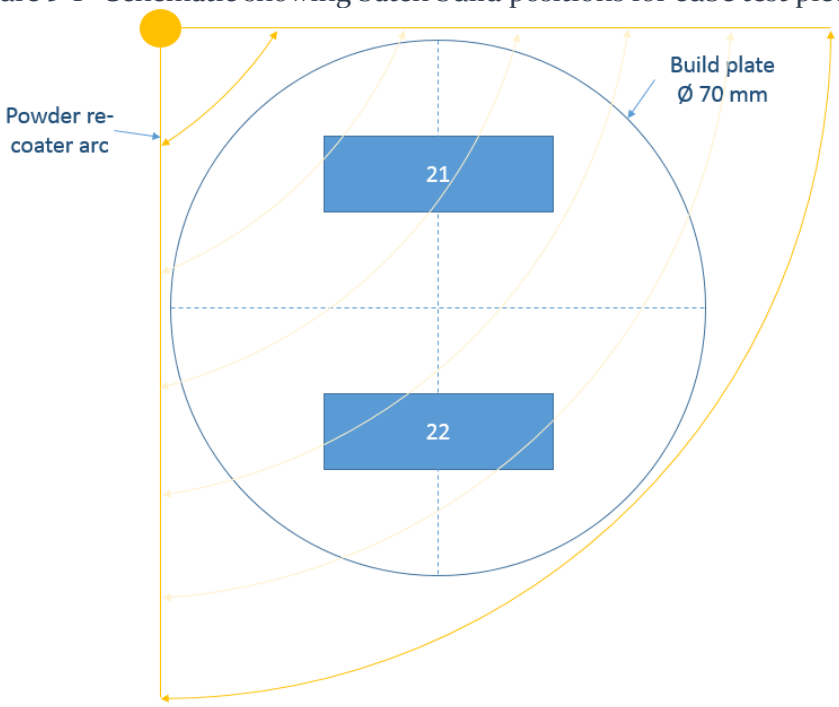

Figure 5-2 - Schematic showing build positions for oblong test pieces.

A summary of all test pieces is given in Table 5-1 with a test piece reference, build position, test piece shape, void diameter and z-distance indicated.

Table 5-1 - Seeded defects test pieces.

Reference	Build	Position	Type	Void Ø (mm)	Z distance (mm)
S1	1	1	Cube	n/a	n/a
S2	1	2	Cube	0.200	0.040
S3	1	3	Cube	0.200	0.250
S4	1	4	Cube	0.200	0.500
S5	1	5	Cube	0.200	0.750
S6	1	6	Cube	0.200	1.000
S7	1	7	Cube	0.200	1.500
S8	1	8	Cube	0.200	2.000
S9	1	9	Cube	0.200	2.500
S10	1	10	Cube	0.200	3.000
S11	2	1	Cube	0.050	0.250
S12	2	2	Cube	0.100	0.250
S13	2	3	Cube	0.150	0.250
S14	2	4	Cube	0.200	0.250
S15	2	5	Cube	0.250	0.250
S16	2	6	Cube	0.300	0.250
S17	2	7	Cube	0.350	0.250
S18	2	8	Cube	0.400	0.250
S19	2	9	Cube	0.450	0.250
S20	2	10	Cube	0.500	0.250
S21	3	21	Oblong	n/a	n/a
S22	3	22	Oblong	a: 0.200 b: 0.200 c: 0.200 d: 0.200	0.250 0.500 0.250 0.250

5.3 Results

In this section, issues relating to the building of the test pieces are discussed before LU results are presented and discussed for each experiment within this study.

5.3.1 Build

Unfortunately, some issues occurred during set-up and build of the cube test pieces. For example, the standard supports selected for the first build (S1-S10) failed to anchor test pieces S3, S6, S7 and S10 to the build plate. Support structures were designed to be strong enough to anchor the component to the build plate during manufacture, but easy to remove afterwards, without the need for machining. In this case, it seems the distortion caused by the residual stress of the components exceeded the anchoring strength of the chosen supports. As a result of the test pieces lifting during the build, these cubes were not fully formed (Figure 5-3), but were still analysed.

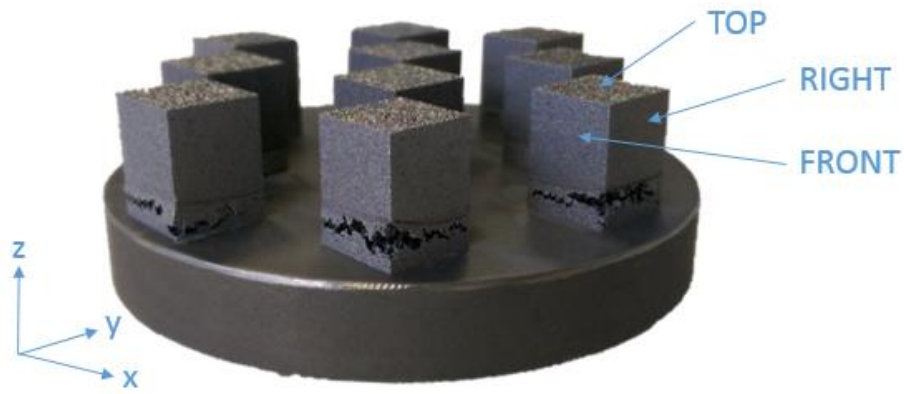

Figure 5-3 – Photograph of build 1 showing broken support structures on test pieces S3, S7 and S10.

Secondly, when XCT was used to check the formation of the seeded voids centrally below the top surface (Figure 5-4a), no porosity was evident in the expected location. Instead, the build files were assumed to have rotated 90 degrees about the x-axis (Figure 5-4b) when imported into the build software as the seeded pore was found centrally below the rear face (Figure 5-4c and d). This is discussed further in the following section.

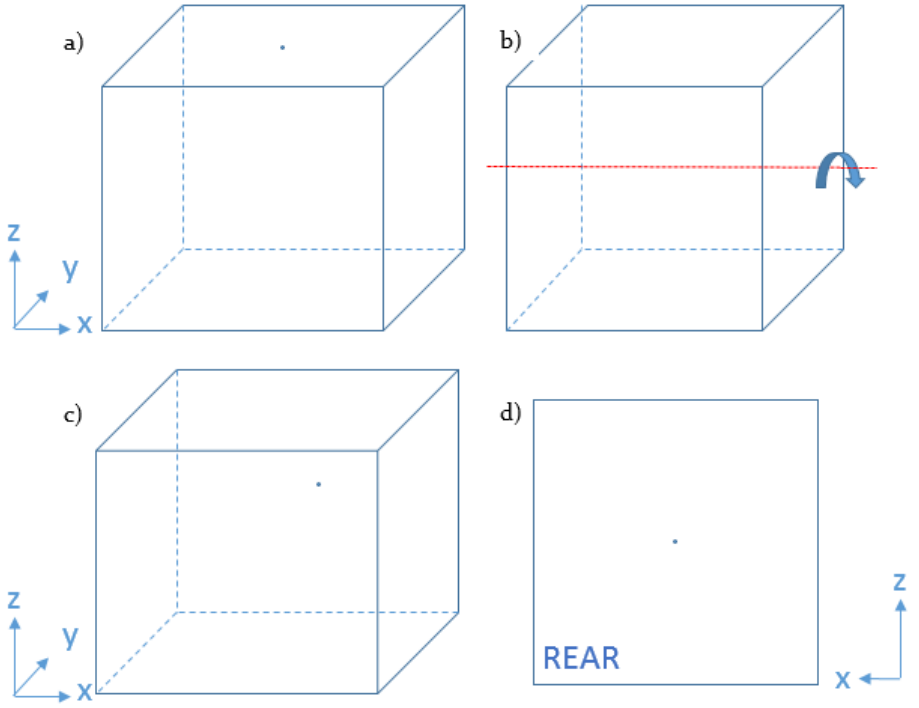

Figure 5-4 - Schematics showing a) intended location of void, beneath top surface, b) axis of rotation, c) manufactured position of void, centrally close to the rear face and d) rear face showing position of void in x-z.

This import error was also found to have occurred for all the cube test pieces, but not for S22. To continue the study, the cubes were instead rotated and scanned along the rear face which was mounted facing upwards, i.e., rather than scanning the AM top surface, the side walls were scanned instead. The side walls of the AM build are usually found to be rougher than the top surface and

are typically less reflective. LU scanning the rougher, less reflective surface was expected to return a lower magnitude signal.

To avoid any orientation errors in importing build files in the future, it is recommended that asymmetric components be built, or a marker be added to the build file so that orientations can be more easily checked before processing.

5.3.2 Experiment 1 – seeding voids

In order to establish if a void had been formed in the seeded position, a Zeiss XRADIA Versa XRM-500 @ 160 kV was used to image S3, which was chosen at random. 1024 slides were taken at approximately 0.4X magnification. Settings of 160 kV, 63 µA, a HE3 filter and 1 second exposure were selected, resulting in a scan time for the cube of 7 hours; the smallest 3D volume element or voxel size was 14.6 µm. Slices in the x-y plane were extracted from the XCT reconstruction, shown schematically in Figure 5-5, and analysed using software package *ImageJ*.

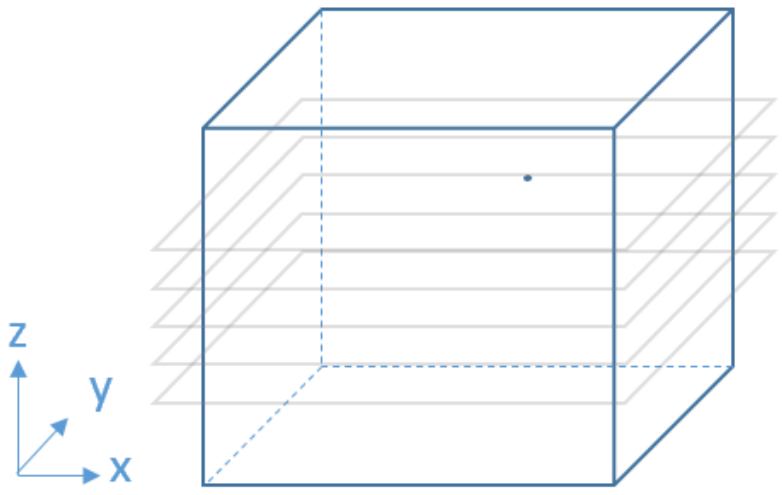

Figure 5-5 - Schematic showing x-y orientation of image slices (grey) generated using XCT.

The image slice in Figure 5-6 is taken at z = -5 mm, half way down the cube and shows an indication of a void in the (revised) expected location.

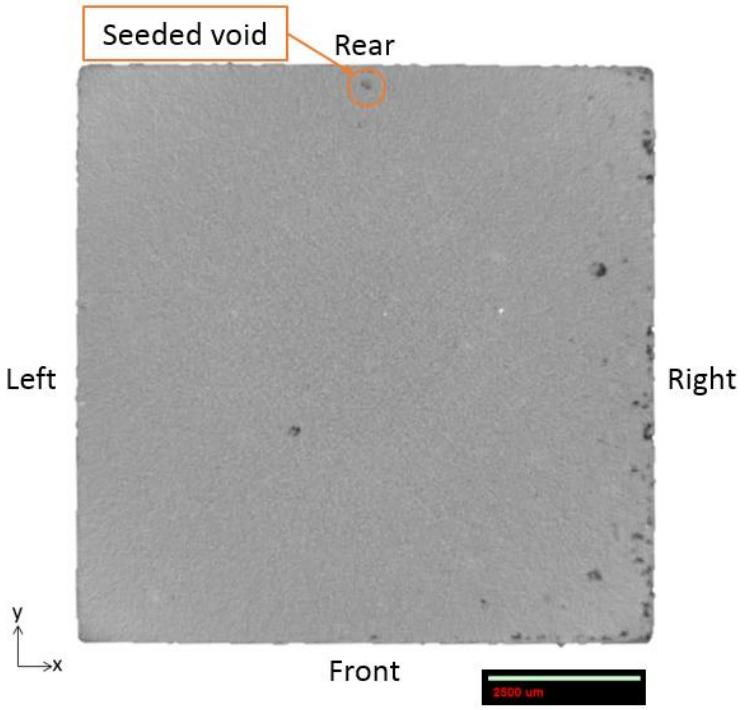

Figure 5-6 – XCT image of S3 (x-y) at -5 mm, showing indication of seeded "defect" near rear wall and unintended porosity.

Lots of additional, unintentional porosity was seen throughout the x-y images, particularly along the right edge of build. This grouping of porosity along the right edge of a component had been noted by other researchers in the group using the SLM50 AM machine.

The void left in the CAD file for S3 was 200 µm diameter, 250 µm from the wall. Free, open source software '*Image J v1.50e*' was used to further analyse the indication seen in the XCT image slice, at the rear wall. A box is drawn around the hole and rear edge of the sample (Figure 5-7a), before the image is converted to 8-bit and a threshold applied (Figure 5-7b).

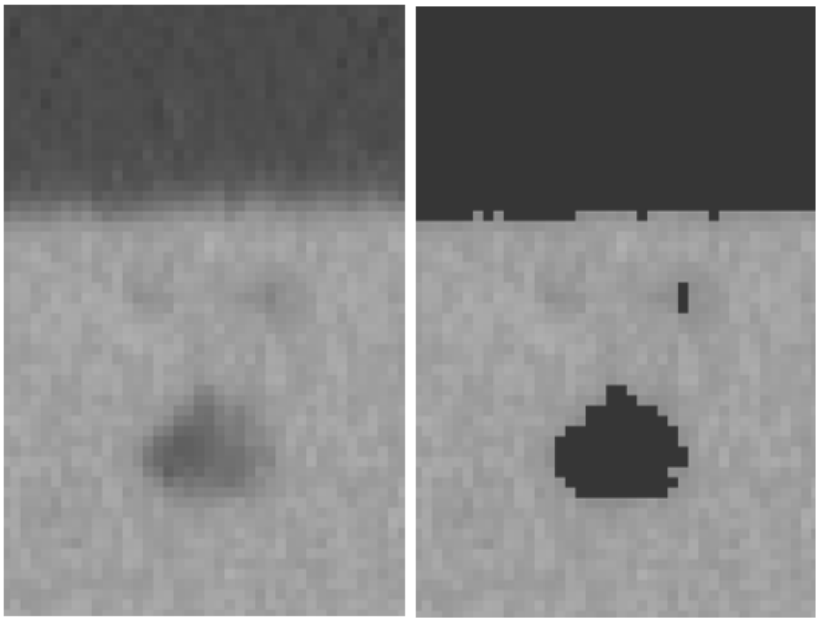

Figure 5-7 - Images showing a) focus area for interrogation and b) area with 8-bit and thresholding applied using ImageJ.

Using this approach across all the slices the indication appears in, the void was measured as being roughly spherical and having 161 µm ± 29 µm diameter, appearing at 262 µm ± 29 µm from the rear wall. It cannot be determined if the void is powder-filled or hollow, but this analysis concludes that material discontinuities can be seeded in AM parts, by leaving voids in the CAD files.

5.3.3 Experiment 2 – LU assessment of cube test pieces and validation using XCT

5.3.3.1 *LU scanning*

To interrogate the B-scans, the same methodology as used in Chapter 4 was utilised. A B-scan is shown without annotation and then repeated with the identified features overlaid; the same colour scheme is maintained.

The LU equipment was set up with a translation step of 0.1 mm selected. Although this extends the scanning time, a higher resolution B-scan is obtained. The generation and detection laser separation was set close to 3.0 mm with the generation line along the edge of the test piece. A-scans were taken at 70 points, meaning 6.9 mm along cube rear surface was scanned, leaving the detection spot on the opposite test piece edge. The starting (green) and finishing (red) laser positions are shown in Figure 5-8.

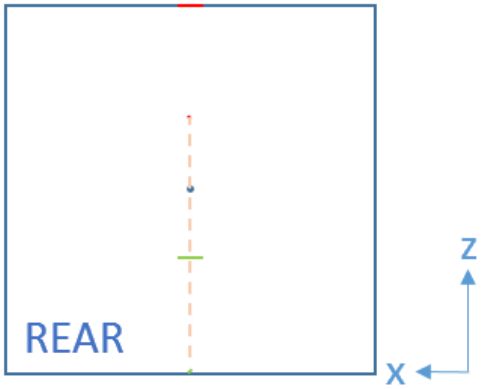

Figure 5-8 - Schematic showing LU scanning path.

The raw B-scan generated for S3 is shown in Figure 5-9:

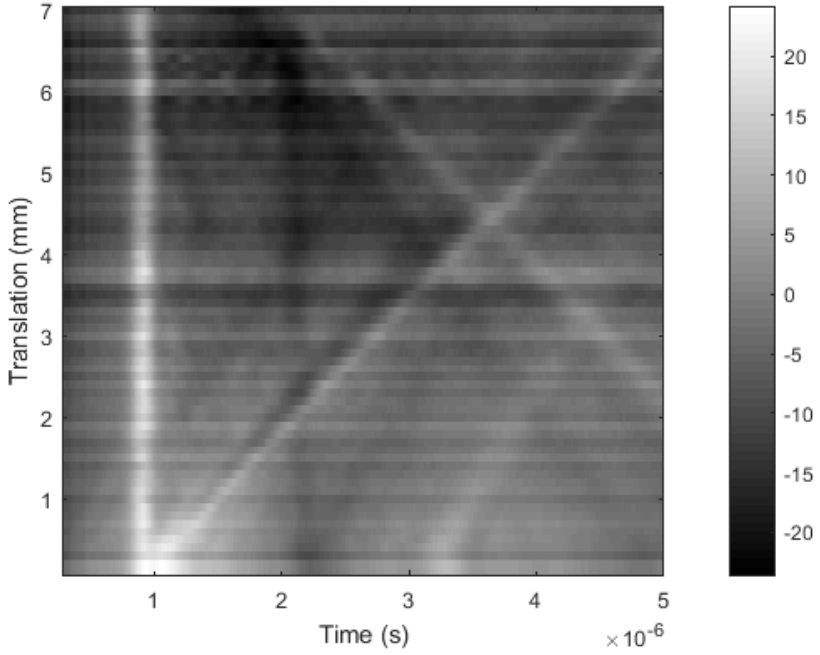

Figure 5-9 - B-scan of S3.

Eight different types of indications have been identified and shown across three duplicate B-scans, for illustrative purposes. The B-scan in Figure 5-10 is overlaid with the identified indications of arrival times for the direct longitudinal (dashed lilac) and direct Rayleigh (dashed purple) waves. The longitudinal waves reflected off the sidewalls (dashed green) and the bottom of the test piece (solid green) and finally, the mode converted waves reflected off the bottom of the test piece (dot-dashed blue). Analysis of the wave arrival times suggests a generation-detection laser separation of 3.74 mm was achieved, larger than the 3 mm target.

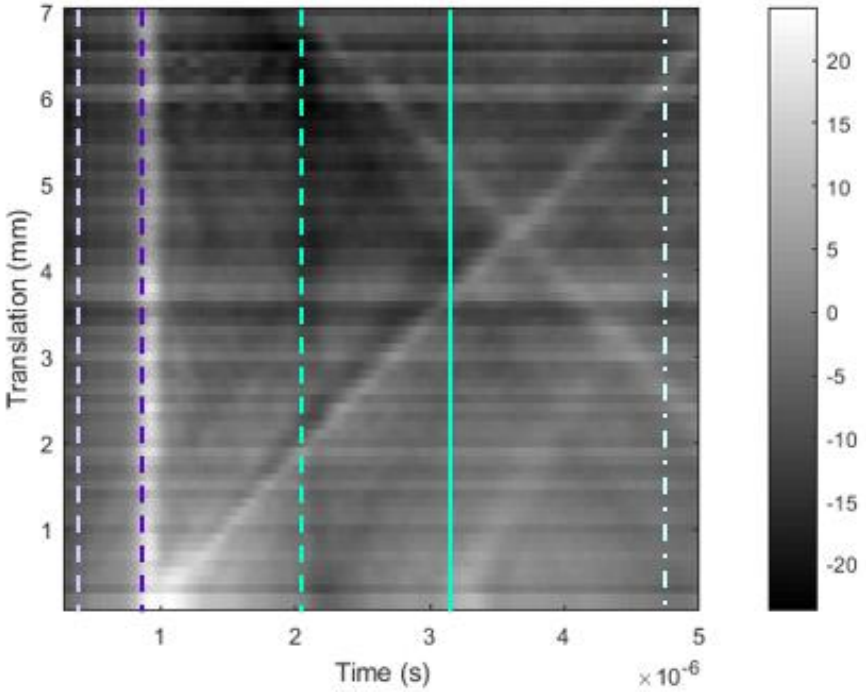

Figure 5-10 - B-scan for S3 overlaid with direct, reflected and mode converted waves from the base and side-walls.

In Figure 5-11, the waves reflected off the end walls of the test piece are overlaid on the B-scan. As the LU scanning path was only 6.9 mm long on the small cube, the reflected waves appeared more prominent than on previous scans using 26.9 mm long LU scan paths. These indications were interesting to note, but did not yield any information regarding the presence of a "defect".

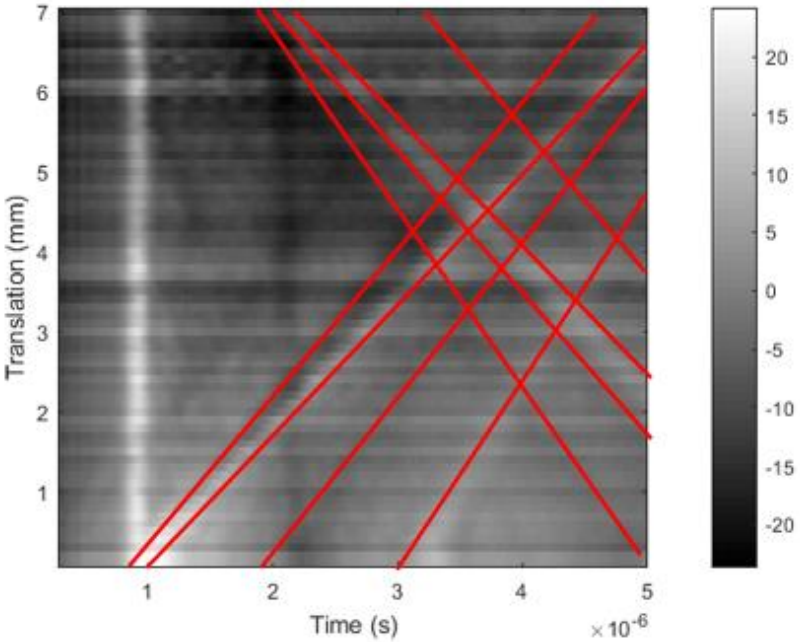

Figure 5-11 - B-scan for S3 overlaid with waves reflected off the test piece end walls.

In Figure 5-12, the B-scan is overlaid with indications of possible material discontinuities, including:

- Two blue parabolas indicating the arrival of diffracted direct Rayleigh wave signals, caused by interaction with a "defect" were identified with apexes at 3.6 mm and 5.7 mm.
- A partial parabola shown with an orange line, peaking at 0.7 mm is caused by a diffracted direct longitudinal wave.

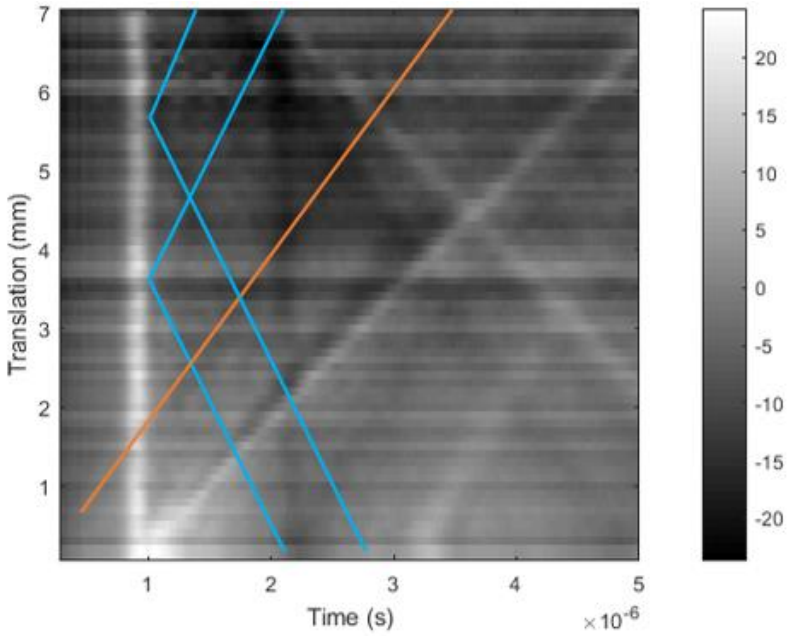

Figure 5-12 - B-scan for S3 overlaid with indications of material discontinuities.

5.3.3.2 *XCT validation*

The XCT reconstruction described in the previous section (5.3.2) was sectioned into image slices and examined using *'ImageJ'*. Although the whole test piece was imaged, only the area on the image adjacent to the path of the LU was assessed for porosity. A zone extending out 1.5 mm in either direction from the scanning line and 3 mm into the sample, was interrogated. Eight voids were identified within this region. A summary of these voids is given in Table 5-2.

The first column displays the XCT slice which correlates to the distance along the scan path. The LU translation is listed in the second column. The maximum measured hole diameter and Z-distance are presented, along with the distance out from the central LU scanning line.

Table 5-2- Showing void analysis for S3 using *ImageJ* to interrogate XCT data.

XCT slice	LU translation (mm)	Max diameter (µm)	Z-distance (µm)	Distance from scan line (µm)
113	0.1	46	160	-731
239	2.0	40	149	733
254	2.2	16	153	-947
282	2.6	112	84	-993
346	3.6	124	292	0
363	3.8	34	164	-301
393	4.2	46	87	-413
491	5.7	35	43	208

The two voids highlighted in Table 5-2 were found to correspond to translation positions of the two blue parabolas identified on the B-scan. The seeded "defect" at a translation of 3.6 mm had the largest diameter, but is also the furthest below the surface at 292 µm z-distance. The picture in Figure 5-13 shows images generated in ImageJ for the two voids:

Figure 5-13 – Image generated through 'ImageJ' analysis of LU scan area showing a) the seeded void and b) unintended porosity (circled), at slice 491 equivalent to a translation of 5.7 mm.

It is not clear from analysis of the XCT images what caused the diffraction of the direct longitudinal wave, leaving the partial orange parabolic indication (orange) in Figure 5-12. None of the voids identified from the XCT analysis correlate with the position of the parabola. It is thought that interaction with a feature on the test piece surface had caused this.

The graph in Figure 5-14 shows the void positions below the surface (Z-distance) and distance from the LU scanning path. The size of the marker scales with the max 2D void area, calculated using *ImageJ*. This analysis helps to establish the window of detection for the LU system – it is as useful to know which voids have not been detected.

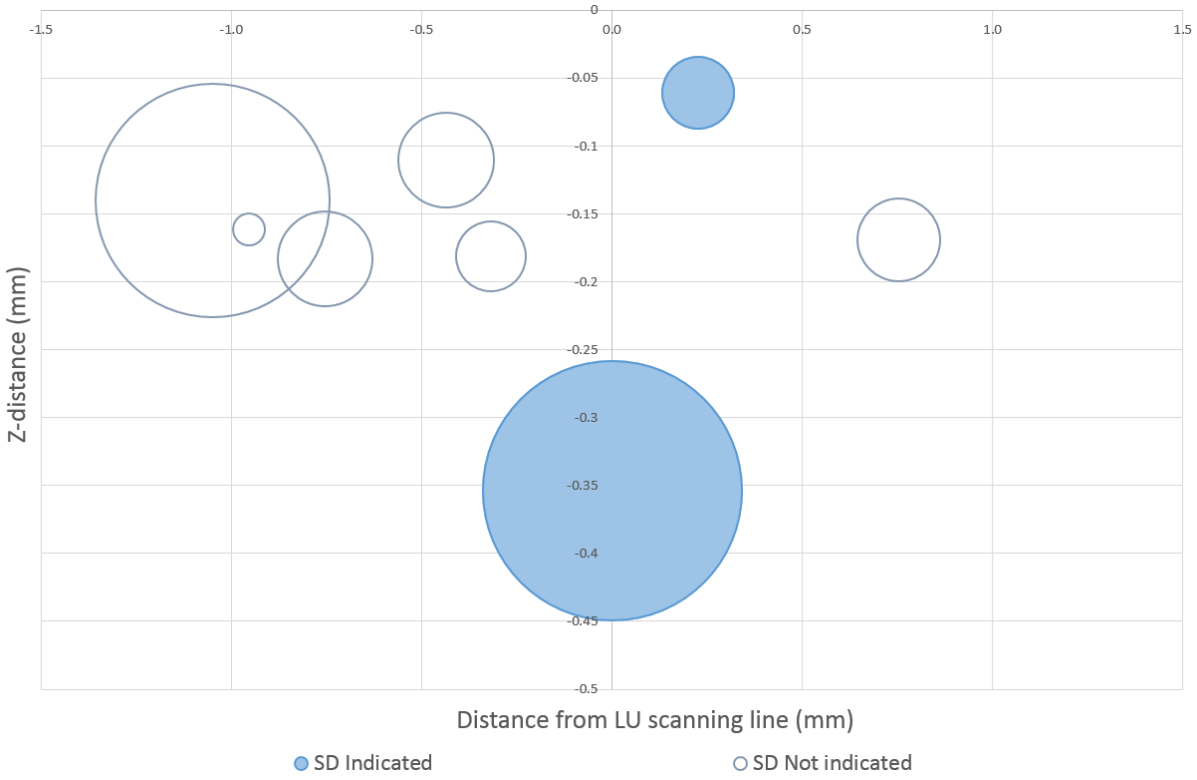

Figure 5-14- Graph showing void positions below the surface and distances from the scanning path, along with void area.

Initially, LU software *LaserScan* was used to display and interrogate the B-scans. Assessment of the B-scan generated for S3 and the other cube test pieces did not reveal the presence any indications and it was thought that pores had not been detected using LU and no further cubes were assessed by XCT. However, using a more advanced data processing method developed in *Matlab*, additional information was garnered from the LU signal and the indications described above noted. It is recommended that future work be carried out to assess the remaining cube test piece, by LU and XCT.

5.3.4 Experiment 3 – LU assessment of oblong test pieces

A solid AM block, S21 was made for reference and test piece S22 was manufactured with a "defect free" zone ahead of four evenly spaced 200 µm voids, at 250 or 500 µm below the top surface. LU scans of both test pieces will be compared and validated using XCT, processing *ImageJ*.

5.3.4.1 *LU scanning*

LU was carried out with a generation-detection laser separation of 5.34 mm at 0.1 mm step size. A raw B-scan of S21 is shown in Figure 5-15. Five types of features were indicated, overlaid in Figure 5-16, including the direct longitudinal (dashed lilac) and direct Rayleigh (dashed purple) waves. The longitudinal waves reflected off the sidewalls (dashed green) and the bottom of the test piece (solid green) and finally, the waves reflecting off the test piece start and end walls (red). No indications of any "defects" were identified, as expected from the reference block.

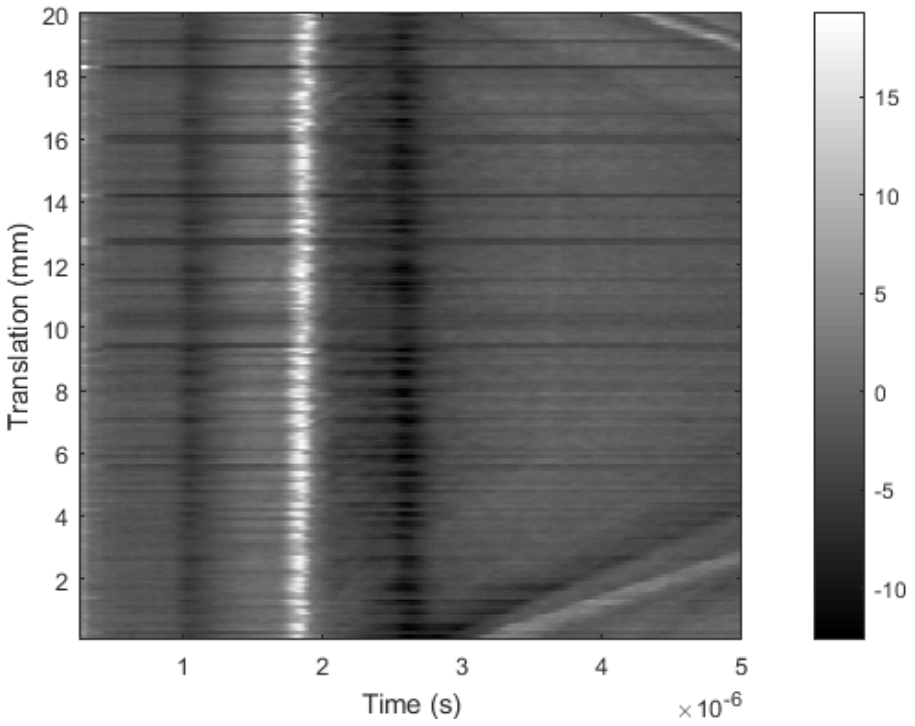

Figure 5-15 - B-scan of S21.

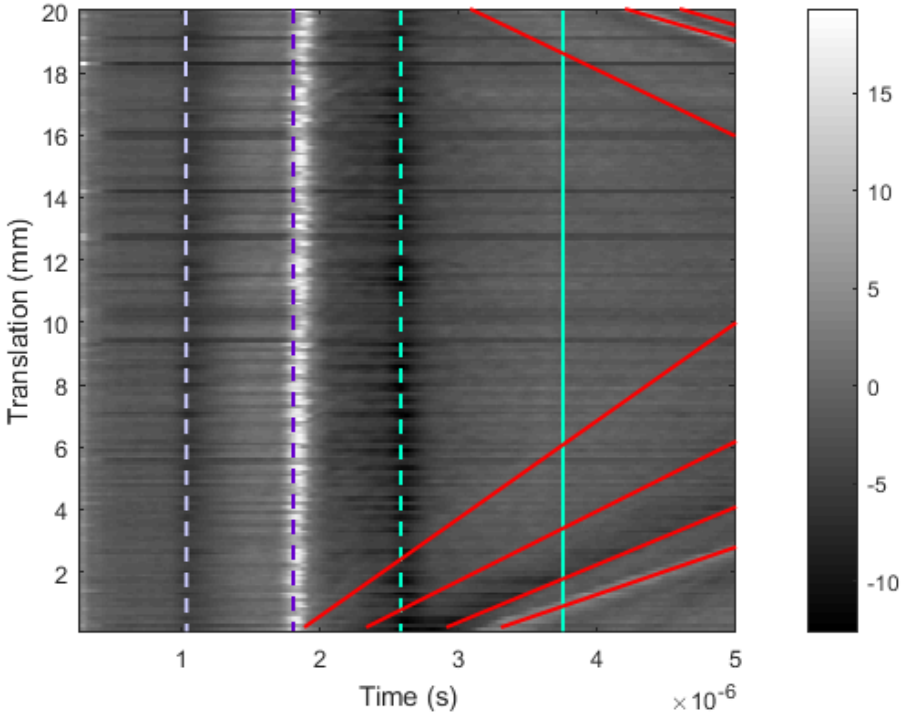

Figure 5-16 - B-scan of S21 overlaid with direct, reflected and mode converted waves from the base, side-walls and end walls.

In S22, four voids were seeded below the top surface, as shown in Figure 5-17. The positioning of these voids mimicked the through holes manufactured for the post build defects study in Chapter 4.

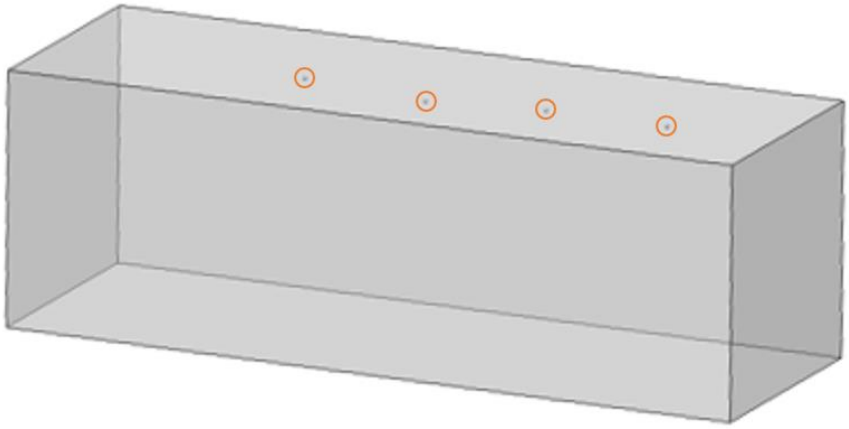

Figure 5-17 - Schematic of S22 with four voids in the CAD model.

The test piece was scanned using the same LU settings as for S21 and Figure 5-18 shows the resulting raw B-scan; the direct, and reflected wave arrivals are overlaid in Figure 5-19.

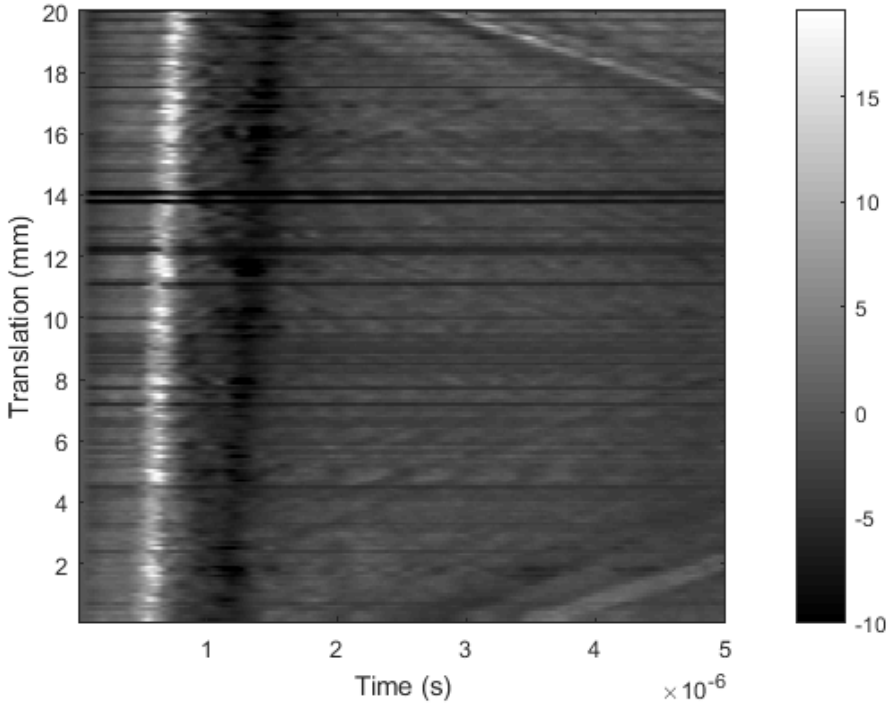

Figure 5-18 - B-scan of S22.

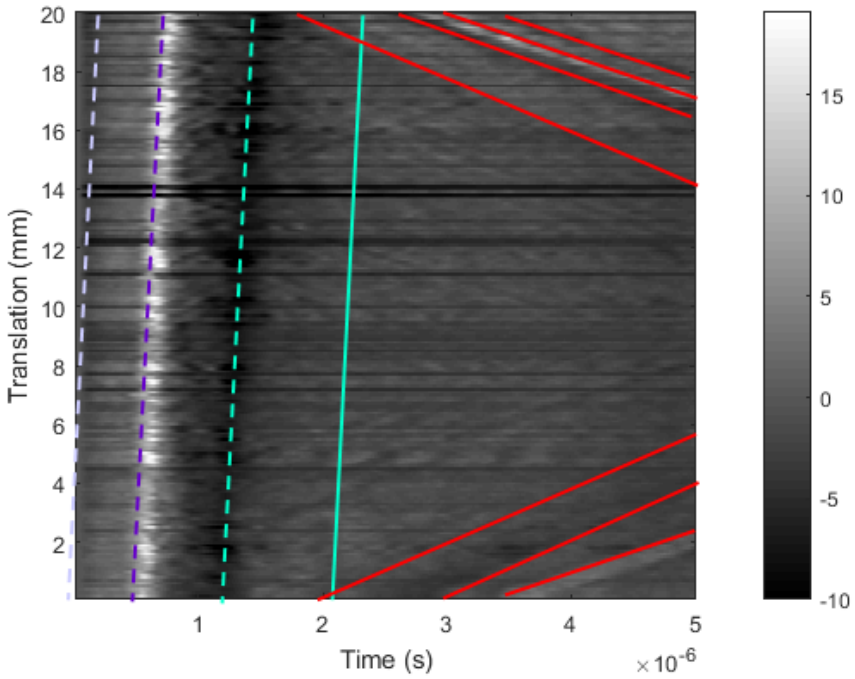

Figure 5-19 - B-scan of S22 overlaid with direct, reflected and mode converted waves from the base, side-walls and end walls.

Unusually, the indications of the arriving direct longitudinal (lilac dashed), direct Rayleigh (purple dashed), longitudinal waves reflected from the side walls (green dashed) and base (green solid) are not vertical, but angled. As the LU measurement head translated across the sample surface, the elapsed time before arrival of the waves increased. It is thought that this is implying the sample top surface is slightly curved, possible as a result of the AM build supports failing. LU scanning of a curved surface would result in an increase in separation distance between the generation and detection lasers.

Many indications of diffracted direct Rayleigh waves arriving at the detection point are overlaid in Figure 5-20, far more than the four expected to have been caused by interaction with the seeded voids.

It is not possible to correlate any of the 15 partial parabolas with the translation positions of the seeded voids.

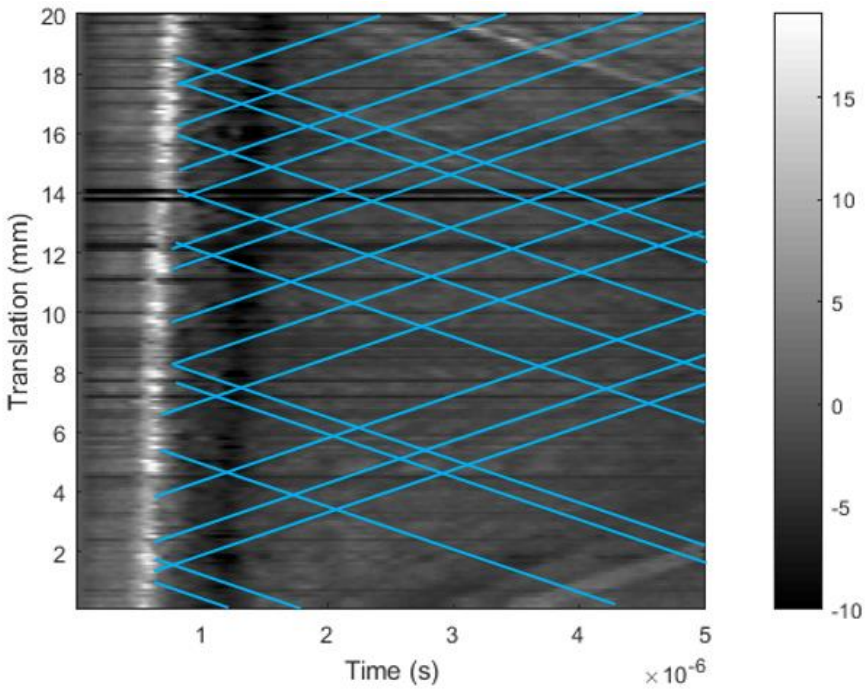

Figure 5-20 - B-scan for S22 overlaid with indications of material discontinuities.

5.3.4.1 *XCT validation*

To discover whether the porosity indicated from the B-scans was in fact present, the Nikon XT H 225 XCT system was used to image S21 and S22, with 27 µm voxel size. An example slice of the XCT reconstruction of reference sample (S21) is shown in Figure 5-21.

Figure 5-21 - XCT image of AM solid block sample (x-y plane at 250 µm from top surface) – no indications have been identified.

Analysis of the XCT reconstruction for S21 did not reveal any indicated material discontinuities, this is in agreement with the LU B-scan of the test piece (Figure 5-15).

XCT slices of S22 at 250 µm and 500 µm from the test piece top surface are shown in Figure 5-22. The red circled areas indicate where a void was intended to be seeded.

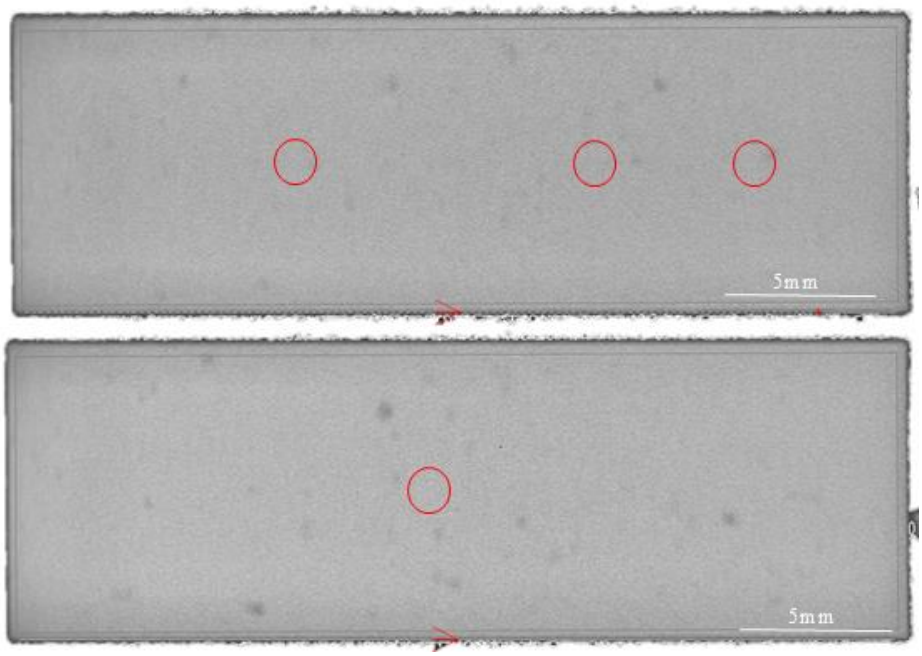

Figure 5-22 - XCT image of AM block showing intended locations of seeded "defects" - x-y plane at 250 µm from top surface (left) and x-y plane at 500 µm from top surface (right).

Analysis of these images gives no suggestion that a void was formed in the seeded area, although other, unintended porosity is apparent in the greyscale. To further analyse S22 and to try and explain the diffracted Rayleigh wave indications (blue) shown in Figure 5-20, automated defect recognition (ADR) software built into the 'VGStudio MAX 2.2' package was used.

A total of 1549 voids were identified by the algorithm in the LU scanning region and 28 were larger than 150 µm diameter. The

analysis indicated the presence of seven large voids with diameters between 610 µm and 860 µm. These are shown in Figure 5-23.

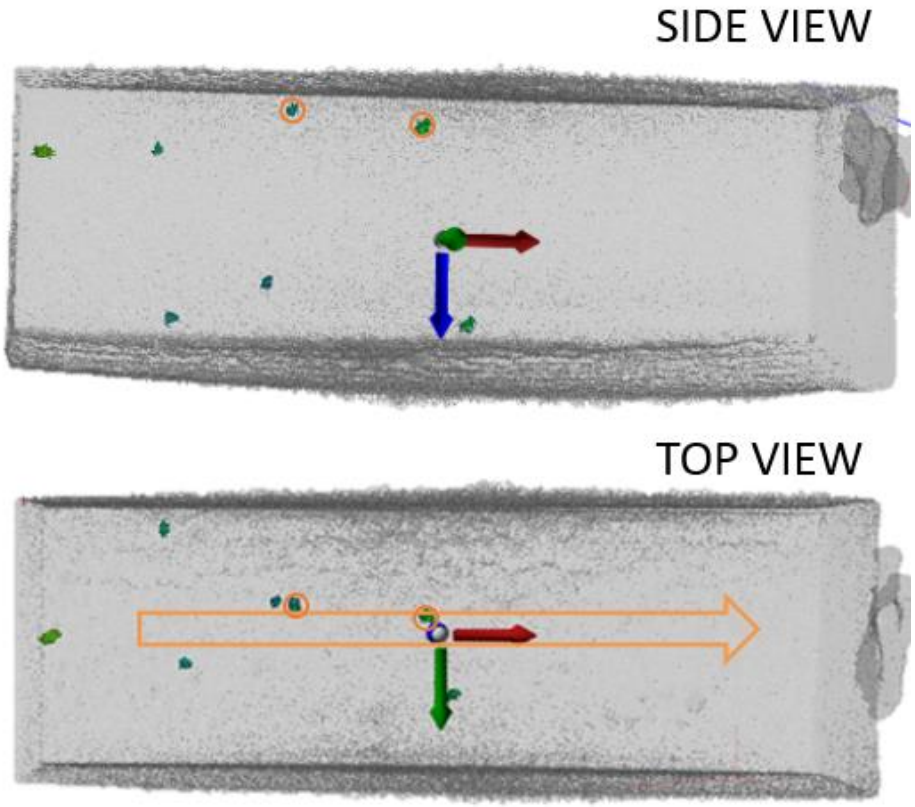

Figure 5-23 - ADR images showing locations of "defects" within the blocks from a) the side view and b) the top view. The circled "defects" are within the approximate LU scanning region, shown with an arrow.

Two of these seven "defects" (circled in orange on both views), are located sufficiently close to the top surface and along the central channel traversed by LU, to explain some of the indications seen in the B-scans. However, S22 is too porous to reasonably correlate the ADR voids with the LU indications. That said, the presence of the partial parabolas in Figure 5-20 does visually indicate that the sample has a high level of porosity, when compared to the S21 B-scan in Figure 5-15. LU has been used here as a qualitative assessment tool, with limited quantitative application.

5.4 Summary

Seeding “defects” is not straight forward; simply leaving a void in the AM sample CAD model does not necessarily result in a void. In the instances where a void was seeded such as for S3, the void was indicated by laser ultrasound. When the data was processed using an advanced tool, three distinct indications are seen on the LU B-scan. Using XCT and analysis in ImageJ, 8 voids were identified in the LU scanning region. Two of the 8 voids correlate to the positions of voids indicated on the B-scan. The third indication does not correlate to the XCT voids found, but is thought to have been caused by a surface undulation. The 6 voids which were found using XCT, but are not indicated by LU, are useful in determining the window of detection. In order to establish a window of detection for the LU system, void diameter and distance from the scanning path (sideways and into the sample) should be considered.

It is not known why voids were not seeded in the desired locations in S22 when the analysis of S3 shows this is possible. It is thought that during manufacture, the seeded voids in the larger samples were “healed” when processing subsequent layers.

It is also not clear why S22 has such a high level of porosity when S21 was relatively dense and was built on the same build plate. This porosity and the band of porosity along the right edge of the test pieces is thought to be due to underlying issues with the AM SLM50 build machine.

It is easy to make a mistake when importing a model with rotational symmetry. Marking of the part in some way or using asymmetrical test piece shapes is recommended for future work.

Finally, LU has been used to identify voids intentionally seeded in a test piece at a known location. Additionally, the LU scans indicate the presence of unintended, naturally occurring porosity in some cases. Whilst the pore density creates a high number of overlapping indications on the B-scans which can be difficult to interpret, a comparison of the B-scans with those taken of a "defect-free" sample can be used to qualitatively assess the test pieces.

The process of identifying the indications on the scans is recognised to be subjective. It is suggested that before LU is be implemented as an ex-situ or in-situ measurement tool, further work is required to create a library of acceptable and unacceptable B-scan images. This library would help to remove the subjectivity of a manual operator through training. Alternatively, image processing techniques could be used to assess the images computationally.

It is recommended that a similar study be continued now that a more advanced method of creating the B-scans in *Matlab* has been established, although it is recognised that the cost of XCT scanning required to validate the LU results, might be prohibitive. Also, the effect of LU scanning on the rougher, duller side surface of the AM cubes might artificially limit the sensitivity of the LU system which has been designed for in-process measurement in the longer term, and consequently returns a larger amplitude signal from the top AM processed surface. Rather than manufacture a large number of

AM samples to establish the window of detection, a computer modelling approach could be used – this is explored in Chapter 7

In this chapter, LU has been used to detect porosity in laser-PBF samples with seeded porosity. Pores were seeded by leaving a void in the AM build model although this method has not been found to repeatedly yield a pore. It has proven difficult to manufacture AM test pieces with pores with different sizes, at a known location. Instead, a method of creating zones of "defects" is explored in Chapter 6, through manipulation of AM build parameters in select areas. Computer modelling of test pieces with single voids was investigated and is presented in Chapter 7.

Chapter 6 - Process “defects” study

6.1 Introduction

This chapter details work carried out to LU assess AM test pieces intentionally manufactured with zones of porosity, created by manipulating the AM build parameters. The aim was to create test pieces that were almost fully dense, but had a small volume, termed the “defect zone”, close to the upper surface. Within this “defect zone” intentionally poor AM build parameters, garnered from the review of literature in Chapter 2, were used to promote the formation of naturally occurring pores. The test pieces were assessed by laser ultrasound (LU), imaged using X-ray computed tomography (XCT) and focus variation microscopy (FVM) and finally, were destructively analysed.

6.2 Methodology

Five 20 *x* 20 *x* 10 mm blocks were manufactured predominantly using optimised build parameters for Ti6Al4V, termed the bulk parameters. Additionally, each sample was designed to have a “defect zone”, embedded below a covering bulk layer (Figure 6-1). In the “defect zone”, sub-optimal parameters were intentionally selected to promote generation of naturally occurring process “defects”. The “defect zone” was generally 10 mm x 1080 μm x 200 μm in size and was manufactured beneath a covering region with 200 μm thickness, unless otherwise stated. A small surface notch was removed from the top face, for part traceability during post-processing.

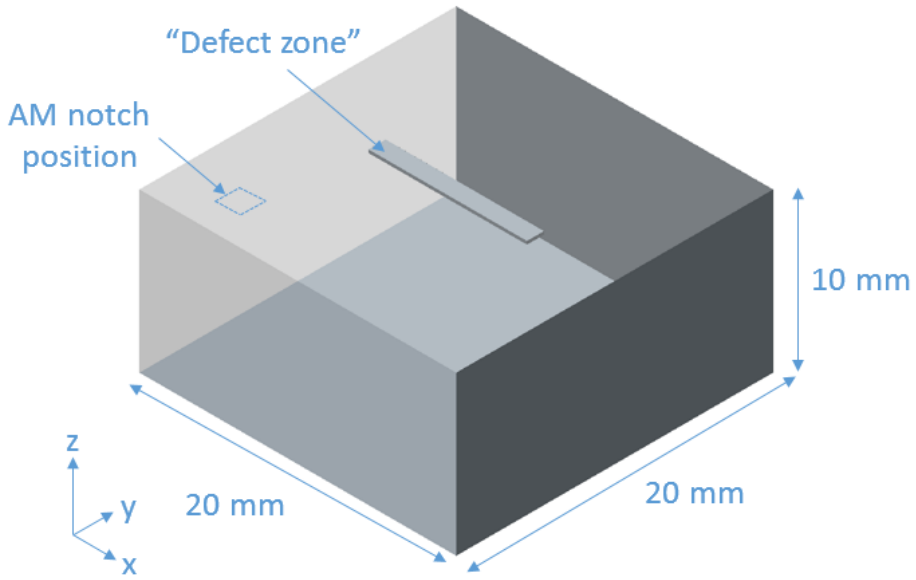

Figure 6-1 – Schematic of test piece with embedded "defect zone".

The test pieces were built from Ti6Al4V gas atomised powder using a Realizer SLM50. Each test piece was built in a separate build on a virgin Ti6Al4V buildplate. The machine was fully cleaned using the standard laboratory procedure, between builds, and the powder sieved with a 53 µm mesh, to remove spatter particles and agglomerated powder particles.

The bulk material was processed at a power of 100 W, 500 mm/s scanning speed at 90 µm hatch spacing. The "back and forth" build pattern was rotated by 90° after each 40 µm layer. Rather than risk support structure failures seen previously, 1 mm of sacrificial material was added to the base of the test pieces, which were melted directly on to the baseplate.

In the "defect zone", the impact of changing hatch spacing and scanning speeds on the type and density of porosity created were investigated. The AM build parameters used for scanning the "defect zone" for each test piece are listed in Table 6-1.

Table 6-1 - Summary of selected input variables for bulk, covering layer and "defect" zones

Test piece	Hatch spacing (μm)	Scan speed (mm/s)	Covering layer (μm)	"Defect zone" depth (μm)	Notch dimension x, y, z (μm)
BULK	90	500	120	n/a	n/a
P1	270	500	120	200	50, 50, 250
P2	90	1000	120	200	80, 90, 500
P3	90	50	120	200	80, 90, 500
P4	180	500	40	200	n/a
P5	180	1000	120	120	n/a

For test piece P1, an increased hatch spacing of 270 microns was used to avoid adjacent melt tracks from fully overlapping. In this instance, elongated voids with linear regularity were expected. For P2, the scan speed was doubled from 500 to 1000 mm/s. It was anticipated that there would be insufficient energy penetration for full melting of the layer and elongated voids would result between subsequent layers. Conversely a lower scan speed of 50 mm/s was selected for P3. Pores were expected to be produced as a result of over-melting in the "defect zone". Data regarding the transition point from conduction to keyhole mode was not available for Ti6Al4V, so spherical or keyhole pores could have resulted. For P4, a less extreme increase in hatch spacing than P1 was selected, although elongated voids were still anticipated. Additionally, a single covering layer was selected to reduce the depth of the resulting voids from the top surface. For P5, a combination of increased hatch spacing and increased scanning speed were selected.

A surface notch was created in the CAD model for the first test piece, P1 to enhance traceability during post processing. The notch size was

increased for P2 and P3 after the first build, as the original smaller notch was difficult to distinguish. The notches were removed for P4 and P5 as the AM scan strategy required for their manufacture resulted in significant surface undulation. This will be described in more detail in section 6.3.1

Once built, the samples were removed from the build chamber, de-powdered and the test pieces were removed from the baseplates by wire EDM. The test pieces were then scanned using FVM to produce a height map of the surface, before processing by LU. The test pieces were clamped, in turn, under the LU measurement head and scans were taken across and along each "defect zone". In some cases, the side walls and bulk material (regions away from the "defect zone") were also scanned. The four different scanning lines (1-4) are indicated in Figure 6-2. The green markers show the starting positions and the red, the end positions for the generation laser (line) and detection laser (dot); the dotted orange lines show the translation path.

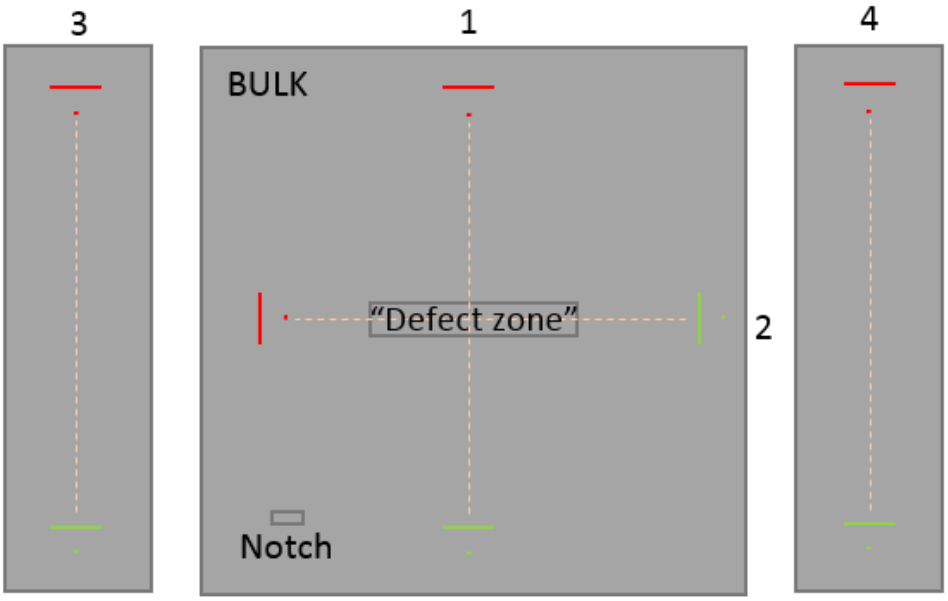

Figure 6-2 – Schematic showing LU scanning lines across (1) and along (2) "defect zone" and for the left (3) and right (4) side walls.

A laser spacing of 3 mm was sufficient to avoid interference between reflected waves and the Rayleigh wave arrival and a 15 mm scan path was traversed in 0.1 mm steps. The signal was measured over 5 μs at each acquisition point and the average of 64 shots recorded. Following LU testing, the test pieces were reassessed by FVM and by XCT before being destructively analysed.

6.3 Results

In this section, the results from LU of the test pieces built to contain voids in a "defect zone" are presented. Firstly, a few problems relating to the AM manufacture are discussed, including the scan strategy and lifting and cracking of the test pieces.

The success of creating voids through manipulation of AM process parameters and the suitability of LU to detect these is assessed. In order to visualize the "defect zones" created, the blocks have been subjected to XCT using a Nikon MCT225 X-ray CT machine at the University of Nottingham; a voxel size of 38 μm was achieved. Subsequently, this data has been analysed using 'ImageJ' and also, FVM has used to map the test piece top surfaces.

For the first five experiments, the same format is followed for presenting the results: Firstly, a micrograph image of a slice through the "defect zone" is shown, followed by an image of the corresponding location taken by XCT. Secondly, the B-scan taken along scanning line 1, across the "defect zone", is then shown and subsequently, the same B-scan is repeated with identified features overlaid, utilising the methodology introduced in section 4.3.1 . The XCT results are then presented and a comparison made between the LU and XCT. Thirdly, the same analysis is carried out for the LU scan taken along scanning line 2, along the "defect zone" and the systematic analysis methodology applied.

For experiment 6, LU scanning along scanning lines 3 and 4 (Figure 6-2) are compared. Where it is deemed useful, a FVM height map of the test piece top surface is added. For the annotations overlaid on B-scans, the same colour scheme introduced in Chapter 4 for highlighting indications is maintained.

Additionally, the effect of operating in the ablation regime during LU is assessed using FVM.

6.3.1 Build

The build scanning areas generated by the build software for the test piece geometry are shown schematically in Figure 6-3. The build was set up with the standard, "meander" scanning strategy setting, meaning that for the bulk slices, the laser rastered up and down the sample, starting in the bottom, left-hand corner for the first layer (Figure 6-3a). For the subsequent slice, the laser rasters at 90°, left and right, from the bottom left-hand corner. The build continues until a slice containing the "defect zone" is reached. The layer is then split into four scanning regions which the laser rasters in the order indicated (Figure 6-3b). For build slices which contain both the "defect zone" and the notch, seven scanning regions are utilised (Figure 6-3c). Finally, for slices with only the notch present, four regions are used (Figure 6-3d).

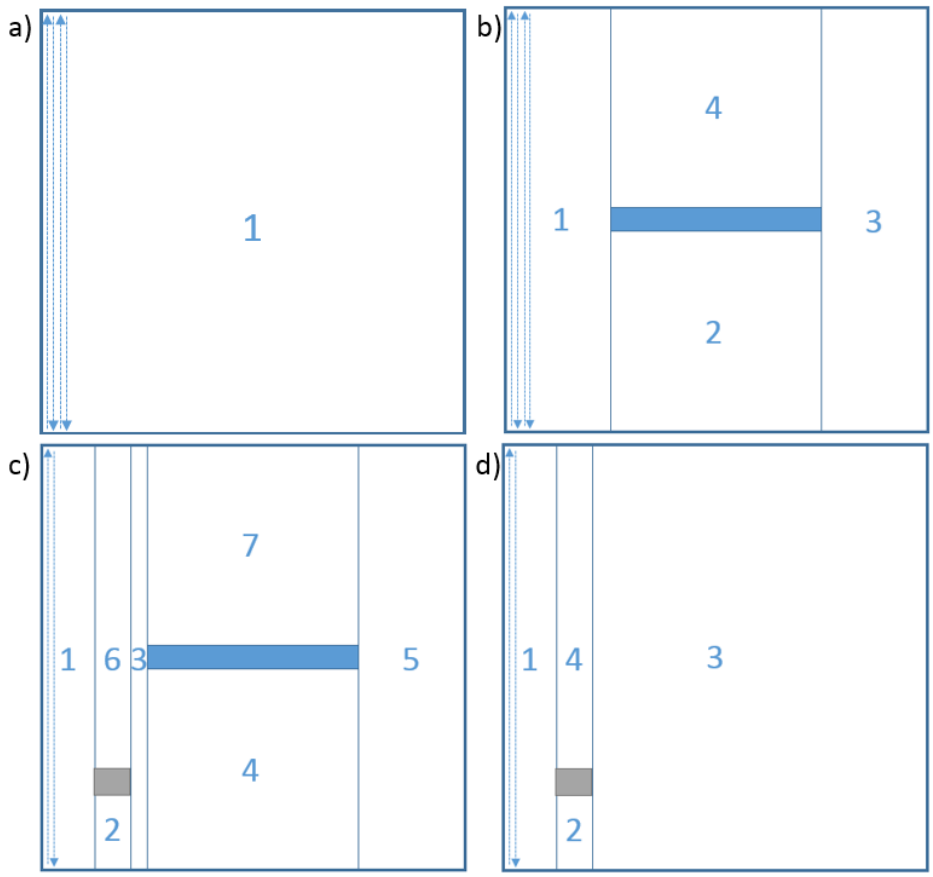

Figure 6-3 - Schematic showing scanning areas for a) bulk material, b) "defect zone" only layers, c) layers with "defect zone" and notch and d) notch only layers.

After the P1 build was complete, the notch size and depth were increased for P2 and P3 to make the notches more defined. For builds P4 and P5, the notches were removed to minimise the surface undulations on the top surface which had resulted. FVM height maps of the resulting surfaces are shown in Figure 6-4. Please note, the scales have been selected to give the best contrast for each individual test piece, so do differ. NM indicates an area that was not measured.

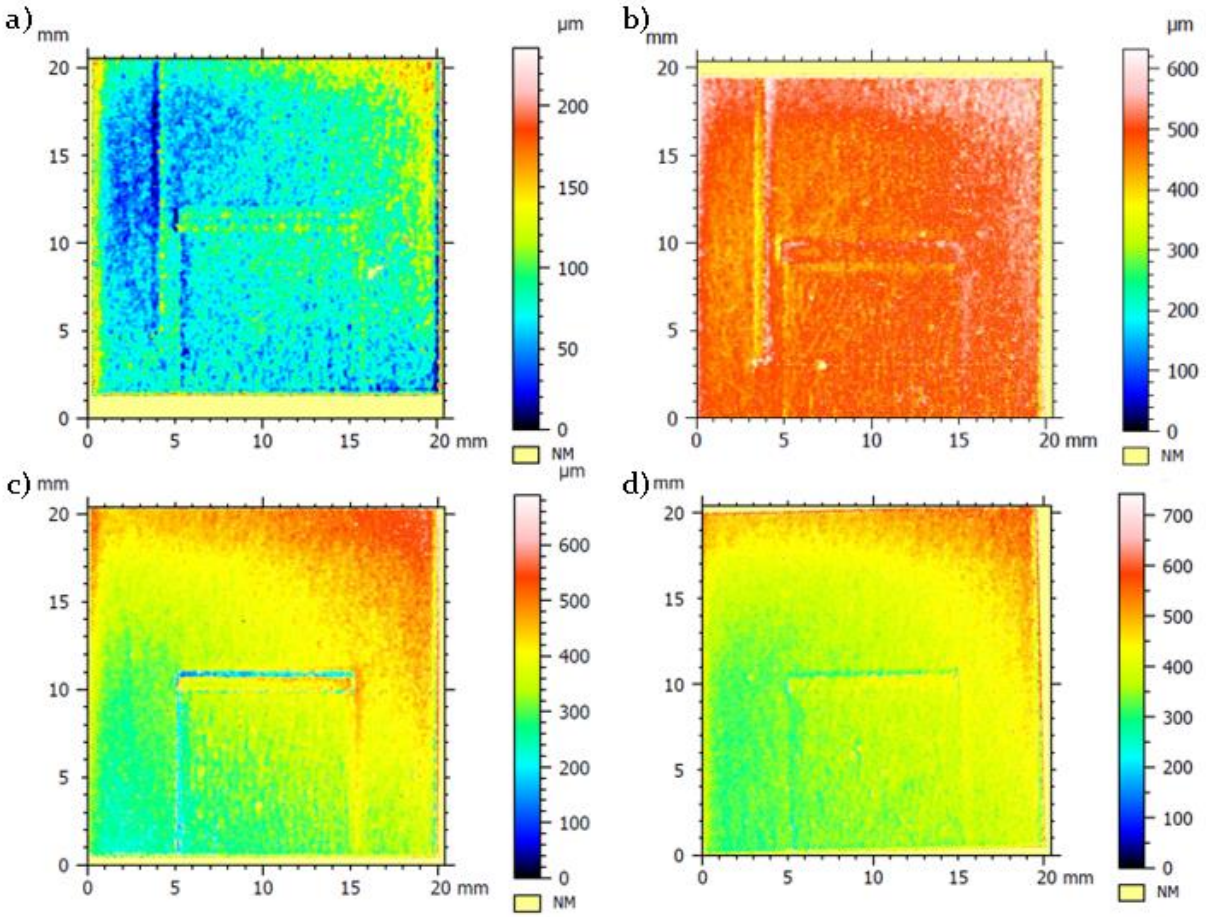

Figure 6-4 – FVM height maps showing a) P1, b) P3, c) P4 and d) P5 top surfaces, post-build.

The FVM height maps in Figure 6-4 show that the AM scan strategy utilised to build the notch and "defect" layers, described above, resulted in surface undulations where the scanning regions overlapped. It is thought that at the join between regions, the melt pool did not overlap sufficiently with the already processed, solidified regions. Alternatively, the lack of overlap could have been due to shrinkage caused by the differing cooling rate resulting from the dwell time between processing of the adjacent sections.

For P1 the deepest undulation was in the region of 100 μm along the edge of the zone caused by the presence of the notch. For P3 where the larger notch was introduced, the undulation in this area was nearer 150 μm. As the notches were removed from the build files for P4 and 5, the deepest surface undulations revealed from the FVM were caused by the presence of the "defect zone" and were approximately 50 μm deep.

On all test pieces, the "defect zone" was surrounded by a trough, suggesting that an error was made in selecting the skin parameters at the interface between the bulk and "defect zone". It is not known why the trough surrounding the "defect zone" for P2 was wider than on the other test pieces, as the same build parameters were selected.

Although unintended, these surface undulations caused by the presence of the notches and "defect zones" can be considered material discontinuities and the LU system was used to try and detect them.

To ensure traceability, an additional notch (500 *x* 90 *x* 30 μm) was added to each test piece by micro-milling, at a distance of 5 mm from the top right hand corner. A schematic of the revised, micro-milled notch location and an FVM image of the notch shape are shown in Figure 6-5.

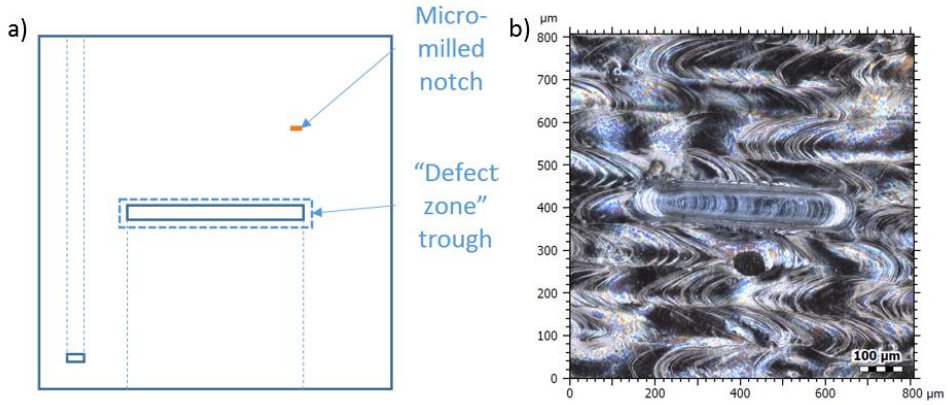

Figure 6-5 –a) schematic showing position of micro-milled notch and b) FVM image of micro-drilled notch in P1.

A second issue noted after the build was that for P4, the test piece had lifted from the buildplate at the rear face, as shown in Figure 6-6.

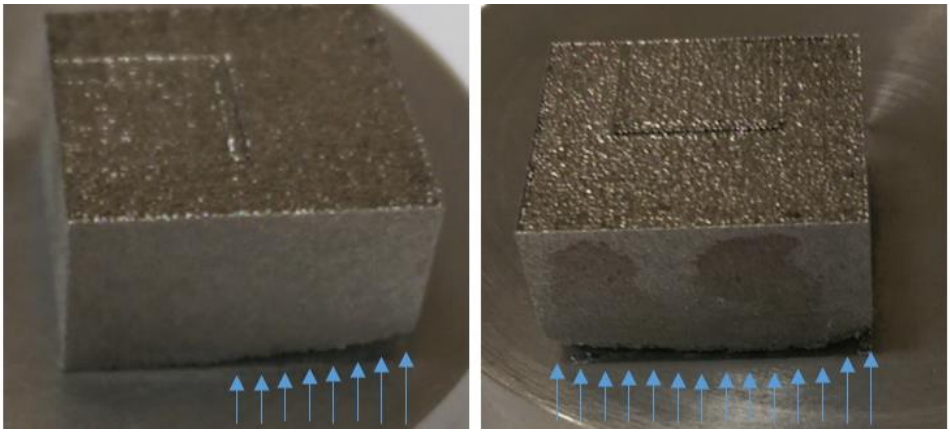

Figure 6-6 - Photographs showing lifting of test piece P4 from the baseplate - a) right hand wall and b) rear wall – indicated with blue arrows.

This lifting is due to the initial powder layer not being fully melted to the buildplate. This can be a result of the buildplate not being exactly level in the x-y plane. A locally thicker layer of powder is coated across the buildplate and the penetration of the laser is insufficient to fully anchor the test piece. The subsequent stresses caused during the build are sufficient to distort the test piece. Although a best effort was made when setting up the machine, this was a manual, subjective procedure. P4 was built on a virgin buildplate that had not previously been used, so the build surface was known to be in good condition. It is thought

that the threaded lug, which screws into the SLM50, was not manufactured fully perpendicular to the build surface and hence the build plate was not horizontal. Although the test piece distorted, manufacture of the "defect zone" was unaffected so the sample was still interrogated.

During the manufacture of P5, cracks were unintentionally created when the build paused for a period of time, due to an oxygen level sensor being triggered within the AM build machine. The build was idle for a period of two hours, two thirds of the way through the build and in this time, the chamber cooled to ambient temperature. The build continued once the gas feed had been restored, however the thermal cycle had an adverse effect on the test piece. Cracks can be seen on the rear and right hand faces in Figure 6-7, indicated by the blue arrows. Again, as the "defect zone" was unaffected, the sample was still interrogated; the effect of the cracking in the test pieces was also investigated.

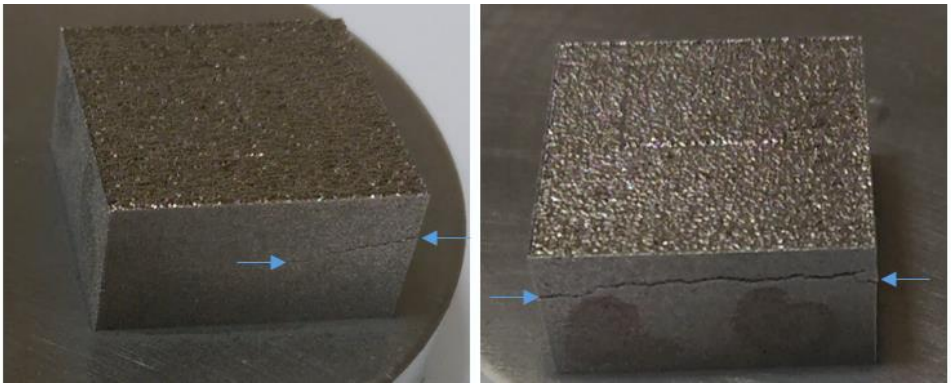

Figure 6-7 - Photographs showing cracking in test piece P5 - a) right hand wall and b) rear wall – indicated with blue arrows.

Importantly, research carried out in the department since the test pieces were built and analysed has revealed that the formula used for calculating and setting scanning speeds was incorrect. The machine manufacturer states that scanning speed (mm/s) is equal to the point distance (μm) divided by exposure time (μs), so for a desired scanning

speed of 1000 mm/s, a point distance of 20 μm and exposure time of 20 μs were selected. The study carried out shows that the actual scan speeds for these builds are lower than intended as the above equation does not hold true (Table 6-2). Of particular importance for this study, the point distance and exposure time selected for under-melting have not resulted in a scan speed which would be expected to necessarily cause under-melting.

Table 6-2 - Showing achieved scan speeds.

Test piece	Intended scan speed (mm/s)	Point distance (μm)	Exposure time (μs)	Processed scan speed (mm/s)
BULK	500	20	40	333
P1	500	20	40	333
P2	1000	20	20	493
P3	50	2	40	33
P4	500	20	40	333
P5	1000	20	40	493

Results of the six LU experiments assessing the manufactured test pieces will now be presented and discussed.

6.3.2 Experiment 1 – Elongated pores

For P1, the hatch spacing was increased in the "defect zone" from 90 to 270 microns in order to avoid adjacent melt tracks from fully overlapping. Elongated voids with linear regularity were expected to form.

6.3.2.1 *P1 "defect zone" analysis*

The image in Figure 6-8 shows a horizontal cross-section of the central portion of the "defect zone" for P1 taken at a depth of 370 µm from the test piece top surface. The image was taken using an optical microscope at 25X magnification. The corresponding area imaged using XCT is shown in Figure 6-9.

Encouragingly, a high amount of porosity has resulted in the "defect zone" with the changes in scan strategy yielding isolated elongated pores and interconnected elongated pores, shown in black. The "defect zone" outer edge is almost a continuous pore, likely a result of the skin parameters selected for the build not overlapping where the "defect zone" and bulk material intersect.

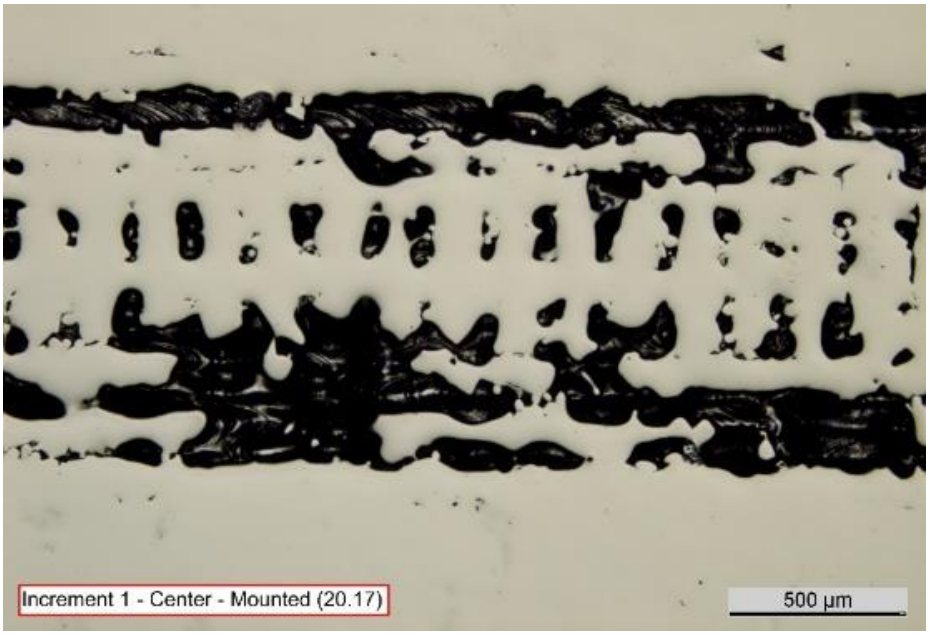

Figure 6-8 - Optical microscope image through "defect zone" in x-y plane for P1 at -370 µm.

The XCT image in Figure 6-9 shows a correlation with the destructive analysis, an outline of which is overlaid in blue.

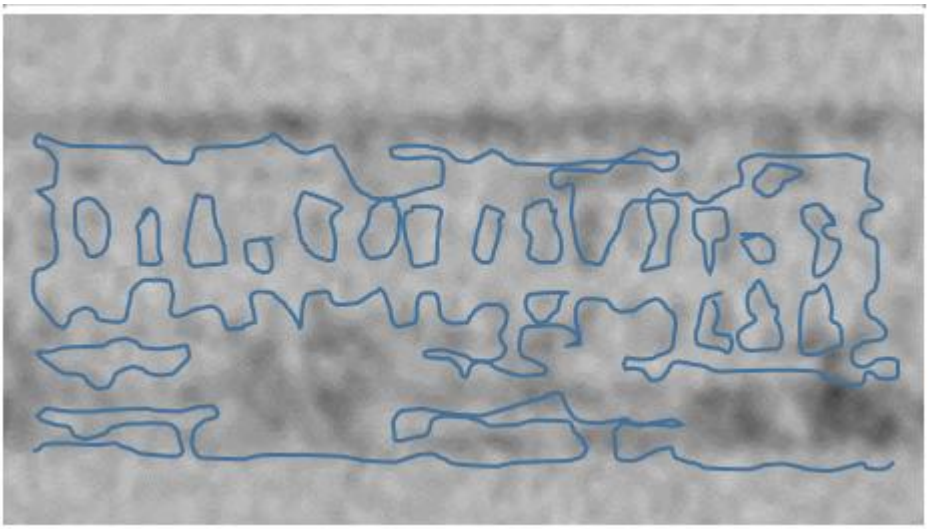

Figure 6-9 - Section of XCT slice at -370 μm, cropped to area of interest, overlaid with a "void pattern", traced from Figure 6-8.

A LU analysis of P1 was carried out to ascertain whether any of the generated elongated pores were indicated. LU scanning along the two scanning paths (shown in Figure 6-2) produced two B-scans which are shown and discussed below. Following this, the XCT data was processed through *ImageJ* using the methodology outlined in section 5.3.2 which was used for validation of the LU B-scan analyses.

6.3.2.2 *Assessment of LU of P1 - scanning line 1 – across "defect zone"*

The raw B-scan taken across the "defect zone" (scanning line 1) is shown in Figure 6-10, for reference. Seven different types of indications have been identified and these have been split across two duplicate B-scans, for illustrative purposes.

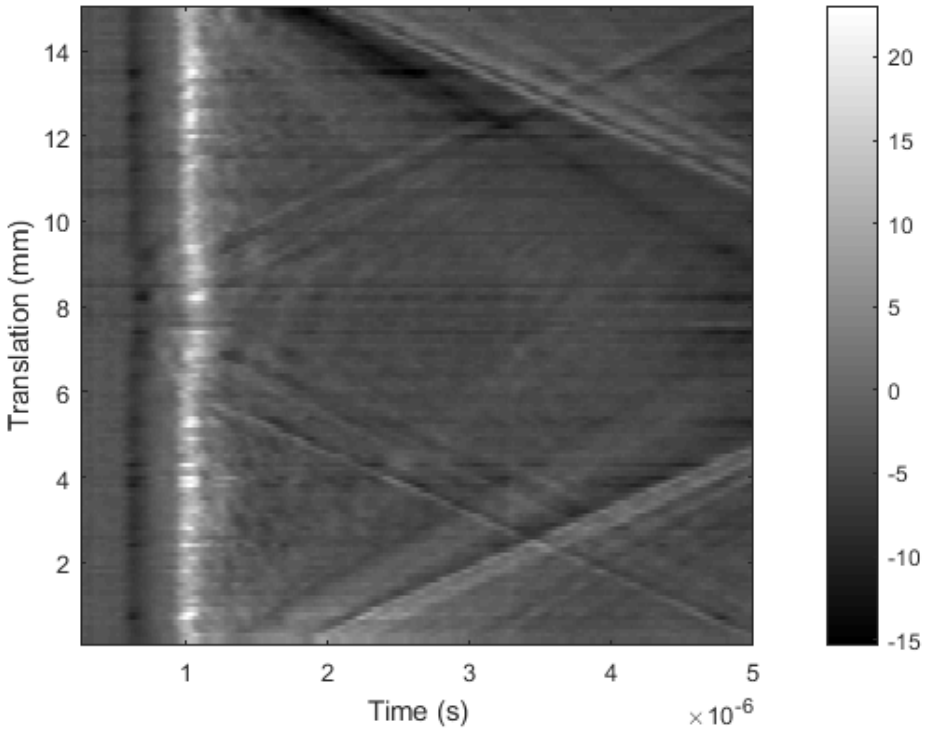

Figure 6-10 - B-scan of P1 along scanning line 1.

The first group of features identified on the B-scan are highlighted on Figure 6-11, using the methodology established in section 4.2

- The red, angled lines show displacements at the detection point caused as waves are bounced back from the near and far end-walls of the sample. The green vertical line arriving at 3.2 μs represents the arrival of a reflected longitudinal wave. Whilst these features are useful to check whether the laser head is translating, no information relating to any "defects" can be garnered.
- Two horizontal bands of signal drop out can be identified, either side of 8 mm translation, these are indicated with blue lines. These are caused by surface undulations defocussing the generation laser. As a result of this, the energy penetrating into the test piece is insufficient to register a signal at the detection point.

- The final two indications identified in Figure 6-11 are two vertical dashed lines. The lilac line at 0.5 μs is the direct longitudinal wave and the purple dashed line at 0.9 μs is caused by the direct arrival of the Rayleigh wave along the top edge of the test piece.

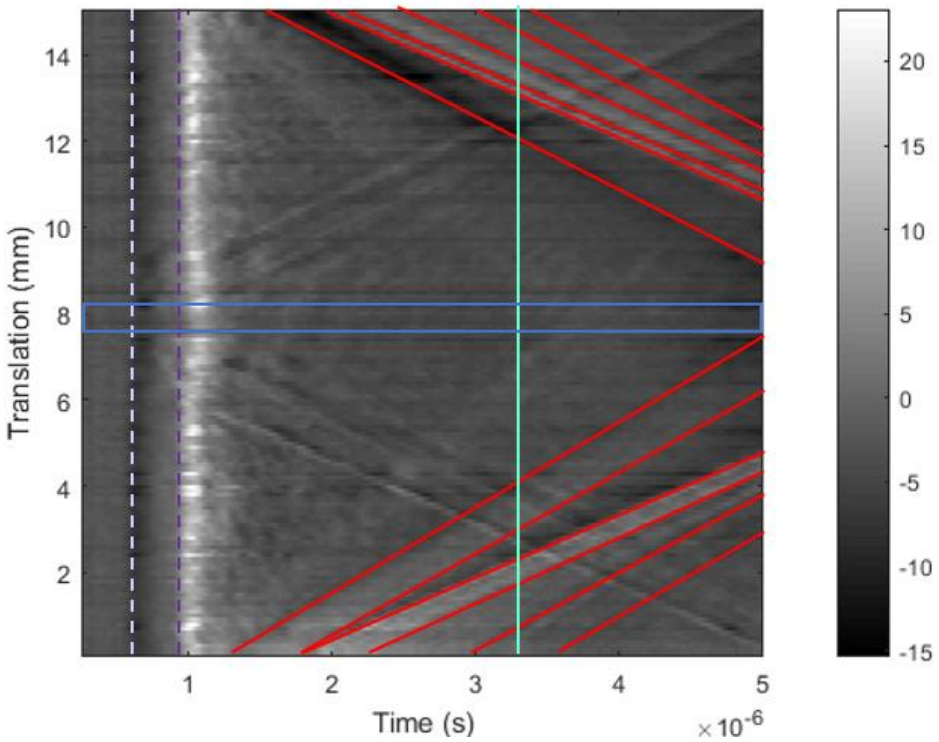

Figure 6-11 - B-scan of P1 along scanning line 1 overlaid with direct, reflected and mode converted waves from the base and end walls and the "defect zone" highlighted.

The second group of features identified on the B-scan are highlighted on Figure 6-12.

- The two orange parabolas indicate the top surface displacement caused by the diffracted longitudinal wave. This diffraction must be caused by interference with a "defect", as explained in section 3.2.1.5 The apex of the parabolas align with the arrival of the direct longitudinal wave (dashed lilac line shown in Figure 6-11).
- The three blue parabolas indicate the top surface displacement caused by the diffracted Rayleigh wave, travelling directly

between the generation and detection point. Again, this diffraction is caused by interaction of the direct Rayleigh wave, with a "defect". The apex of the parabolas align with the arrival of the direct Rayleigh wave (dashed purple line shown in Figure 6-11). Two of the blue parabola apexes coincide with the two orange parabolas. The bottom blue parabola at 4.4 mm stands out, having no corresponding orange parabola. This is further discussed below.

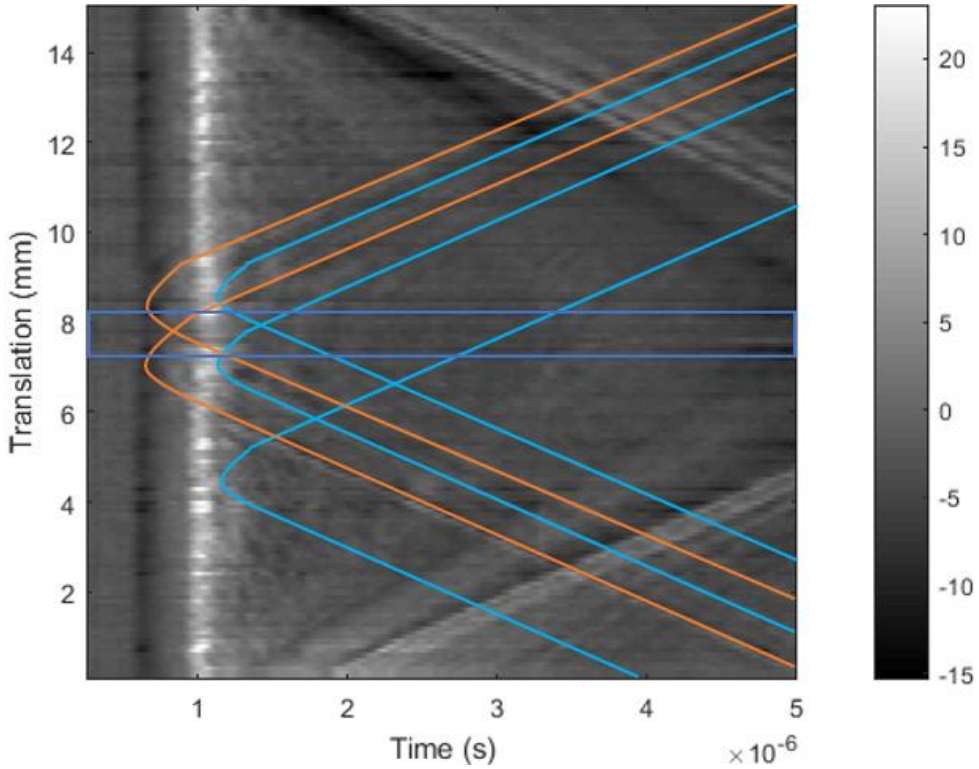

Figure 6-12 - B-scan of P1 along scanning line 1 overlaid with indications of material discontinuities.

The features highlighted on the B-scan were compared to the XCT results post-processed in *ImageJ,* an example processed image slice is shown in Figure 6-13.

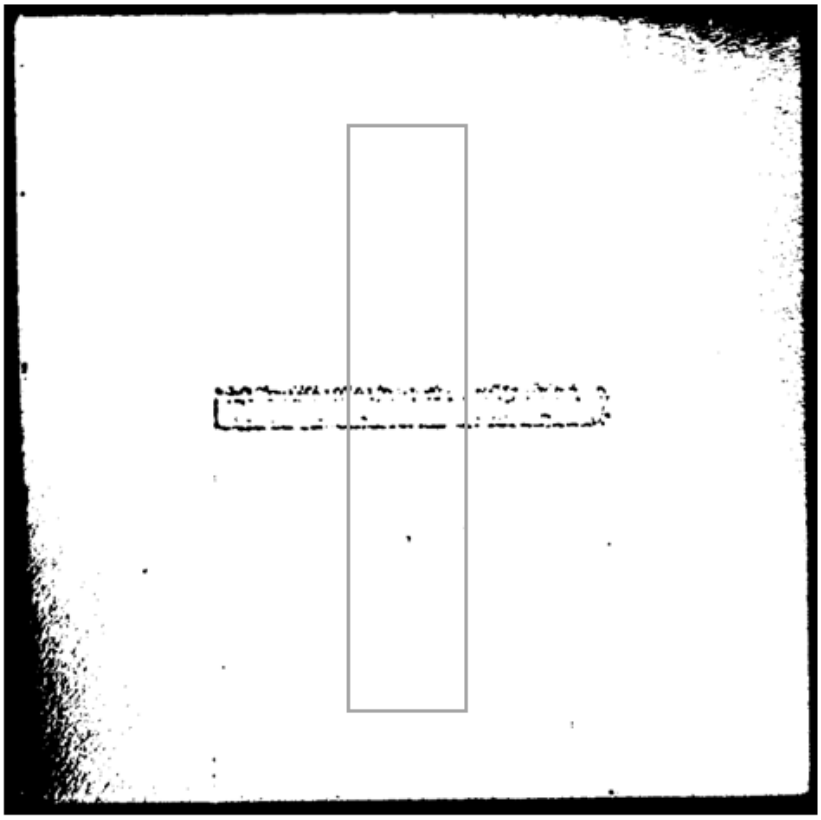

Figure 6-13 - *ImageJ* image at -228 μm, overlaid with approximate LU scanning area surrounding scanning line 1.

This analysis revealed the "defect zone" to be present between 7.4 and 8.4 mm translation, which corresponds with the dark blue box highlighting the horizontal lines of signal drop out on the annotated B-scan images. Both orange parabolas and two of the blue parabolas indicated from the LU align with the position of the "defect zone", measured in *ImageJ*.

The third blue parabola indicated by LU, peaking at 4.4 mm translation, is found to align with two voids identified by XCT which are both at a translation of 4.4 mm. The first is measured with a diameter of 108 μm, 76 μm below the surface and the second with a

diameter of 180 μm, 228 μm below the surface. As discussed previously, it is not unexpected that only a diffracted Rayleigh wave be produced, given the increased magnitude of the Rayleigh wave. No other voids are indicated by the XCT analysis in the LU scanning path.

6.3.2.3 *Assessment of LU of P1- scanning line 2 – along "defect zone"*

P1 was also scanned along the "defect zone" down scanning path 2 – the resulting raw B-Scan is shown in Figure 6-14, for reference.

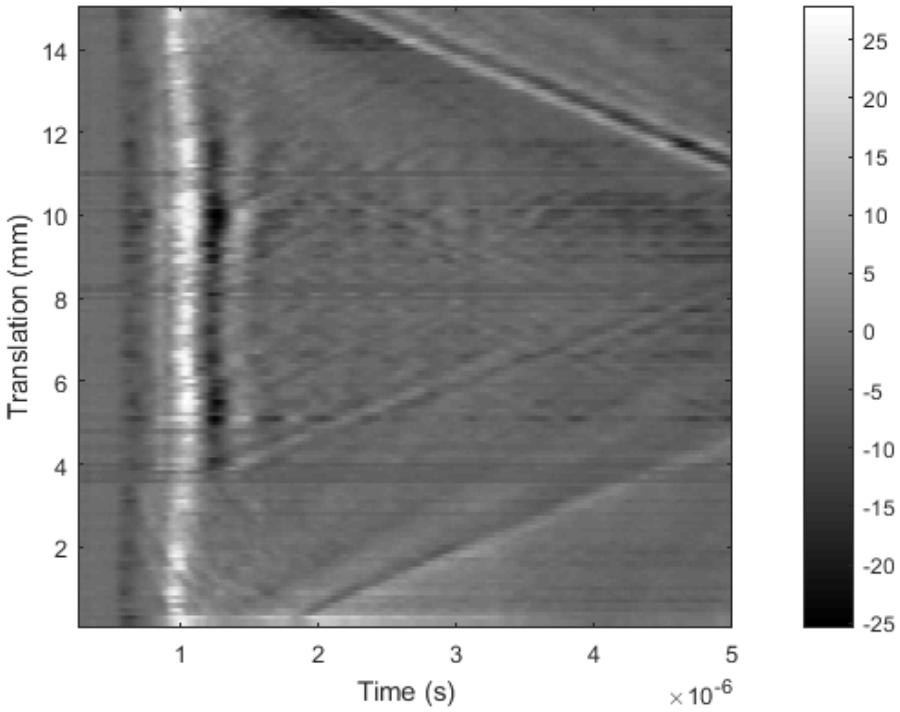

Figure 6-14 - B-scan of P1 along scanning line 2 (reversed).

Again, seven different types of indications were identified on the B-scan and these have been split across two duplicate B-scans, for illustrative purposes. The first group of features identified are very similar to those found when scanning across the "defect zone" (Figure 6-11) and are highlighted on the B-scan in Figure 6-15:

- The red, angled lines are caused by waves which have bounced back from the near and far end-walls of the sample. The green vertical line arriving at 3.2 μs represents the arrival of a reflected

longitudinal wave. Again, although these features are useful to check whether the laser head is translating, no information relating to any "defects" can be garnered.

- Two horizontal bands of signal drop out can be identified, but this time they are at 4.0 mm and 13.6 mm translation, indicated with blue lines. These are caused by surface undulations defocussing the generation laser. As a result of this, the energy penetrating into the test piece is insufficient to register a signal at the detection point. Following the last analysis, it was expected that these would correlate with the position of the "defect zone".
- The final two indications identified are two vertical lines indicating the arrival of the direct longitudinal wave at 0.5 μs and the direct arrival of the Rayleigh wave at 0.8 μs.

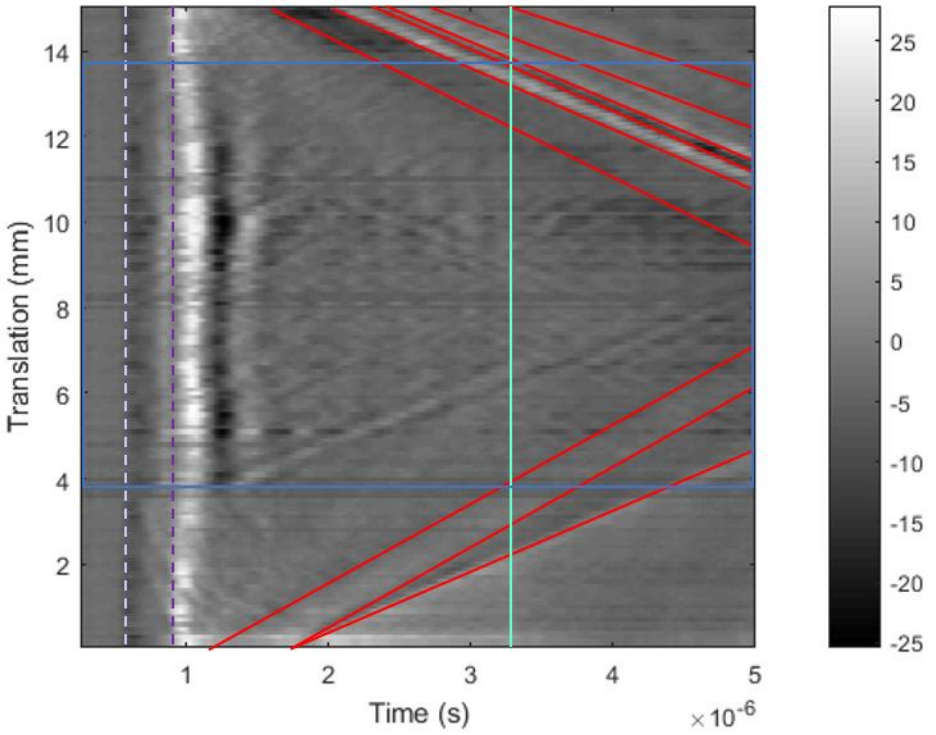

Figure 6-15 - B-scan of P1 along scanning line 2 (reversed) overlaid with direct, reflected and mode converted waves from the base and end walls and the "defect zone" highlighted.

The second group of features identified on the B-scan are highlighted on Figure 6-16.

- There are no full orange parabolas caused by diffraction of the direct longitudinal waves, only three partial indications peaking at 2.2 mm, 3.0 mm and 3.4 mm translation.
- The density of the indications in the time region after the Rayleigh wave arrival at 0.9 μs makes it difficult to distinguish full parabolas. A total of 31 partial indications are highlighted in blue, peaking roughly every 0.6 mm. Although most of the indications peaked within the area of signal drop out, a single blue indication was noted, at 1.4 mm translation.

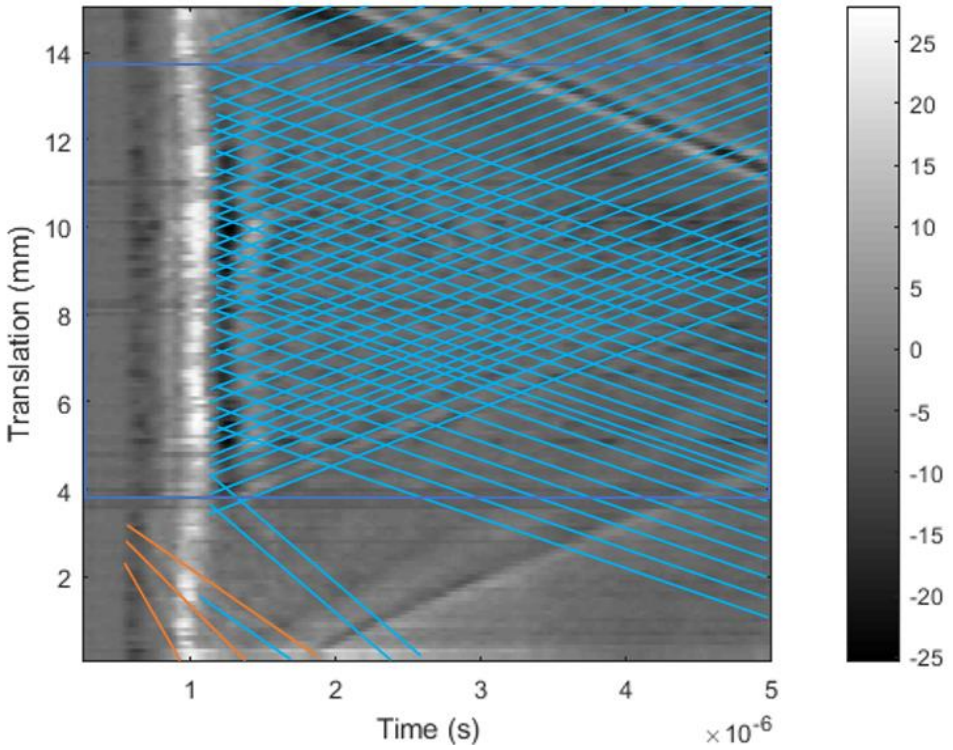

Figure 6-16 - B-scan of P1 along scanning line 2 (reversed) overlaid with indications of material discontinuities and with the "defect zone" highlighted.

The features identified on the B-scan were again compared to the XCT reconstructions, which were post-processed in *ImageJ*, an example processed image is shown in Figure 6-17.

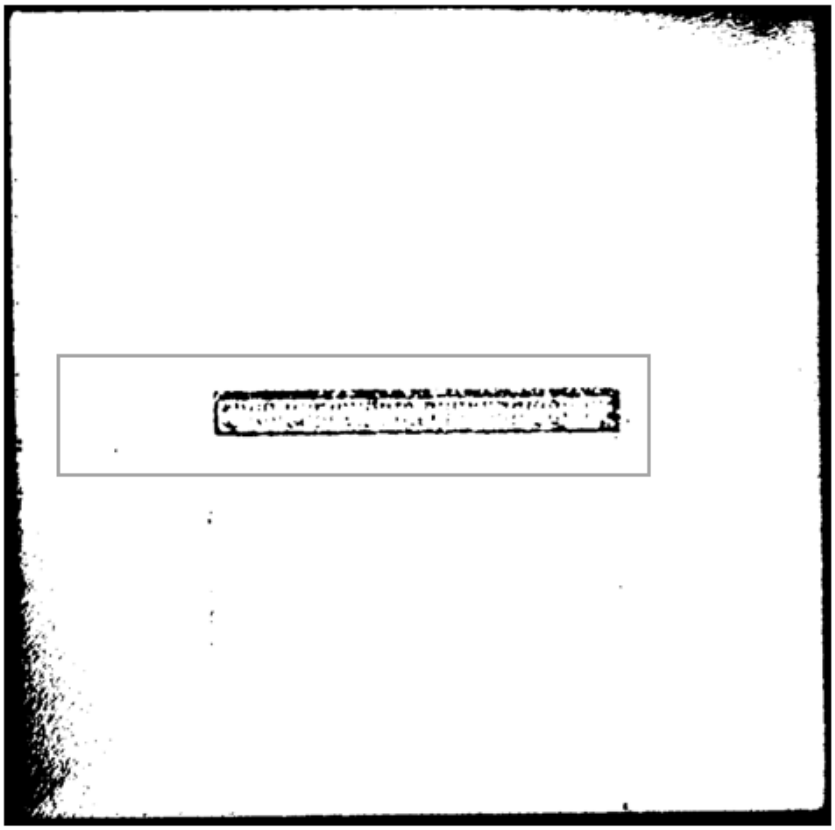

Figure 6-17 - *ImageJ* image at -266 μm, overlaid with approximate LU scanning channel for scanning line 2.

Using I*mageJ*, the "defect zone" was found to be between 4.0 and 13.6 mm translation, which corresponded with the dark blue box highlighting the horizontal lines of signal drop out, on the annotated B-scan images (Figure 6-15 and Figure 6-16).

ImageJ analysis of the "defect zone" along its length reveals 56 voids along the scanning path, occurring with regularity every ~170 μm or so. The indications on the B-scan in Figure 6-16 are pretty dense but the overlaid indications were found to occur roughly every ~600 μm, suggesting a spatial resolution for the LU system of 600 μm. Only 31 indications were identified from the B-scan (Figure 6-16) compared to the 56 found using *ImageJ*.

Analysis using *ImageJ* also revealed one void with a diameter of 83 μm at 3.4 mm translation, 266 μm depth below surface. A partial blue

parabola was identified on the B-scan at 3.4 mm translation (Figure 6-16).

No other sub-surface voids were noted. The remaining blue partial parabola at 1.4 mm translation and the three orange partial parabolas at 2.2 mm, 3.0 mm and 3.4 mm translation identified on the LU B-scan cannot be correlated with voids using *ImageJ*. However, analysis of the FVM image taken of the top surface (Figure 6-20), revealed that in the region between 2.6 mm and 3.6 mm translation, there was a surface undulation caused by AM processing of the notch.

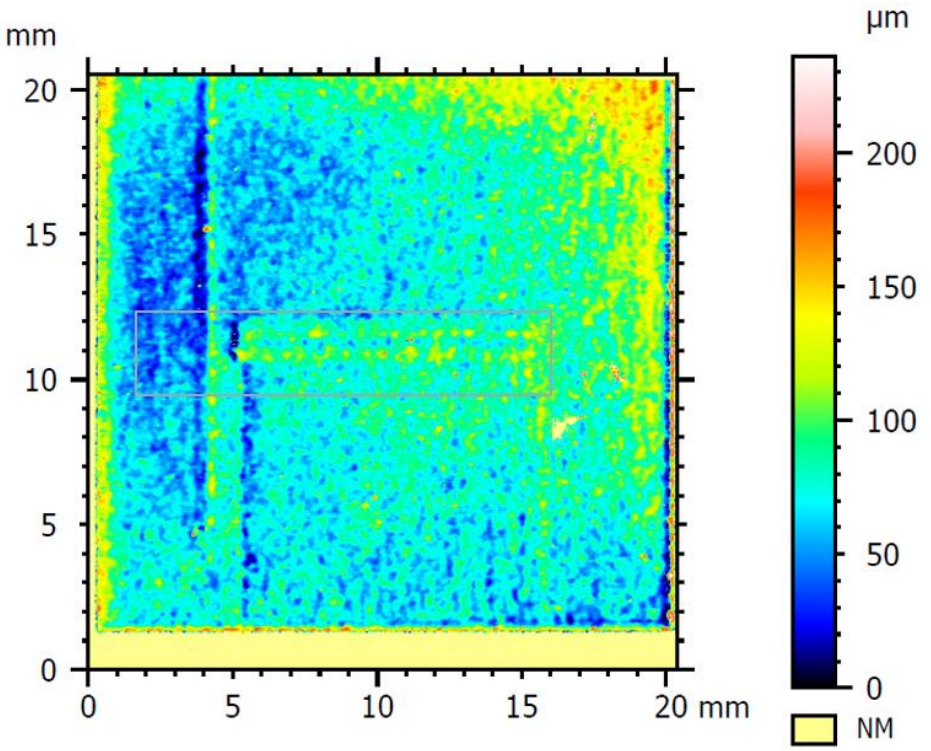

Figure 6-18 - FVM image of top surface of P1, overlaid with LU scanning region along scanning path 2.

6.3.3 Experiment 2 – Under-melting

For P2, the AM scan speed was increased from 333 mm/s to 493 mm/s with a view to promoting under-melting in the "defect zone". The notch size was increased to 80 *x* 90 *x* 500 µm.

6.3.3.1 *P2 "defect zone" analysis*

An FVM image of the top surface is shown in Figure 6-19. As noted previously in section 6.3.1 the surface undulation surrounding the "defect zone" in this case is wider than for any of the other test pieces at 600 µm, and therefore appears more prominently. The trough is approximately 150 µm deep.

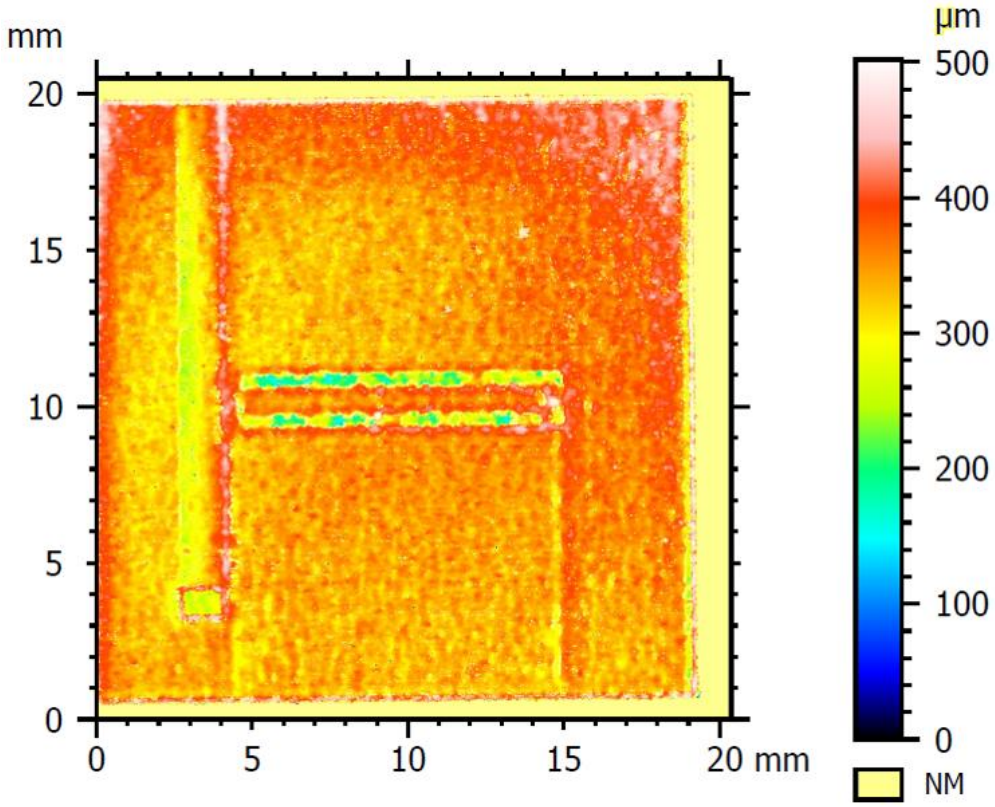

Figure 6-19 - FVM image of top surface of P2.

The image in Figure 6-20 shows an optical microscope image through the “defect zone”, displaying a series of elongated and interconnected voids. The voids occur along four main horizontal lines which bound the “defect zone” centrally (turquoise arrows), and the 600 µm trough surrounding the “defect zone” (purple arrows).

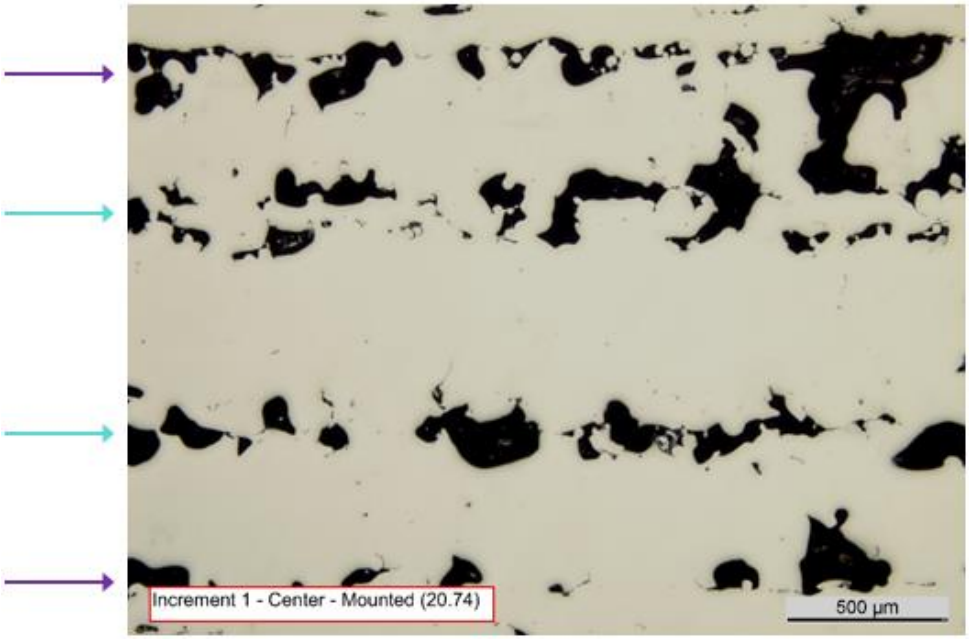

Figure 6-20 - Optical microscope image through "defect zone" in x-y plane for P2 at -370 µm.

Is was anticipated that the increased AM scanning speed selected for processing the “defect zone” would reduce the melt pool width, preventing the adjacent scan tracks from overlapping. Additionally, voids were expected along the scanning paths if balling had occurred, interrupting the melt pool tracks due to insufficient penetration into previously laid down layers. The bands of pores visible in Figure 6-20 are more likely due to a lack of overlap of the AM scanning zones or incorrect selection of the skin parameters.

Figure 6-21 shows the XCT image cropped to the area matching the optical microscopy image in Figure 6-20. The four lines of porosity are discernible bounding the “defect zone” centrally (turquoise arrows),

and around the 600 µm trough surrounding the "defect zone" (purple arrows).

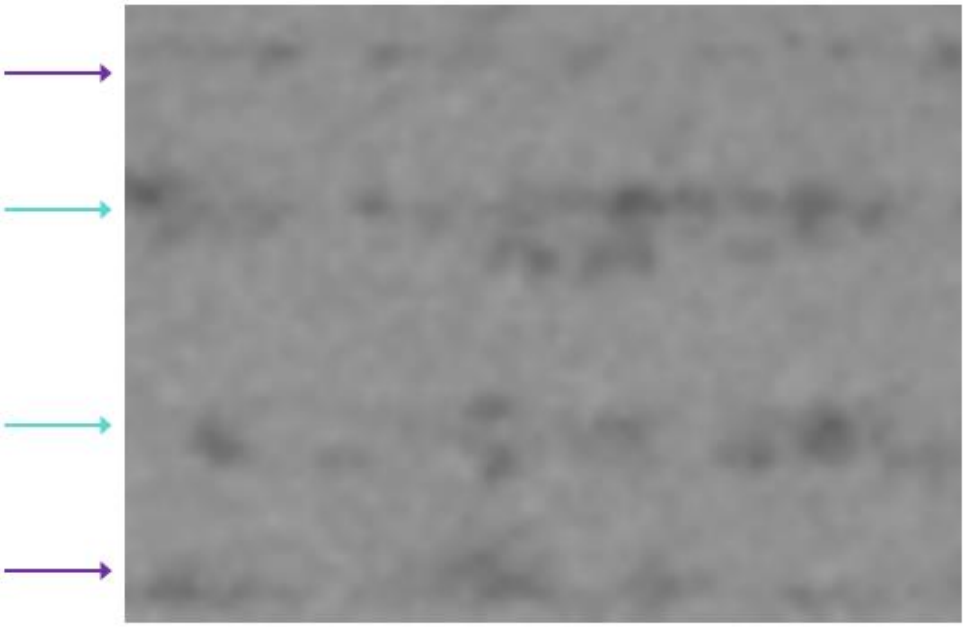

Figure 6-21 - Section of P2 XCT slice at -370 µm, cropped to area matching optical microscope image.

LU analysis of P2 was carried out to ascertain whether any of the generated bands of interconnected, elongated pores were indicated on the B-scans. LU scans were taken translating scanning path 1 (across the "defect zone") and along scanning path 2 (along the "defect zone"). Again, two B-scans are shown and discussed below and validated using slices from the XCT reconstruction, processed in *ImageJ*.

6.3.3.2 *Assessment of LU of P2 - scanning line 1 – across "defect zone"*

The raw B-scan taken of P2, across the "defect zone" is shown in Figure 6-22.

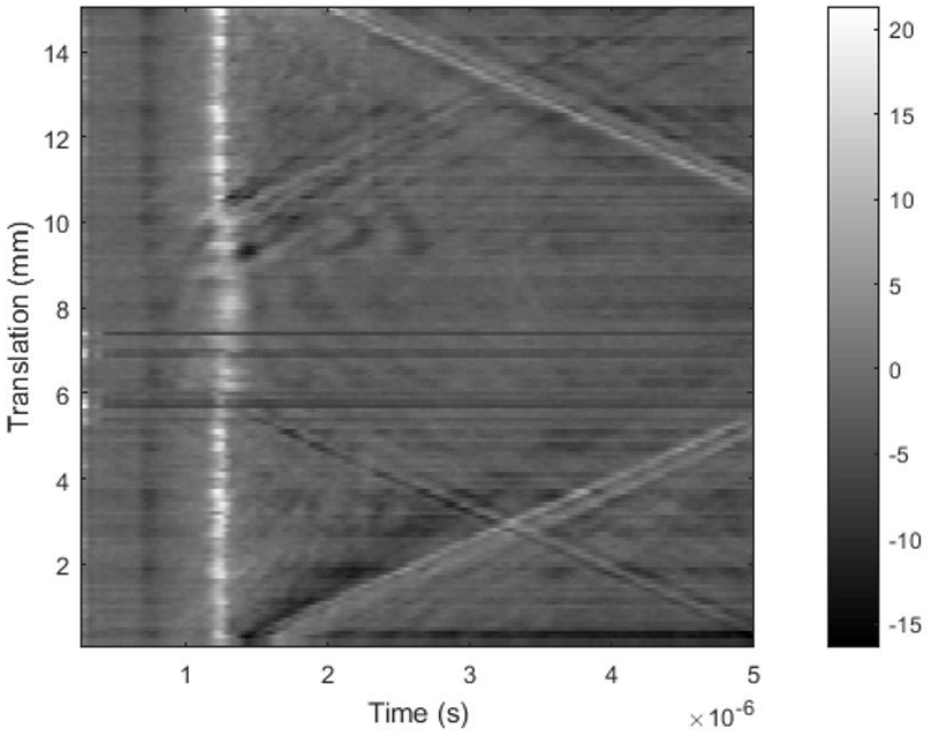

Figure 6-22 - B-scan of P2 along scanning line 1.

From this image, eight feature types were identified, the first group of which were overlaid on the duplicated B-scan shown in Figure 6-23.

- The red, angled lines indicate waves arriving, reflected from the start and end walls of the sample. The vertical solid green line arriving at 3.2 μs represented the arrival of the longitudinal wave, reflecting off the base of the sample. The two green dashed lines arriving at 2.2 μs and 4.4 μs are two reflections from the side walls. This suggests that the sample was not scanned centrally with an equal wave path to each side wall, but offset by approximately 3 mm. If the sample had been scanned centrally, the retuned signal would arrive at the same time as the wave reflected off the base of the sample, 3.2 μs. Whilst

these features are useful to check whether the laser head is translating, no information relating to any “defects” can be garnered.

- Four horizontal bands of signal drop out were observed at translation positions of 7.0, 7.6, 8.2 and 8.8 mm, indicated with dark blue lines.
- Finally for Figure 6-23, the lilac line at 0.5 μs marks the arrival of the direct longitudinal wave and the signal amplification corresponding purple dashed line at 0.9 μs is caused by the direct arrival of the Rayleigh wave.

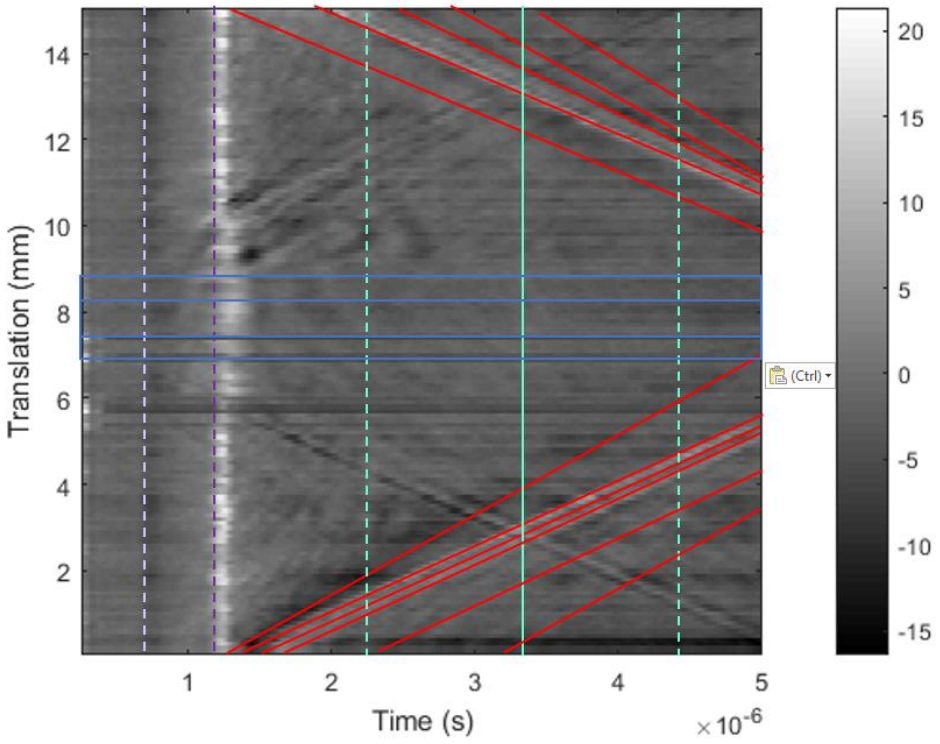

Figure 6-23 - B-scan of P2 along scanning line 1 overlaid with direct and reflected waves from the base, side-walls and end walls and areas of signal drop out highlighted.

The second group of features are indicated on Figure 6-24:

- The same four horizontal bands highlighting translation positions with signal drop out have again been overlaid.

- Four orange parabolas indicate the arrival of diffracted longitudinal wave, after the direct wave arrival at 0.9 μs previously overlaid as a lilac dashed line in Figure 6-23.
- A total of 8 blue parabolas have been identified. A single parabola had an apex peaking at 3.8mm, well outside the expected "defect zone" position. Four of the parabolas had apexes corresponding with the positions of signal drop out at of 7.0, 7.6, 8.2 and 8.8. There was a further indication peaking within this group and two closely positioned around 10 mm translation.

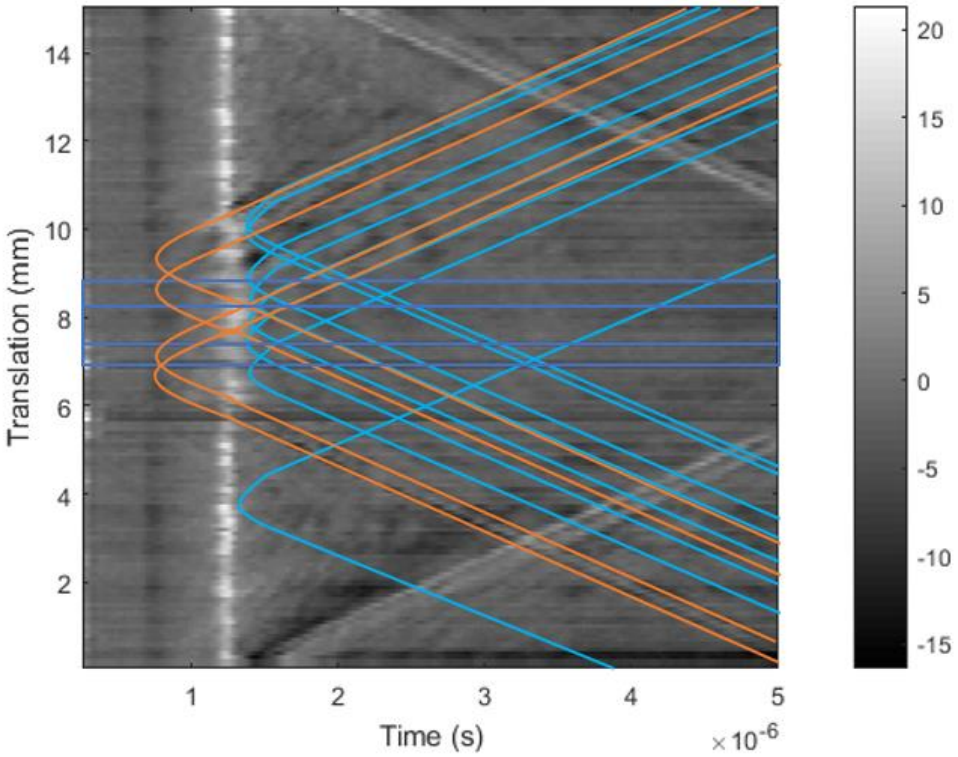

Figure 6-24 - B-scan of P2 along scanning line 1 overlaid with indications of material discontinuities and "defect zone".

The features highlighted on the B-scan were compared to the XCT results post-processed in *ImageJ*. The dark blue horizontal indications overlaid at positions of signal drop out were found to correlate with the four bands of porosity indicated in Figure 6-21. Four of the blue

parabolas indicating the arrivals of the diffracted Rayleigh waves matched these positions.

The blue parabola centrally within the "defect zone" at 7.8 mm translation was found through comparison with the XCT slices in *ImageJ* to correspond with a 141 μm diameter void, 40 μm below the top surface.

The lone blue parabola at 3.8 mm translation was found to be indicating a naturally occurring 185 μm diameter void, 300 μm below the top surface. Similarly, the two blue parabolas peaking around 10 mm translation indicate the presence of two unintended voids at 9.9 mm and 10.2 mm translation, which are 240 μm and 93 μm in diameter, 40 μm below the test piece top surface.

The four orange parabolas showing the diffracted waves from the direct longitudinal wave were seen to have a spacing similar to the overlaid position of the "defect zone" and trough, but are not in the correct translation location. Taking the positions of the "defect zone" and surrounding trough from FVM, rather than ImageJ analysis of the XCT images, it is found that the orange parabolas align with the "defect zone" surface undulations which are broader than the internal bands of porosity measured using *ImageJ*.

Interestingly, *ImageJ* analysis of the XCT images revealed the presence of two voids 43 μm in diameter at a z-distance of 300 μm, within the anticipated LU scanning region. No indications were identified on the B-scan at their corresponding translation distances of 5.41 mm and 5.62 mm. Consequently, these voids have been deemed to be outside the window of detection for the LU system.

6.3.3.3 *Assessment of LU of P2- scanning line 2 – along "defect zone"*

Test piece P2 was also scanned along the length of the "defect zone" and a raw B-scan is shown in Figure 6-25, for reference.

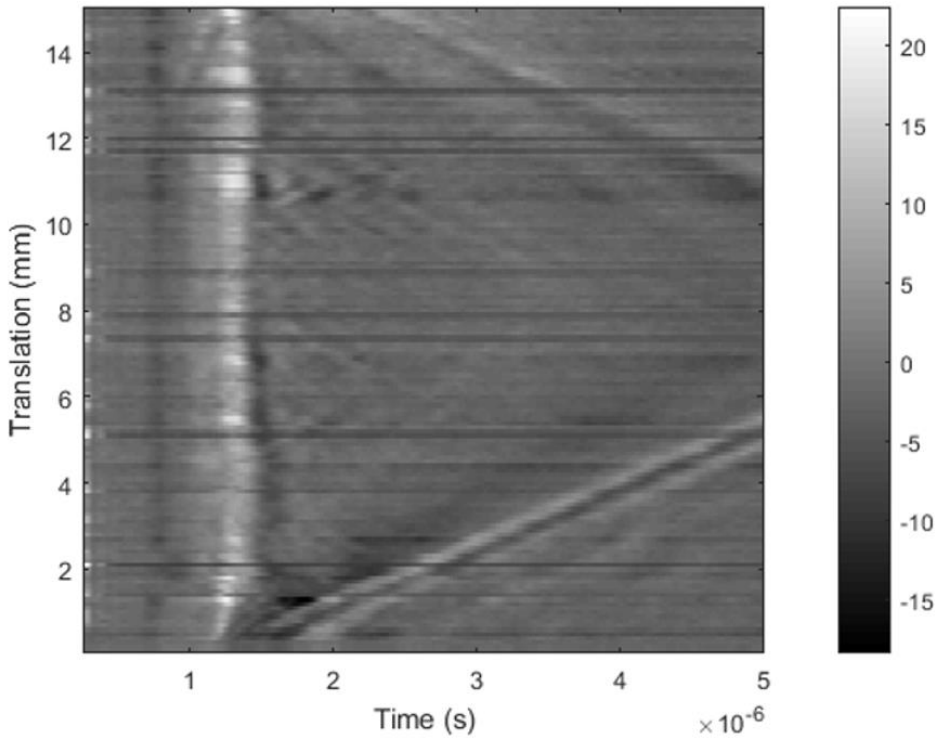

Figure 6-25 - B-scan of P2 along scanning line 2.

The seven different types of features identified have again been overlaid on two duplicated B-scans, the first of which is shown in Figure 6-26 with the arriving direct longitudinal, direct Rayleigh and reflected longitudinal waves shown. The diagonal indications of the returning waves bouncing off the start and end walls are also indicated. Several areas of signal dropout can be identified.

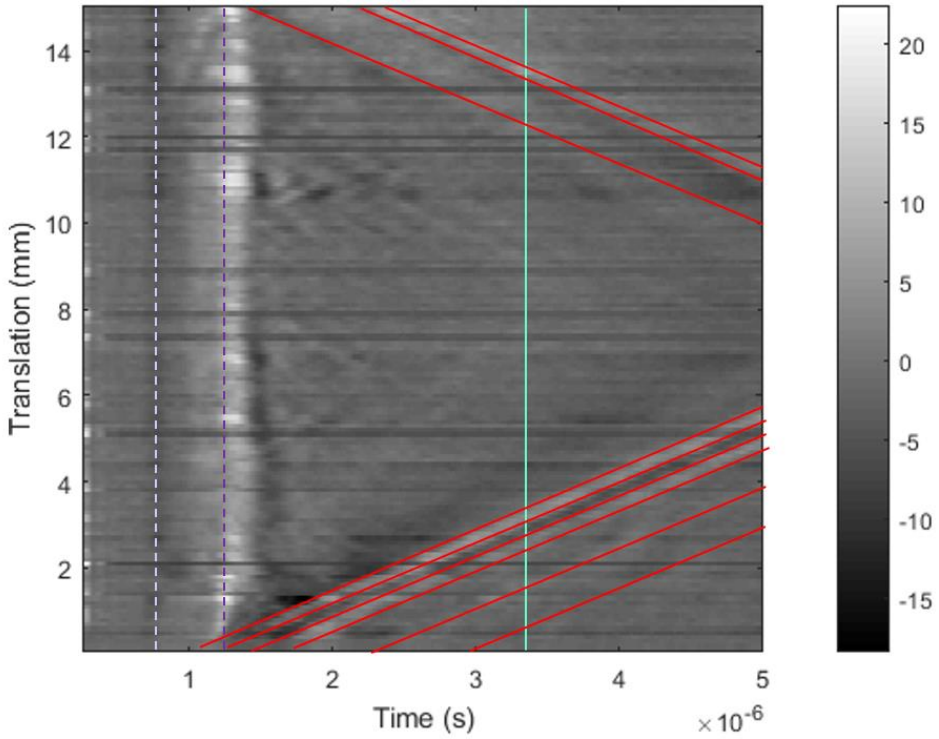

Figure 6-26 - B-scan of P2 along scanning line 2 overlaid with direct, reflected and mode converted waves from the base, side-walls and end walls.

All identified indications associated with the presence of "defects" are shown overlaid on Figure 6-27.

- There are four diffracted longitudinal wave parabolas (orange) at 1.2, 2.2, 11.5 and 12.5 mm translation. An additional partial parabola was identified peaking at 13.0 mm.
- There are also 16 blue parabolas caused by diffraction of the Rayleigh wave. Four of these correspond with areas of signal drop out thought to have been caused by scanning over the "defect zone", indicated with horizontal dark blue lines.

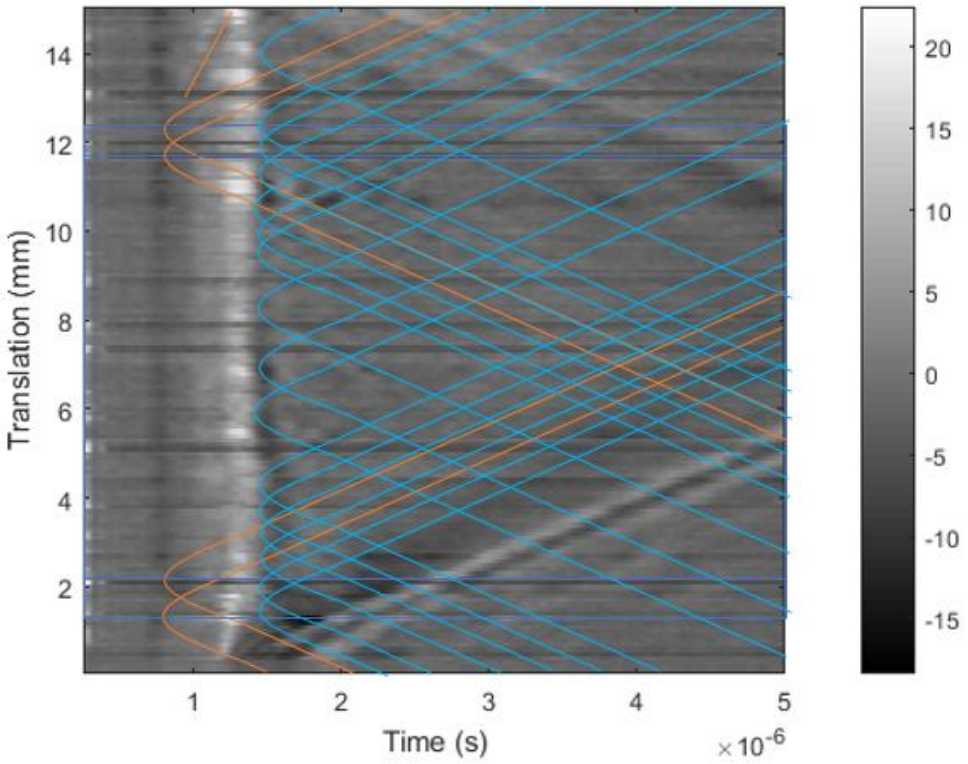

Figure 6-27 - B-scan of P2 along scanning line 2 overlaid with indications of material discontinuities and areas of signal drop out thought to be the "defect zone" and surrounding trough.

Employing *ImageJ* again to interrogate the XCT reconstructions, the four orange parabolas were found to coincide with the position of the four bands of porosity at the perimeter of the "defect zone" and surrounding trough. The orange partial parabola was found, using FVM, to correspond with a surface undulation caused when manufacturing the AM notch, between 13 mm and 14 mm.

Four of the blue parabolas were found to coinciding with the "defect zone" perimeter and trough perimeter, also aligning with the four orange parabolas and the horizontal lines of signal dropout at 1.2, 2.2, 11.5 and 12.5 mm translation.

Eleven blue parabolas peaking within the "defect zone" were found to correlate with voids visible in the *ImageJ* analysis. The 11 voids vary in

diameter from 46 µm to 307 µm. The z-distance varies from 37 µm to 411 µm and all voids identified were within a 687 µm central region.

The lone blue parabola at 14.2 mm translation was found, from comparison with FVM, to also correlate with the position of the notch anomaly on the surface.

6.3.4 Experiment 3 – Over-melting

For P3, a lower AM scan speed was selected in the hope of transitioning to the over-melting regime within the "defect zone".

6.3.4.1 *P3 "defect zone" analysis*

An optical microscope image of the "defect zone" is shown in Figure 6-28, with turquoise arrows added to highlight the expected position of "defect zone" perimeter. The destructive analysis carried out, revealed a line of porosity at a position corresponding to the upper, outer edge of the zone, but showed very little porosity within it. This section was taken at the very base of the "defect zone". Analysis of the XCT reconstruction in the "defect zone" revealed limited porosity across the other edge of the "defect zone". Very little porosity was observed within the "defect zone". Using FVM, the perimeter of the "defect zone" was identified.

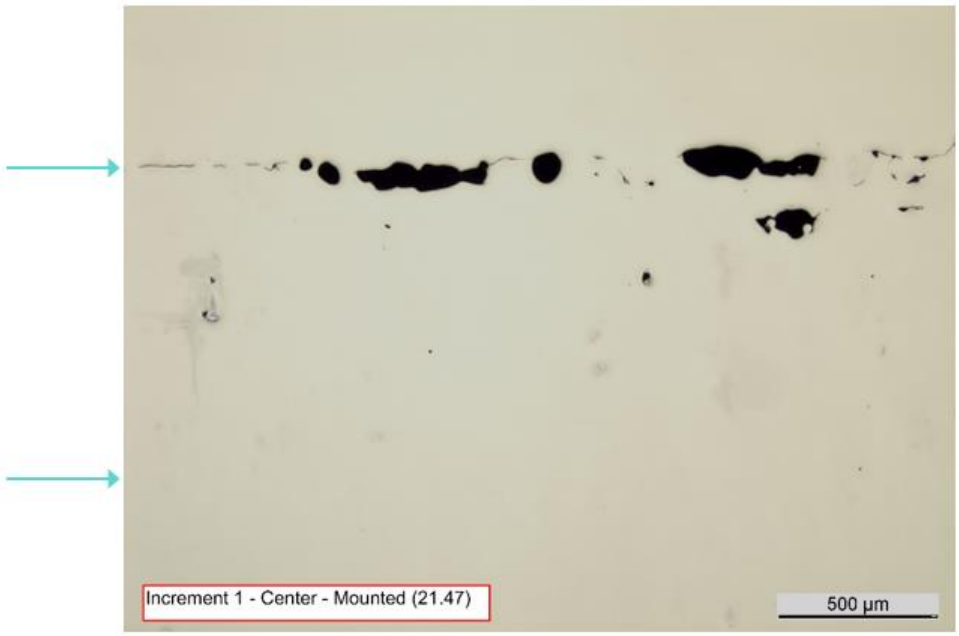

Figure 6-28 - Optical microscope image through "defect zone" in x-y plane for P3 at -360 µm.

6.3.4.2 *Assessment of LU of P3 - scanning line 1 – across "defect zone"*

The raw B-scan, taken translating scanning line 1, across the "defect zone" is shown in Figure 6-29, for reference.

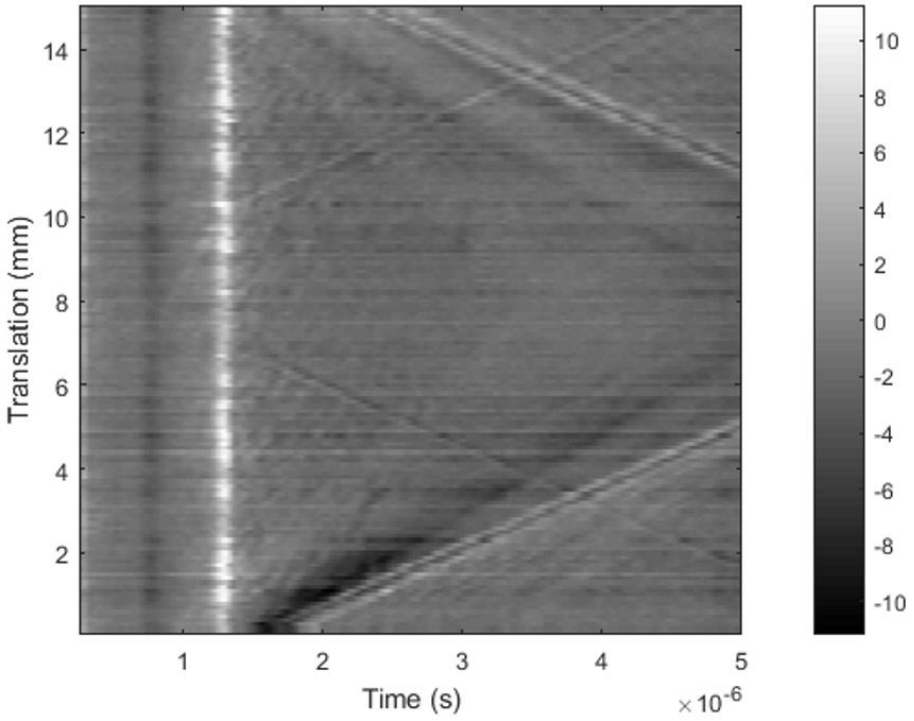

Figure 6-29 - B-scan of P3 along scanning line 1.

The seven feature types identified were overlaid on duplicate B-scans, the first of which is shown in Figure 6-30.

- Angled red lines indicated the waves reflecting off the start and end walls. The vertical solid green line at 2.9 µs indicated the arrival of the longitudinal wave reflected off the base of the sample. The arrival of the direct longitudinal (lilac dashed) and direct Rayleigh waves (purple dashed) were indicated at 0.7 µs and 1.3 µs. These arrivals were later than for previous scans as an increased generation and detection laser separation resulted from focussing the lasers.
- Two areas of signal drop out were noted at 9.3 mm and 10.3 mm translation, marked with dark blue horizontal lines.

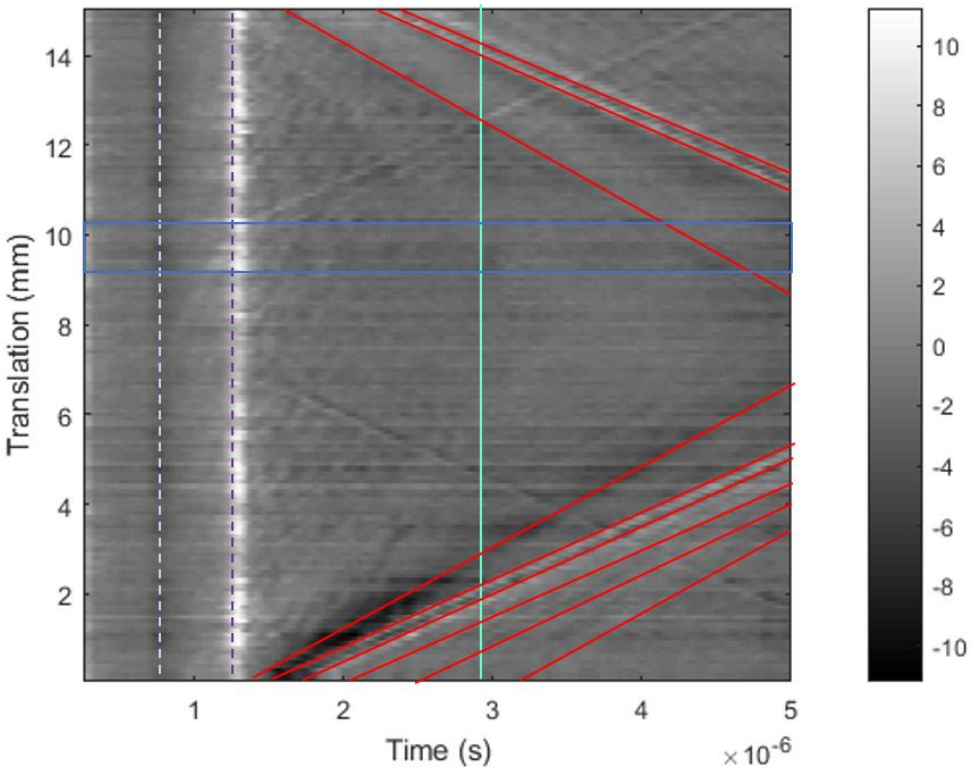

Figure 6-30 - B-scan of P3 along scanning line 1 overlaid with direct, reflected and mode converted waves from the base, side-walls and end walls.

The second group of features which were identified, giving indications of material discontinuities, are shown on another duplicate B-scan in Figure 6-31.

- Two full orange parabolas were highlighted, peaking at 9.3 mm and 10.3 mm translation. A partial orange indication which was triangular, rather than parabolic was identified between 6.0 mm and 10.0 mm, peaking at 7.5 mm.
- Four blue parabolas were highlighted, peaking at 7.5, 9.3, 9.6 and 10.0 mm.

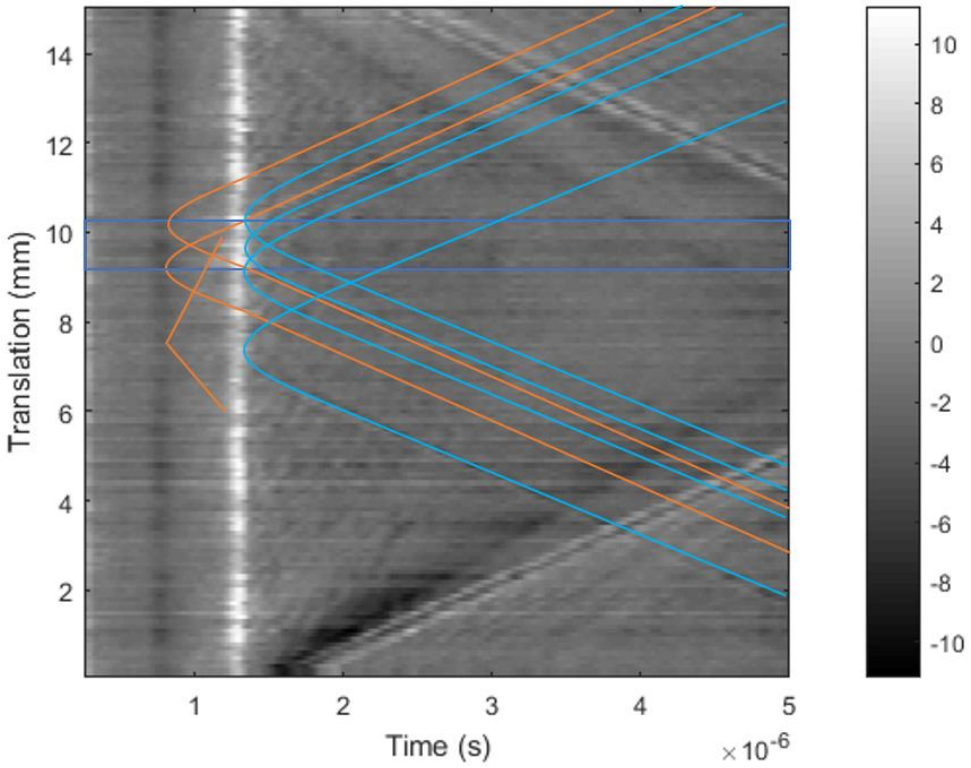

Figure 6-31 - B-scan of P3 along scanning line 1 overlaid with indications of material discontinuities and "defect zone".

Through *ImageJ* analysis of the XCT data, the two horizontal lines of LU signal dropout at 9.3 mm and 10.3 mm were found to correlate with the two bands of porosity at the edge of the "defect zone". Two orange and two blue parabolas were also highlighted in this position.

The blue parabola at 9.6 mm translation, within the "defect zone", correlated with a 134 µm diameter void at 224 µm z-distance, 625 µm from the scanning line. Additionally, the blue parabola at 7.5 mm

translation correlates with a 155 µm diameter void at -224 µm, directly under the LU scanning path.

Using FVM, the head of the triangular orange marking at 7.5 mm translation matched the position of a depression on the test piece top surface.

All LU indications were attributed to material discontinuities or surface undulations. No other features were found during XCT analysis.

6.3.4.3 *Assessment of LU of P3- scanning line 2 – along "defect zone"*

After LU scanning along the "defect zone" translating scanning line 2, the B-scan in Figure 6-32 was generated.

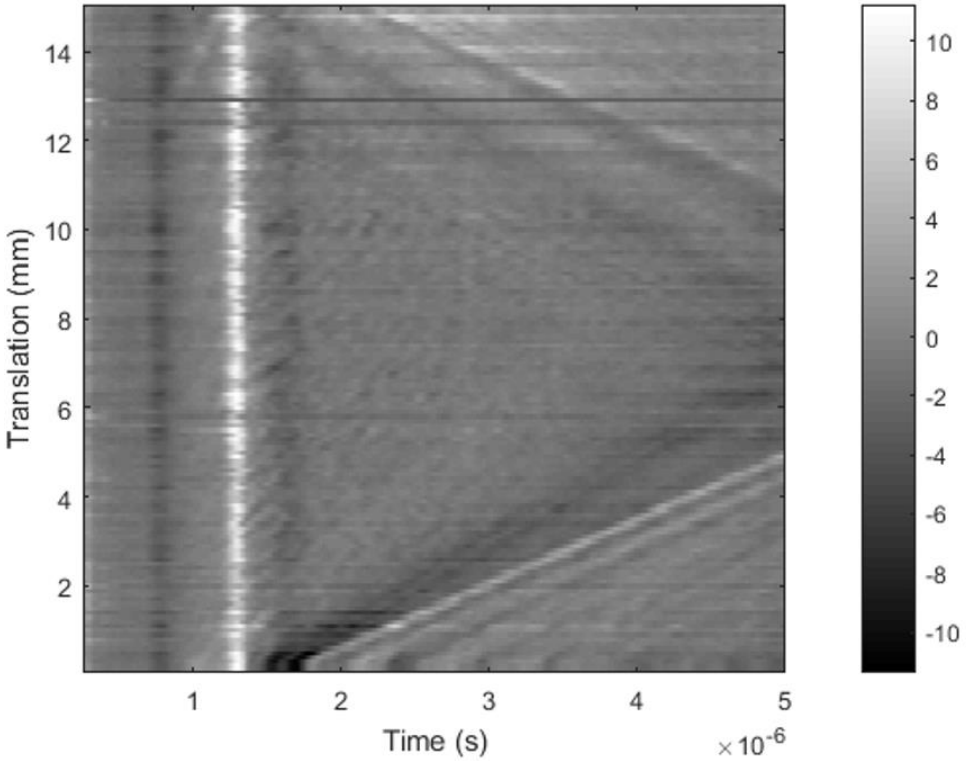

Figure 6-32 - B-scan of P3 along scanning line 2.

Eight feature types have been identified and overlaid on two duplicate B-scans, the first of which is shown in Figure 6-33.

- The diagonal lines (red) representing the waves reflected from the start and end walls of the sample were again evident. The arrivals of the direct longitudinal (dashed lilac), direct Rayleigh (dashed purple) and reflected longitudinal (green) were at the same times as when the sample was scanned along scanning line 1.
- An indication was highlighted in dark green at 1.6 μs, between 2.2 mm and 13.2 mm translation.

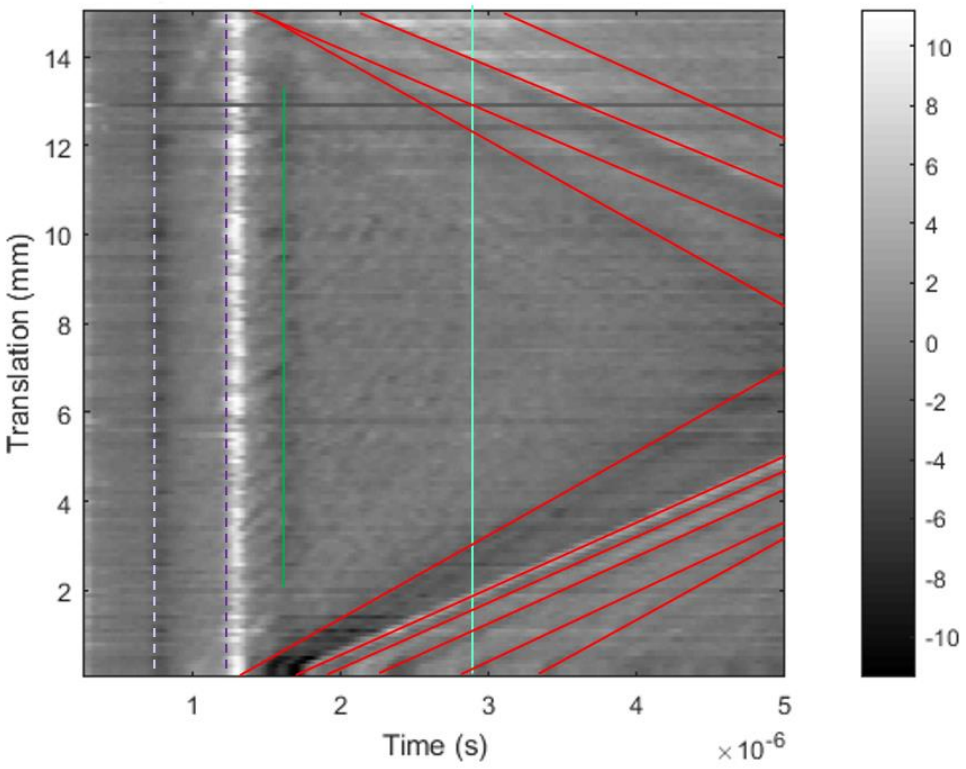

Figure 6-33 - B-scan of P3 along scanning line 2 overlaid with direct, reflected and mode converted waves from the base, side-walls and end walls.

The second set of features are overlaid on the B-scan in Figure 6-34.

- Two partial orange parabolas are overlaid. One peaks at 12.8 mm and the other peaks outside the LU translation path.
- 21 overlapping blue parabolas, indicating the arrival of the diffracted Rayleigh wave are shown, peaking roughly every 600 µm between 1.4 mm and 13.4 mm.

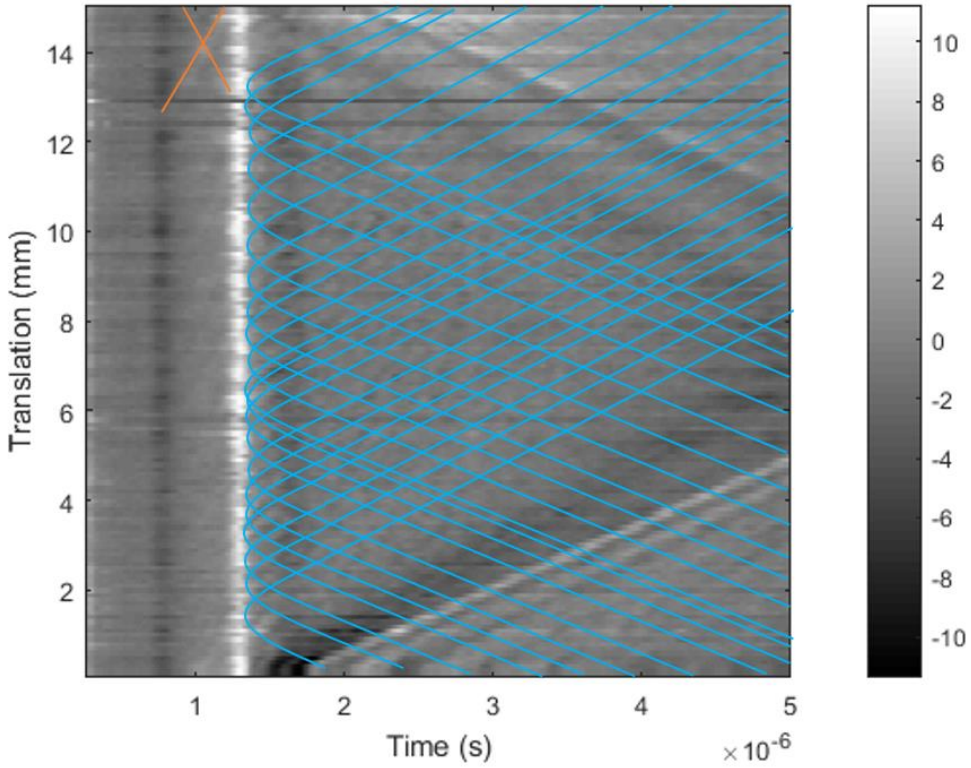

Figure 6-34 - B-scan of P3 along scanning line 2 overlaid with indications of material discontinuities and "defect zone".

An analysis of the XCT data was carried out using *ImageJ*. No voids were visible in the region between 12.8 and 14.9 mm translation, where the LU partial orange parabolas were identified. Although 21 overlapping blue parabolas were overlaid, analysis of the XCT images using ImageJ did not reveal the presence of multiple individual voids, but rather a series of interconnected voids in this translation range. This again suggests a minimum LU spatial resolution of 600 µm. It is thought the dark green indication in Figure 6-33 arriving at 1.6 µs is

caused by the longitudinal waves reflecting back off the two bands of interconnecting pores, bounding the “defect zone”.

Comparison of the orange indication translations with the FVM image revealed that the indications are in region of surface undulations, caused by AM processing of notch.

6.3.5 Experiment 4 – Elongated pores, close to the surface

Test piece P4 was manufactured with an increase in hatch spacing of 180 µm in the "defect zone"; this was a less extreme increase than for P1, where a hatch spacing of 270 µm generated elongated pores. The "defect zone" for P4 was processed over five AM build layers, but for only a single bulk layer was processed over the top, rather than the three used otherwise. No notch was added to the AM build file.

6.3.5.1 *P4 "defect zone" analysis*

An optical microscopy image taken to image through the "defect zone" is shown in Figure 6-35. Unfortunately, the decreased covering layer thickness was not taken into account and 360 µm of material was removed before the image was taken. Consequently, only the very base of the "defect zone" is visible.

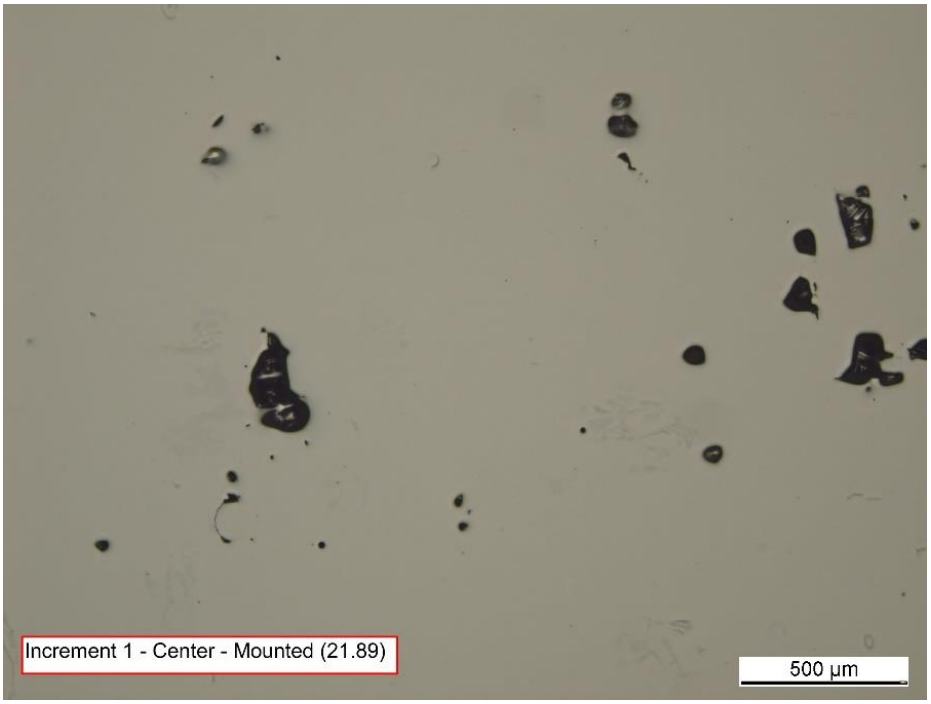

Figure 6-35 - Optical microscope image through "defect zone" in x-y plane for P4 at -360 µm.

Comparing the central slice of the "defect zone" using the thresholding technique in *ImageJ*, no voids are distinguishable in P4, unlike for P1

as the greyscale contrast was inadequate. The raw XCT images are shown below in Figure 6-36 to allow a comparison of the two test pieces.

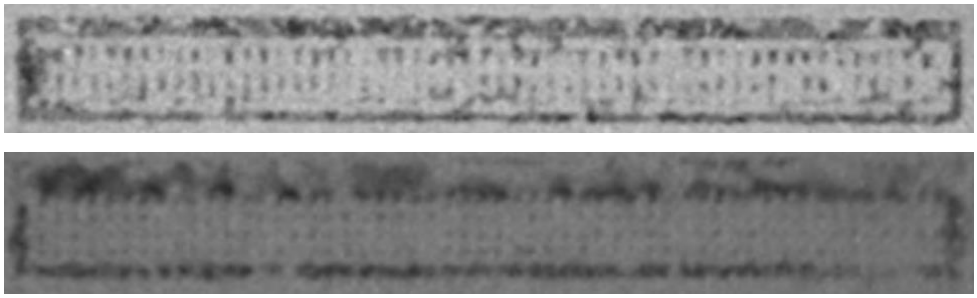

Figure 6-36 - Section of XCT slices through x-y plane at centre of "defect zone" for P1 (top) and P4 (bottom).

Comparing the images, P4 was deemed to have a more regular series of smaller voids. In both cases, there were 56 vertically aligned indications with approximately 170 µm separation, but for P4 the horizontal spacing was reduced from approximately 140 µm to approximately 112 µm. Again, there was a border around the "defect zone", where it is assumed the skin parameter setting selected did not result in adequate overlapping of the "defect" and bulk zones. The border is in the region of 200 µm at the front edge (bottom edge of zone in Figure 6-36) and 300 µm at the rear edge (top edge of zone in Figure 6-36).

P4 was assessed by LU across and along the defect zone and the results were validated against the XCT image shown above using the measurement tool in ImageJ, but without using the thresholding techniques employed previously.

6.3.5.2 *Assessment of LU of P4 - scanning line 1 – across "defect zone"*

The B-scan across the "defect zone" along scanning path 3 is shown in Figure 6-37.

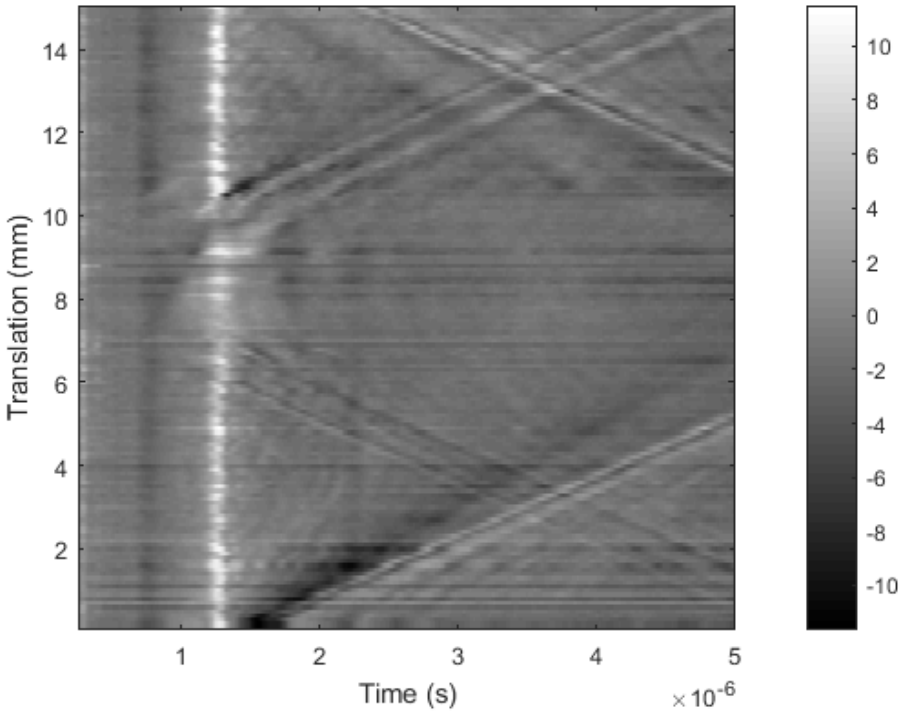

Figure 6-37 - B-scan of P4 along scanning line 1.

Eight feature groups were identified and are overlaid in the duplicate B-scans in Figure 6-38 and Figure 6-39.

- The angled lines indicating the waves reflected off the start and end walls were overlaid in red. Four horizontal bands of significant signal drop out were indicated in dark blue.
- Vertical indications show the arrival of waves which have not interacted with any "defects". The direct longitudinal wave (lilac dashed) and direct Rayleigh wave (purple dashed) arrived at 0.7 μs and 1.2 μs respectively, signifying a generation-detection laser spacing of 3.7 mm, at maximum detection spot focus.
- The longitudinal wave reflecting off the base of the sample returned at 3.5 μs with the arrival of the reflected wave from one of the side walls at 2.2 μs suggesting that the test piece was not scanned centrally.

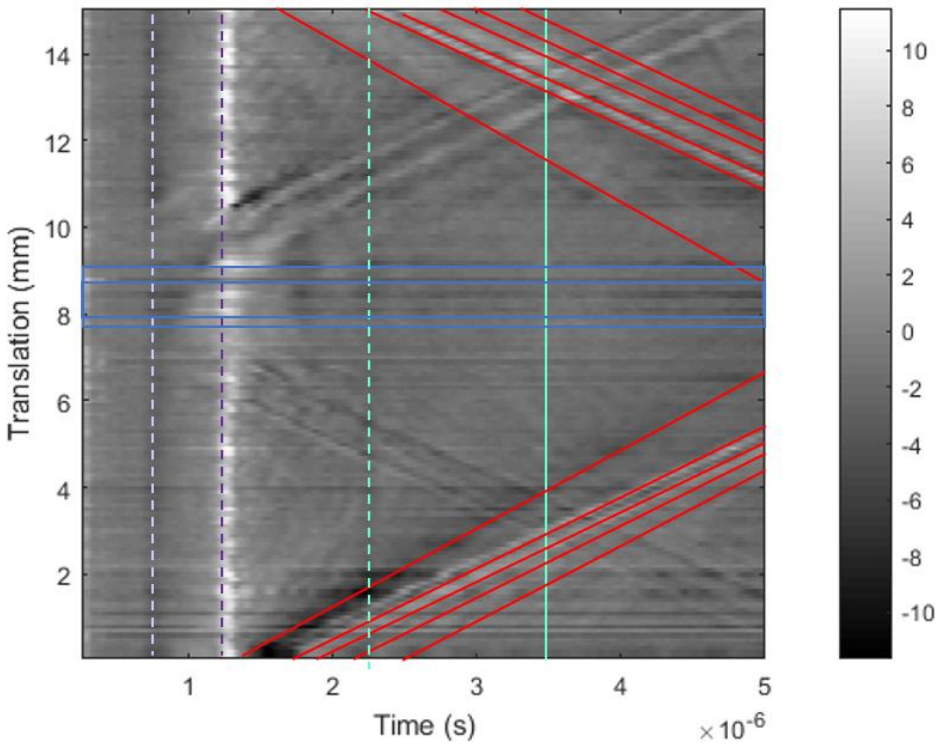

Figure 6-38 - B-scan of P4 along scanning line 1 overlaid with direct, reflected and mode converted waves from the base, side-walls and end walls.

Identified indications of material discontinuities are overlaid on Figure 6-39.

- Two orange parabolas indicating diffracted direct longitudinal waves were found to peak at 7.0 mm and 9.5 mm.
- Seven blue parabolas with apexes clustered between 6.9 mm and 9.6 mm were also found.

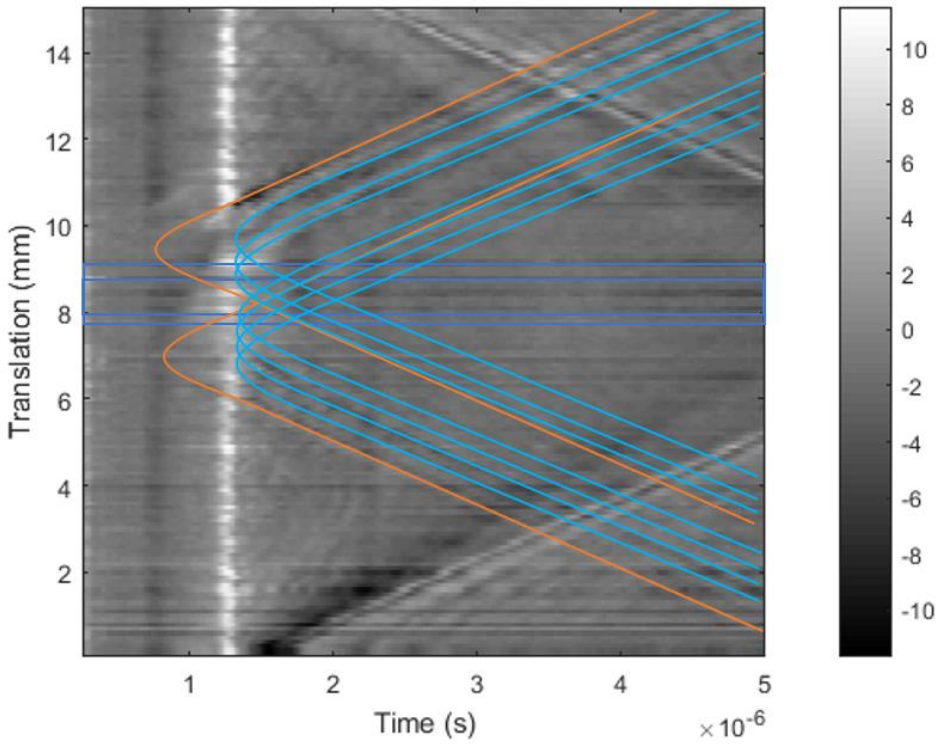

Figure 6-39 - B-scan of P4 along scanning line 1 overlaid with indications of material discontinuities and "defect zone".

The spacing of the two orange parabolas was not found to correlate with the known location of the "defect zone", measured from the XCT slice image although four of the blue parabolas did correlate with the inner and outer edges of the trough surrounding the "defect zone".

Unlike for test piece P1, there are no LU indications of material discontinuities within the "defect zone" itself. In this case, correlation with the XCT data through ImageJ could not be carried out as the greyscale contrast was inadequate. Analysis of the raw XCT scan did not reveal any obvious porosity in these areas, but did reveal five small indications within the same region, which are deemed to have been beyond the limit of detection of the LU system. The poor resolution achieved with XCT is insufficient to allow sizing of these indications.

The three blue parabolas at 6.9 mm, 7.3 mm, and 9.6 mm translation could not be correlated with the XCT data.

6.3.5.3 *Assessment of LU of P4 - scanning line 2 – along "defect zone"*

Scanning along the "defect zone" along scanning path 2 yielded the B-scan shown in Figure 6-40, for reference.

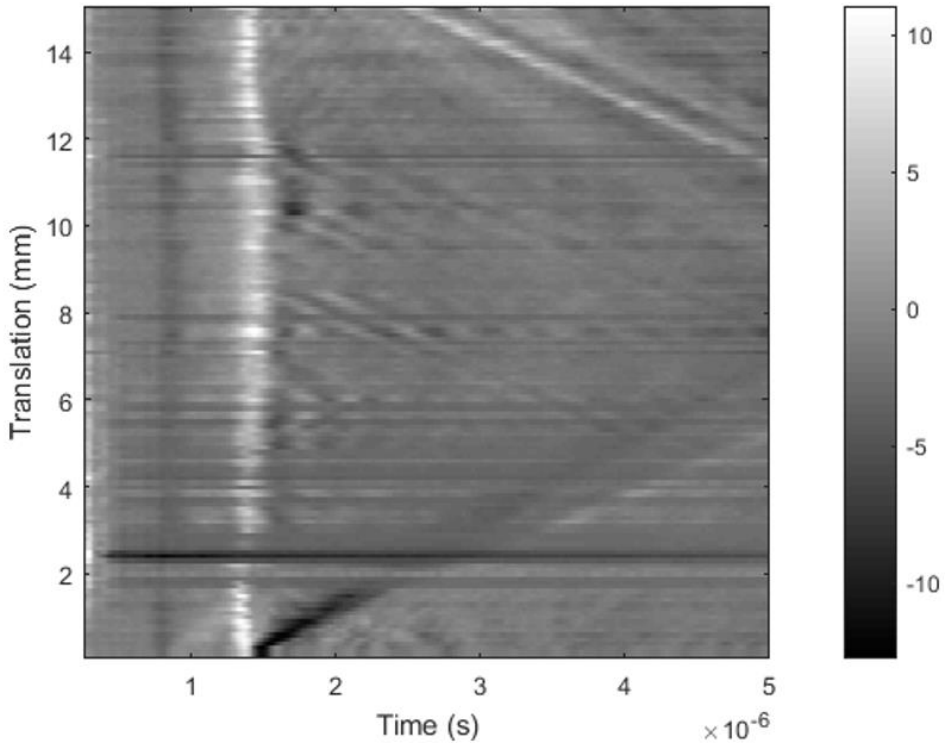

Figure 6-40 - B-scan of P4 along scanning line 2.

Seven feature types were identified and are split across two duplicate B-scans, for clarity. The first set are shown in Figure 6-41, including:

- Arrivals of reflected waves from start and end walls (red), direct longitudinal wave at 0.8 μs (lilac dashed), direct Rayleigh wave at 1.3 μs (purple dashed) and the reflected longitudinal wave off the base of the test piece at 3.6 μs (green).
- Two horizontal bands of signal drop out at 2.4 mm and 12.4 mm.
- An indication was identified at 1.6 μs, between 3 mm and 12 mm translation (dark green).

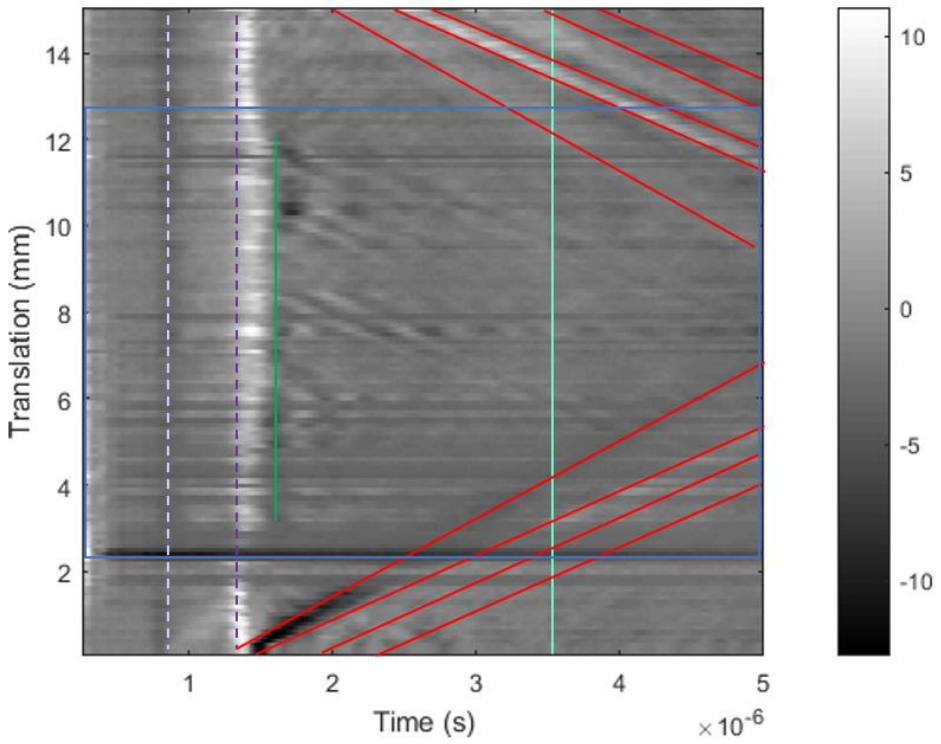

Figure 6-41 - B-scan of P4 along scanning line 2 overlaid with direct and reflected waves from the base, side-walls and end walls.

The second set of indications is shown on the duplicated B-scan in Figure 6-42, including:

- 20 blue parabolas indicating the diffracted Rayleigh wave were seen in the region between 2.0 mm and 13.6 mm. Between 3.8 mm and 12.2 mm, the apexes were spaced roughly every 500 μm.
- There was a region between translations of 2.3 mm and 3.7 mm where no indications were distinguishable.

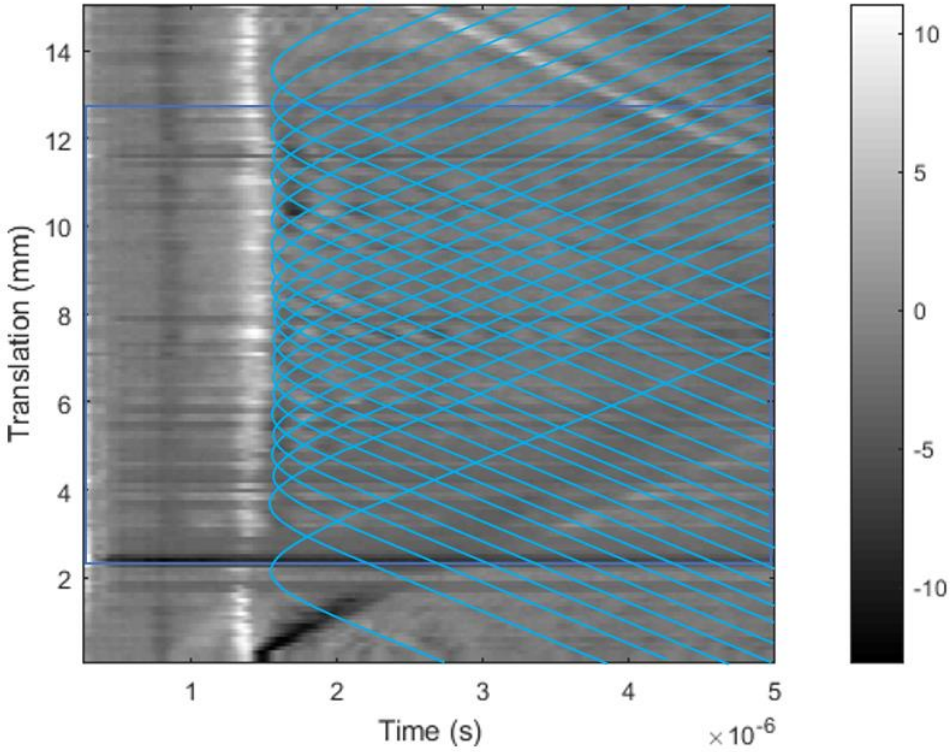

Figure 6-42 - Figure 34 - B-scan of P4 along scanning line 2 overlaid with indications of material discontinuities and "defect zone".

Again, as in section 6.3.5.2 the greyscale contrast of the XCT did not allow the desired thresholding analysis to be carried out using *ImageJ*. Instead the *ImageJ* measuring tool was used on the XCT image slices to determine the position of the "defect zone" and the spacings of any visible voids.

The "defect zone" was found from XCT to be positioned between 2.4 mm and 12.4 mm. A corresponding blue parabola is found at each translation.

56 bands of porosity were distinguished along the "defect zone" from analysis of the raw XCT slices, repeating about every 170 microns, however, only 20 blue parabolic indications were identified on the B-scan, with 500 μm spacing, a reduction from the previously identified spacing of 600 μm.

The region between translations of 2.2 mm and 3.7 mm where no indications are distinguishable was found using FVM to correlate to the surface undulation caused by the AM processing strategy around the "defect zone". This effect is more pronounced in this sample as only a single layer is processed with bulk parameters above the "defect zone" for P4. A height map of the measurements taken by FVM is shown in Figure 6-43.

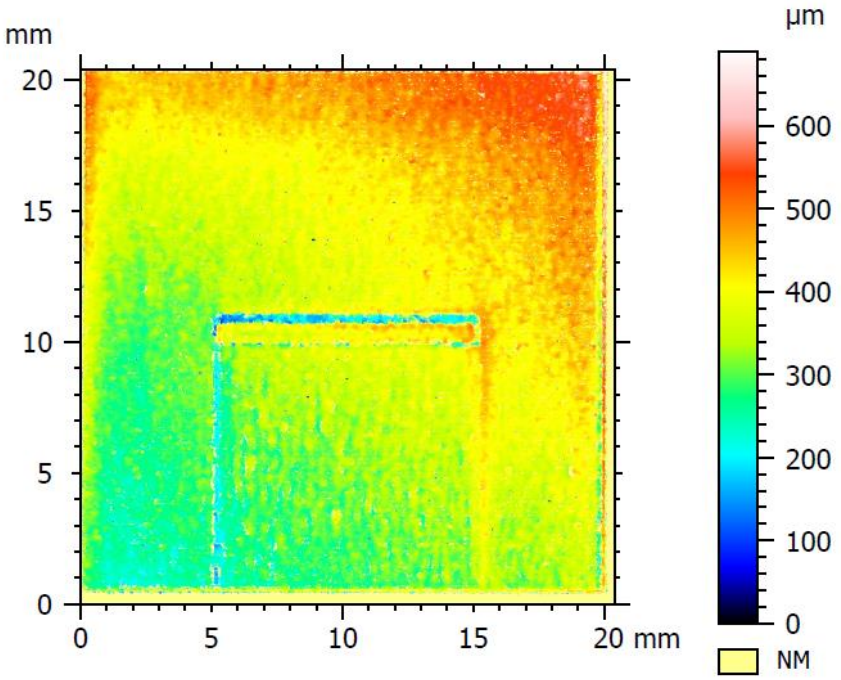

Figure 6-43 - FVM height map of P4.

6.3.6 Experiment 5 – Elongated pores with under-melting conditions

Test piece P5 was also built with an increase in hatch spacing to 180 µm in the "defect zone", but also had an increased AM scan speed of 1000 mm/s (as did test piece P2). This combination was expected to yield the test piece with the highest relative level of porosity in the "defect zone", compounding a lack of fusion between layers and between adjacent scanning tracks which were not expected to overlap. The "defect zone" was processed over three AM build layers, rather than five for the other test pieces; no AM notch was added to P5. During the manufacture of P5, cracks were unintentionally created when the build paused for a period of time, due to an oxygen level sensor being triggered within the AM build machine. The presence of these cracks on LU was also evaluated.

6.3.6.1 *P5 "defect zone" analysis*

An optical microscopy image taken to image through the "defect zone" is shown in Figure 6-44. Again, due to the reduction in depth of the "defect zone", the first increment removed for destructive analysis of 370 µm equates to just over nine build layers. Consequently, very little of the "defect zone" is visible.

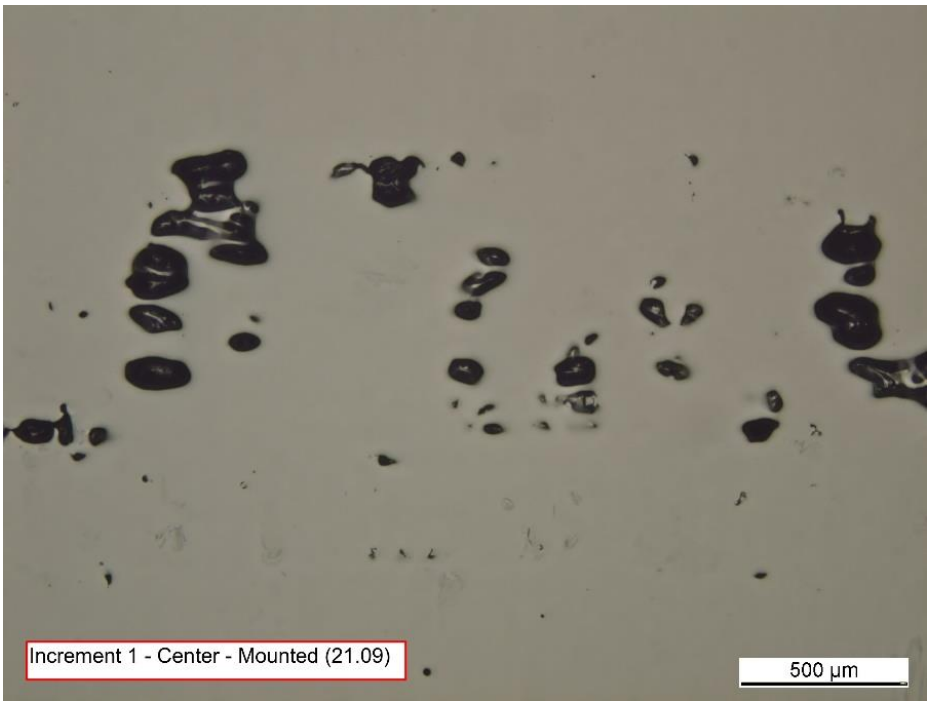

Figure 6-44 - Optical microscope image through "defect zone" in x-y plane for P5 at -370 µm.

Comparing the central slice of the "defect zone" using the thresholding technique in *ImageJ*, no voids are distinguishable in P5. Just like for P4, the greyscale contrast was inadequate to enable this analysis method to be utilised. Instead, the raw XCT images were used to allow comparison with the LU results to be made. Figure 6-45 shows the "defect zone" section of the XCT slice for P5, at -112 µm depth.

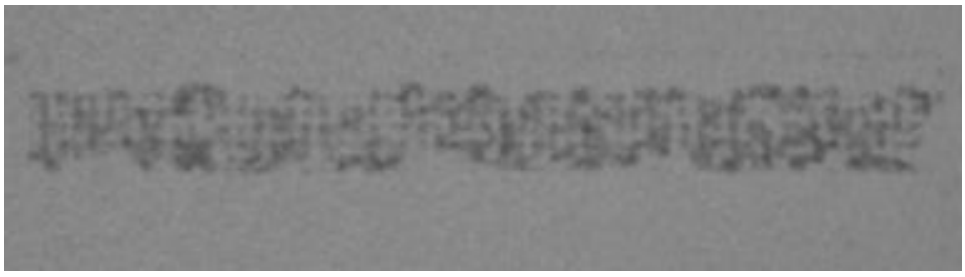

Figure 6-45 – Section of XCT slice through x-y plane for P5 at -112 µm.

As anticipated, there is a high level of porosity in this region. As with P4, 56 vertical bands of porosity are distinguishable from analysis of the raw XCT slices, repeating about every 170 µm; 6 horizontal bands

can also be identified with the same spacing, although lots of the pores appear interconnected.

6.3.6.2 *Assessment of LU of P5 - scanning line 1 – across "defect zone"*

LU scanning across the "defect zone" along scanning line 1 yields the raw B-scan shown in Figure 6-46, for reference.

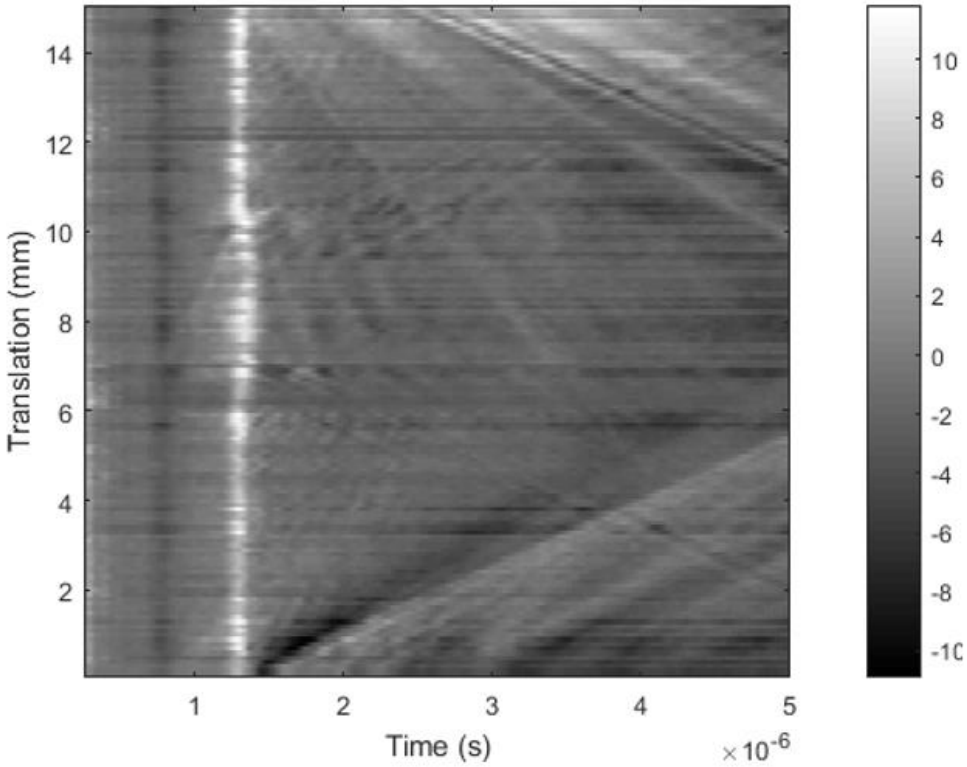

Figure 6-46 - B-scan of P5 along scanning line 1.

Seven feature types were identified and are overlaid on duplicate B-scans. The first is shown in Figure 6-47:

- Reflected waves from the start and end walls of the sample were overlaid in red with the direct longitudinal (lilac dashed) and direct Rayleigh (purple dashed) waves arriving at 0.8 μs and 1.3 μs respectively. The reflected longitudinal wave (green) returns at 3.3 μs.

- Four horizontal lines of LU signal drop out are highlighted in dark blue at 7.0, 8.2, 9.0 and 9.4 mm.

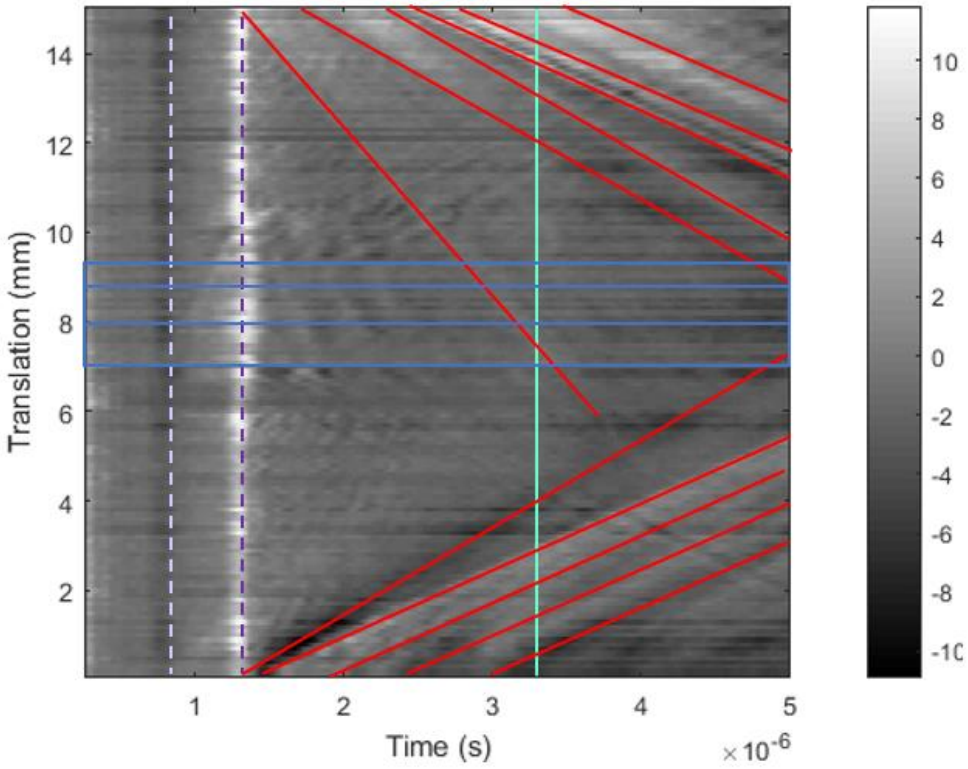

Figure 6-47 - B-scan of P5 along scanning line 1 overlaid with direct, reflected and mode converted waves from the base, side-walls and end walls.

The second batch of features indicating the presence of material discontinuities through the diffraction of the longitudinal (orange) and Rayleigh (blue) waves were overlaid in Figure 6-48.

- One full and one partial orange parabola indicating the return of diffracted longitudinal waves are overlaid, both peaking at 7.4 mm. The partial parabola did not take the same profile as the other parabolas, but was more similar to the triangular indications seen previously in 6.3.4 , which indicated a surface anomaly.
- Five blue diffracted Rayleigh wave parabolas were identified at 7.0, 8.2, 8.6, 9.0 and 9.4 mm.

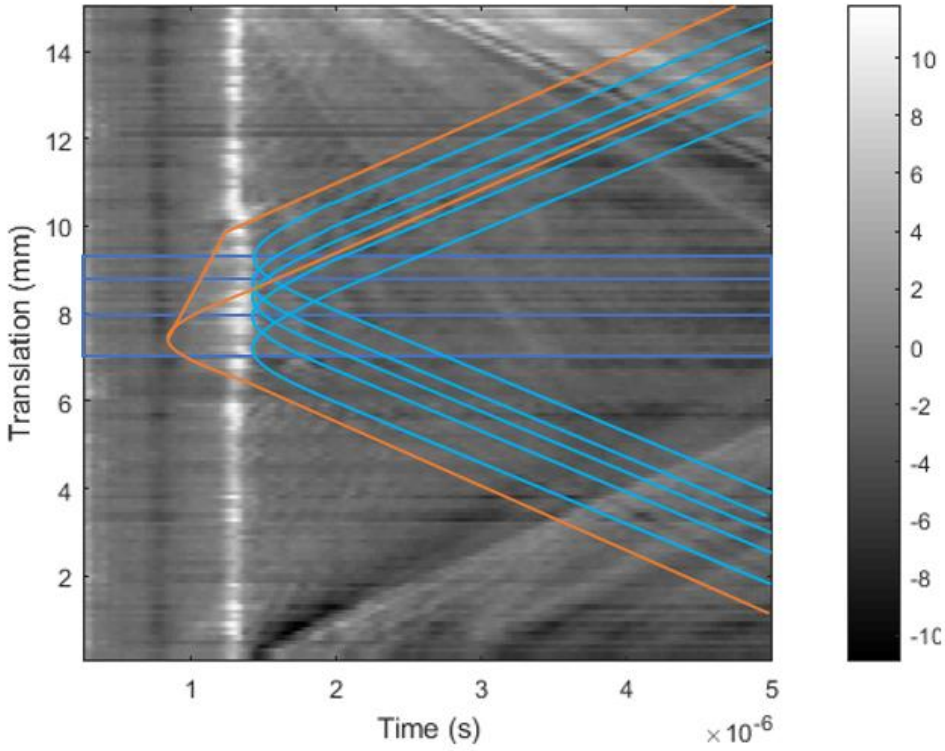

Figure 6-48 - B-scan of P5 along scanning line 1 overlaid with indications of material discontinuities and "defect zone".

Comparing the LU indications with the raw XCT image slices, the full orange parabola was not found to correlate with the position of a void, however this parabola and the partial parabola were in roughly the same position as surface undulations caused by the presence of the "defect zone", indicated on the FVM images.

Four of the five blue parabolas were visible at translation positions coinciding with the dark blue horizontal lines of signal drop out indicating the position of the "defect zone" and surrounding trough. Additionally, as was the case for P2, there was only a single blue parabola positioned within the "defect zone", even though 6 horizontal bands at 112 μm intervals were visible on the XCT slice. It was thought that the voids could have become interconnected, resulting in a single

enlarged void within the “defect zone”. The resolution of the XCT image was not sufficient to determine if this was the case.

6.3.6.3 *Assessment of LU of P5 - scanning line 2 – along “defect zone”*

Scanning along the “defect zone” reveals an interesting B-scan shown in Figure 6-49.

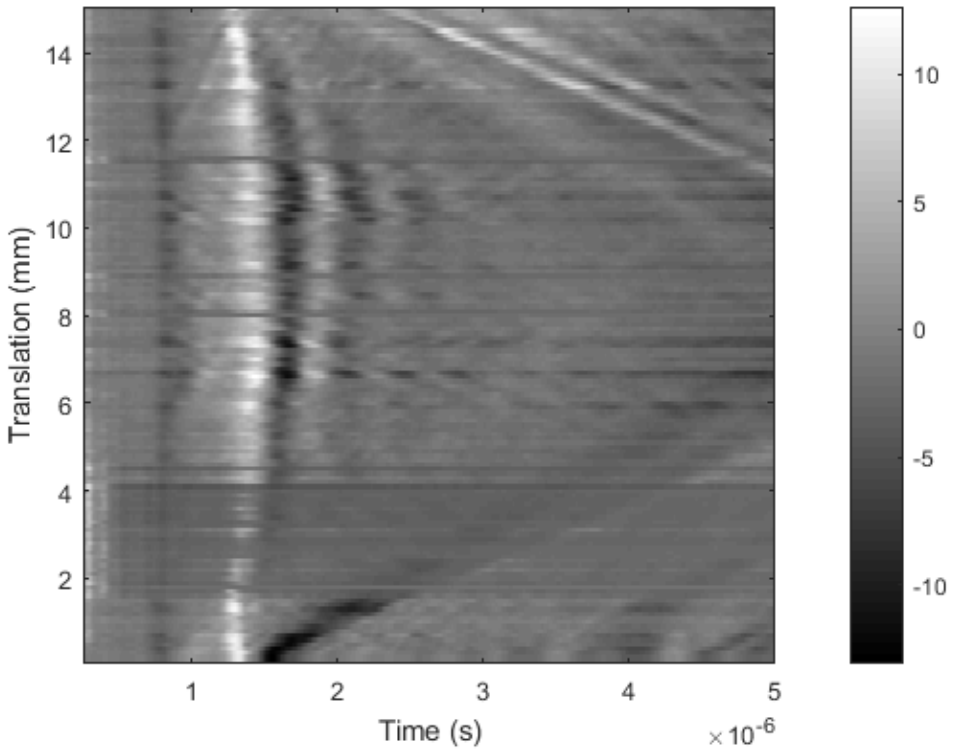

Figure 6-49 - B-scan of P5 along scanning line 2.

One set of features was overlaid in Figure 6-50:

- The waves reflected off the start and end walls were overlaid in red. The direct longitudinal (dashed lilac) wave and reflected longitudinal (green) wave arrive at 0.8 μs and 3.3 μs, as seen previously.
- Four horizontal lines of significant signal drop out were noted at 2.4, 2.6, 12.8 and 13. 2 mm.
- The direct Rayleigh wave highlighted with a dashed purple line first arrived at 1.3 μs, but this time increased as the test piece was translated to 8.0 mm, to a maximum of 1.5 μs. The arrival time then decreased again.
- Four additional wave arrivals with similarly curved appearance were also noted (pink).

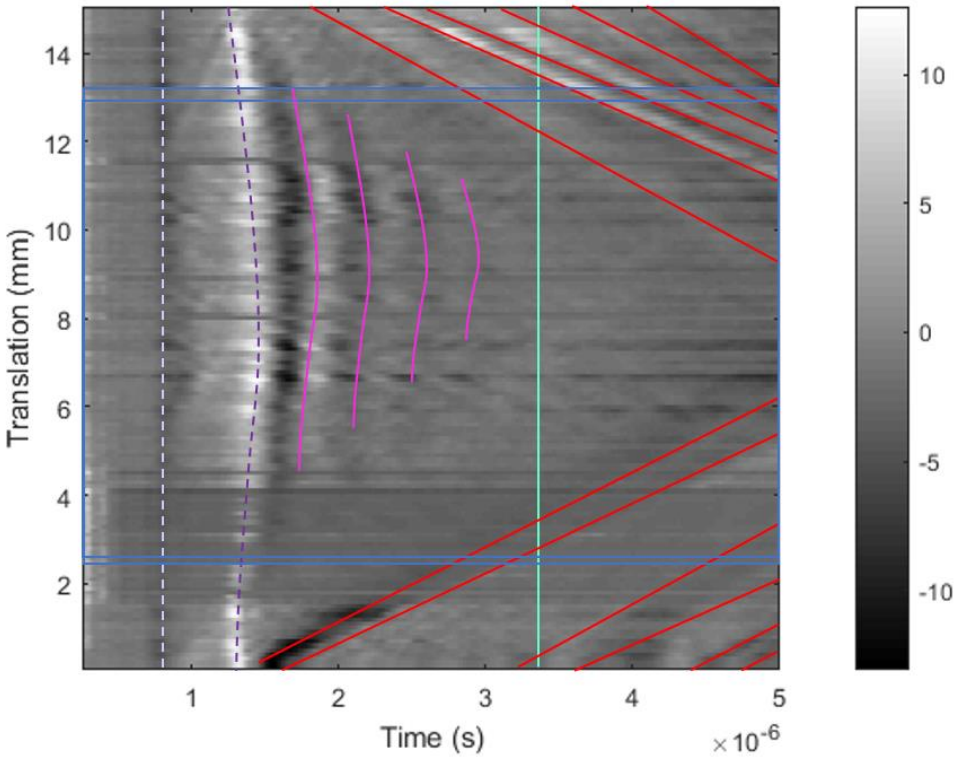

Figure 6-50 - B-scan of P5 along scanning line 2 overlaid with direct, reflected and mode converted waves from the base, side-walls and end walls.

All indications of material discontinuities caused by diffracted direct longitudinal waves (orange) or diffracted direct Rayleigh waves (blue) are highlighted on the duplicate B-scan in Figure 6-51.

- Two full orange parabolas were indicated at 2.4 and 2.6 mm. Six partial parabolas at 5.0, 7.0, 8.6, 10.0, 10.5 and 12.0 mm were evident.
- A total of 15 full blue parabolas between 2.4 and 13.2 mm were indicated, but no parabolas were visible between 4.0 and 7.6 mm where a region of signal drop out was seen.

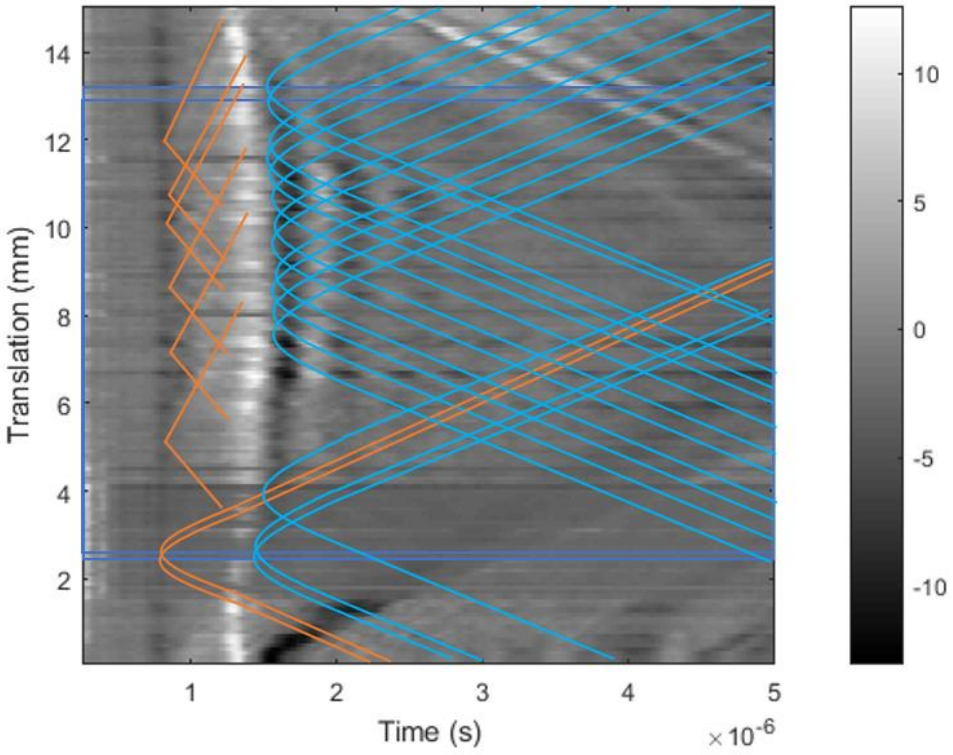

Figure 6-51 - B-scan of P5 along scanning line 2 overlaid with indications of material discontinuities and "defect zone".

Comparing the LU indications with the XCT image slices the four dark blue horizontal lines of significant signal drop out at 2.4, 2.6, 12.8 and 13. 2 mm were found to correspond to the position of inner and outer edges of the bands of porosity bounding the "defect zone". The signal

dropout between 1.8 mm and 4.1 mm has made it difficult to discern any indications in this region.

The arrival of the Rayleigh wave (dotted purple) was seen to have been delayed by varying degrees, as the test piece was translated across the region of the "defect zone". This delay and the four wave arrivals marked in pink were thought to have been caused by the resonance resulting from the generation of a Lamb wave between the test piece surface and the "defect zone" in the z-direction. Lamb waves, also known as plate waves, are usually generated in materials a few wavelengths thick and propagate parallel to the test piece surface. It was thought that the interconnected nature of the porosity within the "defect zone" was sufficient to make the material between the test piece surface and the "defect zone" behave as a thin plate.

The two full orange parabolas at 2.4 mm and 2.6 mm are aligned with the one of the inner and outer edges of the "defect zone", but not the other. The 6 partial orange parabolas overlaid between the arrival of the reflected longitudinal and direct Rayleigh waves have previously been indicative of surface undulation in this area, although FVM analysis did not provide any indications of these.

Of the 15 full blue parabolas, four were found to correspond to the inner and outer edges of the "defect zone". Eleven were identified within the region of the "defect zone", however the area of signal drop out possibly masked the additional indications expected after analysis of the XCT images. The closest spacing of the parabolas was every 500 μm translation, as was the case for P4.

It is not thought that the cracking which was induced during the build of P5 affected the LU scans presented. Although the largest crack initiated only 1.5 mm below the test piece top surface and propagated

down to 5.3 mm, it was not located within the vicinity of the LU scanning paths shown in Figure 6-52 below.

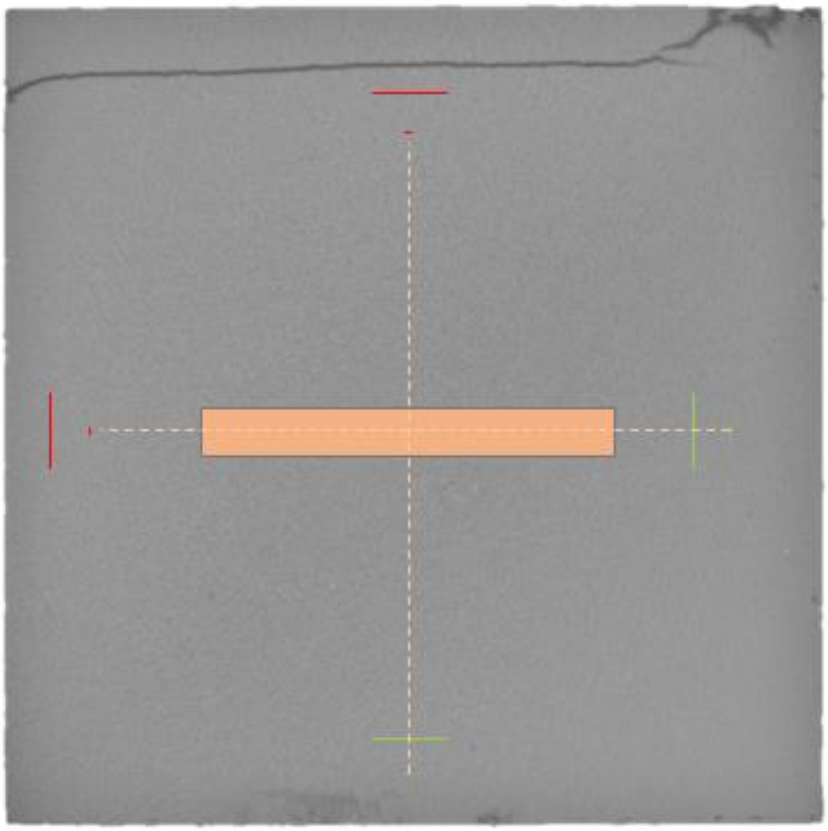

Figure 6-52 - XCT slice through x-y at -3.10 mm showing crack position.

6.3.7 Experiment 6 – Sidewall porosity

It was noted when analysing the XCT (x-y) image slices in this and previous studies that a band of porosity occurs on the right hand edge of the components built. After succeeding in Chapter 5 at scanning test piece S3 on the side wall, albeit with increased noise, P1 was also LU scanned on the left and right hand walls along scanning lines 3 and 4.

The resulting raw B-scan are shown in Figure 6-53 and Figure 6-54.

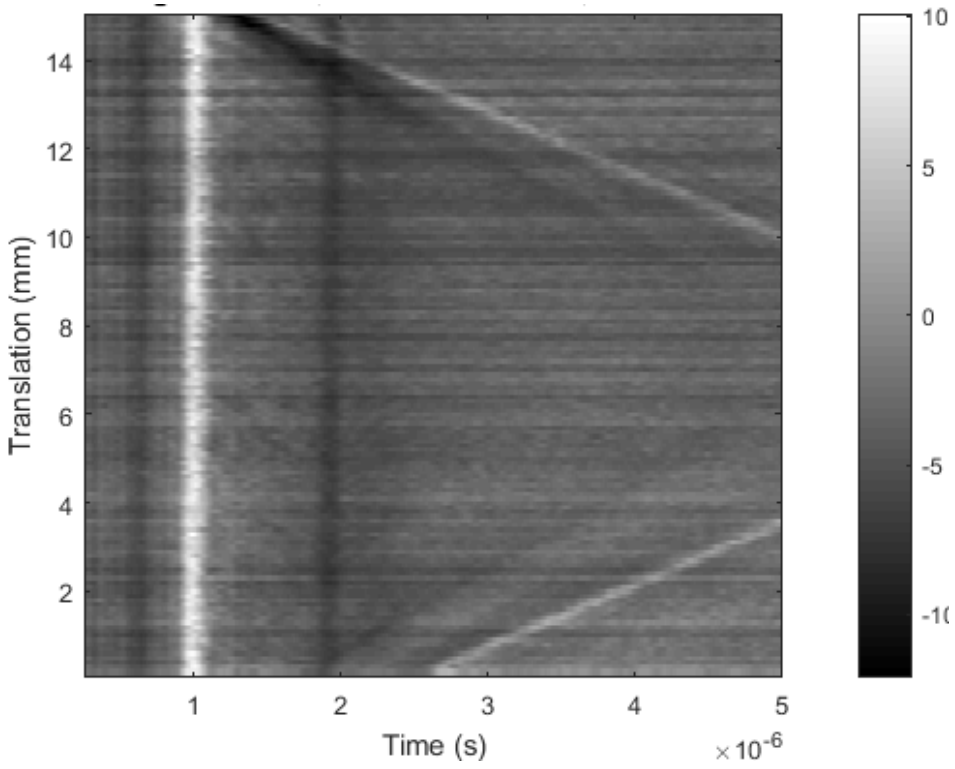

Figure 6-53 - B-scan of P1 on left-hand wall (along scanning line 3).

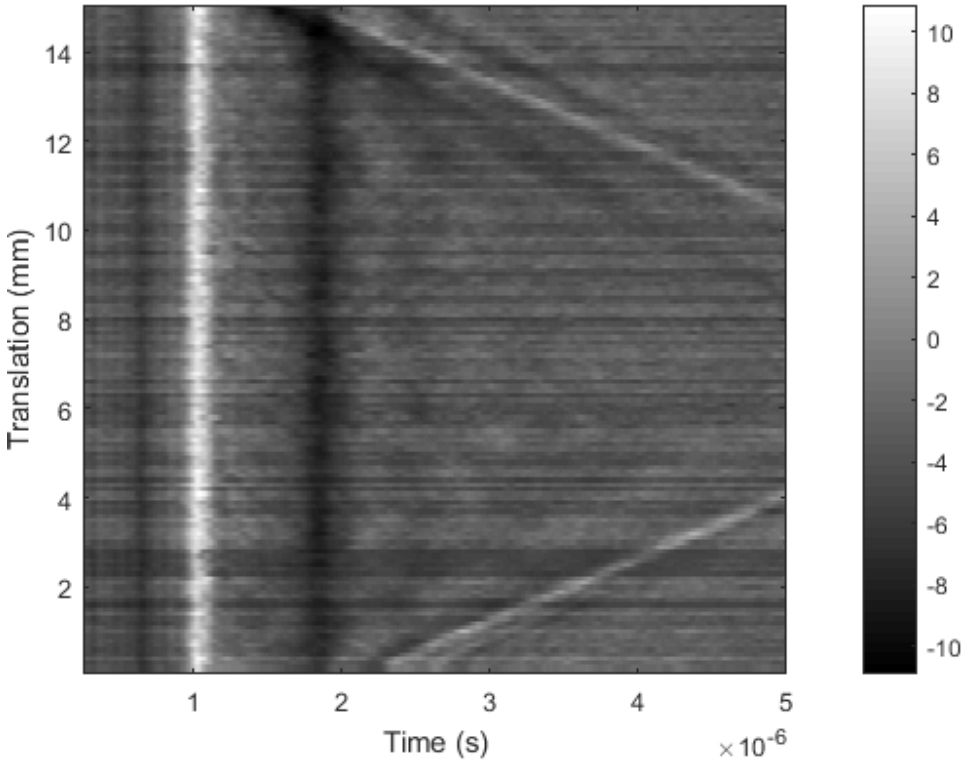

Figure 6-54 - B-scan of P1 on right-hand wall (along scanning line 4).

Comparing the two, the B-scan of the right hand wall (scanning line 4) in Figure 6-54 shows many more indications of diffracted Rayleigh waves; these were overlaid in Figure 6-55. No indications were identified for the left hand wall.

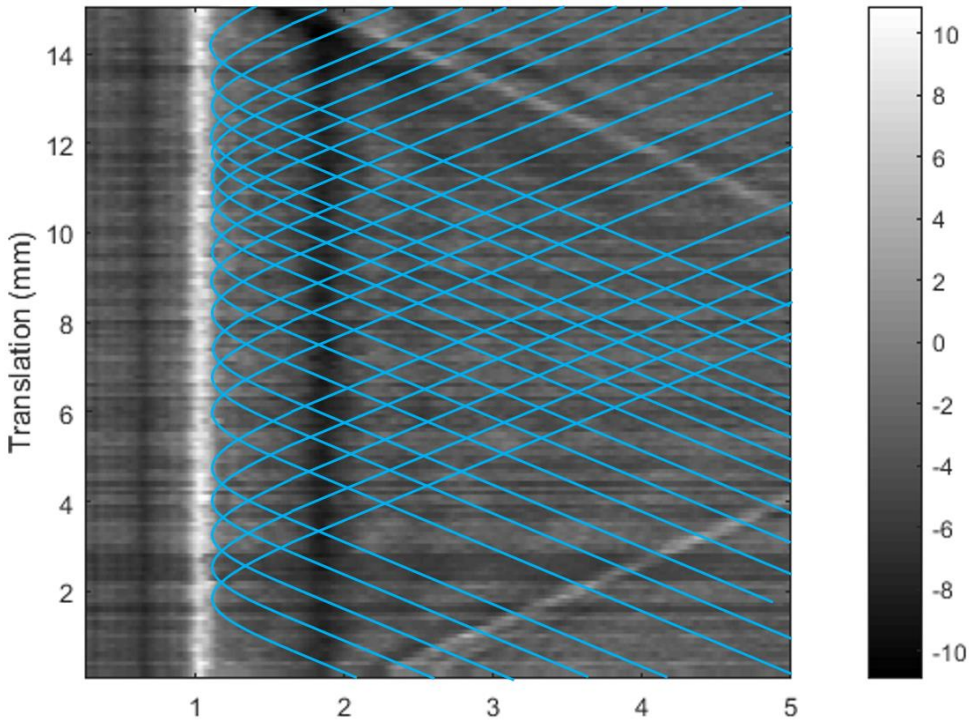

Figure 6-55 - B-scan of P1 of right-hand wall (along scanning line 4) overlaid with indications of material discontinuities.

Although the indications indicating porosity (blue parabolas) identified on Figure 6-55 were too dense for quantitative analysis when comparing to the XCT data, the porosity can be characterised from the B-scan images, albeit subjectively.

6.3.8 Experiment 7 - FVM analysis of effect of ablation during LU

To assess the effect of operating in the ablation regime during LU, P1 was scanned by FVM before and after processing and the results are presented here. The test piece was scanned using the *Alicona G5*, using a 20X objective. A vertical resolution of 100 nm was achieved using ring light illumination. The FVM image of the whole test piece, taken before LU is shown in Figure 6-56. The (2.5 *x* 2.5) mm area extracted for further analysis is highlighted.

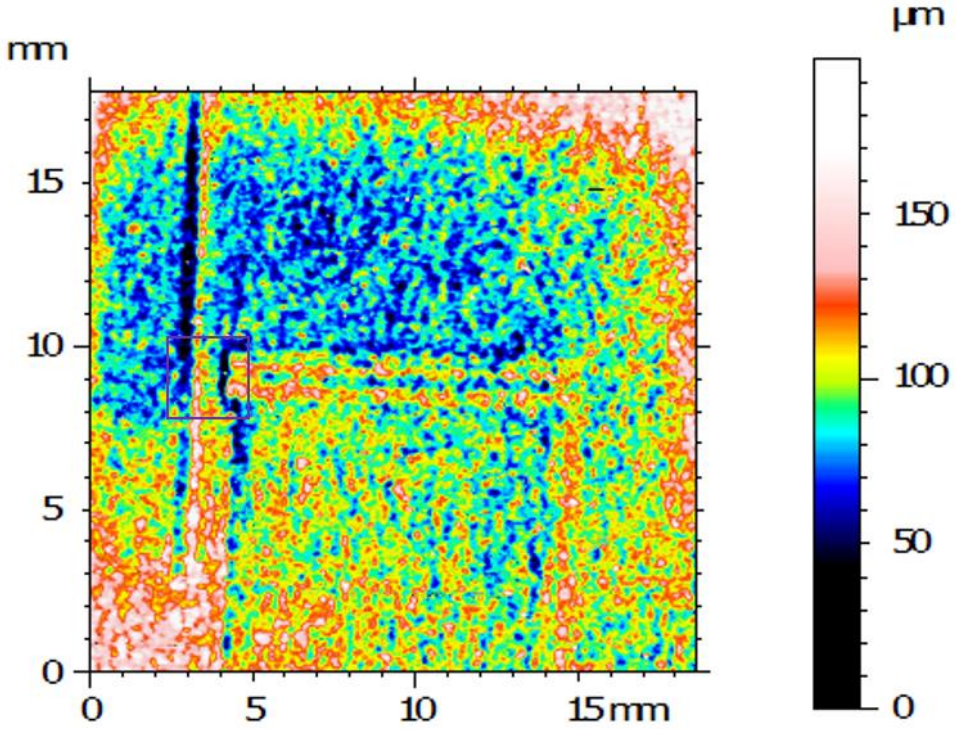

Figure 6-56 - FVM image of P1, before LU, showing location of area compared in mountains.

The extracted regions were exported into '*MountainsMap7*' and aligned within the XY co-ordinate system, shown in Figure 6-57. Some small scale changes have been noted, circled in white, which could have been dust particles blown away, or adhered particles removed by laser ablation. Either way, the physical changes made to the surface as a consequence of operation in the ablative laser regime are not deemed sufficient to prevent inspection during AM build, between layers.

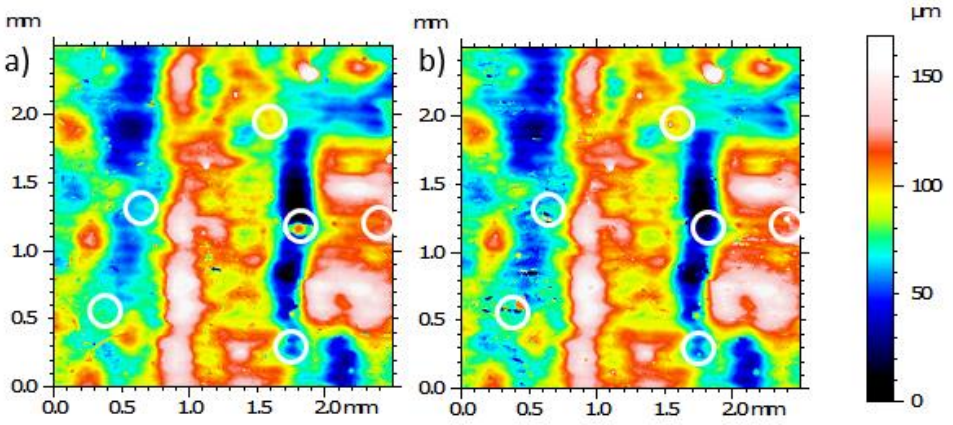

Figure 6-57 – '*MountainsMap7*' comparison of extracted regions of FVM images of PI, a) before LU and b) after LU. Differences are circled (white).

6.4 Discussion

In sample P1, a high amount of porosity was generated in a "defect zone", by manipulation of the AM build parameters and this was imaged using XCT and then destructively. Isolated elongated pores and interconnected elongated pores were generated. The "defect zone" outer edge is almost a continuous pore, likely a result of the skin parameters selected for the build not overlapping where the "defect zone" and bulk material intersected. Test piece P1 was subject to LU evaluation which was then validated using XCT, post-processed using *ImageJ*. FVM imaging was also employed.

P1 was scanned across the "defect zone", first following scanning path 1 and secondly along the length of the "defect zone", along scanning path 2. B-scans were generated in each case and groups of indications overlaid. The arriving waves returning from the sample end walls, the reflected longitudinal wave and the arrival of the direct longitudinal and Rayleigh waves were marked although these waves do not provide any information regarding any possible porosity and would appear if scanning a fully dense sample. Areas of signal drop out in the B-scans were found to correlate with surface undulations found around the perimeter of the "defect zone", on the sample surface, using XCT and FVM.

When scanning across the "defect zone", the edges of the zone were found to be indicated on the B-scan by diffracted direct longitudinal (orange) and diffracted direct Rayleigh (blue) waves. The apex of the parabolas was found to align at LU translation positions which corresponded with the location of the "defect zone" ascertained from analysis of the XCT, using *ImageJ*. A lone blue LU parabola was found to correlate with the position of two naturally occurring voids with

diameters of 108 μm and 180 μm, 76 μm and 228 μm below the surface respectively, found by XCT.

When scanning along the "defect zone", areas of LU signal drop out were again correlated with the position of the "defect zone", using *ImageJ*. LU scanning along the "defect zone" which was known from the XCT to have a number of closely located "defects" spaced at 170 μm intervals resulted in many overlapping indications of diffracted direct Rayleigh waves (blue). Although the density of the indications made it more difficult to interpret the B-scan, it was still clear from analysis of the raw B-scan that a high level of porosity was present in the region. A LU spatial resolution of 600 μm was indicated. The apex of the three identified diffracted direct longitudinal waves (orange) were found to correlate with the position of surface undulation caused during AM manufacture by the presence of the notch.

Test piece P2 was manufactured using an increased AM scan speed within the "defect zone". It was anticipated that there would be insufficient energy penetration for full melting of the layer and elongated voids would result between subsequent layers.

Destructive analysis revealed that a series of elongated and interconnected voids had been generated. The voids were observed to occur along four main horizontal lines bounding the "defect zone" and the 600 μm trough surrounding the "defect zone". It is thought that these bands of porosity were formed due to a lack of overlap of the AM scanning zones or because of an incorrect selection of the skin parameters.

Prior to destructive analysis, the test piece was subjected to LU evaluation which was then validated using an XCT, post-processed using *ImageJ*; FVM analysis was also carried out.

After scanning across the "defect zone", translating scanning line 1, eight feature types were identified on the resulting B-scan. The presence of two waves returning at 2.2 μs and 4.4 μs suggested that the test piece was not scanned centrally but offset by 3 mm – this was taken into account when assessing the XCT image using *ImageJ*. Four horizontal bands of signal drop out were observed on the B-scan at translation positions of 7.0, 7.6, 8.2 and 8.8 mm, matching the spacing of the four bands of porosity. Four orange and four blue parabolas were found to have approximately the same spacing. One of the remaining four blue parabolas were found using ImageJ to correlate with one void, 141 μm diameter at 40 μm below the top surface within the "defect zone". The other three blue parabolas indicated the presence of three unintended voids. These were a 185 μm diameter void, 300 μm below the top surface and two voids with 240 μm and 93 μm in diameters, 40 μm below the test piece top surface. Additionally, *ImageJ* analysis of the XCT images revealed the presence of two voids 43 μm in diameter at a z-distance of 300 μm, within the anticipated LU scanning region. No indications were identified on the B-scan at their corresponding translation distances and these voids have been deemed to be outside the window of detection for the LU system.

When scanning along the "defect zone", several areas of LU signal drop out were identified, with four of the horizontal indications correlating to the position of the "defect zone" and surrounding trough, found using *ImageJ*. Both blue and orange parabolic indications peaking at the same translation locations were identified. A partial orange parabola was found, using FVM, to correspond with a surface undulation caused when manufacturing the AM notch, between 13 mm and 14 mm. A lone blue parabola at 14.2 mm translation was also found correlate with the position of the deep notch anomaly on the surface. Eleven blue parabolas peaking within the "defect zone" were found to

correlate with voids visible in the *ImageJ* analysis. The 11 voids varied in diameter from 46 µm to 307 µm. The z-distance varied from 37 µm to 411 µm and all voids identified were within a 687 µm central region.

For P3, a lower AM scan speed was selected in the "defect zone" to replicate the conditions expected for over-melting and therefore promote conduction mode or keyhole mode pores. The destructive analysis carried out, revealed a line of porosity at a position corresponding to the upper, outer edge of the zone, but showed very little porosity within it. Analysis of the XCT reconstruction in the "defect zone" revealed a second band of porosity at the other edge.

The test piece was scanned across and then along the "defect zone". Seven feature types were identified on the first B-scan, including two horizontal bands of signal drop out which correlated with the position of the "defect zone". Two orange and two blue parabolas were also highlighted in this position. A 134 µm diameter void at 224 µm z-distance, 625 µm from the scanning line and a 155 µm diameter void at 224 µm z-distance, directly under the LU scanning path were correlated to the position of two blue parabolas. Using FVM, the head of a triangular orange marking was matched to the position of a depression on the test piece top surface. All LU indications were attributed to material discontinuities or surface undulations, no other features were found during XCT analysis of the LU scanning region using *ImageJ*.

The test piece was also scanned along the length of the "defect zone" translating scanning line 2. Two partial orange parabolas were identified between 12.8 and 14.9 mm translation, but no voids were visible in the region on the *ImageJ* analysis. Comparison with FVM revealed that the indications are in region of surface undulations, caused by AM processing of notch. There were 21 overlapping blue

parabolas overlaid on the LU B-scan which were found to have been caused by the series of interconnected voids in this translation range. This again suggests a minimum LU spatial resolution of 600 µm. The same region of porosity was indicated by the arrival of reflected longitudinal waves reflecting back at 1.6 µs, occurring between 2.2 mm and 13.2 mm translation.

Test piece P4 was manufactured with an increased in hatch spacing of 180 µm in the "defect zone" to generate elongated pores between AM scanning tracks. Only a single AM layer was processed with bulk material parameters over the "defect zone" and no notch was added by AM. The resulting test piece was assessed by LU, XCT, FVM and destructive testing.

LU scanning across the "defect zone" translating scanning path 1, four of the seven blue parabolas identified correlated with the inner and outer edges of the trough surrounding the "defect zone" measured from the XCT image. The poor resolution achieved with XCT was insufficient to allow validation of the three blue parabolas indicated at 6.9 mm, 7.3 mm, and 9.6 mm translation.

Scanning across the "defect zone" along scanning path 2 yielded horizontal lines of signal drop out and blue parabolas at the positions correlating to the ends of the "defect zone" at 2.4 mm and 12.4 mm translation. 20 blue parabolic indications were identified with 500 µm spacing, indicating some of the 56 voids found in this region by XCT. A region of signal drop out was found using FVM to correlate to the surface undulation caused by the AM processing strategy around the "defect zone".

Test piece P5 was also built with an increase in hatch spacing to 180 µm in the "defect zone", but also had an increased AM scan speed of

1000 mm/s. This yielded a test piece with the highest relative level of porosity. Again, the poor resolution achieved with XCT prevented analysis of the XCT image slices using the thresholding technique in *ImageJ*.

When LU scanning along scanning path 1, one full and one partial orange parabola indicating the arrival of diffracted longitudinal waves were identified. These were found to be in roughly the same position as surface undulations caused by the presence of the "defect zone", indicated on the FVM images. Five full blue parabolas indicating the arrival of diffracted Rayleigh waves were identified, four of which were found to correlate with the "defect zone" and surrounding trough, also highlighted by lines of signal drop out. Additionally, a single blue parabola positioned within the "defect zone" was identified, even though 6 horizontal bands at 112 μm intervals were visible on the XCT slice.

Scanning across the "defect zone", four dark blue horizontal lines of significant signal drop out were found to correspond to the position of inner and outer edges of the bands of porosity bounding the "defect zone". The arrival of the Rayleigh wave (dotted purple) was seen to have been delayed and four additional wave arrivals marked in green were thought to have been caused by resonance resulting from the generation of a Lamb wave between the test piece surface and the "defect zone", in the z-direction. The two full orange parabolas at 2.4 mm and 2.6 mm are aligned with the one of the inner and outer edges of the "defect zone", but not the other. Four blue parabolas were found to correspond to the inner and outer edges of the "defect zone". Another 11 were identified within the region of the "defect zone", however an area of signal drop out possibly masked some additional indications. The closest spacing of the parabolas was every 500 μm

translation, as was the case for P4, so the spatial resolution of the LU system was revised to this figure. The cracking which was induced during the build of P5 did not influence the LU scans presented.

6.5 Summary

This study has shown that it is possible to create test pieces with sub-surface zones of porosity, through manipulation of AM build parameters which can then be used to assess inspection techniques.

Inspection of the test pieces by laser ultrasound and XCT has enabled an increased understanding of the window for detection of material discontinuities, by LU on AM surfaces. A plot showing the void distances perpendicular from the LU scanning path and z-distance is shown in Figure 6-58; the markers are scaled with void diameter.

LU indications of a range of voids from 46 μm to 307 μm diameter at z-distances from 38 μm to 411 μm have been successfully correlated with voids identified on the XCT images, along a 1037 μm LU scanning channel. The two voids "missed" by LU were both 43 μm diameter, at 300 μm z-distance, directly under the LU scanning path. Given the XCT voxel size of 38, it is reasonable to assume that all measurements have a possible error of ± 76 μm, so it is possible a false indication was given. Generally, these voids have been indicated by diffracted Rayleigh waves, overlaid as blue parabolas on the B-scans.

A level of naturally occurring porosity was noted from the XCT images, particularly at the right hand edge of the test pieces. This is suggestive of an inherent issue with the SLM50 AM build machine or the associated build software package. LU scanning of the AM sidewalls qualitatively indicated the presence of this porosity.

The zonal AM scan strategy utilised by the build software and the skin parameters selected when processing the layers with "defect zone" or a notch present resulted in surface undulations which were generally picked up by LU, causing diffraction of the direct longitudinal wave and highlighted on the B-scans as an orange full or partial parabola.

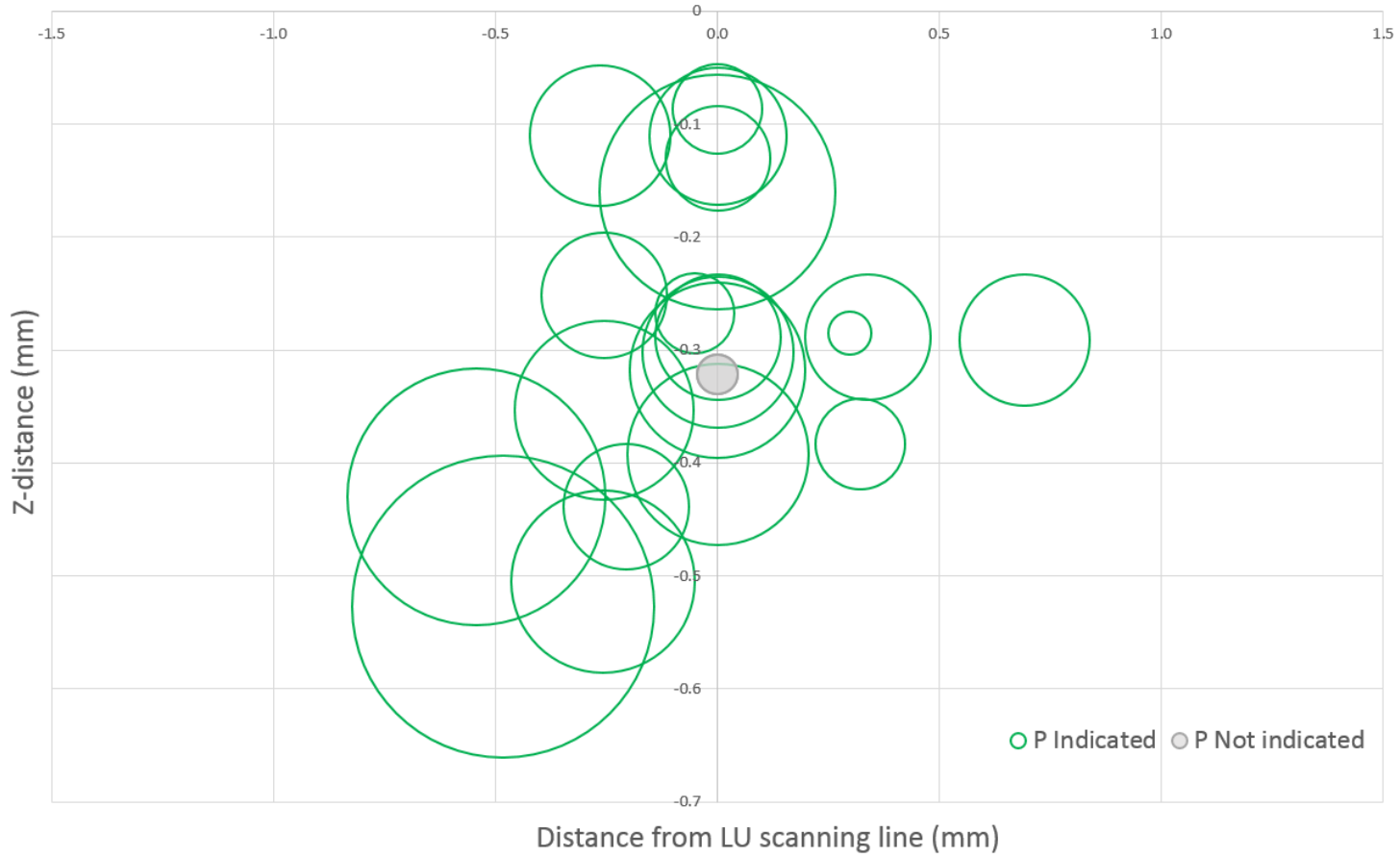

Figure 6-58 - Graph showing distance from LU scanning line vs. void centre z-distance, with markers scaled by void diameter

Chapter 7 - Modelling laser ultrasound

7.1 Introduction

An alternative method for establishing a window of detection for the laser ultrasound (LU) system is to use finite element analysis (FEA) to solve the physical governing equations. An overview of projects carried out, seeking to model ultrasound, is given in the introduction of Pantano and Cerniglia's paper, "Simulation of laser generated ultrasound with application to "defect" detection" [131].

As discussed in chapters 5 and 6, it has proven difficult to generate AM samples with isolated porosity, in known positions. For this reason, an alternative approach through modelling of LU is suggested, in order to rapidly establish the LU detection window for different types of "defects" in different materials, without the need for manufacture of many AM samples. The work presented here sought to establish the feasibility of this approach, following a methodology set out by Edwards et al. [125].

A 2D model was first created using 'ABAQUS' and a series of cases run translating the generation and detection laser across the sample surface, replicating a LU scan carried out in Chapter 4. The data was then used to generate a B-scan in 'Matlab' and the physical and modelled B-scans compared. Once validated, the model was used to begin modelling "defects" with varying sizes, at differing z-distances.

The term z-distance has been used throughout this thesis to mean the minimum distance of a void from the top edge of a sample, using the build co-ordinates of the AM machine. As a 2D model has been created in 'ABAQUS', please note the change in co-ordinate system orientation in the modelling, as shown in Figure 7-1.

7.2 Modelling - Methodology

The following section describes the procedure followed and options selected in modelling a 2D cross section of sample M4, using 'ABAQUS'.

7.2.1 Geometry

A 2D slice down the centre of M4, first discussed in Chapter 4, was replicated using the 'Section Sketch' tool within the 'Feature' menu. A 2D case was deemed sufficient in this case, as interrogation of the waves reflected from the side walls in the LU B-scans had not indicated the presence of any "defects". Additionally, only solving a 2D case reduces the associated computational cost and running time.

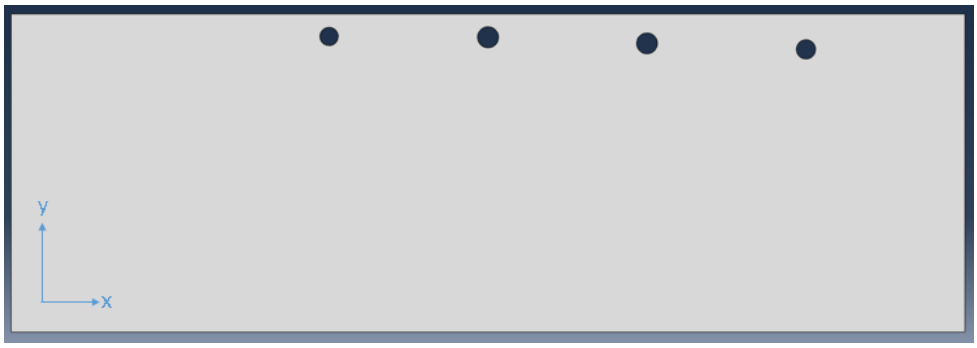

Figure 7-1 – 'Section Sketch' of cross section through M4 with four holes (left to right: 0.581, 0.669, 0.662 and 0.638 mm diameters at the following distances from the top surface: 0.417, 0.398, 0.593 and 0.807 mm respectively.

7.2.2 Mesh

Laser generated ultrasound has frequencies in the MHz range, which requires small time steps between the solutions. These high frequencies have very short wavelengths. Accordingly, the size of the finite elements must be at least 1/20 of the shortest wavelength for a reasonable spatial resolution of the propagating waves [132]. The slowest ultrasonic wave speed is the Rayleigh wave at 3035 ms^{-1} and

the maximum possible frequency is equal to 1 x 10^9 Hz. Consequently, a maximum cell size of 1.5175 x 10^{-7} m is specified.

A horizontal, rectangular band encompassing all four holes was created using the feature tool and a box was created around each hole to improve the mesh quality and reduce solution gradients between cells. At the intersections, diagonal lines were drawn, crossing the hole, shown in yellow in Figure 7-2. A structured mesh was selected, resulting in the mesh pattern. A total of 1,227,321 tetrahedral elements were created.

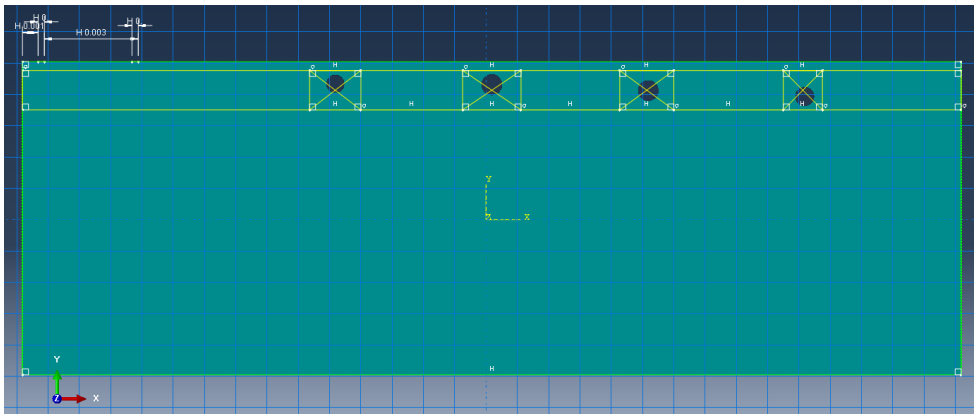

Figure 7-2 – Screen shot from 'ABAQUS' showing meshing regions.

7.2.3 Solver pre-processing

The following cell condition material properties for Ti6Al4V were used: density of 4430 kg/m^3, Young's modulus of 113.8 GPa and a Poisson's ratio of 0.342 [133]. No thermal effects were modelled and isotropic material behaviour was assumed in this case.

7.2.4 Boundary conditions

Two point constraints in the 'ABAQUS' y-direction were added, in the bottom left and right corners, to stop the component translating through space when the load was applied to the top edge. This

represented the physical constraint of the stage upon which the test pieces were mounted for LU scanning.

7.2.5 Load

A simplified model, neglecting the optical penetration and thermal diffusion effects induced by the laser has been created [134]. Excitation in the ablation regime can be modelled using a vertical force [92]. As such, an Achenbach pressure function [135] was applied as a load on the top edge along a 0.2 mm length, using an amplitude file. The file comprises a table of 501 time periods at 1 x 10^{-8} second intervals and the starting location is shown by the orange arrows in Figure 7-3.

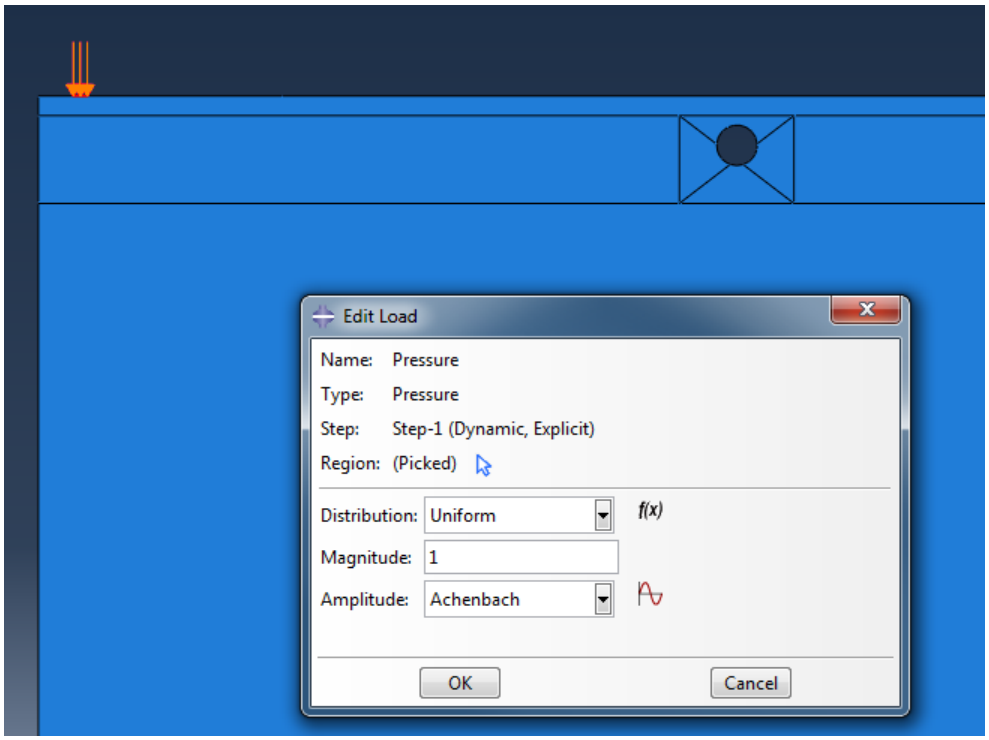

Figure 7-3 - Screen shot from 'ABAQUS' indicating location of pressure load applied (orange arrows).

7.2.6 Output request

A detection area was set up along a 0.2 mm length on the top surface, at a fixed, 3 mm distance from load, as shown in Figure 7-4. This represents the physical detection-generation laser separation aimed for in the experiments, shown in chapters 4-6. In order to keep the

resulting output database file as small as possible and to minimise the run time for the model processing, this detection area must be selected before a case is run. Displacement in the y-direction at all edge nodes within this detection zone were recorded at every time-step during processing.

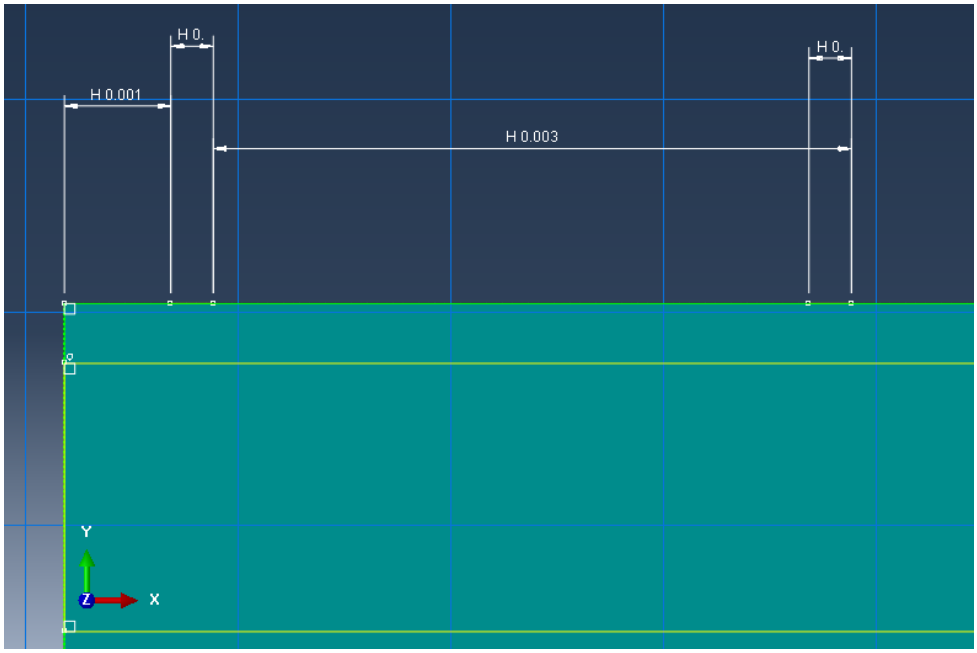

Figure 7-4 - Screen shot from 'ABAQUS' indicating the initial location of pressure load area and detection area, at a fixed distance.

Each model took 57 minutes to run on a standard PC, running an Intel® Core™ i3-3220 CPU @ 3.30 GHz, with 4 GB RAM; 4 Cores were utilised. A total of 256 models were run, representing the laser translation at 0.1 mm steps across the top of the test piece. A total running time of 10 days, 3 hours and 12 minutes elapsed for this case.

7.2.7 Post-processing

A script was written to open the model, increase the x-translation by 0.1 mm, shifting the generation and detection zones along the top surface, re-mesh the model and save it as an input file. A batch file was generated so that once all the input files were created, they were sequentially submitted for processing in the solver. Once all files had

been processed, an output database file (.odb) was created in each case. A second script was used to open each file sequentially and save an average of the y-direction displacement over the detection area, for each time step. A further macro was used to create an array for exporting the data to Matlab and a B-scan was then produced.

7.3 Modelling - Results and discussion

7.3.1 Modelling of M4

A B-scan generated from the LU data is shown in Figure 7-5 and the B-scan created using the modelled data over a 5 μs time window is shown in Figure 7-6; an annotated version is shown in Figure 7-7.

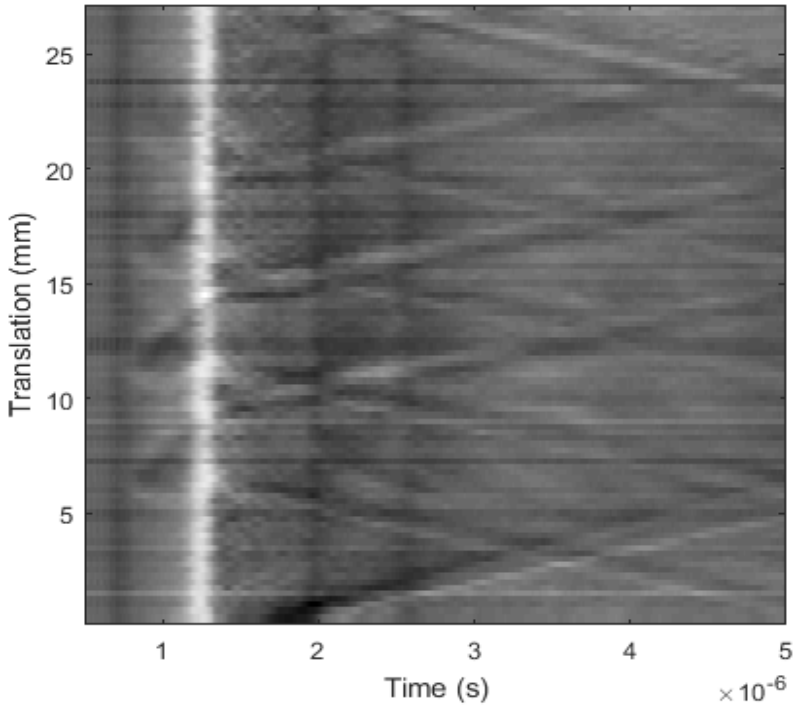

Figure 7-5 - B-scan generated in Matlab from LU data of M4.

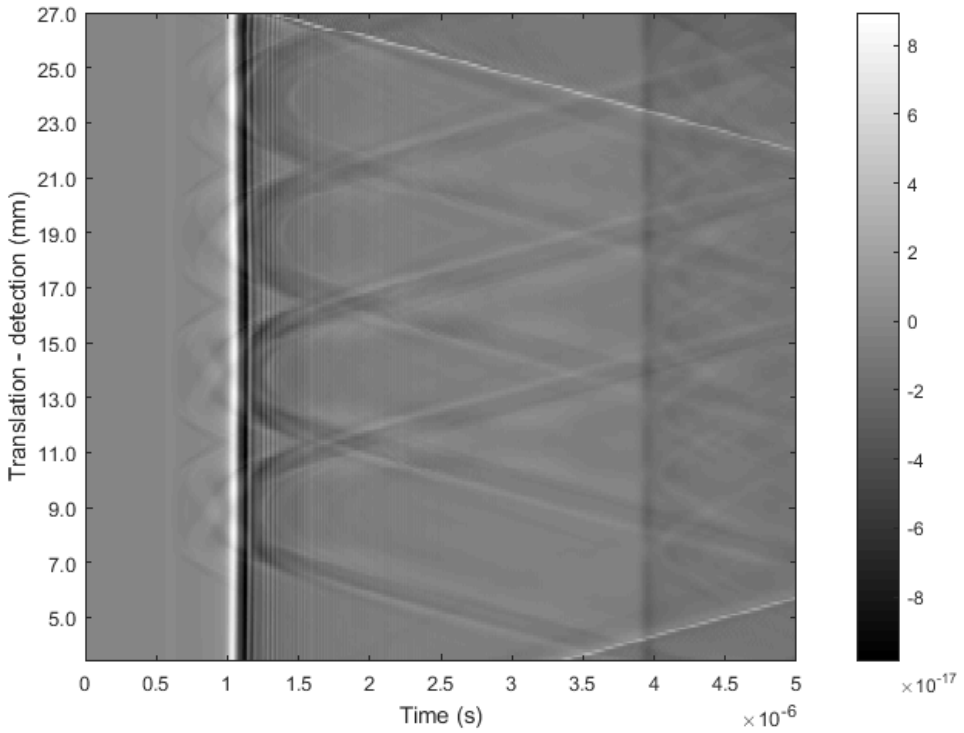

Figure 7-6 - B-scan generated in Matlab from modelled data of M4.

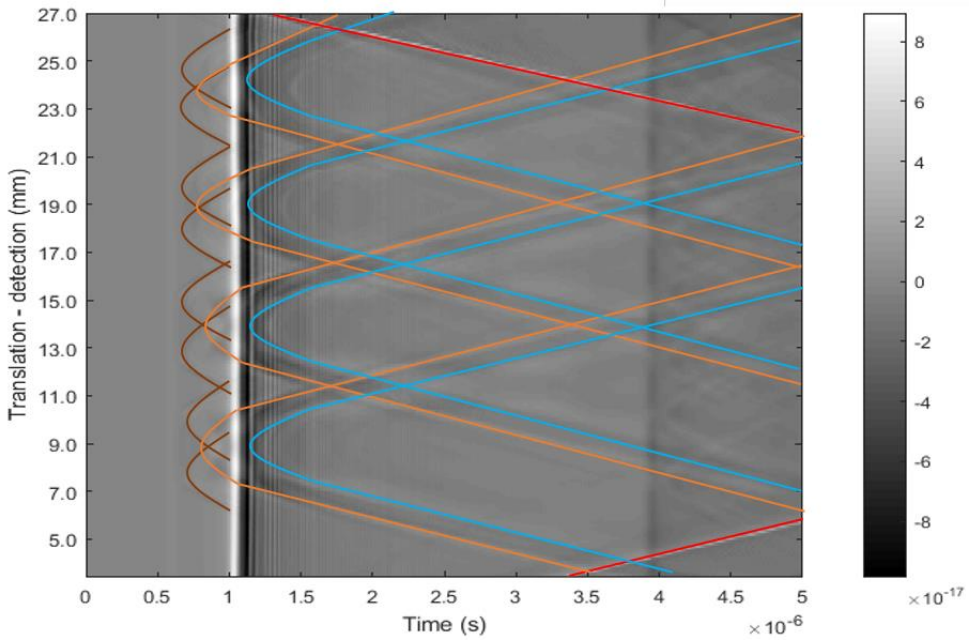

Figure 7-7 - B-scan generated in Matlab from modelled data of M4 annotated with wave arrivals and indications.

Generally, there is a good agreement between the B-scans produced by the two methods, for example, when comparing the wave arrivals. For the experimental case in Figure 7-5, four wave arrivals are apparent at 0.7s, 1.2s, 2.0s and 2.6s. These are indicative of the arrival of the skimming longitudinal wave, the arrival of the direct Rayleigh wave and the reflected longitudinal waves from the side walls, respectively. As the modelled case was only in 2D, the reflected waves from the side walls were not present, but the other two wave arrivals were. A third indication was seen at 4s in Figure 7-5, which was thought to be a mode-converted wave arriving. This was not seen experimentally and is thought to be due to the model being a simplified case.

In both cases, there were four parabolas with apexes spaced at 5 mm intervals, corresponding with the spacing of the manufactured through-holes or the holes/voids in the model. The lasers were translated from different starting positions, along different length scanning paths, accounting for the differences in translation position of the apexes in each B-scan.

In the modelled case, additional partial parabolas were seen in the region between the arrival of the reflected longitudinal wave and the direct Rayleigh wave arrival, these are shown in brown on Figure 7-7. The presence of these two extra parabolas for each "defect" in the reflected waves was thought to be caused by the longitudinal waves reflecting of the smoothed edge of the simulated hole, rather than caused by diffraction; this has been seen in studies of LU on DED samples with drilled holes [31, 136]. These extra parabolas are not present on the physically generated B-scan. This is thought to be because the manufacture of the through-holes by EDM does not yield a perfect surface so diffracted, rather than reflected waves are returned.

The resolution of the modelled B-scan could be improved by increasing the number of time-steps and by reducing the LU scan interval from 0.1 mm to a smaller value although both of these options would carry a computational cost.

7.3.2 Establishing a detection window

To begin establishing the window of detection, the same modelling methodology was used to model 100, 300 and 500 micron voids, at 300 μm and 1 mm distance from the top surface. A total of 80 models were run per case, representing the laser translation at 0.1 mm steps across the top of the test piece. A total run time of 3 days, 1 hour and 20 minutes elapsed per case. The resulting B-scans are shown below in Figure 7-8 to Figure 7-13:

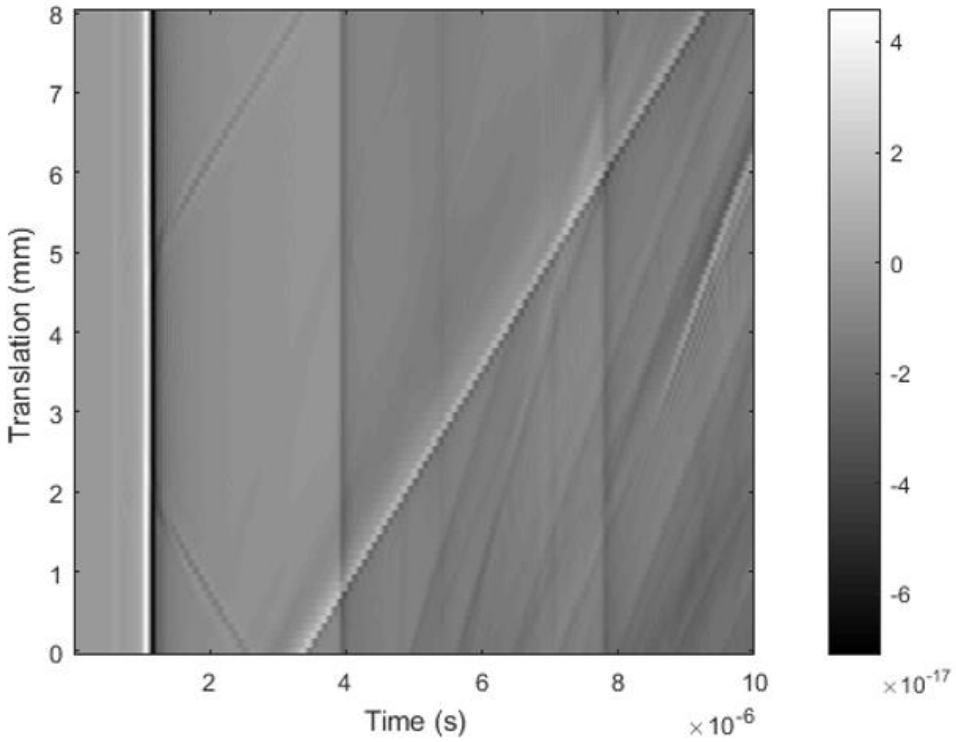

Figure 7-8 – B-scan of 2D modelled 100 μm diameter spherical pore at 300 um z-distance.

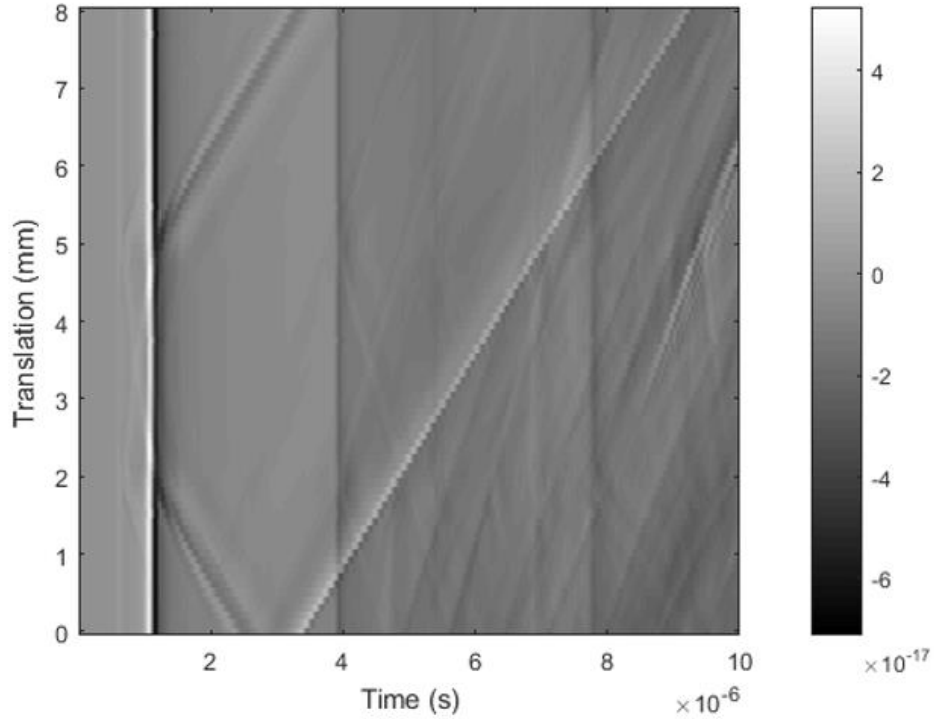

Figure 7-9 – B-scan of 2D modelled 300 μm diameter spherical pore at 300 um z-distance.

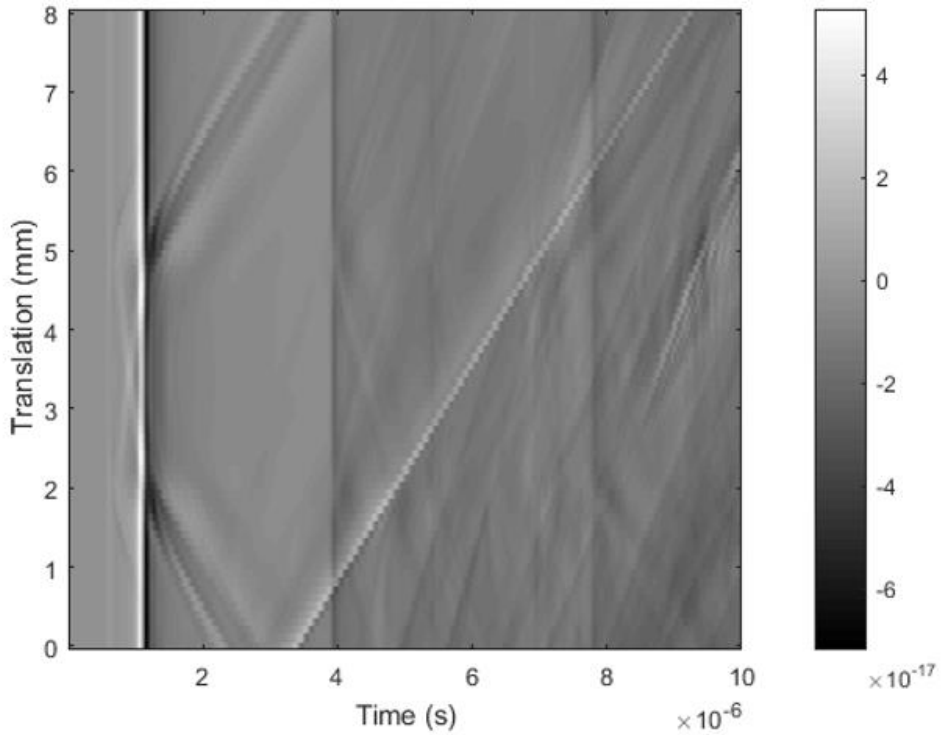

Figure 7-10 – B-scan of 2D modelled 500 μm diameter spherical pore at 300 um z-distance.

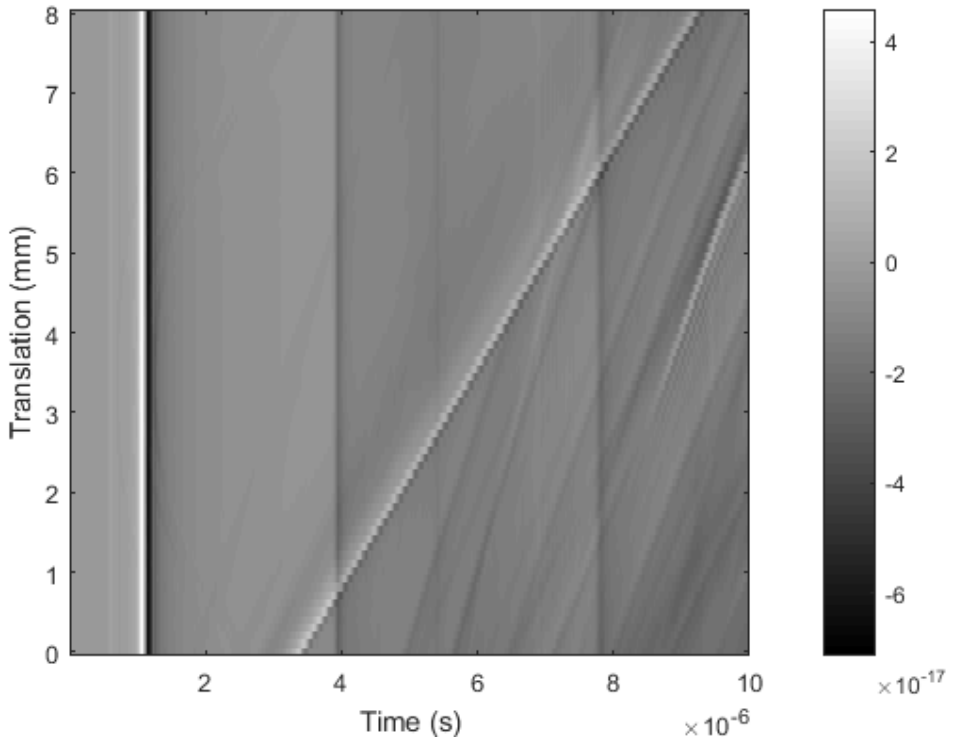

Figure 7-11 – B-scan of 2D modelled 100 μm diameter spherical pore at 1 mm z-distance.

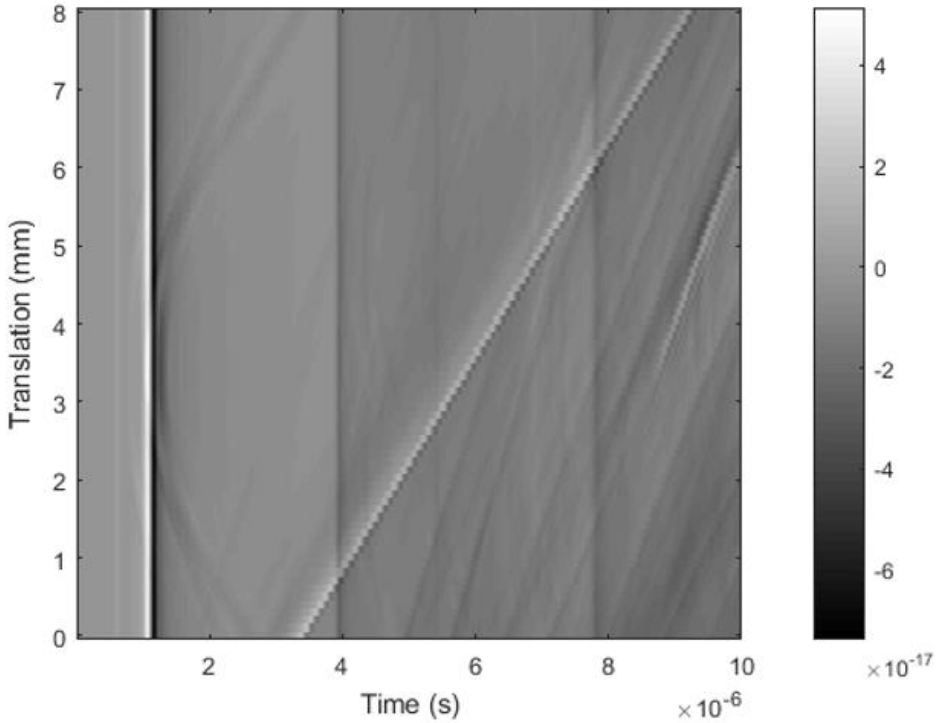

Figure 7-12 – B-scan of 2D modelled 300 μm diameter spherical pore at 1 mm z-distance.

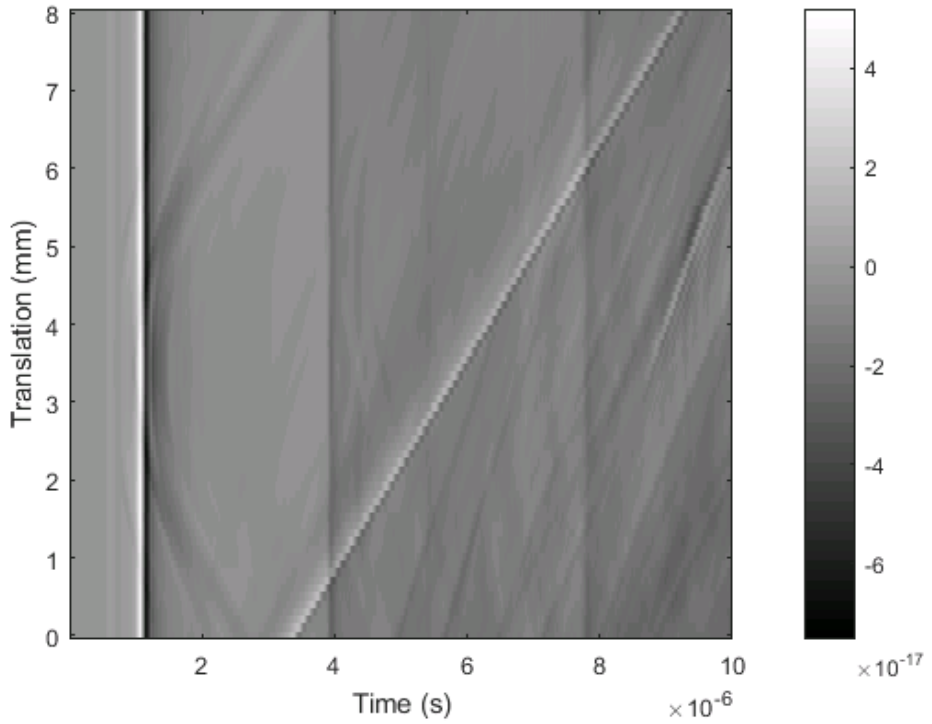

Figure 7-13 – B-scan of 2D modelled 500 μm diameter spherical pore at 1 mm z-distance.

Having generated B-scans from the modelled data, coloured lines have again been overlaid, to show the position of identified indications. An example is shown in Figure 7-14.

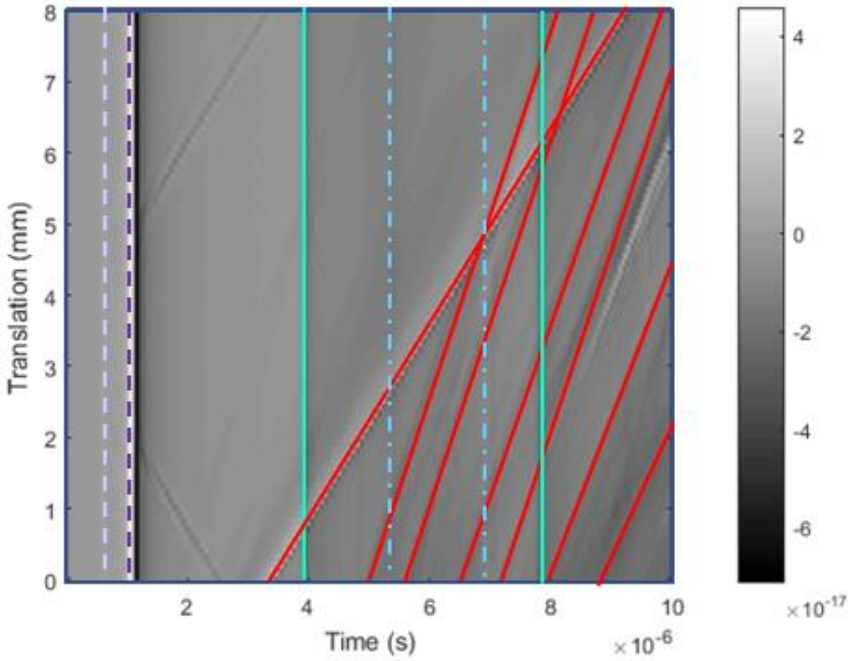

Figure 7-14 – B-scan of 2D modelled 100 μm diameter spherical pore at 300 um z-distance, overlaid with direct and reflected wave arrivals.

As the same part geometry was modelled, except for the size and position of the void, the same pattern of un-diffracted waves arrives in each case. More importantly, the changing arrival times of diffracted longitudinal and diffracted Rayleigh waves, caused by interaction with the void, did in some cases result in the characteristic parabolas seen experimentally. The raw B-scan shown in Figure 7-9, is overlaid with the unique wave arrivals in Figure 7-15.

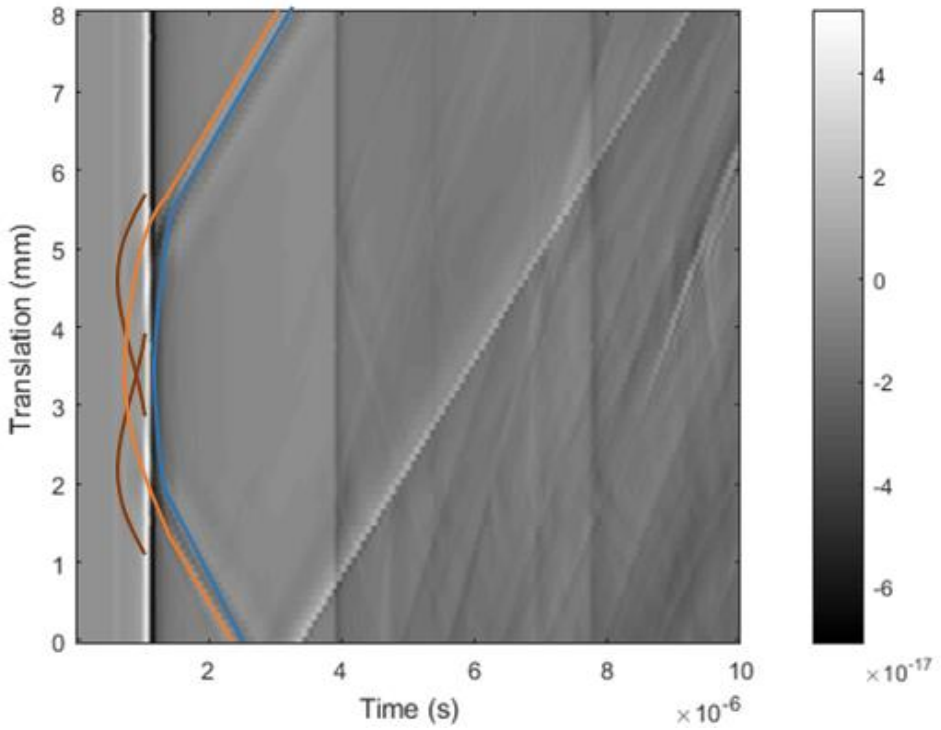

Figure 7-15 – B-scan of 2D modelled 300 μm diameter spherical pore at 300 um z-distance, overlaid with unique wave arrivals.

- The orange parabola marked the arrival of the diffracted direct longitudinal wave at the detector. The apex peaked at 3.5 mm translation, the known location of the centre of the void in the model.
- The blue parabola indicated the arrival of the diffracted Rayleigh wave and again, the apex matches the location of the 300 μm void.

- The brown partial parabolas were again seen in the modelled data. These are thought to be caused by the longitudinal waves reflecting of the smoothed edge of the void, rather than caused by diffraction of the wave.

For the series of voids at 300 µm z-distance, modelling of the 100 µm diameter void (Figure 7-8) yielded only an indication of a diffracted Rayleigh wave. The larger 300 µm and 500 µm voids (B-scans shown in Figure 7-9 and Figure 7-10) generated diffracted Rayleigh waves and also diffracted and reflected longitudinal waves with increasing contrast. The shape and positions of the diffracted wave indications appeared the same in both cases, however, the partial parabolas caused by the reflected longitudinal waves occurred over a wider translation distance as the void size increased. It was noted that the intersection of the two partial parabolas remained at 3.5 mm, the known position of the centre of the modelled void.

For the series of voids at 1 mm z-distance, a similar pattern occurred. No indications of diffracted waves were identified for the 100 µm void (Figure 7-11), suggesting that this void is outside the window of detection. The B-scans of the larger diameter 300 µm (Figure 7-12) and 500 µm (Figure 7-13) voids showed the diffracted and reflected waves with increasing definition. Again, the translation distance over which the reflected waves span increased with void size, as expected.

This modelling approach could be used, with some refinements, to establish the sensitivity of a LU system. Interpretation of the resulting data remains a manual task which is naturally subjective. Computational image analysis methods could be explored.

7.4 Modelling - Conclusions

The initial study carried out here has shown that laser ultrasound scanning of a Ti6Al4V test piece, with four simple voids can be modelled in 2D FEA using 'ABAQUS'. Comparison with the LU data revealed a good correlation of wave arrival times and positioning of diffracted direct waves caused by the presence of the "defects" in the experimental and modelled data.

This activity validates the modelling methodology to establish a window of LU for voids in this alloy. Initial modelling has already begun to establish the window for spherical "defects" in Ti6Al4V.

Although reasonable results have been obtained from 2D modelling of the LU system, limitations include the computational expense of modelling the accurate shape of a naturally occurring void. With greater computing resource, this methodology could be extended to include:

- 3D modelling which would enable of the interaction of the reflected, longitudinal waves from the side walls of a test piece, with the use of a higher specification machine.
- Detailed geometry of fully representative, more complex void shapes.
- Finer mesh for even higher accuracy.
- Detailed sensitivity analyses to identify key geometrical and material parameters, due to the reduced solver time.
- Modelling of AM surfaces.
- Modelling of noise sources (E.g. Pulsed laser generation, AM grain structures).

Implementation of the methodology presented above, with the adaptations suggested, would eliminate the need to manufacture numerous AM test pieces.

Chapter 8 – Discussion, conclusions, novelty & recommendations

8.1 Discussion

Prior to the practical work undertaken, a comprehensive review of globally published works has been carried out to collate information allowing the categorisation of different "defects" produced during laser PBF processing, based on their appearance. Explanations of the mechanisms by which these "defects" are generated are given and these are linked to the process inputs selected and the resulting processing conditions. Understanding the conditions under which "defects" are generated and simplifying the terminology used to describe these "defects" and their formation will aid the drive for quality improvement required for widespread implementation of the technology.

A lack of assurance of the quality of additively manufactured materials is currently limiting the widespread adoption of this technology. For powder bed fusion build machines, a range of non-destructive testing methods have been used in order to improve the quality of manufactured components and realise some of the potential benefits. Some of these methods have been aimed at aiding development of process understanding, whilst others have been installed solely with the goal of enabling in-situ inspection and ultimately, closed-loop control of the systems.

After a thorough review of the studies previously carried out, the opportunity to use a laser generated and detected ultrasound (LU) system to observe sub-surface material discontinuities was identified, with a view to implementing a system in-situ at a later date. A commercial system has been operated on laser powder bed fusion

(PBF) surfaces to detect a range of manufactured, seeded and process generated material discontinuities in Ti6Al4V samples, ex-situ.

Previous work had used LU on AM components with optically polished surfaces. The use of a photo-EMF detector in the interferometer in this system returned higher magnitude signal responses from the AM surfaces than from the less rough, wire-electrical discharge machined surfaces, enabling identification of more indications of waves, diffracted by material discontinuities, on the resulting B-scan images.

In Chapter 4, the results of LU scanning a series of test pieces with four through-holes manufactured by EDM, at various z-distances have been presented. The same systematic methodology outlined in section 4.3.1 was used for interrogation of all B-scans generated. Using this approach, all but four of the 48 through-holes were indicated on the B-scans in some way. The four unidentified holes were all in test pieces with an EDM surface finish. There were 20 holes with diameters in the range 0.563 – 0.708 mm, up to a z-distance of 0.622 mm and 15 with diameters in the range 0.963 – 1.241 mm, up to a z-distance of 1.148 mm were successfully identified from the LU B-scans (see Figure 4-20).

In Chapter 5, a method for seeding pores in AM samples by simply leaving a spherical void in the CAD build model was evaluated. In some instances a pore was seeded and could be identified using LU, however generation of the pores was not reliable. ImageJ analysis of the XCT scans revealed a level of naturally occurring, unintentionally manufactured pores, only some of which were found by LU. The void diameters and distances from the scanning path both sideways and into the sample have been recorded and used to create a window of detection for the LU system.

In some test pieces, the relatively high naturally occurring pore density created a high number of overlapping indications on the B-scans, which could be difficult to interpret. A comparison of the B-scans with those taken of a "defect-free" sample can be used to qualitatively assess the test pieces.

In Chapter 6, it was shown that it was possible to create test pieces with sub-surface zones of intentionally created porosity, through manipulation of AM build parameters. These test pieces could then be used to assess inspection techniques. LU indications of a range of voids from 46 μm to 307 μm diameter at z-distances from 38 μm to 411 μm have been successfully correlated with voids identified on the XCT images, along a 1037 μm LU scanning channel. The two voids "missed" by LU were both 43 μm diameter, at 300 μm z-distance, directly under the LU scanning path. Given the XCT voxel size of 38, it is reasonable to assume that all measurements have a possible error of ± 76 μm, so it is possible a false indication was given.

A level of naturally occurring porosity was noted from the XCT images, particularly at the right hand edge of the test pieces. This is suggestive of an inherent issue with the SLM50 AM build machine or the associated build software package. LU scanning of the AM sidewalls qualitatively indicated the presence of this porosity, supporting the results found in Chapter 5.

Generally, sub-surface porosity was found to diffract the direct Rayleigh waves and surface features diffracted the direct, skimming longitudinal waves.

The process of identifying the indications on the scans is recognised to be subjective. It is suggested that before LU is implemented as an ex-situ or in-situ measurement tool, further work is required to create a

library of acceptable and unacceptable B-scan images. This library would help to remove the subjectivity of a manual operator through training or could be used to assess the images computationally.

The study carried out in Chapter 7 has shown that laser ultrasound scanning of a Ti6Al4V test piece, with four simple voids can be modelled in 2D FEA using 'ABAQUS'. This activity validates the modelling methodology to establish a window of LU for voids in this alloy. In the future it is recommended that this modelling approach could be used to establish a window of detection for LU, without the need for manufacture of AM test pieces. This would allow many more "defect" sizes and shapes to be investigated along with many more materials, at a vastly reduced cost, and if sufficient computing power was available, in a shorter timeframe. A design of experiments approach could reduce the number of cases further.

8.2 Conclusions

- Information regarding the formation mechanism of laser PBF "defects" has been collated and the cyclic nature of "defect" formation highlighted.
- A method of seeding a single void in a laser PBF sample by leaving a void in the AM CAD model and a method to generate zones of porosity through manipulation of AM build parameters were evaluated and proved difficult.
- The capability of LU to detect "defects" when scanning laser PBF test pieces on as-built surfaces has been established using test pieces with large manufactured through-holes, seeded spherical pores and zones of porosity.
- A methodology was outlined to assess a LU B-scan, albeit subjectively. Eleven feature types were identified and correlated

with the expected physical behaviour of ultrasonic waves, using the time-of-flight technique.

- XCT was used to validate the LU results with FVM and destructive analyses employed where necessary.
- Diffracted direct longitudinal wave arrivals were linked to surface breaking "defects" and areas of surface undulation whilst diffracted Rayleigh waves were found to be indicative of sub-surface porosity. A spatial resolution of 500 μm was established between adjacent indications.
- Void diameter, depth below the top surface and distance radially from the LU scanning path need to be considered when stating the sensitivity of the system. The smallest void to have been indicated was 35 μm, well below the expected limit of detection of LU, however it was located only 43 μm below the top surface. The "deepest" void detected was 411 μm below the surface and the most extreme radial distance was 625 μm.
- Modelling was used to replicate the LU analysis of an experimentally scanned test piece, showing good correlation. A methodology was developed to computationally estimate the sensitivity of the LU system.

8.3 Novelty

The following points outline the novelty in this thesis:

- The comprehensive review of literature carried out in this project yielded a review paper, published in *Journal of Materials and Design*, summarising approaches taken for in-situ monitoring of powder bed fusion processes [16]. Additionally, the review of laser powder bed fusion "defect" types and generation mechanisms presented here is also unique.
- For the first time, laser ultrasound has been used:
    - to analyse laser powder bed fusion surfaces in their as-built condition.
    - to detect laser powder bed fusion "defects", intentionally manufactured through manipulation of the build file and build parameters.
- Modelling methodology for laser ultrasound, using sequential transient FEA analysis to create B-scans is novel and has been presented in this thesis.

8.4 Future work

A number of recommendations are made for future work to be carried out to enable use of LU for in-situ inspection of AM processing:

- Most importantly, characterisation of identified indications to allow quantitative assessment, rather than just qualitative evaluation should be pursued.
- LU in the ablation regime cannot be considered a non-destructive testing (NDT) technique as the surface of the test piece has been found to be scorched by the generation laser line, during assessment. The impact of this surface marking on bonding of subsequent AM layers and an assessment of the resulting change in elemental composition is recommended.
- LU was suggested for in-situ monitoring of AM systems due to its ability to work at high temperatures and in harsh environments – this has not been evaluated during this study and is an important consideration.
- Configuration of the measurement head optics systems to fit in the limited space inside an AM machine will be required. Utilising the AM operating lasers to perform LU could be explored.
- Currently, the time taken to LU scan a relatively short line compared to the total build area makes LU infeasible as an in-situ monitoring method. Reducing the number of averages and increasing the LU scan step size were evaluated in Chapter 4, but significant advancements are required for LU to be a viable choice.
- Modelling should be explored further in enable a window of detection for LU to be established, without the need for manufacture of AM test pieces. Many more “defect” sizes and

shapes in different materials could be investigated, at a vastly reduced cost. With sufficient computing power, this could also be achieved in a shorter timeframe and the option to model in 3D could be explored. A design of experiments approach could reduce the number of cases further.

- Creation of a "defect library" to aid manual interpretation of the generated images or computer image analysis methods should be explored to reduce or ideally remove the subjectivity of assessment.

8.5 Publications

Everton, S., Dickens, P., Tuck, C. and Dutton, B., **Using laser ultrasound to detect sub-surface defects in metal laser powder bed fusion components.** *Journal of Materials* 2018. 70(3), p.378-383.

Everton, S., Dickens, P., Tuck, C., Dutton, B., and Wimpenny, D., **The Use of Laser Ultrasound to Detect Defects in Laser Melted Parts**, in *TMS 2017 146th Annual Meeting & Exhibition Supplemental Proceedings*. p. 105-116.

Everton, S., Hirsh, M., Stravroulakis, P., Leach, R., Clare, A., **Review of in-situ process monitoring and in-situ metrology for metal additive manufacturing**. *Materials & Design* 2016. p.431-445.

Everton, S., Dickens, P., Tuck, C. and Dutton, B., **Identification of Sub-surface Defects in Parts Produced by Additive Manufacturing, Using Laser Generated Ultrasound**, in *Contributed Papers from Materials Science & Technology 2016*. Paper presented at MS&T16, Salt Lake City, UT, USA.

Everton, S., Dickens, P., Tuck, C., and Dutton, B. **Evaluation of laser ultrasonic testing for inspection of metal additive manufacturing**, in proceedings from *SPIE* 2015. Paper presented at SPIE 2015, San Francisco, CA, USA.

Chapter 9 - References

1. Wohlers, T.T., *Wohlers Report 2015*. Vol. 22. 2015: Wohlers Associates.
2. Nathan, S., *Aerospace takes to additive manufacturing*, in *The Engineer*. 2015, Centaur Communications Ltd: Online.
3. Energetics_Incorporated, *Measurement science roadmap for metal-based additive manufacturing*. 2013, National Institute of Standards and Technology: Maryland, US.
4. Additive_Manufacturing_UK, *National Strategy 2018-25*, J. Logan, Editor. 2017, UK Additive Manufacturing Steering Group.
5. Van Elsen, M., *Complexity of selective laser melting: A new optimisation approach*, in *Mechanical Engineering*. 2007, Katholieke Universiteit Leuven: Belgium. p. 31-42.
6. Gong, H., Rafi, K., Gu, H., Janaki Ram, G.D., Starr, T., and Stucker, B., *Influence of defects on mechanical properties of Ti–6Al–4 V components produced by selective laser melting and electron beam melting.* Materials & Design, 2015. **86**: p. 545-554.
7. Tammas-Williams, S., Zhao, H., Léonard, F., Derguti, F., Todd, I., and Prangnell, P.B., *XCT analysis of the influence of melt strategies on defect population in Ti–6Al–4V components manufactured by selective electron beam melting.* Materials Characterization, 2015. **102**(4): p. 47-61.
8. Olakanmi, E.O., Cochrane, R.F., and Dalgarno, K.W., *A review on selective laser sintering/melting (SLS/SLM) of aluminium alloy powders: Processing, microstructure, and properties.* Progress in Materials Science, 2015. **74**: p. 401-477.
9. Brandl, E., Heckenberger, U., Holzinger, V., and Buchbinder, D., *Additive manufactured AlSi10Mg samples using Selective Laser Melting (SLM): Microstructure, high cycle fatigue, and fracture behavior.* Materials & Design, 2012. **34**: p. 159-169.
10. Monroy, K., Delgado, J., and Ciurana, J., *Study of the pore formation on CoCrMo alloys by selective laser melting manufacturing process.* Procedia Engineering, 2013. **63**: p. 361-369.
11. Kempen, K., Thijs, L., Yasa, E., Badrossamay, M., Verheecke, W., and Kruth, J.P., *Process optimization and microstructural analysis for selective laser melting of AlSi10Mg*, in *Proc. of Solid Freeform Fabrication Symposium*. 2011: Austin, TX.
12. Gong, H., Gu, H., Dilip, J.J.S., Pal, D., and Stucker, B., *Melt pool characterization for selective laser melting of Ti-6Al-4V pre-alloyed powder*, in *Proc. of Solid Freeform Fabrication Symposium*. 2014: Austin, TX.

13. King, W.E., Barth, H.D., Castillo, V.M., Gallegos, G.F., Gibbs, J.W., Hahn, D.E., Kamath, C., and Rubenchik, A.M., *Observation of keyhole-mode laser melting in laser powder-bed fusion additive manufacturing.* Journal of Materials Processing Technology, 2014. **214**(12): p. 2915-2925.
14. Gong, H., Rafi, K., Starr, T., and Stucker, B. *The effects of processing parameters on defect regularity in Ti-6Al-4V parts fabricated by selective laser melting and electron beam melting*. in *Proc. of Solid Freeform Fabrication Symposium*. 2013. Austin, TX.
15. Yadroitsev, I., Krakhmalev, P., and Yadroitsava, I., *Hierarchical design principles of selective laser melting for high quality metallic objects.* Additive Manufacturing, 2015. **7**: p. 45-56.
16. Everton, S.K., Hirsch, M., Stravroulakis, P., Leach, R.K., and Clare, A.T., *Review of in-situ process monitoring and in-situ metrology for metal additive manufacturing.* Materials & Design, 2016. **95**: p. 431-445.
17. Schwerdtfeger, J., Singer, R.F., and Körner, C., *In situ flaw detection by IR-imaging during electron beam melting.* Rapid Prototyping Journal, 2012. **18**(4): p. 259-263.
18. Rodriguez , E., Medina, F., Espalin, D., Terraraz, C., Muse, D., Henry, C., MacDonald, E., and Wicker, R.B., *Integration of a thermal imaging feedback control system in electron beam melting*, in *Proc. of Solid Freeform Fabrication Symposium*. 2012: Austin, TX.
19. Price, S., Lydon, J., Cooper, K., and Chou, K., *Experimental temperature analysis of powder-based electron beam additive manufacturing*, in *Proc. of Solid Freeform Fabrication Symposium*. 2013, UT, Austin: Austin, TX.
20. Krauss, H., Eschey, C., and Zaeh, M.F., *Thermography for monitoring the selective laser melting process*, in *Proc. of Solid Freeform Fabrication Symposium*. 2012: Austin, TX.
21. Scharowsky, T., Bauereiß, A., Singer, R.F., and Körner, C., *Observation and numerical simulation of melt pool dynamic and beam powder interaction during selective electron beam melting* in *Proc. of Solid Freeform Fabrication Symposium*. 2012, UT, Austin: Austin, TX.
22. Berumen, S., Bechmann, F., Lindner, S., Kruth, J.-P., and Craeghs, T., *Quality control of laser- and powder bed-based Additive Manufacturing (AM) technologies.* Physics Procedia, 2010. **5**(Part B): p. 617-622.
23. Craeghs, T., Clijsters, S., Kruth, J.P., Bechmann, F., and Ebert, M.C., *Detection of process failures in layerwise laser melting with optical process monitoring.* Physics Procedia, 2012. **39**(1): p. 753-759.

24. Craeghs, T., Clijsters, S., Yasa, E., and Kruth, J.-P. *Online quality control of selective laser melting*. in *Proc. of Solid Freeform Fabrication Symposium*. 2011. Austin, TX.
25. Lott, P., Schleifenbaum, H., Meiners, W., Wissenbach, K., Hinke, C., and Bültmann, J., *Design of an optical system for the in situ process monitoring of selective laser melting (SLM).* Physics Procedia, 2011. **12**(Part A): p. 683-690.
26. Kleszczynski, S., zur Jacobsmühlen, J., Sehrt, J., and Witt, G. *Error detection in laser beam melting systems by high resolution imaging*. in *Proc. of Solid Freeform Fabrication Symposium*. 2012. Austin, TX.
27. Edwards, R.S., Dutton, B., Clough, A.R., and Rosli, M.H., *Scanning laser source and scanning laser detection techniques for different surface crack geometries*, in *Review of Progress in Quantitative Nondestructive Evaluation*. 2012, AIP Conference Proceedings: Burlington, VT. p. 251-258.
28. Klein, M., Sienicki, T., and Eichenbergeer, J., (2007). *Laser-ultrasonic detection of subsurface defects in processed metals. United States Patent, US7278315,* 4th October 2005.
29. Everton, S., Dickens, P., Tuck, C., and Dutton, B. *Evaluation of laser ultrasonic testing for inspection of metal additive manufacturing*. in *SPIE*. 2015. San Francisco, CA. US.
30. Santospirito, S.P., Łopatka, R., Cerniglia, D., Słyk, K., Luo, B., Panggabean, D., and Rudlin, J. *Defect detection in laser powder deposition components by laser thermography and laser ultrasonic inspections*. in *SPIE*. 2013. San Diego, CA.
31. Cerniglia, D., Scafidi, M., Pantano, A., and Rudlin, J., *Inspection of additive-manufactured layered components.* Ultrasonics, 2015. **62**: p. 292-298.
32. ISO/ASTM, *Standard Terminology for Additive Manufacturing - General Principles - Terminology*, in *ISO/ASTM 52900:2015(E)*. 2015, ISO: Geneva, Switzerland. p. 9.
33. AM_Special_Interest_Group, *Shaping our national competency in additive manufacturing*, T.S. Board, Editor. 2012, UK Government: Online.
34. ASTM, *Standard Specification for Additive Manufacturing File Format (AMF) Version 1.1*, in *F2915-12*. 2012, ASTM: United States. p. 15.
35. Materialise. *STL editor*. 2012 [cited 2013 28 November]; Available from: http://software.materialise.com/magics.
36. Karlsson, J., Snis, A., Engqvist, H., and Lausmaa, J., *Characterization and comparison of materials produced by Electron Beam Melting (EBM) of two different Ti–6Al–4V powder fractions.* Journal of Materials Processing Technology, 2013. **213**(12): p. 2109-2118.

37. Liu, B., Wildman, R., Tuck, C., Ashcroft, I., and Hague, R. *Investigation the effect of particle size distribution on processing parameters optimisation in Selective Laser Melting process*. in *Proc. of Solid Freeform Fabrication Symposium*. 2011. Austin, Texas, US.
38. Capus, J.M., *Metal Powders: A Global Survey of Production, Applications and Markets 2001-2010*. 2005: Elsevier Science.
39. Neikov, O.D., Naboychenko, S., Mourachova, I.B., Gopienko, V.G., Frishberg, I.V., and Lotsko, D.V., *Handbook of Non-Ferrous Metal Powders: Technologies and Applications*. 2009: Elsevier Science.
40. Ahsan, M.N., Pinkerton, A.J., Moat, R.J., and Shackleton, J., *A comparative study of laser direct metal deposition characteristics using gas and plasma-atomized Ti–6Al–4V powders.* Materials Science and Engineering: A, 2011. **528**(25–26): p. 7648-7657.
41. Murr, L.E., Martinez, E., Amato, K.N., Gaytan, S.M., Hernandez, J., Ramirez, D.A., Shindo, P.W., Medina, F., and Wicker, R.B., *Fabrication of Metal and Alloy Components by Additive Manufacturing: Examples of 3D Materials Science.* Journal of Materials Research and Technology, 2012. **1**(1): p. 42-54.
42. Dawes, J., Bowerman, R., and Trepleton, R., *Introduction to additive manufacturing powder metallurgy supply chain.* Johnson Matthey Technology Review, 2015. **59**(3): p. 243.
43. Sames, W.J., List, F.A., Pannala, S., Dehoff, R.R., and Babu, S.S., *The metallurgy and processing science of metal additive manufacturing.* International Materials Reviews, 2016. **61**(5): p. 315-360.
44. Van Elsen, M., *Complexity of selective laser melting: A new optimisation approach, EngD Thesis*, in *Mechanical Engineering*. 2007, Katholieke Universiteit Leuven: Belgium. p. 31-42.
45. Rafi, H.K., Karthik, N.V., Gong, H., Starr, T.L., and Stucker, B.E., *Microstructures and Mechanical Properties of Ti6Al4V Parts Fabricated by Selective Laser Melting and Electron Beam Melting.* Journal of Materials Engineering and Performance, 2013. **22**(12): p. 3872-3883.
46. Gibson, I., Rosen, D.W., and Stucker, B., *Additive Manufacturing Technologies: Rapid Prototyping to Direct Digital Manufacturing*. 2009: Springer.
47. Vayre, B., Vignat, F., and Villeneuve, F., *Identification on Some Design Key Parameters for Additive Manufacturing: Application on Electron Beam Melting.* Procedia CIRP, 2013. **7**(0): p. 264-269.

48. AB, A. *Schematic EBM setup*. [cited 2013 28 November]; Available from: http://www.arcam.com/technology/electron-beam-melting/hardware/.
49. Murr, L.E., Esquivel, E.V., Quinones, S.A., Gaytan, S.M., Lopez, M.I., Martinez, E.Y., Medina, F., Hernandez, D.H., Martinez, E., Martinez, J.L., Stafford, S.W., Brown, D.K., Hoppe, T., Meyers, W., Lindhe, U., and Wicker, R.B., *Microstructures and mechanical properties of electron beam-rapid manufactured Ti–6Al–4V biomedical prototypes compared to wrought Ti–6Al–4V.* Materials Characterization, 2009. **60**(2): p. 96-105.
50. Weiwei, H., Wenpeng, J., Haiyan, L., Huiping, T., Xinting, K., and Yu, H., *Research on Preheating of Titanium Alloy Powder in Electron Beam Melting Technology.* Rare Metal Materials and Engineering, 2011. **40**(12): p. 2072-2075.
51. Cormier, D., Harrysson, O., West, H., *Characterization of H13 steel produced via electron beam melting.* Rapid Prototyping Journal, 2004. **10**(1): p. 35-41.
52. Uriondo, A., Esperon-Miguez, M., and Perinpanayagam, S., *The present and future of additive manufacturing in the aerospace sector: A review of important aspects.* Proceedings of the Institution of Mechanical Engineers, Part G: Journal of Aerospace Engineering, 2015. **229**(11): p. 2132-2147.
53. Maskery, I., Aremu, A.O., Simonelli, M., Tuck, C., Wildman, R.D., Ashcroft, I.A., and Hague, R.J.M., *Mechanical Properties of Ti-6Al-4V Selectively Laser Melted Parts with Body-Centred-Cubic Lattices of Varying cell size.* Experimental Mechanics, 2015. **55**(7): p. 1261-1272.
54. Liu, W. and DuPont, J.N., *Effects of melt-pool geometry on crystal growth and microstructure development in laser surface-melted superalloy single crystals: Mathematical modeling of single-crystal growth in a melt pool (part I).* Acta Materialia, 2004. **52**(16): p. 4833-4847.
55. Weingarten, C., Buchbinder, D., Pirch, N., Meiners, W., Wissenbach, K., and Poprawe, R., *Formation and reduction of hydrogen porosity during selective laser melting of AlSi10Mg.* Journal of Materials Processing Technology, 2015. **221**: p. 112-120.
56. Gong, H., Rafi, K., Karthik, N.V., Starr, T., and Stucker, B. *Defect morphology in Ti-6Al-4V parts fabricated by Selective Laser Melting and Electron Beam Melting*. in *Proc. of Solid Freeform Fabrication Symposium*. 2013. Austin, TX.
57. Gong, H., Rafi, K., Gu, H., Starr, T., and Stucker, B., *Analysis of defect generation in Ti–6Al–4V parts made using powder bed fusion additive manufacturing processes.* Additive Manufacturing, 2014. **1–4**: p. 87-98.

58. Engeli, R., Etter, T., Hövel, S., and Wegener, K., *Processability of different IN738LC powder batches by selective laser melting.* Journal of Materials Processing Technology, 2016. **229**: p. 484-491.
59. Khairallah, S.A., Anderson, A.T., Rubenchik, A., and King, W.E., *Laser powder-bed fusion additive manufacturing: Physics of complex melt flow and formation mechanisms of pores, spatter, and denudation zones.* Acta Materialia, 2016. **108**: p. 36-45.
60. Thijs, L., Kempen, K., Kruth, J.P., and Van Humbeeck, J., *Fine-structured aluminium products with controllable texture by selective laser melting of pre-alloyed AlSi10Mg powder.* Acta Materialia, 2013. **61**(5): p. 1809-1819.
61. Yadroitsev, I., Bertrand, P., Antonenkova, G., Grigoriev, S., and Smurov, I., *Use of track/layer morphology to develop functional parts by selective laser melting.* Journal of Laser Applications, 2013. **25**(5): p. 052003.
62. Thijs, L., Verhaeghe, F., Craeghs, T., Humbeeck, J.V., and Kruth, J.-P., *A study of the microstructural evolution during selective laser melting of Ti–6Al–4V.* Acta Materialia, 2010. **58**(9): p. 3303-3312.
63. Matthews, M.J., Guss, G., Khairallah, S.A., Rubenchik, A.M., Depond, P.J., and King, W.E., *Denudation of metal powder layers in laser powder bed fusion processes.* Acta Materialia, 2016. **114**: p. 33-42.
64. Teng, C., Gong, H., Szabo, A., Dilip, J.J.S., Ashby, K., Zhang, S., Patil, N., Pal, D., and Stucker, B., *Simulating Melt Pool Shape and Lack of Fusion Porosity for Selective Laser Melting of Cobalt Chromium Components.* Journal of Manufacturing Science and Engineering, 2016. **139**(1): p. 011009-011009-11.
65. Qiu, C., Panwisawas, C., Ward, M., Basoalto, H.C., Brooks, J.W., and Attallah, M.M., *On the role of melt flow into the surface structure and porosity development during selective laser melting.* Acta Materialia, 2015. **96**: p. 72-79.
66. Pengpeng, Y. and Dongdong, G., *Molten pool behaviour and its physical mechanism during selective laser melting of TiC/AlSi10Mg nanocomposites: simulation and experiments.* Journal of Physics D: Applied Physics, 2015. **48**(3): p. 035303.
67. Zhou, X., Wang, D., Liu, X., Zhang, D., Qu, S., Ma, J., London, G., Shen, Z., and Liu, W., *3D-imaging of selective laser melting defects in a Co–Cr–Mo alloy by synchrotron radiation micro-CT.* Acta Materialia, 2015. **98**: p. 1-16.
68. Darvish, K., Chen, Z.W., and Pasang, T., *Reducing lack of fusion during selective laser melting of CoCrMo alloy: Effect of laser power on geometrical features of tracks.* Materials & Design, 2016. **112**: p. 357-366.

69. du Plessis, A., le Roux, S.G., Els, J., Booysen, G., and Blaine, D.C., *Application of microCT to the non-destructive testing of an additive manufactured titanium component.* Case Studies in Nondestructive Testing and Evaluation, 2015. **4**: p. 1-7.
70. Davis, J.R. and International, A., *ASM Materials Engineering Dictionary*. 1992: ASM International.
71. Mercelis, P. and Kruth, J.-P., *Residual stresses in selective laser sintering and selective laser melting.* Rapid Prototyping Journal, 2006. **12**(5): p. 254-264.
72. Kempen, K., Vrancken, B., Buls, S., Thijs, L., Van Humbeeck, J., and Kruth, J.-P., *Selective Laser Melting of Crack-Free High Density M2 High Speed Steel Parts by Baseplate Preheating.* Journal of Manufacturing Science and Engineering, 2014. **136**(6): p. 061026-1 - 061026-6.
73. Zaeh, M. and Branner, G., *Investigations on residual stresses and deformations in selective laser melting.* Production Engineering, 2010. **4**(1): p. 35-45.
74. Carter, L.N., Attallah, M.M., and Reed, R.C., *Laser Powder Bed Fabrication of Nickel-Base Superalloys: Influence of Parameters; Characterisation, Quantification and Mitigation of Cracking*, in *Superalloys 2012*. 2012, John Wiley & Sons, Inc. p. 577-586.
75. Carter, L.N., Martin, C., Withers, P.J., and Attallah, M.M., *The influence of the laser scan strategy on grain structure and cracking behaviour in SLM powder-bed fabricated nickel superalloy.* Journal of Alloys and Compounds, 2014. **615**: p. 338-347.
76. Lippold, J.C., Kiser, S.D., and DuPont, J.N., *Welding Metallurgy and Weldability of Nickel-Base Alloys*. 2011: John Wiley & Sons. 456.
77. Gu, H., Gong, H., Pal, D., Rafi, K., Starr, T., and Stucker, B., *Influences of energy density on porosity and microstructure of selective laser melted 17-4PH stainless steel*, in *Proc. of Solid Freeform Fabrication Symposium*. 2013: Austin, TX.
78. Cheng, B., Shrestha, S., and Chou, K., *Stress and deformation evaluations of scanning strategy effect in selective laser melting.* Additive Manufacturing, 2016. **12, Part B**: p. 240-251.
79. Harrison, N.J., Todd, I., and Mumtaz, K., *Reduction of micro-cracking in nickel superalloys processed by Selective Laser Melting: A fundamental alloy design approach.* Acta Materialia, 2015. **94**: p. 59-68.
80. Louvis, E., Fox, P., and Sutcliffe, C.J., *Selective laser melting of aluminium components.* Journal of Materials Processing Technology, 2011. **211**(2): p. 275-284.
81. Kruth, J.P., Froyen, L., Van Vaerenbergh, J., Mercelis, P., Rombouts, M., and Lauwers, B., *Selective laser melting of iron-*

based powder. Journal of Materials Processing Technology, 2004. **149**(1–3): p. 616-622.
82. Tolochko, N.K., Mozzharov, S.E., Yadroitsev, I.A., Laoui, T., Froyen, L., Titov, V.I., and Ignatiev, M.B., *Balling processes during selective laser treatment of powders.* Rapid Prototyping Journal, 2004. **10**(2): p. 78-87.
83. Olakanmi, E.O., *Selective laser sintering/melting (SLS/SLM) of pure Al, Al–Mg, and Al–Si powders: Effect of processing conditions and powder properties.* Journal of Materials Processing Technology, 2013. **213**(8): p. 1387-1405.
84. Simonelli, M., Tuck, C., Aboulkhair, N.T., Maskery, I., Ashcroft, I., Wildman, R.D., and Hague, R., *A Study on the Laser Spatter and the Oxidation Reactions During Selective Laser Melting of 316L Stainless Steel, Al-Si10-Mg, and Ti-6Al-4V.* Metallurgical and Materials Transactions A: Physical Metallurgy and Materials Science, 2015. **46**(9): p. 3842-3851.
85. Senin, N., Thompson, A., and Leach, R.K., *Characterisation of the topography of metal additive surface features with different measurement technologies.* Measurement Science and Technology, 2017.
86. Craeghs, T., Clijsters, S., Kruth, J.P., Bechmann, F., and Ebert, M.C., *Detection of Process Failures in Layerwise Laser Melting with Optical Process Monitoring.* Physics Procedia, 2012. **39**(0): p. 753-759.
87. Maskery, I., Aboulkhair, N.T., Corfield, M.R., Tuck, C., Clare, A.T., Leach, R.K., Wildman, R.D., Ashcroft, I.A., and Hague, R.J.M., *Quantification and characterisation of porosity in selectively laser melted Al–Si10–Mg using X-ray computed tomography.* Materials Characterization, 2016. **111**: p. 193-204.
88. Tammas-Williams, S., Zhao, H., Léonard, F., Derguti, F., Todd, I., and Prangnell, P.B., *XCT analysis of the influence of melt strategies on defect population in Ti–6Al–4V components manufactured by Selective Electron Beam Melting.* Materials Characterization, 2015. **102**: p. 47-61.
89. Karthik, N., Gu, H., Pal, D., Starr, T., and Stucker, B., *High Frequency Ultrasonic Non Destructive Evaluation of Additively Manufactured Components*, in *Proc. of Solid Freeform Fabrication Symposium*. 2013, UT Austin: Austin, TX.
90. Klein, M. and Sears, J. *Laser Ultrasonic Inspection of Laser Cladded 316LSS and Ti-6-4*. in *23rd, International congress on applications of lasers and electro-optics; ICALEO 2004*. 2004. Orlando, Florida: Laser Institute of America.
91. Sarrafzadeh, A., Churchill, R., and Niimura, M., *Laser Generated Ultrasound*, in *Acousto-Ultrasonics*. 1988, Springer. p. 201-207.

92. Scruby, C.B. and Drain, L.E., *Laser Ultrasonics Techniques and Applications*. 1990: Taylor & Francis.
93. Johnson, J.L., van Wijk, K., and Sabick, M., *Characterizing Phantom Arteries with Multi-channel Laser Ultrasonics and Photo-acoustics.* Ultrasound in Medicine & Biology, 2014. **40**(3): p. 513-520.
94. Blodgett, M.P. and Eylon, D., *The influence of texture and phase distortion on ultrasonic attenuation in Ti-6Al-4V.* Journal of Nondestructive Evaluation, 2001. **20**(1): p. 1-16.
95. Pelivanov, I., Buma, T., Xia, J., Wei, C.-W., and O'Donnell, M., *NDT of fiber-reinforced composites with a new fiber-optic pump–probe laser-ultrasound system.* Photoacoustics, 2014. **2**(2): p. 63-74.
96. Edwards, C., Stratoudaki, T., Dixon, S., and Palmer, S. *Laser generated ultrasound: efficiency and damage thresholds in carbon fibre reinforced composites*. IEE Proceedings - Science, Measurement and Technology, 2001. **148**, 139-142.
97. Dutton, B. and Dewhurst, R.J., *Anisotropy measurements in metal alloys using a laser/electromagnetic acoustic transducer array system.* Applied Physics Letters, 2006. **89**(10): p. 101916.
98. Svanström, E., Linder, T., and Löfqvist, T., *Analytical one-dimensional model for laser-induced ultrasound in planar optically absorbing layer.* Ultrasonics, 2014. **54**(3): p. 888-893.
99. Borg, M., Carlson, L., and Mishina, O. *Laser Ultrasonics for Examination of Defects in Aluminium Profiles*. in *European Conference on Non-Destructive Testing*. 2006. Berlin.
100. Dewhurst, R.J., Edwards, C., McKie, A.D.W., and Palmer, S.B., *Estimation of the thickness of thin metal sheet using laser generated ultrasound.* Applied Physics Letters, 1987. **51**(14): p. 1066-1068.
101. Carlson, L., Ericsson, M., and Lindh-Ulmgren, E., *Laser–Ultrasonics (LUS) for examination of structure changes and defects in aluminium*. 2005, KiMab Corrosion & Metals Research Institute: Sweden.
102. Davies, S.J., Edwards, C., Taylor, G.S., and Palmer, S.B., *Laser-generated ultrasound: Its properties, mechanisms and multifarious applications.* Journal of Physics D: Applied Physics, 1993. **26**(3): p. 329-348.
103. Paul, M., Haberer, B., and Arnold, W., *Materials characterization at high temperatures using laser ultrasound.* Materials Science and Engineering: A, 1993. **168**(1): p. 87-92.
104. Lane, C.J.L., Dunhill, T.K., Drinkwater, B.W., and Wilcox, P.D., *3D ultrasonic inspection of anisotropic aerospace components.* Insight - Non-Destructive Testing and Condition Monitoring, 2010. **52**(2): p. 72-77.

105. Dutton, B., Clough, A.R., Rosli, M.H., and Edwards, R.S., *Non-contact ultrasonic detection of angled surface defects.* NDT & E International, 2011. **44**(4): p. 353-360.
106. Dutton, B., Rosli, M.H., and Edwards, R.S., *Defect feature extraction using surface wave interactions and time-frequency behavior.* AIP Conference Proceedings, 2010. **1211**(1): p. 647-654.
107. Clough, A.R., Dutton, B., and Edwards, R.S. *Ultrasonic Rayleigh wave enhancements from angled defects in aluminium*. in *Progress in Quantitative Nondestructive Evaluation*. 2011.
108. Edwards, R.S., Dutton, B., Clough, A.R., and Rosli, M.H., *Scanning laser source and scanning laser detection techniques for different surface crack geometries.* AIP Conference Proceedings, 2012. **1430**(1): p. 251-258.
109. Dubois, M., Drake, T.E., and Klein, M., (2012). *Laser ultrasonic measurement system with movable beam delivery. United States, US8243280 B2,*
110. Clark, D. and Wright, D.C., (2009). *Methodof [sic] producing an object including testing and/or analysing of object. European, EP1815936 B1,*
111. Clark, D., Sharples, S.D., and Wright, D.C., *Development of online inspection for additive manufacturing products.* Insight - Non-Destructive Testing and Condition Monitoring, 2011. **53**(11): p. 610-613.
112. Cerniglia, D., Scafidi, M., Pantano, A., and Lopatka, R. *Laser Ultrasonic Technique for Laser Powder Deposition Inspection*. in *13th International Symposium on Nondestructive Characterization of Materials (NDCM-XIII)*. 2013. Le Mans, France.
113. *"ISO/TC 261: Additive manufacturing"*. 2011 [cited 2015 4th November]; Available from: http://www.iso.org/iso/home/standards_development/list_of_iso_technical_committees/iso_technical_committee.htm?commid=629086.
114. BS_ISO/ASTM_International, *Standard terminology for additive manufacturing: Coordinate systems and test methodologies*, in *ISO / ASTM52921 - 13*. 2013, ISO: Geneva, Switzerland.
115. BS_ISO/ASTM_International, *Standard specification for additive manufacturing file format (AMF) Version 1.2* in *ISO / ASTM52915:2016*. 2016, ISO: Geneva, Switzerland.
116. BS_ISO, *Additive manufacturing. General principles. Part 4: Overview of data processing* in *ISO 17296-4:2014*. 2014, ISO: Geneva, Switzerland.
117. BS_ISO, *Additive manufacturing. General principles. Part 3: Main characteristics and corresponding test methods* in *ISO 17296-3:2014*. 2014, ISO: Geneva, Switzerland.

118. BS_ISO, *Additive manufacturing. General principles. Part 2: Overview of process categories and feedstock*, in *ISO 17296-2:2015*. 2015, ISO: Geneva, Switzerland.
119. Jata, K.V., Kundu, T., and Parthasarathy, T.A., *An Introduction to Failure Mechanisms and Ultrasonic Inspection*, in *Ultrasonic Nondestructive Evaluation: Engineering and Biological Material Characterization*. 2003, Taylor & Francis.
120. Collaboration_for_Nondestructive_Testing, *Introduction to Ultrasonic Testing*. 1996, NDT Resource Centre.
121. Scruby, C.B. and Moss, B.C., *The Launching of Rayleigh Waves from Surface Point Sources*, in *Rayleigh-Wave Theory and Application: Proceedings of an International Symposium Organised by The Rank Prize Funds at The Royal Institution, London, 15–17 July, 1985*, E.A. Ash and E.G.S. Paige, Editors. 1985, Springer Berlin Heidelberg: Berlin, Heidelberg. p. 102-109.
122. Abbate, A., Koay, J., Frankel, J., Schroeder, S.C., and Das, P. *Application of wavelet transform signal processor to ultrasound*. in *Ultrasonics Symposium*. 1994.
123. Hedin, A., Carlson, L., and Borg, M. *Defect Detection by Laser-Ultrasonics in Friction Stir Welded Joints in Aluminium Profiles*. in *1st International Symposium on Laser Ultrasonics: Science, Technology and Applications*. 2008. Montreal, Canada.
124. Gusev, V.Ė. and Karaboutov, A.A., *Laser Optoacoustics*. 1993, United States: American Institute of Physics.
125. Edwards, R.S., Dutton, B., and Clough, A.R., *Interaction of laser generated ultrasonic waves with wedge-shaped samples.* Applied Physics Letters, 2012. **100**(18): p. 184102.
126. Scruby, C.B., *The Evaluation of Materials and Structures by Quantitative Ultrasonics*. 1993: Springer Verlag.
127. Dewhurst, R.J. and Shan, Q., *Optical remote measurement of ultrasound.* Measurement Science and Technology, 1999. **10**(11): p. R139.
128. Murfin, A.S., Soden, R.A.J., Hatrick, D., and Dewhurst, R.J., *Laser-ultrasound detection systems: a comparative study with Rayleigh waves.* Measurement Science and Technology, 2000. **11**(8): p. 1208.
129. Klein, M.B. and Bacher, G.D. *Design and engineering of photorefractive materials for use in adaptive laser ultrasonic receivers*. 1998.
130. Thompson, A., Senin, N., Giusca, C., and Leach, R., *Topography of selectively laser melted surfaces: A comparison of different measurement methods.* CIRP Annals, 2017. **66**(1): p. 543-546.
131. Pantano, A. and Cerniglia, D., *Simulation of laser generated ultrasound with application to defect detection.* Applied Physics A, 2008. **91**(3): p. 521-528.

132. Moser, F., Jacobs, L.J., and Qu, J., *Modeling elastic wave propagation in waveguides with the finite element method.* NDT & E International, 1999. **32**(4): p. 225-234.
133. Boyer, R., Welsch, G., and Collings, E.W., *Materials Properties Handbook: Titanium Alloys*. 1994, Materials Park, OH: ASM International.
134. van Dalen, K.N., *Multi-Component Acoustic Characterization of Porous Media*. 2013: Springer Berlin Heidelberg.
135. Achenbach, J.D., *MATHEMATICAL MODELING FOR QUANTITATIVE ULTRASONICS.* Nondestructive Testing and Evaluation, 1992. **8-9**(1-6): p. 363-377.
136. Scafidi, M., Cerniglia, D., and Ingrassia, T., *2D size, position and shape definition of defects by B-scan image analysis.* 2015, 2015(34).

Chapter 10 - Appendices

10.1 Post-build defects – annotated B-scans for M1-12

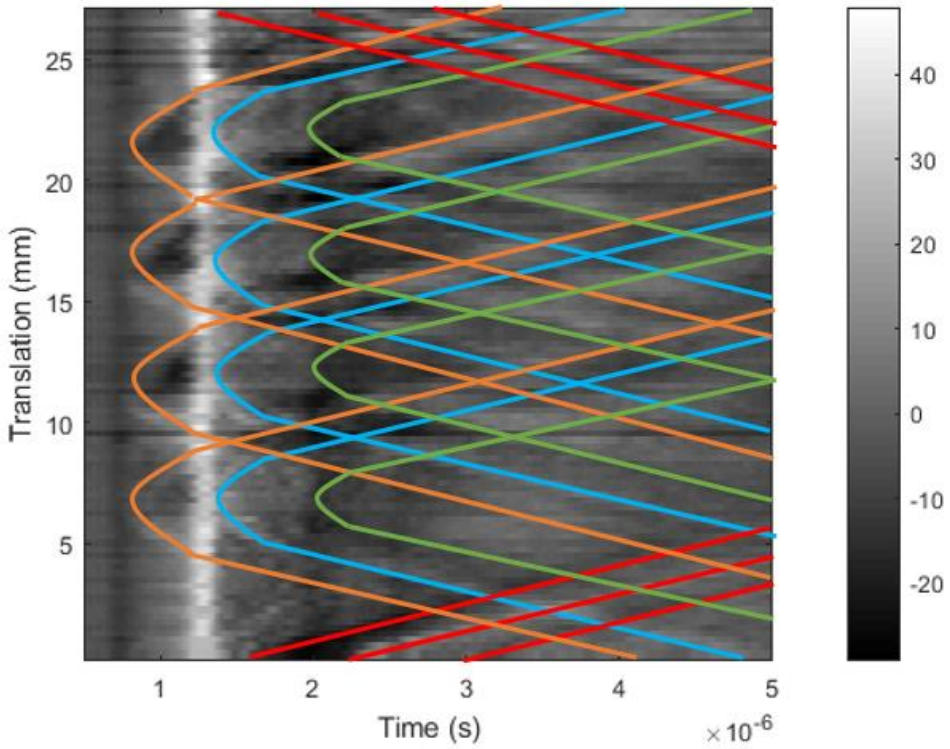

Figure 10-1 - B-scan of M1 (AM, as-built top surface), overlaid with wave arrivals and indications.

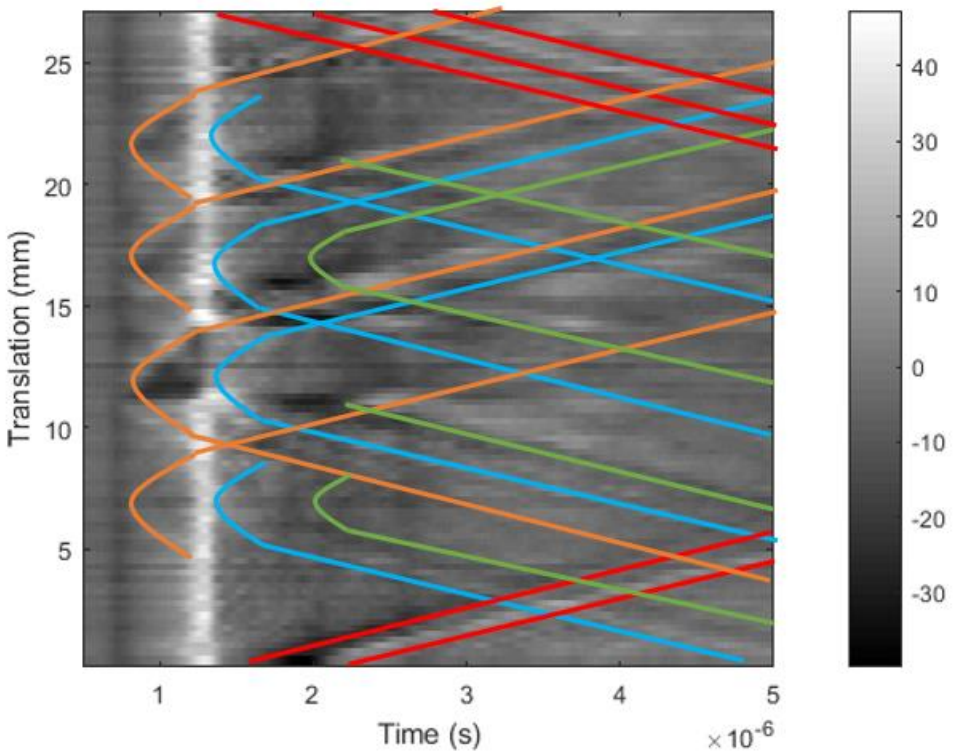

Figure 10-2 - B-scan of M2 (AM, as-built top surface), overlaid with wave arrivals and indications.

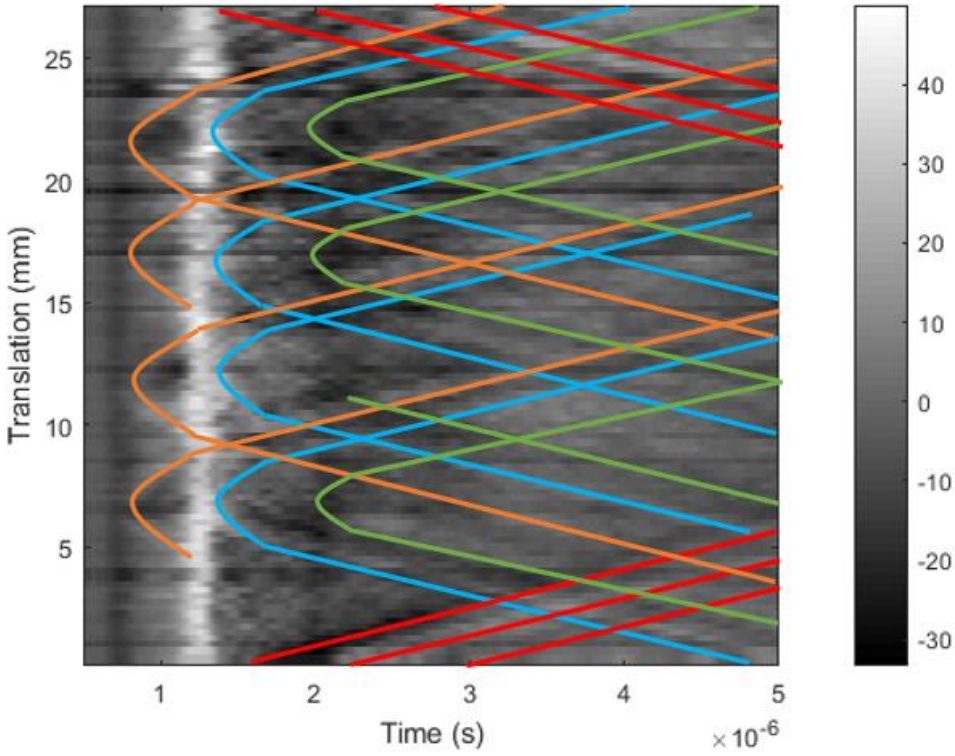

Figure 10-3 - B-scan of M3 (AM, as-built top surface), overlaid with wave arrivals and indications.

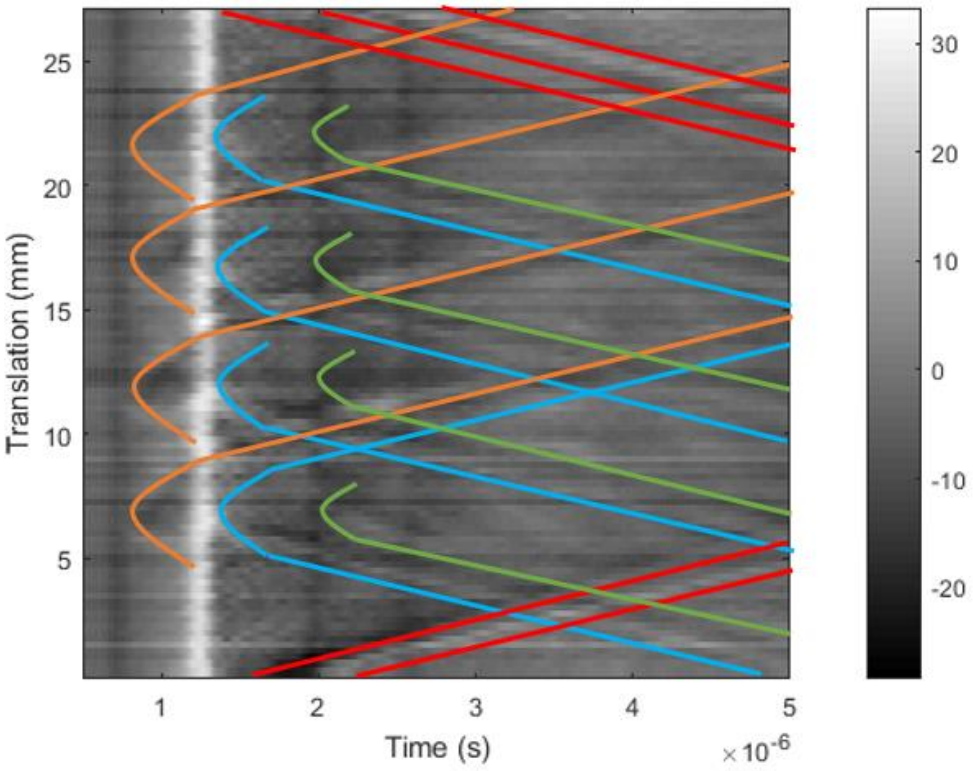

Figure 10-4 - B-scan of M4 (AM, as-built top surface), overlaid with wave arrivals and indications.

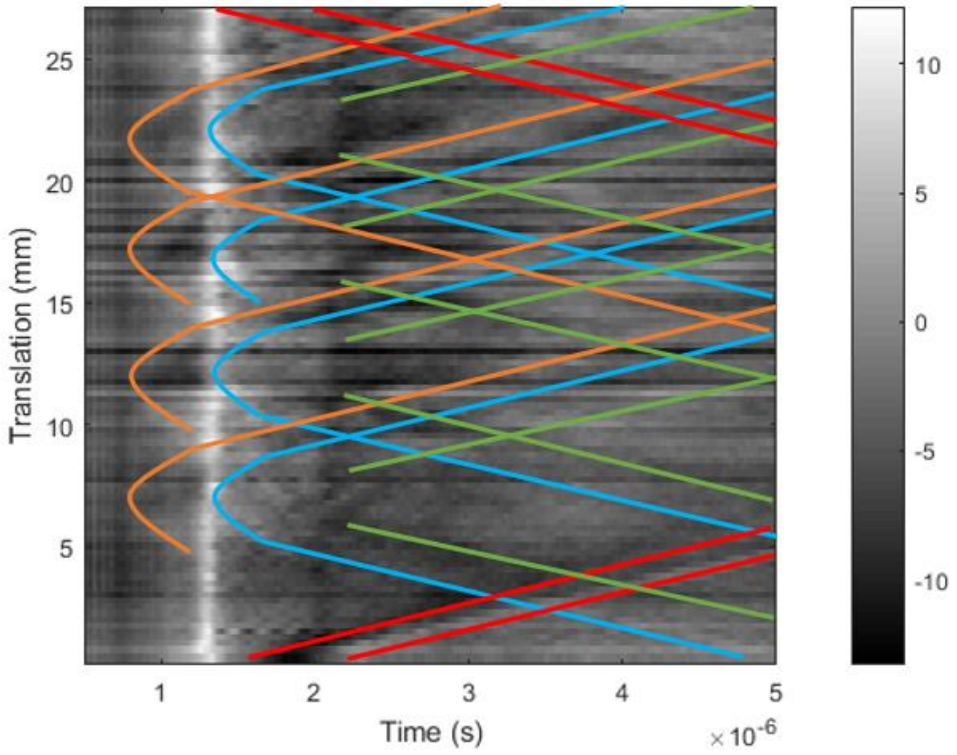

Figure 10-5 - B-scan of M5 (AM, EDM top surface), overlaid with wave arrivals and indications.

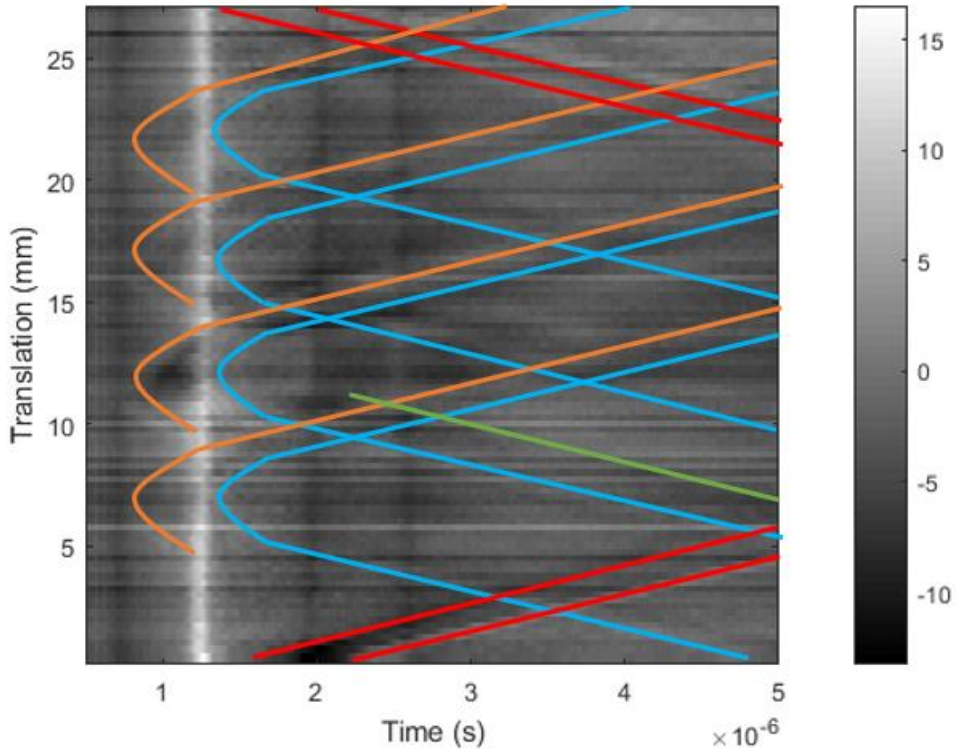

Figure 10-6 - B-scan of M6 (AM, EDM top surface), overlaid with wave arrivals and indications.

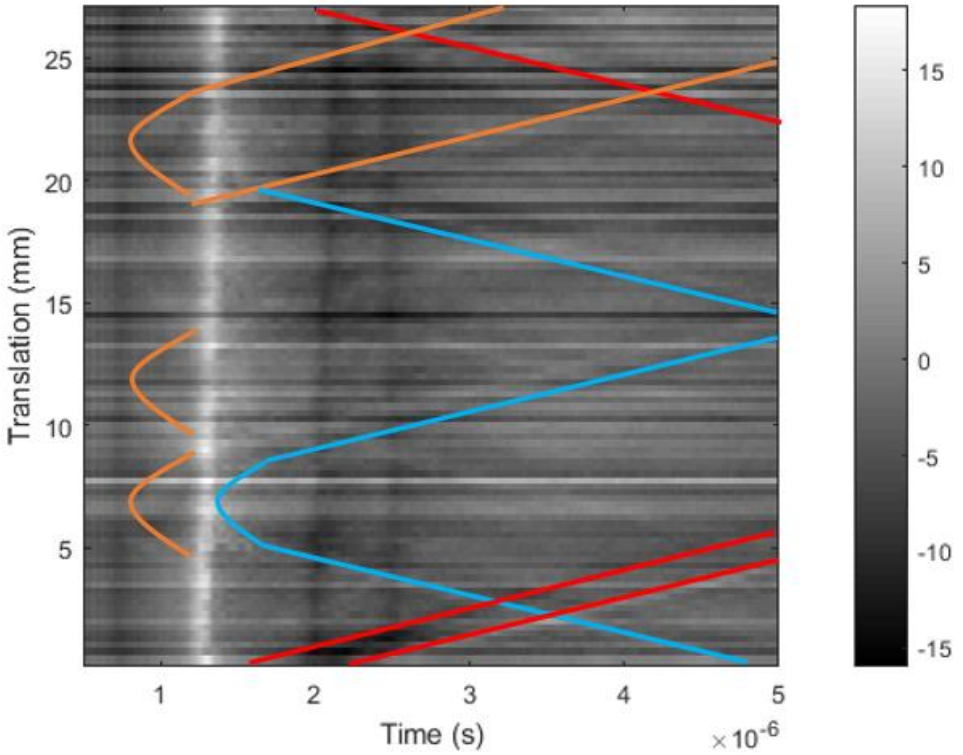

Figure 10-7 - B-scan of M7 (AM, EDM top surface), overlaid with wave arrivals and indications.

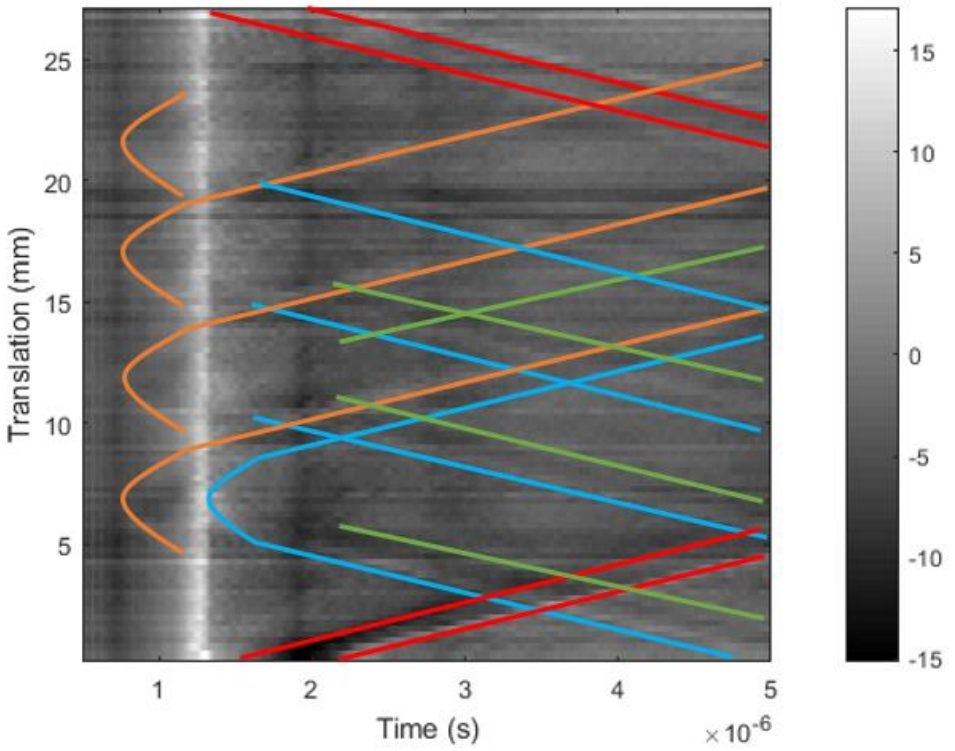

Figure 10-8 - B-scan of M8 (AM, EDM top surface), overlaid with wave arrivals and indications.

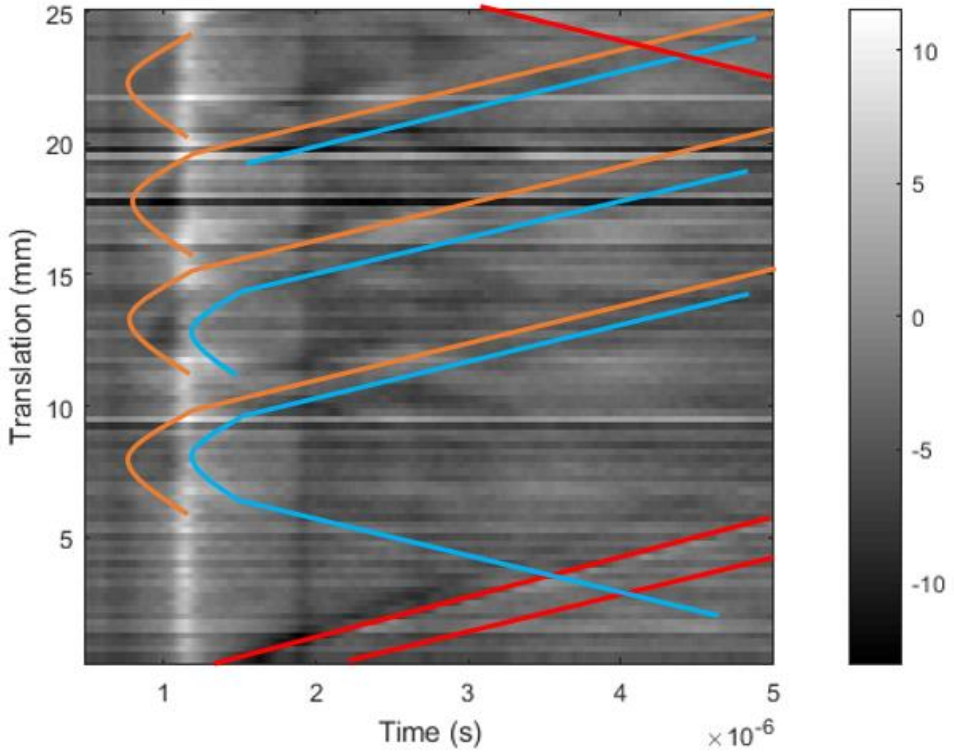

Figure 10-9 - B-scan of M9 (Billet, EDM top surface), overlaid with wave arrivals and indications.

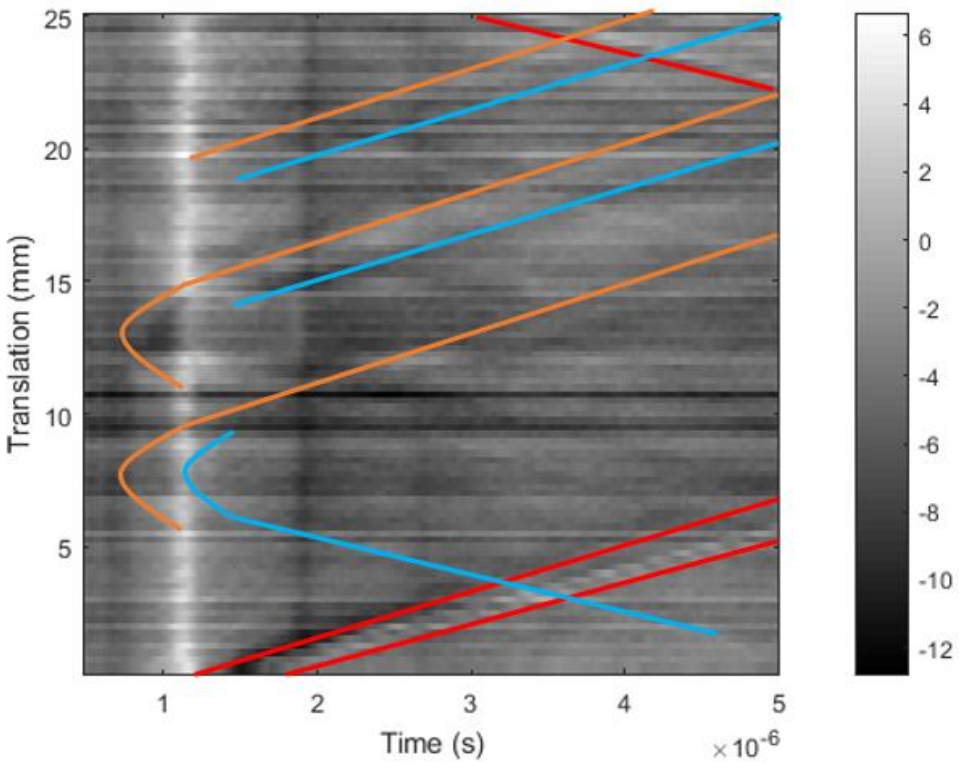

Figure 10-10 - B-scan of M10 (Billet, EDM top surface), overlaid with wave arrivals and indications.

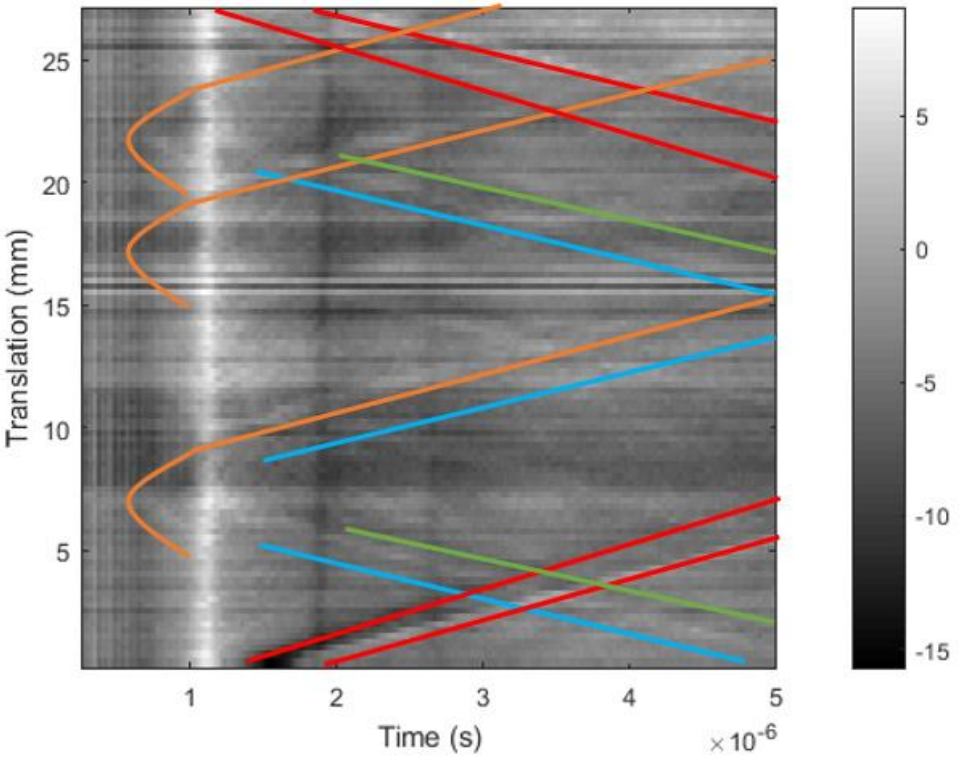

Figure 10-11 - B-scan of M11 (Billet, EDM top surface), overlaid with wave arrivals and indications.

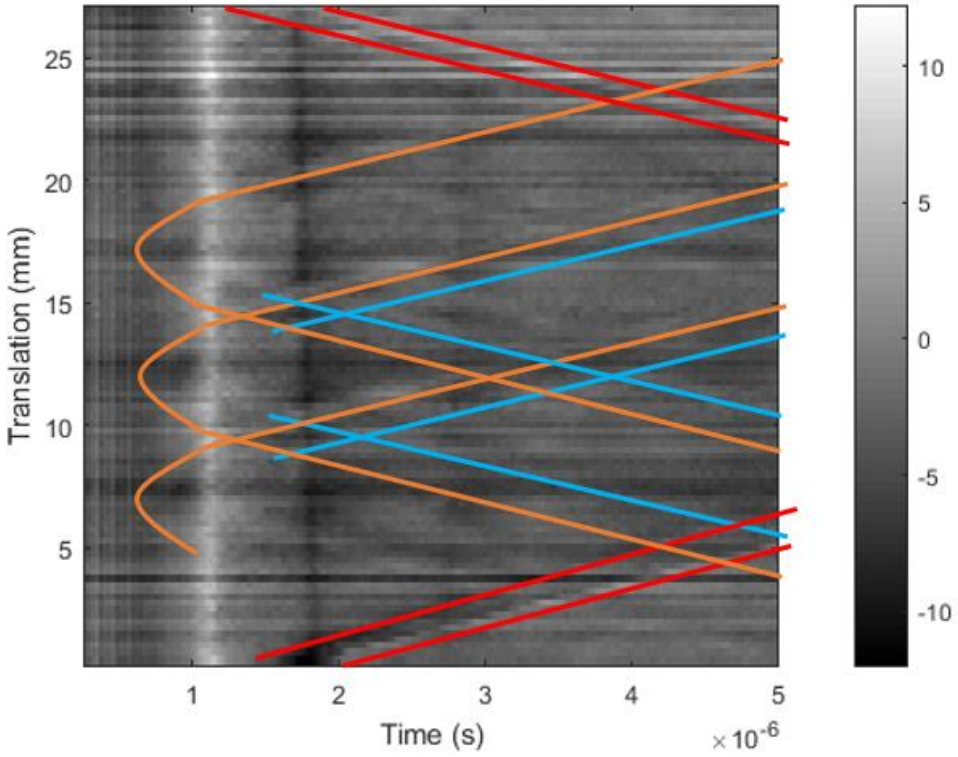

Figure 10-12 - B-scan of M12 (Billet, EDM top surface), overlaid with wave arrivals and indications.